

## **IONOSPHERIC MEASUREMENTS IN THE WAKE OF SOLAR MAXIMUM**

**Angela M. Andreasen  
John Begenesich  
Edward Fremouw  
Elizabeth Holland  
Andrew J. Mazzella, Jr.**

**Jens Ostergaard  
John Rasmussen  
James A. Secan  
A. Lee Snyder**

**NorthWest Research Associates  
14508 NE 20<sup>th</sup> St.  
P. O. Box 3027  
Bellevue, WA 98009-3027**

**30 April 2004**

**Final Report**

**APPROVED FOR PUBLIC RELEASE; DISTRIBUTION UNLIMITED**

**20041105 117**



**AIR FORCE RESEARCH LABORATORY  
Space Vehicles Directorate  
29 Randolph Rd  
AIR FORCE MATERIEL COMMAND  
Hanscom AFB, MA 01731-3010**

This technical report has been reviewed and is approved for publication.

/Signed/  
GREGORY BISHOP  
Contract Manager

/Signed/  
ROBERT A. MORRIS  
Branch Chief

This document has been reviewed by the ESC Public Affairs Office and has been approved for release to the National Technical Information Service.

Qualified requestors may obtain additional copies from the Defense Technical Information Center (DTIC). All others should apply to the National Technical Information Service.

If your address has changed, if you wish to be removed from the mailing list, or if the addressee is no longer employed by your organization, please notify AFRL/VSIM, 29 Randolph Rd., Hanscom AFB, MA 01731-3010. This will assist us in maintaining a current mailing list.

Do not return copies of this report unless contractual obligations or notices on a specific document require that it be returned.

REPORT DOCUMENTATION PAGE				Form Approved OMB No. 0704-0188	
Public reporting burden for this collection of information is estimated to average 1 hour per response, including the time for reviewing instructions, searching existing data sources, gathering and maintaining the data needed, and completing and reviewing this collection of information. Send comments regarding this burden estimate or any other aspect of this collection of information, including suggestions for reducing this burden to Department of Defense, Washington Headquarters Services, Directorate for Information Operations and Reports (0704-0188), 1215 Jefferson Davis Highway, Suite 1204, Arlington, VA 22202-4302. Respondents should be aware that notwithstanding any other provision of law, no person shall be subject to any penalty for failing to comply with a collection of information if it does not display a currently valid OMB control number. <b>PLEASE DO NOT RETURN YOUR FORM TO THE ABOVE ADDRESS.</b>					
1. REPORT DATE (DD-MM-YYYY) 30-04-2004		2. REPORT TYPE Final Report		3. DATES COVERED (From - To) 01 January 2001 - 31 March 2004	
4. TITLE AND SUBTITLE Ionospheric Measurements in the Wake of Solar Maximum				5a. CONTRACT NUMBER F19628-01-C-0005	
				5b. GRANT NUMBER	
				5c. PROGRAM ELEMENT NUMBER	
6. AUTHOR(S) A. M. Andreasen, J. Begenesich, E. J. Fremouw, E. A. Holland, A. J. Mazzella, Jr., J. Ostergaard, John Rasmussen, James A. Secan, A. Lee Snyder				5d. PROJECT NUMBER 4827	
				5e. TASK NUMBER HR	
				5f. WORK UNIT NUMBER A1	
7. PERFORMING ORGANIZATION(S) AND ADDRESS(ES)  NorthWest Research Associates 14508 NE 20 <sup>th</sup> St. PO Box 3027 Bellevue, WA 98009-3027				8. PERFORMING ORGANIZATION REPORT NUMBER NWRA-BeCR-04-R274	
9. SPONSORING / MONITORING AGENCY NAME(S) AND ADDRESS(ES) Air Force Research Laboratory 29 Randolph Road Hanscom AFB, MA 01731-3010 Contract Manager: Gregory Bishop/VSBXP				10. SPONSOR/MONITOR'S ACRONYM(S) AFRL/VSBXP	
				11. SPONSOR/MONITOR'S REPORT NUMBER(S) AFRL-VS-HA-TR-2004-1125	
12. DISTRIBUTION / AVAILABILITY STATEMENT					
13. SUPPLEMENTARY NOTES					
14. ABSTRACT During three years following the solar maximum of the year 2000, NorthWest Research Associates (NWRA) conducted ionospheric measurements at several Air Force research and operational locations and analyzed the data collected thereby. The measurements were performed using a variety of radiowave techniques, most involving transionospheric radio propagation, and included observations of ionospheric perturbations via high-power transmissions under the High-frequency Active Auroral Research Program (HAARP). Notable among the instruments employed were the Air Force Ionospheric Measuring System (AN/GMQ-35) and the NWRA ITS10S coherent radio receiving system. The primary measurements were of ionospheric total electron content (TEC) and radiowave scintillation, for describing the ionosphere and its plasma-density structures during this solar epoch and under the perturbing influence of HAARP. Records of TEC were inverted tomographically to produce two-dimensional (altitude vs. latitude) images of plasma density. By these and other means, ionospheric features such as the main F-layer trough and polar patches were characterized for application to Air Force environmental models.					
15. SUBJECT TERMS Air Force Ionospheric Measuring System (IMS), Ionosphere, Ionospheric tomography, Navy Ionospheric Monitoring System (NIMS), Polar cap, Radiowave scintillation, Total Electron Content (TEC)					
16. SECURITY CLASSIFICATION OF: NONE			17. LIMITATION OF ABSTRACT	18. NUMBER OF PAGES	19a. NAME OF RESPONSIBLE PERSON
a. REPORT	b. ABSTRACT	c. THIS PAGE			Gregory Bishop
U	U	U	SAR	138	19b. TELEPHONE NUMBER (include area code) (781) 377-3036

# Contents

Figures .....	v
Tables .....	x
Acknowledgements .....	xi
List of Symbols, Abbreviations, and Acronyms .....	xii
1. Project Objectives .....	1
2. Non-HAARP GPS Topics .....	1
2.1 Ionospheric Measuring System (IMS) .....	1
2.1.1 IMS Upgrade .....	1
2.1.2 IMS Documentation .....	17
2.2 Measurements of Polar Patches.....	19
3. Data Collection to Support Polar-cap Modeling .....	21
3.1 Thule/GPS STEL Data Set .....	21
3.2 Thule/GPS IMS Data Set .....	22
3.3 Qaanaaq/GPS RTM Data Set .....	22
3.4 Qaanaaq/LEO ITS10S Data Set .....	24
4. HAARP Topics .....	26
4.1 The Natural Ionosphere .....	26
4.1.2 Ionospheric Research Employing GPS .....	26
4.1.3 Ionospheric Research Employing LEO Satellites .....	27
4.1.3.1 Data Recorded .....	27
4.1.3.2 Tomographic Imaging .....	29
4.1.2.2.1 Procedures .....	29
4.1.2.2.2 Application to Trough Characterization.....	36
4.1.3.3 Enhancements to the NWRA Tomographic Inversion Processor .....	37
4.1.2.3.1 Imposing Positivity .....	37
4.1.2.3.2 Assimilating Complimentary Data.....	40
4.2 The Ionosphere Perturbed by HF Heating.....	45
5. Publications and Presentations .....	54
References .....	57
Appendix A Revised IMS Archive Data File.....	59
Appendix B File Formats for Processed IMS TEC and Scintillation Data .....	63
Appendix C Description of Software for IMS 20-Hz Scintillation Analysis.....	67



C.1 IMS Software.....	67
C.2 Test Results.....	69
C.3 Issues for Further Study.....	75
Addendum .....	81
Appendix D GPS Scintillation Studies.....	83
D.1 Benchtop Testing at WPAFB .....	83
D.1.1 No Scintillation.....	84
D.1.2 Wideband Simulation .....	84
D.1.2.1 Phase Results .....	88
D.1.2.2 Intensity Results .....	94
D.1.3 Tones Simulation.....	99
D.2 Analysis of Nashua Z-12 Data .....	105
D.3 Analysis of Ascension Island Z-12 Data.....	109
Appendix E Consultant Support under NWRA Sub-project AFRL-0005.24 .....	113
Appendix F Consultant Support under NWRA Sub-projects AFRL-0005.24 & AFRL-0005.28 ..	117
Appendix G Consultant Support of the HAARP Classic Riometer under NWRA Sub-project AFRL-0005.24.....	125
Maintenance and Data-quality Assurance .....	125
Computation of Quiet-day Curves.....	125
Design and Construction of a New Riometer .....	125
Appendix H ITS10S/Tomography Data Flow and Archiving Procedures.....	127
Computers Used .....	127
Acquiring Relative Slant-path TEC from the ITS10-S Receivers .....	127
Automatically Retrieving Missing Data from the Remote ITS10S Sites.....	128
Onto the World Wide Web.....	128
Absolute Slant-path TEC .....	129
Building Tomography Images.....	129
Tardy Data.....	129

## Figures

<b>Figure 1.</b> Diagram of the IMS components within the cabinet. ....	4
<b>Figure 2.</b> Data interconnections among the IMS components. ....	5
<b>Figure 3.</b> Electrical interconnections among the IMS components.....	6
<b>Figure 4.</b> Post-processing steps for IMS TEC and scintillation, as performed on the Console Processor. ....	8
<b>Figure 5.</b> Schematic outline of automated bias calibration. Items not yet automated are shaded. The “cumulative phase-averaging” step and the associated “zero-order adjustments” can be eliminated after multipath mitigation is implemented. The bias adjustment for plasmasphere compensation can be eliminated after a calibration process incorporating the plasmasphere is validated. ....	12
<b>Figure 6.</b> Plot of 2-Hz data (Day 002, 2004) showing reduction of multipath after application of multipath template.....	13
<b>Figure 7.</b> Plot of 1minute data (day 002, 2004) from 2-Hz data without template application. ....	14
<b>Figure 8.</b> Plot of one-minute data (Day 002, 2004) from 2-Hz data with template application.....	14
<b>Figure 9.</b> Multipath template from Nashua IMS, Day 001, 2004, PRN 1.....	15
<b>Figure 10.</b> Multipath template from Nashua IMS, Day 002, 2004, PRN 1.....	16
<b>Figure 11.</b> Multipath template from Nashua IMS, Day 005, 2004, PRN 1.....	17
<b>Figure 12.</b> Configurations of receiver arrays for the two polar-patch drift campaigns at Qaanaaq, Greenland, with the DMI site at the southeast location for both.....	20
<b>Figure 13.</b> Sample data set from AFRL’s STEL GPS receiver at Thule.....	21
<b>Figure 14.</b> Relative slant-TEC from the Thule IMS for all GPS passes received on 24 January 2001.....	22
<b>Figure 15.</b> Data from the Qaanaaq GPS receiver from GPS PRN 02 taken on 10 November 2000. The top two panels are the detrended intensity and the intensity trend, and the lower two panels are the detrended phase and phase trend. In both intensity and phase, the trend and detrend components were separated using a low-pass filter with a 60-second cutoff. ....	23
<b>Figure 16.</b> Sample data from a satellite pass over Qaanaaq, Greenland, obtained by means of the NWRA ITS10S receiver deployed there. ....	25
<b>Figure 17.</b> Slant-path TEC and scintillation observed at the Delta ITS10S station (geometry below). ....	28
<b>Figure 18.</b> Five-station chain of TEC receivers deployed to image the ionosphere over Alaska tomographically.....	29
<b>Figure 19.</b> Tomographic image and parameters scaled therefrom (lower panel) obtained from TEC data shown in Figure17 and similar data obtained at the other four receiving stations indicated by triangles above the abscissa. Asterisks show comparative ionosonde measurements. ....	30
<b>Figure 20.</b> State of the ionosphere over Alaska some two hours after that depicted in Figure 19...31	31

<b>Figure 21.</b> Comparison of measured relative TEC (heavy lines) and relative TEC on same raypaths to the receiving stations computed (light lines) by integrating through the tomographic image in Figure 19. ....	33
<b>Figure 22.</b> Histogram of rms residuals computed for all images produced to date. Images whose rms residuals reside in the tail of the histogram beyond 1.0 TEC unit are not posted on the HAARP Web site. ....	34
<b>Figure 23.</b> Example of a plasma-density trough imaged tomographically and selected for quantitative characterization. ....	38
<b>Table 8.</b> Analysis parameters for trough shown is Illustrated in Figure 23.....	39
<b>Figure 24.</b> VTEC (solid line), gradients (dashed lines) and other parameters (diamonds), as enumerated in Table 4, for trough illustrated in Figure 23. ....	40
<b>Figure 25.</b> Image produced by standard WDLs inversion (top) and by combined WDLs/ART inversion (bottom). ....	41
<b>Figure 26.</b> Electron-density image (upper panel) and latitude variation of TEC and $f_oF_2$ (lower panel) generated using only TEC data. The two time-tagged asterisks indicate $f_oF_2$ as measured by the Gakona digisonde at the indicated times (UT).....	43
<b>Figure 27.</b> Image and plots of TEC and $f_oF_2$ , as in Figure 24, generated using both TEC and digisonde data.....	44
<b>Figure 28.</b> Comparison of electron density at an altitude of 840 km extracted from the TEC-only image (solid line, upper panel) and from the TEC+digisonde image (solid line, lower panel) with observations of density measured by DMSP during nearby (in time) passes. ....	46
<b>Figure 29.</b> Slant-path TEC and phase scintillation observed Gakona (left) and Cordova (right) during operation of HAARP's HF transmitter on 25 March 2001. Note different scales in the lower panels (displaying phase scintillation). ....	47
<b>Figure 30.</b> State of the ionosphere during the heating experiment in which the dispersive-phase fluctuations displayed in the left panel of Figure 26 and the corresponding TEC perturbations quantified in the upper panel of Figure 29 were observed. ....	48
<b>Figure 31.</b> Detrended dispersive phase (top) and angle (bottom) between magnetic field and ray-path from satellite to Gakona. ....	50
<b>Figure 32.</b> Geometry of Oscar 32 satellite pass near 1900 UT on 04 March 2003 corresponding to the Gakona (left) and Copper Center (right) data plots displayed in Figure 33. See text for details. ....	51
<b>Figure 33.</b> Detrended phase (upper panels) observed at Gakona (left) and Copper Center (right) during pass whose geometry is shown in Figure 32, together with the angle (bottom panels) between the Oscar-satellite ray paths and the local geomagnetic field in the ionosphere. ....	52
<b>Figure 34.</b> Range-vs-time plot of the echo strength from the Kodiak SuperDARN during 1800-2000 UT on 04 March 2003. Blue lines indicate times that the HAARP heater turned on and off and the time of closest approach of the Oscar-32 pass. Red color indicates strong meter-scale structures in the ionosphere for that range/time bin. ....	53

<b>Figure C-1.</b> Data from PRN01 pass on 23 October 2001 at Qaanaaq, Greenland, used in this analysis. From top to bottom, the plots are the intensity detrended, intensity trend, phase detrended, and phase trend time-series for this pass. ....	70
<b>Figure C-2.</b> Analysis results from the IMS 20-Hz processing. The plots are, from top to bottom, $S_4$ , $\sigma_\phi$ , $p$ (phase spectral slope), and $T$ (phase spectral strength). ....	71
<b>Figure C-3.</b> Analysis results from the IMS 20Hz processing. The plots are, from top to bottom, average (asterisk) and maximum (cross) $S_4$ , $\sigma_\phi$ , $p$ (phase spectral slope), and $T$ (phase spectral strength). ....	72
<b>Figure C-4.</b> Comparison of the $S_4$ (top plot) and $\sigma_\phi$ (bottom plot) indices from the standard processing software (along the X axis) and IMS processing software (along the Y axis). ....	73
<b>Figure C-4 (cont).</b> Comparison of the $p$ (top plot) and $T$ (bottom plot) parameters from the standard processing software (along the X axis) and IMS processing software (along the Y axis). ....	74
<b>Figure C-5.</b> Comparison of the detrended phase records from the standard processing ("Research code" shown as a solid line) and the IMS processing (dotted line) for a single 60-second record. ....	76
<b>Figure C-6.</b> Comparison of the 2Hz $S_4$ results with (1) 2Hz $S_4$ generated using the standard processing code (top plot), and (2) 20Hz $S_4$ generated using the IMS processing code (bottom plot). ....	77
<b>Figure C-7.</b> Sample phase power-density spectra from the 60-second data samples with the highest and lowest $\sigma_\phi$ values in the pass. The spectrum for the highest $\sigma_\phi$ is at the top and the spectrum for the lowest is at the bottom. The straight lines shown overplotted are least-squares fits to the spectra. ....	79
<b>Figure C-8.</b> The $p$ and $T$ values calculated using fits over the spectral frequency range of 0.1 to 2.0 Hz (top two plots) and using fits over the range 2.0 to 10.0 Hz (bottom two plots). The solid lines on the $p$ plots are the WBMOD model value and the dotted lines are $p=2$ . The solid line on the lower $T$ plot is the average $T$ for the pass. ....	80
<b>Figure C-9.</b> Comparison of $T$ calculated from the 0.1 to 2.0 Hz range (Y axis) to that calculated from the 0.1 to 10.0 Hz range (X axis). ....	81
<b>Figure D-1.</b> Examples of phase time-series and spectrum from no-scintillation cases. Plots (a) and (b) are data collected in P-mode, and plots (c) and (d) are Z-mode. ....	85
<b>Figure D-2.</b> Examples of intensity time-series and spectrum from no-scintillation cases. Plots (a) and (b) are data collected in P-mode, and plots (c) and (d) are Z-mode. ....	86
<b>Figure D-3.</b> Time-series plots of 10 seconds of detrended intensity data from the center of the time-series records shown in Figure D.2 (plots (b) and (d)). ....	87
<b>Figure D-4.</b> The L1 intensity (top plot) and DCP (bottom plot) generated from a Wideband Ancon pass for use in the WPAFB GPS testing. The dashed lines in the DCP plot indicate the $\pm\pi$ radian limit on phase fluctuations imposed by the WPAFB simulator. ....	87
<b>Figure D-5.</b> Phase (DCP) results from the Wideband simulation data set. The top panel is the DCP signal provided to the WPAFB simulator, the middle panel is the DCP derived from the P-mode data, and the bottom panel is the DCP derived from the Z-mode data. ....	89
<b>Figure D-6.</b> Reduced time-span plot of phase (DCP) data plotted in Figure D-5. ....	90

<b>Figure D-7.</b> Phase scintillation parameters calculated from the phase (DCP) time-series records shown in Figure D-5. Top plot is $\sigma_\phi$ , middle plot is the phase spectrum parameter T (the spectral density at 1Hz), and the lower plot is the phase spectrum slope, p. In all three plots, the heavy solid line is from the simulation data, the dashed line is P-mode, and the dotted line is Z-mode.....	91
<b>Figure D-8.</b> Phase (DCP) spectra from a 51.2-second data sample centered at time 15426 (simulation-record time) from the time-series records shown in Figure D-5. The plot in panel (a) is from the P-mode set, (b) is from the Z-mode set, and (c) is from the simulation input....	92
<b>Figure D-9.</b> Phase (DCP) spectra from a 51.2-second data sample centered at time 15786 (simulation-record time) from the time-series records shown in Figure D-5. The plot in panel (a) is from the P-mode set, (b) is from the Z-mode set, and (c) is from the simulation input....	93
<b>Figure D-10.</b> Intensity (L1) results from the Wideband simulation data set. The top panel is the L1 intensity signal provided to the WPAFB simulator, the middle panel is the L1 intensity derived from the P-mode data, and the bottom panel is the L1 intensity derived from the Z-mode data. ....	95
<b>Figure D-11.</b> Reduced time-span plot of L1 intensity data plotted in Figure D-10. This is the same time interval plotted in Figure D-6.....	96
<b>Figure D-12.</b> Same data plotted in Figure D-11, but plotted as normalized intensity rather than in dB. ....	97
<b>Figure D-13.</b> A ten-second data sample extracted from the data shown in Figure D-10. Note that this is also plotted as normalized intensity rather than in dB.....	98
<b>Figure D-14.</b> The $S_4$ intensity scintillation parameter calculated from the L1 intensity time-series records shown in Figure D-10. The heavy solid line is from the simulation data, the dashed line is P-mode, and the dotted line is Z-mode.....	99
<b>Figure D-15.</b> Phase (DCP) results from the tones simulation data set. The top panel is the DCP signal provided to the WPAFB simulator, the middle panel is the DCP derived from the P-mode data, and the bottom panel is the DCP derived from the Z-mode data. ....	100
<b>Figure D-16.</b> Phase (DCP) trends removed from the P-mode (middle plot) and Z-mode (bottom plot) data to produce the detrended-phase records in Figure D-15. ....	101
<b>Figure D-17.</b> A subset of the phase (DCP) data shown in Figure D-15.....	102
<b>Figure D-18.</b> L1 intensity results from the tones simulation data set. The top panel is the L1 intensity signal provided to the WPAFB simulator, the middle panel is the L1 intensity derived from the P-mode data, and the bottom panel is the L1 intensity derived from the Z-mode data. ....	104
<b>Figure D-19.</b> Comparison of the L1 intensity for the second and third cases in the tones simulation set. The light curves are the input simulation values and the heavier curves are the P-mode output.....	105
<b>Figure D-20.</b> The L1 intensity detrend and trend time-series records from the Nashua quiet-day data set with the satellite elevation and azimuth angles. ....	106

<b>Figure D-21.</b> The RMS detrended intensity ( $S_4$ ) calculated from the time-series in the top panel of Figure D-20 (solid curve). The other two curves are from the AJ model (dashed line) and the Draper model (dotted line). .....	107
<b>Figure D-22.</b> Samples of intensity (panels (a) and (b)) and phase ((c) and (d)) time-series and power-density spectra from the Nashua quiet-day data set shown in Figure D-20.....	108
<b>Figure D-23.</b> Phase (DCP) spectra from the AFRL "scinda" GPS Ashtech Z-12 receiver located at Ascension Island. These data were taken when the receiver appears to have been operating in Y-mode (keyed) during a time when there was little if any ionospheric scintillation present. ....	110
<b>Figure D-24.</b> Phase (DCP) time-series samples and spectra from data collected by the localhost (panels (a) and (c)) and scinda (panels (b) and (d)) GPS receivers at Ascension Island. These data are from the same GPS satellite and times. ....	111
<b>Figure D-25.</b> Expanded plot of the phase (DCP) from the center of the time-series records in the two bottom panels of Figure D-24. Data from the localhost GPS receiver is in the top plot and data from the scinda GPS receiver is in the lower plot. ....	112
<b>Figure E-1.</b> Shelter and array support structure for 139 MHz Radar.....	113
<b>Figure E-2.</b> Pad-2 Instrumentation Shelter and Spiracone Antenna .....	114
<b>Figure E-3.</b> Pad-3 Instrumentation Shelters .....	115
<b>Figure E-4.</b> Pad-1 Instrumentation Shelter and Satellite Antennas.....	115
<b>Figure H-1.</b> Flow of data from ITS10S stations to HAARP's Maestro computer and of those data plus relative TEC records from the UAF stations via its Gedds computer to NWRA's Poi computer for development of tomographic images transmitted to Maestro for posting on the HAARP Web site. ....	128

## Tables

<b>Table 1.</b> Local Area Network Addresses for IMS Subsystems .....	3
<b>Table 2.</b> Critical Temperature Values.....	6
<b>Table 3.</b> Sample of Revised ESR .....	9
<b>Table 4.</b> Station-availability summary for tomographic images in 2001. ....	35
<b>Table 5.</b> Station-availability summary for tomographic images in 2002. ....	35
<b>Table 6.</b> Station-availability summary for tomographic images in 2003. ....	36
<b>Table 7.</b> Station availability summary for tomographic images in 2004 (first quarter only). ....	36
<b>Table 8.</b> Analysis parameters for trough shown is Illustrated in Figure 23.....	39

### **Acknowledgements**

This report summarizes work completed during the period 1 January 2001 through 31 March 2004 on a project to investigate effects of the earth's ionosphere on transionospheric systems during and immediately following the peak of the current cycle of solar activity.

In addition to the authors, other contributors to the efforts described herein include Northwest Research Associates (NWRA) staff members C. Charley Andreasen, Michael Horgan, Troy Lawlor, Susan Rao, J. Francis Smith, Tyler Wellman, and Tong Xu, as well as NWRA consultants Spencer Kuo and Robert Skrivanek.

We express our appreciation to Mr. Dennis Simpson at Kwajalein; SSgt. Henry Ruelas and TSgt. Troy Bieber at Kadena, Japan; and Peter Thomsen at Thule AB, Greenland, for their support with the IMS units; to MSgt Gigi Kinsell of the Air Force Weather Agency (AFWA) and 2<sup>nd</sup> Lt Kevin Dewever of the Space and Missile Systems Center (SMC) for their assistance at Kadena; and to TSgt. Thomas Schell of AFRL for his efforts in supporting the IMS installations and operational modifications. We also express our appreciation to Helio Zwi of Advanced Power Technologies, Inc. (APTI) for his assistance in the diagnosis and attempted recovery of the GPS data computer at HAARP; to Marty Karjala and Bruno Baureis of BAE Systems Advanced Technologies for installation of a new GPS antenna at HAARP, for assistance in diagnosing problems with the GPS TEC sensor there, and for performing system shutdowns and restarts during power-maintenance activities at that site.

We thank Ethan Merrill, the Navy Ionospheric Monitoring System (NIMS) Satellite Constellation Support Manager in the Naval Satellite Operations Center (NavSOC) at Pt. Mugu, CA, for timely information on status of the NIMS satellites. We express thanks to Svend Erik Ascanius, manager of the Danish meteorological station at Qaanaaq, Greenland, for assistance during the polar-patch measurement campaigns and on many other occasions; to Carlton Curtis of Boston College for his efforts in arranging IMS Ashtech receiver upgrades and preparing materials for shipment to the HAARP site to aid system diagnostics; and to Clayton Coker (formerly of the Applied Research Laboratory of the University of Texas at Austin) for his helpful discussions concerning the intensity and phase data from the Ashtech receivers. Finally, we express our appreciation to Graham Bailey of Sheffield University for providing the Sheffield University Plasmasphere-Ionosphere Model and supporting its use.



## **List of Symbols, Abbreviations, and Acronyms**

55 SWXS	55 <sup>th</sup> Space Weather Squadron
AFRL	Air Force Research Laboratory
AFWA	Air Force Weather Agency
AWN	Automated Weather Network
APTI	Advanced Power Technology, Inc.
CESR	Contingency Equipment Status Report
CORS	Continuously Operating Reference Station
DCP	Differential Carrier Phase
DGD	Differential Group Delay
DMI	Danish Meteorological Institute
ELF	Extremely Low Frequency
ESR	Equipment Status Reports
EOFs	Empirical Orthonormal Functions
FTP	File Transfer Protocol
GPS	Global Positioning System
HAARP	High-frequency Active Auroral Research Program
HF	High Frequency
HP	Hewlett Packard
IMS	Ionospheric Measuring System
IPP	Ionospheric Penetration Point
ITS	Ionospheric Tomography System
LAN	local area network
MBEN	Ashtech GPS receiver measurement data record
MUF	Maximum Usable Frequency
NetCDF	Network Common Data Format
NIMS	Navy Ionospheric Monitoring System
NIPRNET	Internet Protocol
NNSS	Navy Navigational Satellite System
NRL	Naval Research Laboratory
NWRA	NorthWest Research Associates
ONR	Office of Naval Research

OpSEND	Operational Space Environment Network Display
PBEN	Ashtech GPS receiver position data record
PCA	Polar Cap Absorption
PDR	Powerful Diagnostic Radar
PRISM	Parameterized Real-time Ionospheric Specification Model
PRN	Pseudo-Random Noise (GPS identification signature)
RINEX	Receiver Independent Exchange (data format)
rms	root mean square
RTM	Real-Time Monitor
SAO	Standard Archiving Output
SBIR	Small-Business Innovation Research
SCINDA	Scintillation Decision Aid
SCORE	Self-Calibration of Range Errors
SCSI	Small Computer System Interface
SCION	SCION Associates, Inc.
SEE	Stimulated Electromagnetic Emission
SFG	Scale Factor Generator
SNAB	Ashtech GPS receiver satellite ephemeris data record
sps	samples per second
SWN	Space Weather Network
TCNO	Technical Compliance Network Order
TEC	Total Electron Content
TELSI	TEC and Scintillation (message format)
UHF	Ultra High Frequency
UPS	Uninterruptible Power Source
VHF	Very High Frequency
VLF	Very Low Frequency
WDLS	Weighted, Damped, Least-Squares

## **1. PROJECT OBJECTIVES**

Under this contract, Northwest Research Associates (NWRA) performed ionospheric measurements near and immediately following a maximum in the eleven-year solar activity cycle. The research conducted fell within Hanscom Technical Areas 3(a), "Ionospheric Effects Research and Air Force Systems," and 3(b), "Ionospheric Research Technology," of the Broad Agency Announcement VS-00-01 released by the Air Force Research Laboratory (AFRL).

In Technical Area 3(a), NWRA developed and employed techniques that resulted in: (1) specification of both the background ionosphere and its disturbance structures through periods of enhanced solar activity, (2) improved understanding of these regions, and (3) elucidated effects of ionospheric disturbances on communication, navigation, and surveillance systems. To achieve these ends, we (a) enhanced and maintained GPS receivers, including the Air Force Ionospheric Measuring System (AN/GMQ-35), at various locations; (b) deployed and operated an NWRA ITS10S coherent receiving system at Qaanaaq, Greenland; and (c) calibrated, processed, and analyzed records of total electron content (TEC) and of VHF, UHF, and L-band scintillation obtained by means of these instruments. Through such analyses and others, we contributed to characterization of such ionospheric features as the main F-layer trough and polar-cap plasma patches. This research was directed at end products such as capabilities for local and regional assessment of transionospheric propagation conditions in near-real time. These research topics are reported in Sections 2 and 3 and Subsection 4.1.2.2.2.

As a contribution to Technical Area 3(b), we collaborated with scientists and engineers from AFRL, the Naval Research Laboratory (NRL), and other research organizations in the application of diagnostic instrumentation to the High-frequency Active Auroral Research Program (HAARP). Among the HAARP instruments that we applied to ionospheric research are an Ashtech Model Z-FX GPS receiver for measuring absolute TEC and three NWRA ITS10S receiving systems for measuring relative TEC and recording scintillation. We continue to post TEC from these instruments and scintillation records from the latter three on the HAARP Web site for telepresence applications and for decision-making during active experiments. Finally, we focused on inverting the TEC data tomographically to produce images of the F layer over Alaska. Our participation in HAARP and application of its results are reported in Section 4.

## **2. NON-HAARP GPS TOPICS**

### **2.1 Ionospheric Measuring System (IMS)**

#### **2.1.1 IMS Upgrade**

A significant endeavor under this contract was upgrade of the Ionospheric Measuring System (IMS) units to their original design specifications, with other modifications associated with termination of the Automated Weather Network (AWN) and migration to an Internet-protocol network. Among the capabilities added to the IMS units were the following:

- Scintillation parameters ( $S_4$ ,  $\sigma_\phi$ ) at GPS frequencies;
- Scintillation spectral parameters ( $T$ ,  $p$ ) at GPS frequencies;
- Intensity-scintillation parameters at UHF frequencies;
- Automated calibration of TEC measurements;

GPS satellite-exclusion specifications;  
Multipath mitigation for TEC and GPS intensity scintillation.

Among the AWN capabilities to be migrated to an Internet-protocol network were the following:

- Delivery of periodic TEC and scintillation (TELSI) reports for GPS data;
- Delivery of periodic UHF SCINDA reports;
- Delivery of daily Equipment Status Reports (ESR);
- Delivery of event-associated Contingency Equipment Status Reports (CESR);
- Remote commands to IMS units, including GPS bias settings, satellite selections, and swapping of active computer units.

A phased development and implementation of the upgrade and modification items was planned initially, based on the original IMS units deployed between 1994 and 1996 to Otis Air National Guard Base, MA; Croughton Air Base, UK; Thule Air Base, Greenland; Eareckson Air Force Station, Shemya, AK; and Ascension Auxiliary Airfield, Ascension Island. In this original plan, the preliminary network transmission capabilities developed for the 1999 Ascension Island Space Environment Network Display (SEND) campaign would be augmented and applied as other stations migrated from the AWN to the Internet-protocol NIPRNET, while the initial GPS scintillation-index ( $S_4$ ,  $\sigma_\phi$ ) reporting would be based on the 2-Hz data already available within the IMS, to be replaced by values derived from the GPS 20-Hz data when this data collection capability was developed, and augmented by the GPS scintillation spectral parameters ( $T$ ,  $p$ ), which were expected to be reliably available only from the 20-Hz data.

Concern by AFRL personnel that the original IMS Apollo computers would be unable to perform the 20-Hz data collection, plus concerns about the age and unavailability of replacement units for these computers, prompted consideration of a computer upgrade for these GPS data collection computers. However, early deployment schedule constraints coupled with longer term software development needs would have posed an extended downtime for fielded IMS units, had the replacement GPS data collection computers been installed in the original IMS cabinets, displacing the original computers. Thus, NWRA personnel proposed performing the upgrade by developing completely new IMS units that could be deployed within the constrained schedule and would become operational at a later time, when the essential software developments were completed. This plan maintained IMS operational availability while allowing sufficient time for development and testing, and also extended the operational lifetime of the IMS units.

Situational needs arising during the developments for the IMS upgrades resulted in new site selections for several IMS units, with the original IMS unit at Shemya being retained at that site, with some software upgrades. A new IMS unit was deployed to Ascension Auxiliary Airfield in September 2001, but never became operational because of network restrictions. A second new IMS unit was deployed to Thule in October 2001, and became operational in May 2002, replacing the original IMS unit at that site. The new IMS unit was relocated from the Thule radar building to South Mountain in October 2002, with the addition of a UHF subsystem, but network access is still restricted. The IMS units at Otis Air National Guard Base and Croughton Air Base were deactivated and returned to AFRL. New IMS units were deployed to Kadena Air Base, Okinawa, in August 2002 and Kwajalein Atoll, Marshall Islands, in September 2002, with subsequent installations of UHF subsystems in June 2003 at Kadena and July 2003 at Kwajalein. A fifth new IMS unit remains at the NWRA Nashua office for an unspecified future deployment, with a UHF subsystem installed. For development and testing efforts, a full assemblage of IMS components,

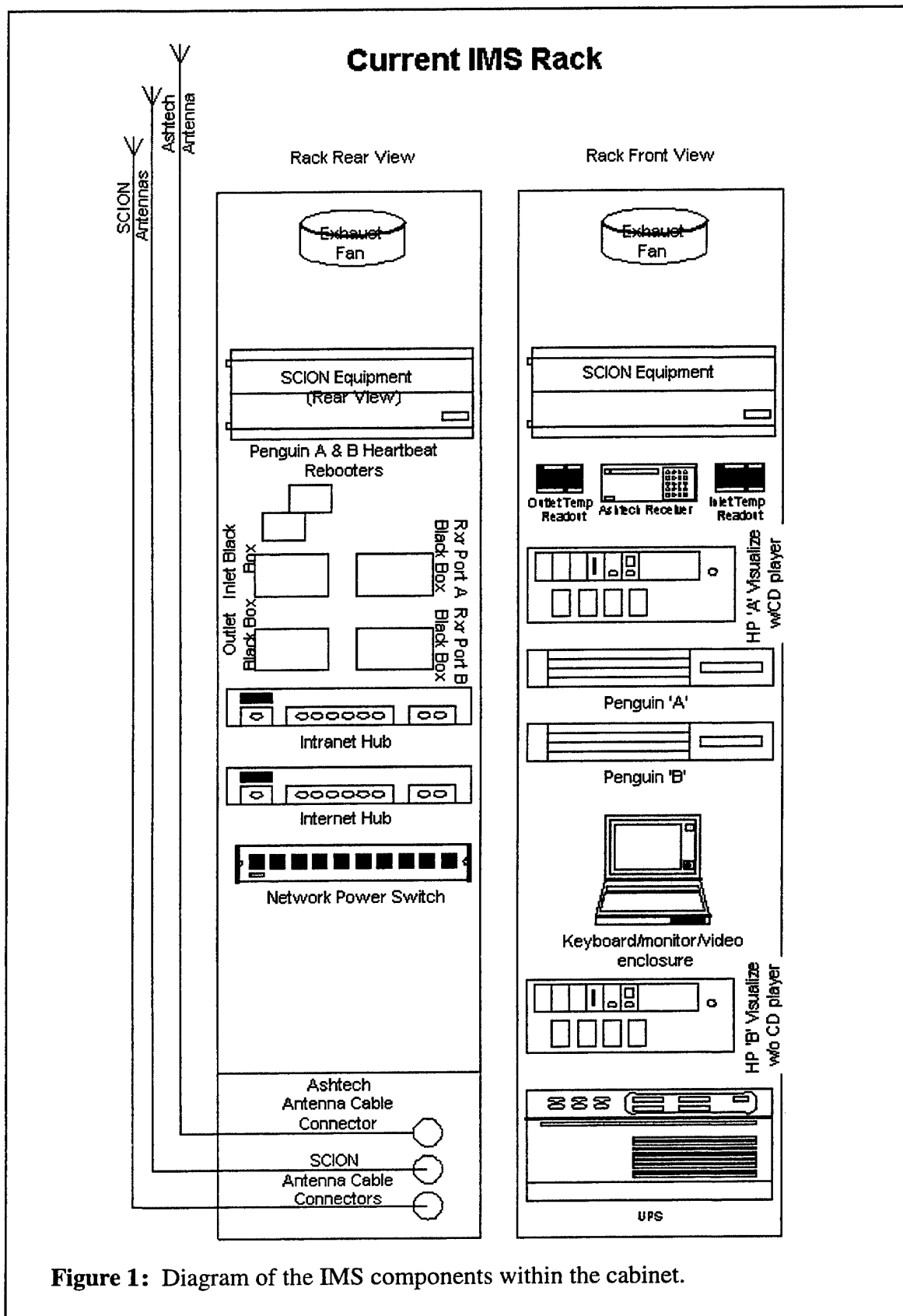
without a cabinet enclosure, also is operated at the NWRA Nashua office, designated as the "Benchtop IMS."

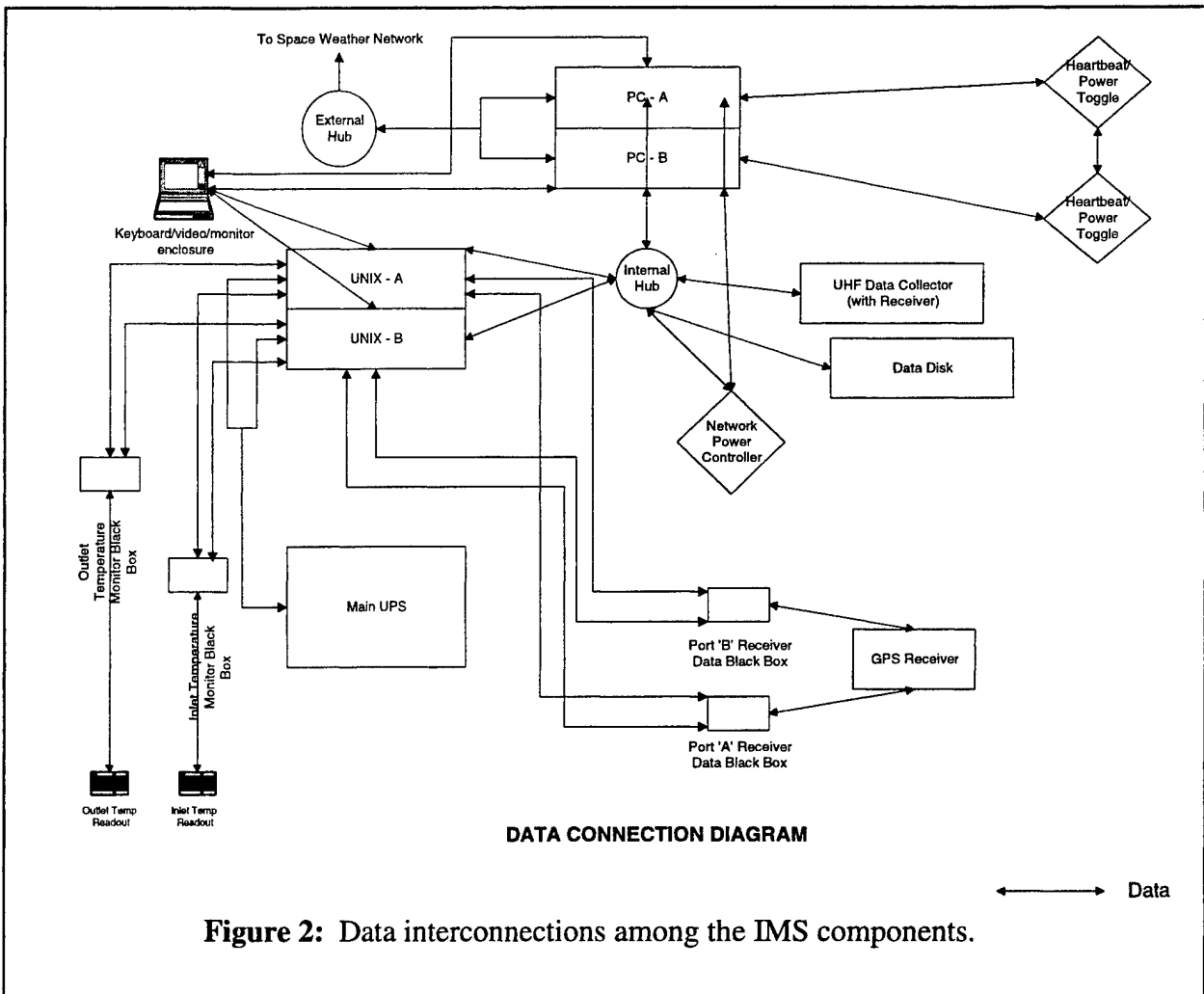
The new IMS units incorporate the former auxiliary operator interface computer as an integral unit, with redundancy, in the same manner as the GPS data collection processors. The interface computer, designated as the Console Processor, also assumed the role of the operational monitor for the GPS data collection computers, denoted as the GPS Processors, replacing the custom device in the original IMS for this role. The Console Processor also monitors operations of the separate UHF Processor, provided by SCION Associates. The operation of the Console Processor is monitored by a small commercial heartbeat monitor unit, which can swap between the two Console Processors. A diagram of the new IMS cabinet layout appears as Figure 1.

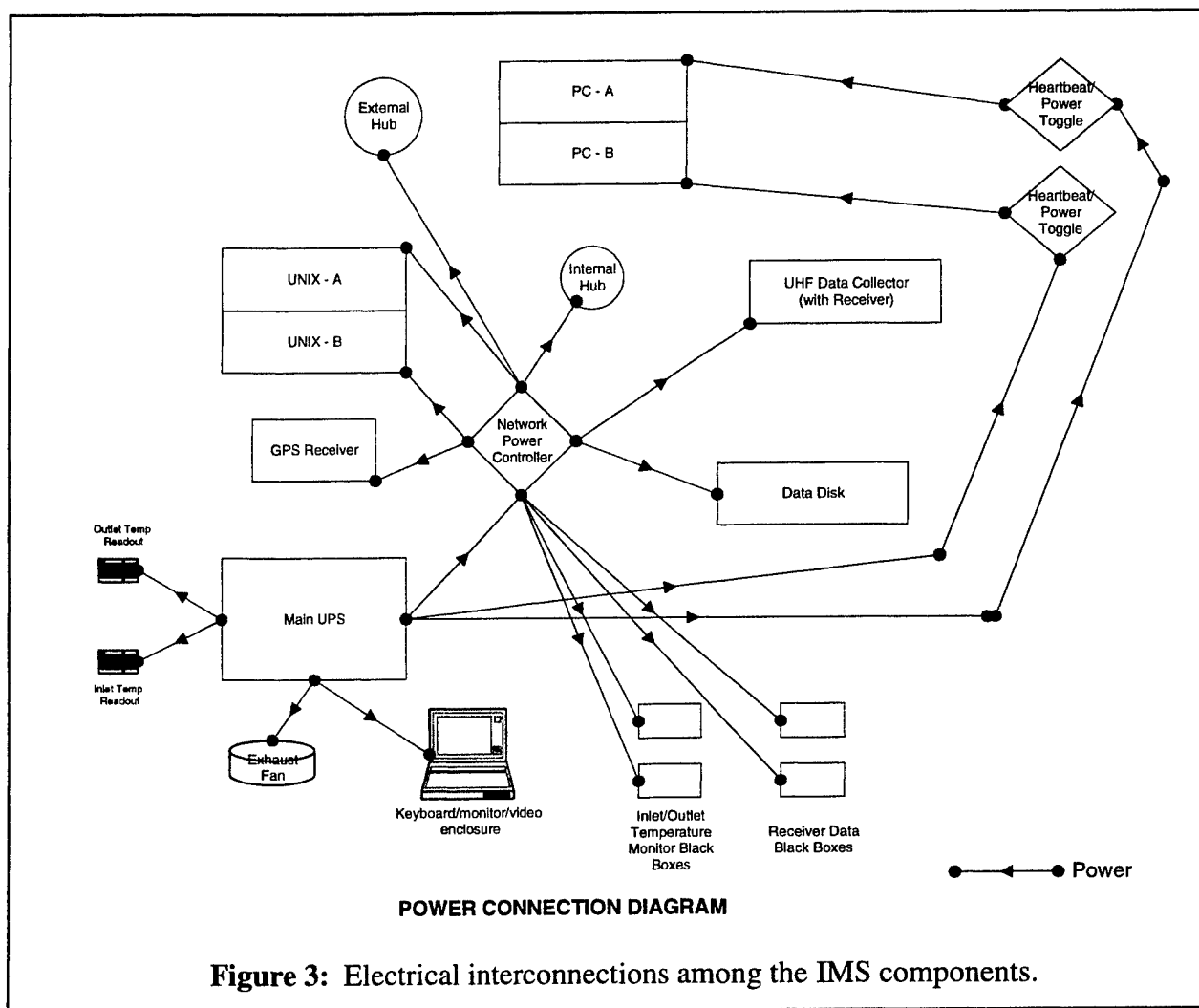
The processors within the IMS cabinet, which is an electromagnetic interference/radio-frequency interference (EMI/RFI) compliant unit, are connected as a local area network (LAN), with only the Console Processor having a separate external Internet interface, unique to each IMS site. The standard LAN addresses for the IMS subsystems are listed in Table 1, and schematics of the data and electrical connections appear as Figs. 2 and 3, respectively. Automated control of the GPS Processor by the Console Processor is provided using Telnet scripts, with further provisions for remote operator access also through Telnet, while access to the UHF subsystem and the networked disk drive are provided using an Internet browser, with supplementary scripts for automated operations.

**Table 1. Local Area Network Addresses for IMS Subsystems**

Console Processor .....	10.1.1.11
GPS Processor .....	10.1.1.10
UHF Processor.....	10.1.1.15
Networked Disk Drive.....	10.1.1.12
Networked Power Controller.....	10.1.1.13







To minimize software revisions, the original GPS Processor capabilities for monitoring the two (inlet and outlet) temperature sensors and the UPS were retained on that processor, with additional provisions on the Console Processor to engage in a coordinated system shutdown triggered by critical conditions reported by the GPS Processor. To avoid unnecessary shutdowns in circumstances that are tolerable to the new equipment, the temperature constraints were expanded, so that the warning and shutdown conditions are those appearing in Table 2. Shutdown conditions prompted by either the temperature sensors or the UPS require intervention by an on-site operation

**Table 2. Critical Temperature Values**

Under-temperature shutdown:	below 10° C for one hour
Low air inlet temperature:	10° C
Recovery from low temperature:	above 12° C, after report for below 10° C
Recovery from high temperature:	below 38° C, after report for above 40° C
High air inlet temperature:	40° C
Over-temperature shutdown:	above 40° C for one hour, or above 45° C



in order to restart the IMS unit.

The expectation of minimizing software developments was somewhat reduced by the need to accommodate new temperature sensor units with a different communications protocol from the units used in the original IMS, because of the unavailability of the original temperature sensor units. Additionally, serial communications switches were incorporated to accommodate signal degradation problems associated with the dual processor configuration. A similar configuration, as indicated in Figure 2, also is used for each of the two serial data connections between the GPS Processors and the GPS receiver.

As for the original IMS units, the GPS receiver provides an accurate time reference for the GPS Processor, with a tolerance of 0.5 seconds. This time reference is propagated to the Console Processor and UHF subsystem using the Network Time Protocol.

The networked disk drive originally was developed solely for storage of the IMS data by the GPS Processor, replacing a common SCSI drive that performed the same role in the original IMS units. The utilization of this networked drive has been augmented by developing separate access by the pair of Console Processors, so that the dormant Console Processor can acquire updated files from the formerly active Console Processor when a swap occurs.

Licensing and maintenance fee considerations for the Matlab software used on the GPS Processors prompted developments to eliminate Matlab usage. To expedite these developments, the equivalent computations performed by the Matlab scripts on the GPS Processor were replaced by Fortran programs on the Console Processor, running in a post-processing mode rather than integrated with the Ada data collection process on the GPS Processor. This implementation also considerably simplified the automated calibration processing, being developed concurrently. Consequently, the format and contents of the raw IMS data files were modified significantly, with the new contents described in Appendix A. Notably, the inclusion of the Sequence ID permitted more accurate time definitions for the 2-Hz data samples, while the inclusion of the PBEN permitted reporting of the estimated site coordinates.

The post-processing steps for TEC and 2-Hz scintillation are diagrammed in Figure 4. This processing is initiated automatically when an IMS archive file is transmitted from the GPS Processor to the Console Processor. Functions of the individual programs are:

PsGn2Hz – generates sequences of 2-Hz IMS data, with one file for each GPS satellite pass;

PassGn1M – generates tables of 1-minute averages for dispersive group delay (DGD), dispersive carrier phase (DCP), and calibrated equivalent vertical TEC, with ancillary values and flags, for each satellite pass;

TECGn15M – generates a table of 15-minute averages for calibrated equivalent vertical TEC, with ancillary values and flags, containing all satellites for each 15-minute interval;

IMSTELSI – generates a TELSI message, with 15-minute average TEC values and summary scintillation statistics (currently derived from the 2-Hz data), with a summary scintillation table also being generated;

GPSSCND – generates a GPS SCINDA message, with scintillation statistics (currently derived from the 2-Hz data).

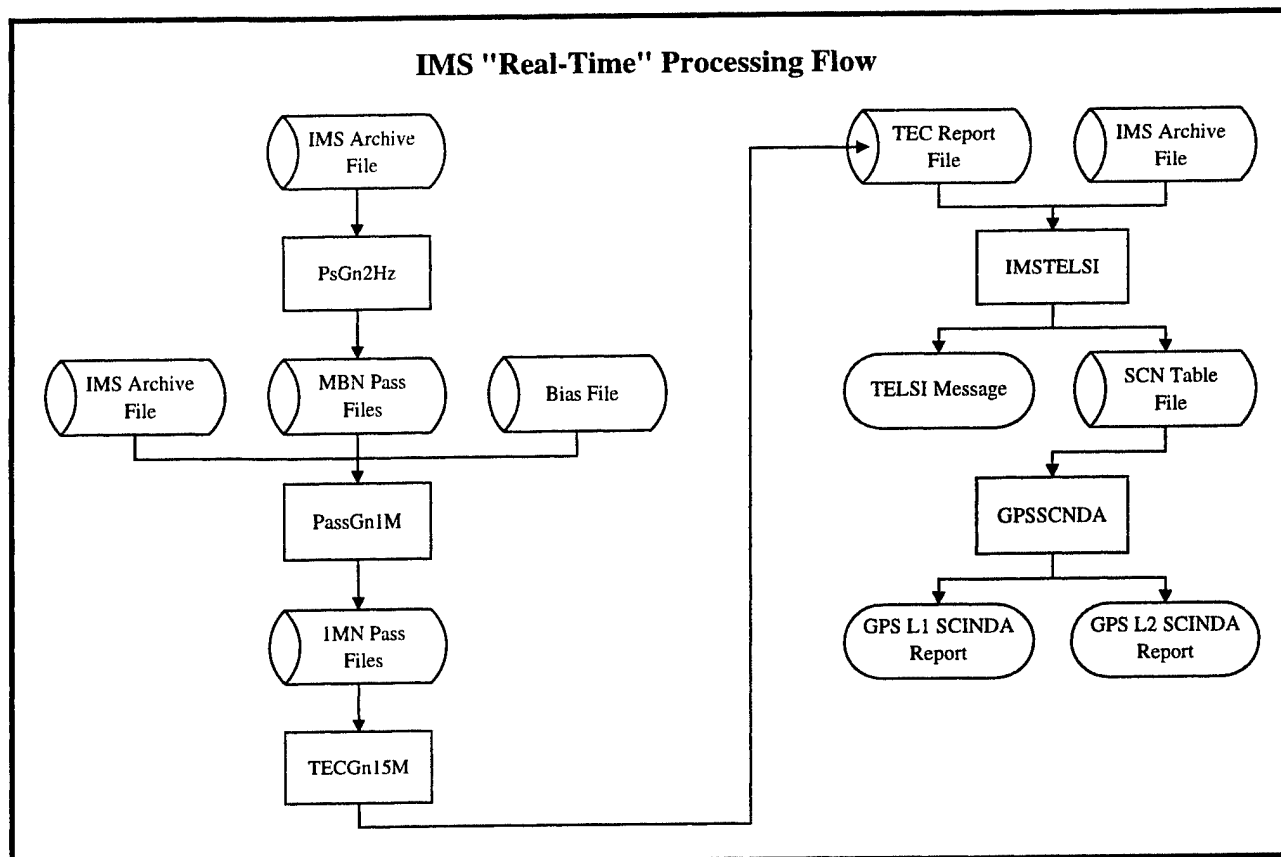


**Figure 4.** Post-processing steps for IMS TEC and scintillation, as performed on the Console Processor.

Data formats for the 2-Hz pass files, 1-Minute pass files, 15-Minute TEC tabulations, and 15-Minute scintillation statistics appear in Appendix B. The bias file is a table of GPS satellite identifiers and associated biases (combined with the receiver bias), derived from either an operator-initiated calibration or an automated calibration.

The Shemya IMS was upgraded for the new TEC processing in March 2003, in conjunction with the installation of a replacement Apollo computer for the GPS data collection. Slight differences in format and longitude range conventions prompted development of an auxiliary program to convert the new 15-Minute TEC tabulation into the old format used by the Scale Factor Generator (SFG), which operates at Shemya exclusively.

The TELSI (Total Electron and Scintillation) messages are generated in the format defined for the original IMS units, for compatibility with the decoding software, operating initially at 55<sup>th</sup> Space Weather Squadron (55SWXS) in Colorado but later transferred to the Air Force Weather Agency (AFWA) in Nebraska. The original IMS units had provided only TEC information, with the scintillation statistical and spectral parameters being replaced by filler characters, but the upgraded IMS units are providing the intensity and phase indices ( $S_4$  and  $\sigma_\phi$ ), based on the 2-Hz data. Initial developments were conducted to determine these scintillation indices and additional scintillation spectral parameters from 20-Hz data provided by the receiver, but some performance uncertainties associated with the 20-Hz data and Y-code (GPS decryption) operations have deferred the completion of this implementation. The analysis and assessment of the 20-Hz data are described in Appendix C and Appendix D, with a preliminary assessment of the Y-code performance also

appearing in Appendix D. Data collection and preliminary scintillation processing for the 20-Hz data are being conducted on the upgraded IMS units at Nashua and Thule, with the results being transmitted to the NWRA Nashua office as they are generated, separately from the TELSI transmissions. Upgrades of additional receivers for Y-code capability were terminated, after three receivers were upgraded, based on the uncertain performance advantages. The TELSI format is described in the original IMS Software Requirements Specification (Draper Laboratory, 1994).

SCINDA (Scintillation Decision Aid) messages are generated for both the GPS and UHF data, with appropriate accommodation of the different nature of the two types of measurements. The GPS measurements between a single receiver and multiple satellites, while the equatorial-region UHF measurements are between two separate receiver/antenna channels and a single (geostationary) satellite, although for Thule the circumstances are slightly different, with two distinct satellites being used for the UHF measurements. The processing and transmission for the separate GPS and UHF SCINDA messages are conducted independently, with the GPS processing being initiated as an event-driven process (the arrival of an IMS archive file at the Console Processor) and the UHF processing occurring as a scheduled data retrieval and processing, for every quarter-hour. The SCINDA format is described in a memorandum from Radex (Caton, 2001).

The daily Equipment Status Report (ESR), initiated at 00:05 UT, was modified significantly in format, to facilitate interpretation by an operator rather than a decoding program, and somewhat in content, to report on all the subsystems within the IMS. A sample ESR appears as Table 3.

**Table 3. Sample of Revised ESR**

Equipment Status Report	
Site: Nashua	
Date/time: 2003-03-21 00:05 UTC	
GPS Processor B	
Maximum Inlet Temperature	27°C at time 21:07
Current Inlet Temperature	25°C
Maximum Outlet Temperature	26°C at time 20:58
Current Outlet Temperature	23°C
LRU status:	
GPS receiver	operational
Outlet Temperature Sensor	operational
Inlet Temperature Sensor	operational
UPS	operational
Scion	operational
Console Processor A	
Average Of Lowest Five S4	0.00
Average Of Lowest Five Sigma-Phi	0.009
Loss Of Lock	1643
Receiver Bias	32.6007042 (TEC Unit)

The Contingency Equipment Status Reports (CESR) also were modified in format for interpretation by an operator, and were initially implemented for transmission using electronic mail facilities, but administrative network restrictions at the IMS sites have prevented this mode of

transmission, so FTP was implemented as an alternative. CESR are generated for the following conditions:

- Under-temperature shutdown
- Low air inlet temperature
- Recovery from low temperature
- Recovery from high temperature
- High air inlet temperature
- Over-temperature shutdown
- Inlet temperature not available
- Outlet temperature not available
- Lost communications with inlet temperature sensor
- Lost communications with outlet temperature sensor
- GPS receiver outage
- GPS Processor automatic swap
- GPS Processor commanded swap
- GPS Processor restart
- Power outage shutdown
- Commanded shutdown
- Lost communications with UPS
- System restart
- Reboot for UHF subsystem
- Power restart for UHF subsystem
- Shutdown for UHF subsystem
- Missing UHF data file.

The TELSI, ESR, and CESR messages, and, where generated, the UHF SCINDA messages and 20-Hz scintillation summaries, are transmitted to an FTP server at the NWRA Nashua facilities and ultimately are stored on the IMS Web Server, which was developed as a display and control interface for the IMS field units. However, communications into most of the IMS field site regional networks are generally restricted, except for limited time intervals by special arrangement, so the control capabilities from the IMS Web Server are unimplemented. The anticipated control capabilities were bias settings for the receiver and satellites, and exclusion status for GPS satellites. These capabilities are available through the more versatile remote control application (pcAnywhere) available to the IMS operator at Nashua, with restrictions on the source computer for access and times of access. The remote control application also permits operating system and application software updates to be conducted on the fielded units, in response to Time-Compliance Network Orders (TCNOs).

The data and display items available from the IMS Web Server are as follows:

- TELSI messages
- UHF SCINDA messages
- 20-Hz scintillation summaries
- ESR messages
- CESR messages
- Absolute equivalent-vertical TEC plot (versus UT or IPP LT), all data
- Absolute equivalent-vertical TEC plot (versus UT or IPP LT), in 9 latitude segments
- GPS L1 S<sub>4</sub> plot (versus UT or IPP LT)
- GPS L2 S<sub>4</sub> plot (versus UT or IPP LT)
- GPS  $\sigma_\phi$  plot (versus UT or IPP LT)

- UHF S<sub>4</sub> plot
- GPS S<sub>4</sub> threshold plot, by satellite
- Satellite time coverage and identifier plot (versus UT or IPP LT)
- Satellite and receiver biases
- Satellite exclusion/inclusion.

For the original IMS units, the satellite and receiver biases were determined by a TEC calibration process conducted by the IMS monitoring operator at a central site, for subsequent installation on the IMS units. Evolutionary enhancements to this process, particularly for the data pre-processing and quality checking steps of DGD outlier editing and DCP discontinuity corrections, have reduced the operator time requirements, but still required an operator assessment of the calibration results before the bias values were installed on the IMS units.

Sufficient developments for both initial data assessment (such as adequate time coverage) and calibration evaluation have been accomplished to allow implementation of an automated calibration process, diagrammed in Figure 5, on a daily basis for all of the IMS units. This process is scheduled for 05:00 UT, which was selected to allow sufficient time for satellite passes initiated during the previous day to proceed to completion. A report of the calibration processing is transmitted to the NWRA Nashua facilities, and any updated calibrations are posted on the bias settings page of the IMS Web Server for the respective site. The bias adjustment for plasmasphere compensation can be eliminated after a calibration process incorporating the plasmasphere is validated.

As a result of the IMS modifications, fewer monitoring activities are necessary. Data transfer from the sites to the central Web Server occurs automatically, as does the display of these data on the Web site. The automated calibration process runs every day to assure quality data, although an examination of these results still is conducted. An ESR is issued daily and reports a summary of IMS operations. CESR are generated when a problem is detected, automatically notifying the operator. A general periodic review (at least twice a month) still will be necessary to assess overall system status, especially for trends that may indicate declining performance. Monthly cataloguing of the data archive tapes also will be necessary (as well as assuring that the tapes are changed each month at each site). Some additional special provisions are required to sustain the SFG operations at Shemya. Additional activities are imposed by the networking operations, however, to assure the current status of all required security updates and to conduct at least preliminary investigations of transmission outages, to isolate the source of the outage as an IMS unit or the network. Further activities are required to maintain the operations for the Web Server and associated supporting computers at the NWRA Nashua facilities.

To address the effects on measurement accuracy caused by multipath resulting from the antenna environment, preliminary TEC multipath mitigation studies were conducted. A multipath template for each MBN (2-Hz) pass file can be created by subtracting the phase-averaged DCP from the DGD. Given a stable multipath environment, this template can be applied to the MBN pass for the same PRN from a subsequent day. The template and data are aligned by azimuth, elevation, and time, taking into account a time shift of 3 minutes, 56 seconds earlier for each day's difference between the template day and the data day. Each multipath value in the template is then subtracted from each corresponding DGD measurement. This de-multipathed MBN pass file continues through the 1-minute processing, which removes some of the noise through averaging, into 1 MN (1-minute) pass files.

## Automated TEC Calibrations

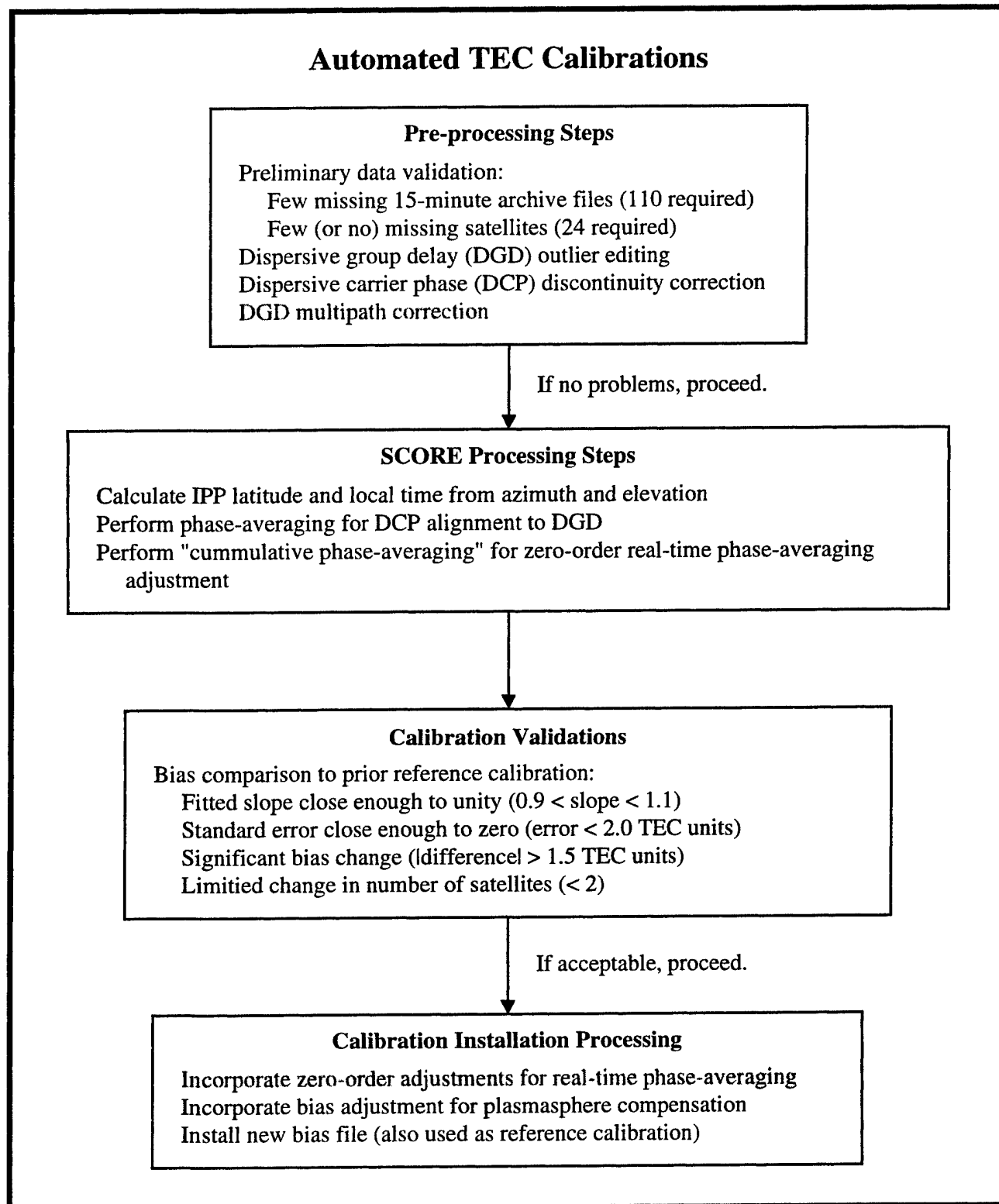


**Figure 5.** Schematic outline of automated bias calibration. Items not yet automated are shaded. The "cumulative phase-averaging" step and the associated "zero-order adjustments" can be eliminated after multipath mitigation is implemented. The

bias adjustment for plasmasphere compensation can be eliminated after a calibration process incorporating the plasmasphere is validated.

Initial testing was performed on data from the Nashua IMS. A template from day 001, 2004 was applied to data from day 002, 2004. The de-multipathed DGD (DMPCODE) is noisier, but does show a reduction in multipath relative to unaltered DGD (CODE), as shown in Figure 6. Figure 7 shows the 1 minute data that results from the unaltered MBN pass file. Figure 8 shows the reduction in multipath in the one-minute data that results from the same MBN file with the multipath template applied.

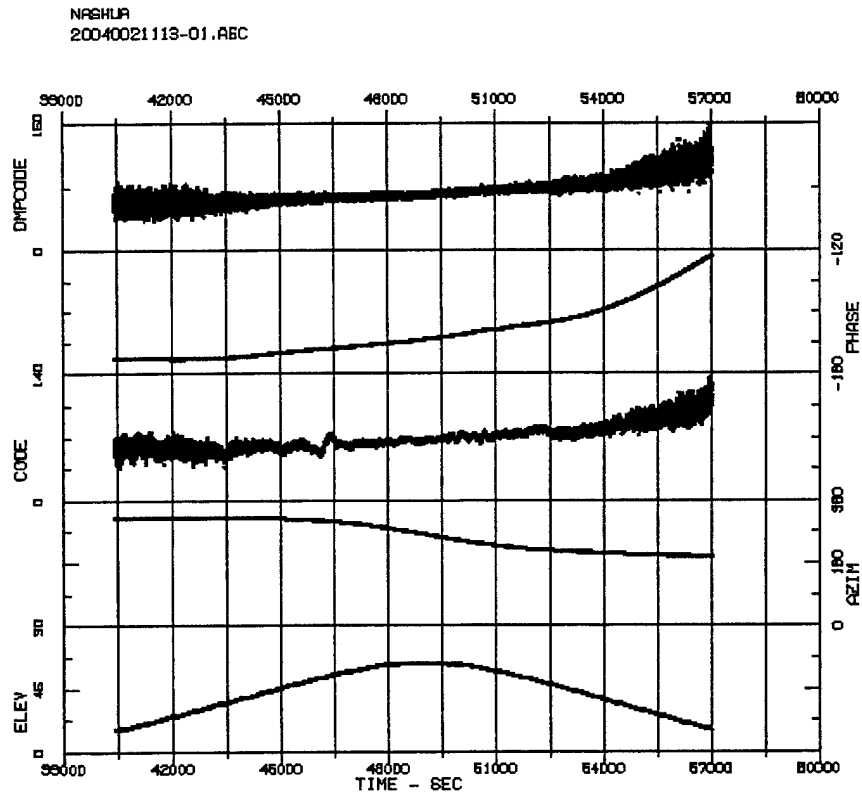


**Figure 6.** Plot of 2-Hz data (Day 002, 2004) showing reduction of multipath after application of multipath template.

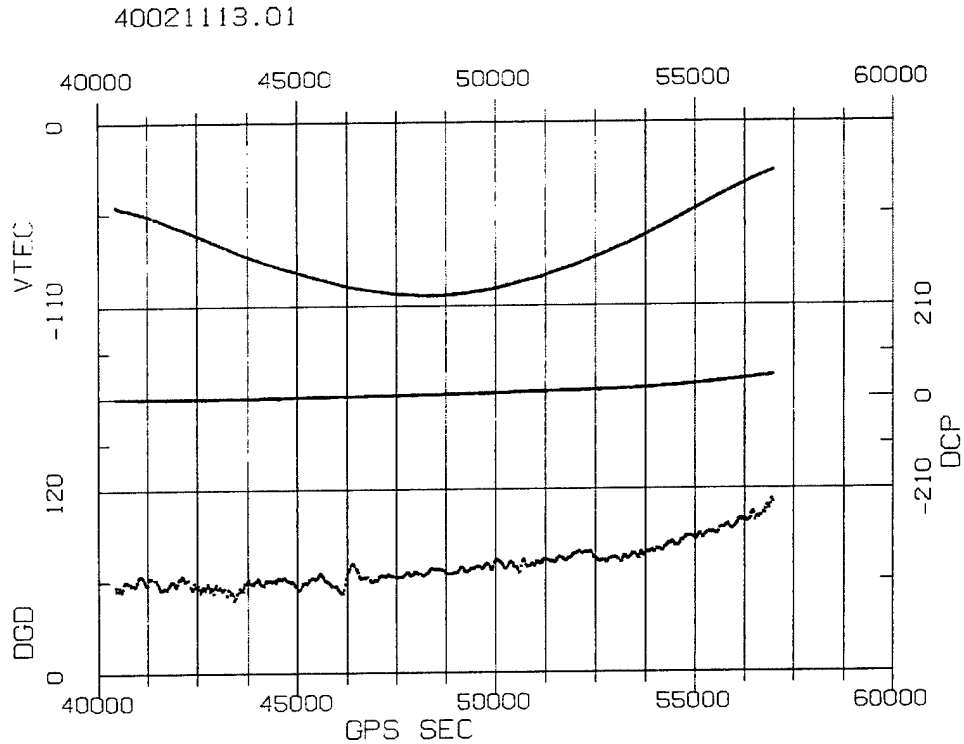


**Figure 7.** Plot of 1minute data (day 002, 2004) from 2-Hz data without template application.

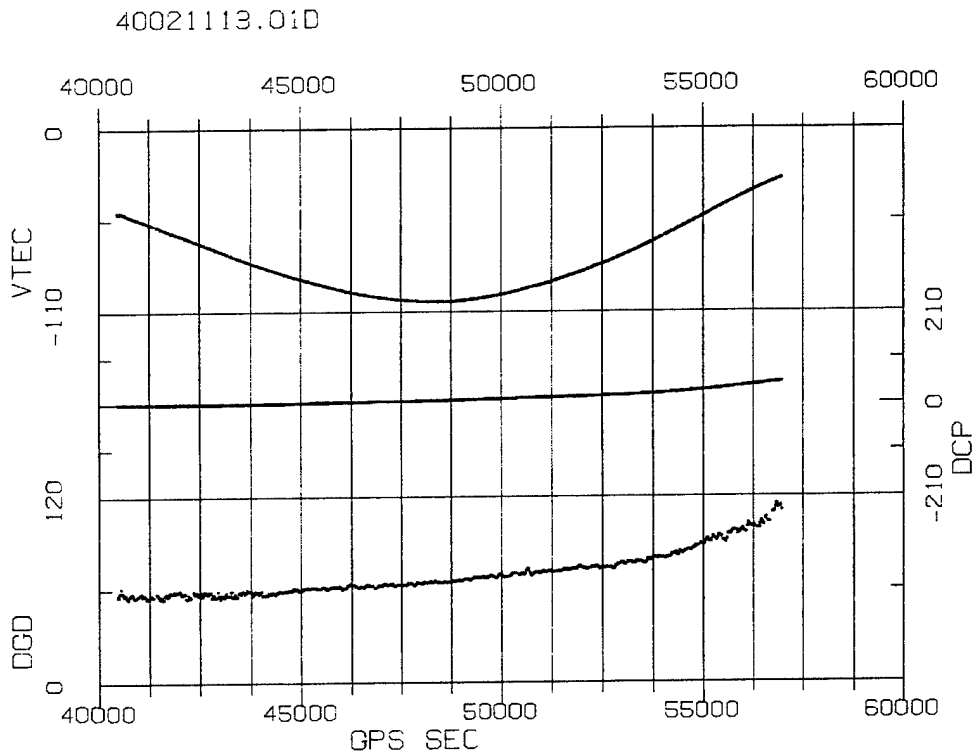


**Figure 8.** Plot of one-minute data (Day 002, 2004) from 2-Hz data with template application.

Application of the day 001 template to data from day 005 did not improve data quality, and investigation of the multipath template from day 005 data showed that the Nashua multipath



environment had changed. Figures 9, 10, and 11 provide a comparison of the multipath templates from days 001, 002, and 005, respectively. While the multipath environment is stable on days 001 and 002, by day 005 it had changed considerably. The IMS antenna is located on the roof of a building and is affected by snow accumulations, human activities, and variable multipath caused by low-flying aircraft approaching a nearby airport. These results may indicate problems with the antenna position at the Nashua site, but they illustrate the need for extensive evaluation of the multipath environment at each site.

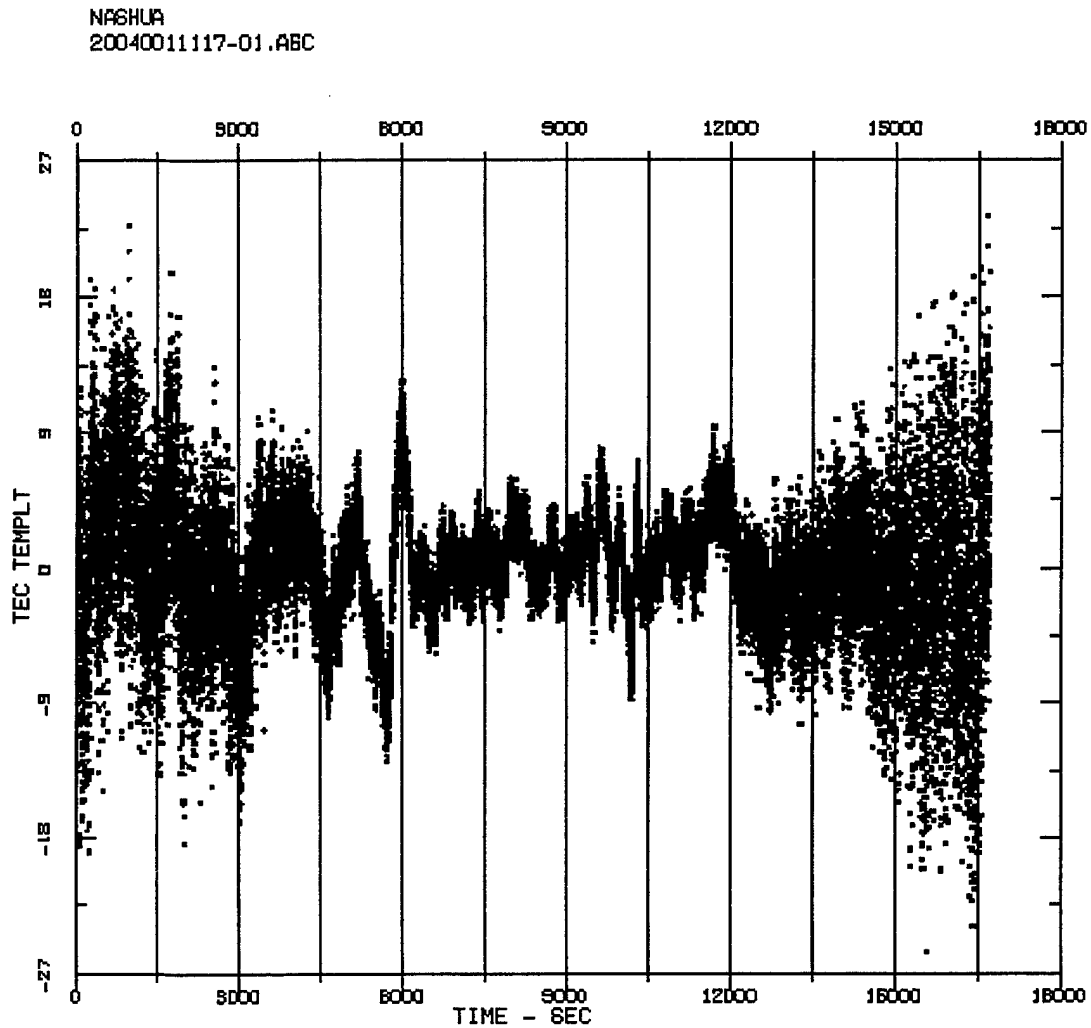


**Figure 9.** Multipath template from Nashua IMS, Day 001, 2004, PRN 1.

NASHUA  
20040021113-01.ABC

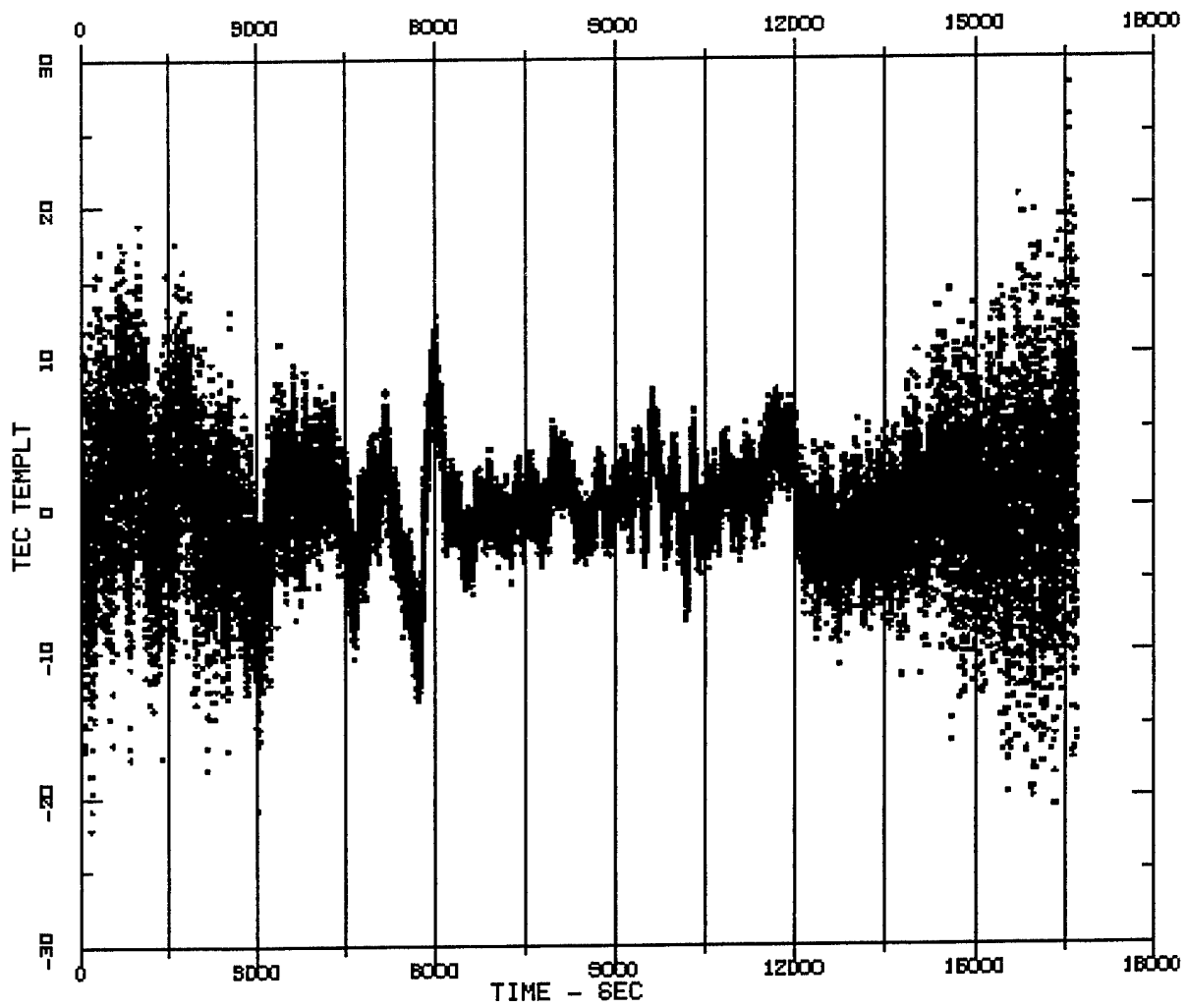
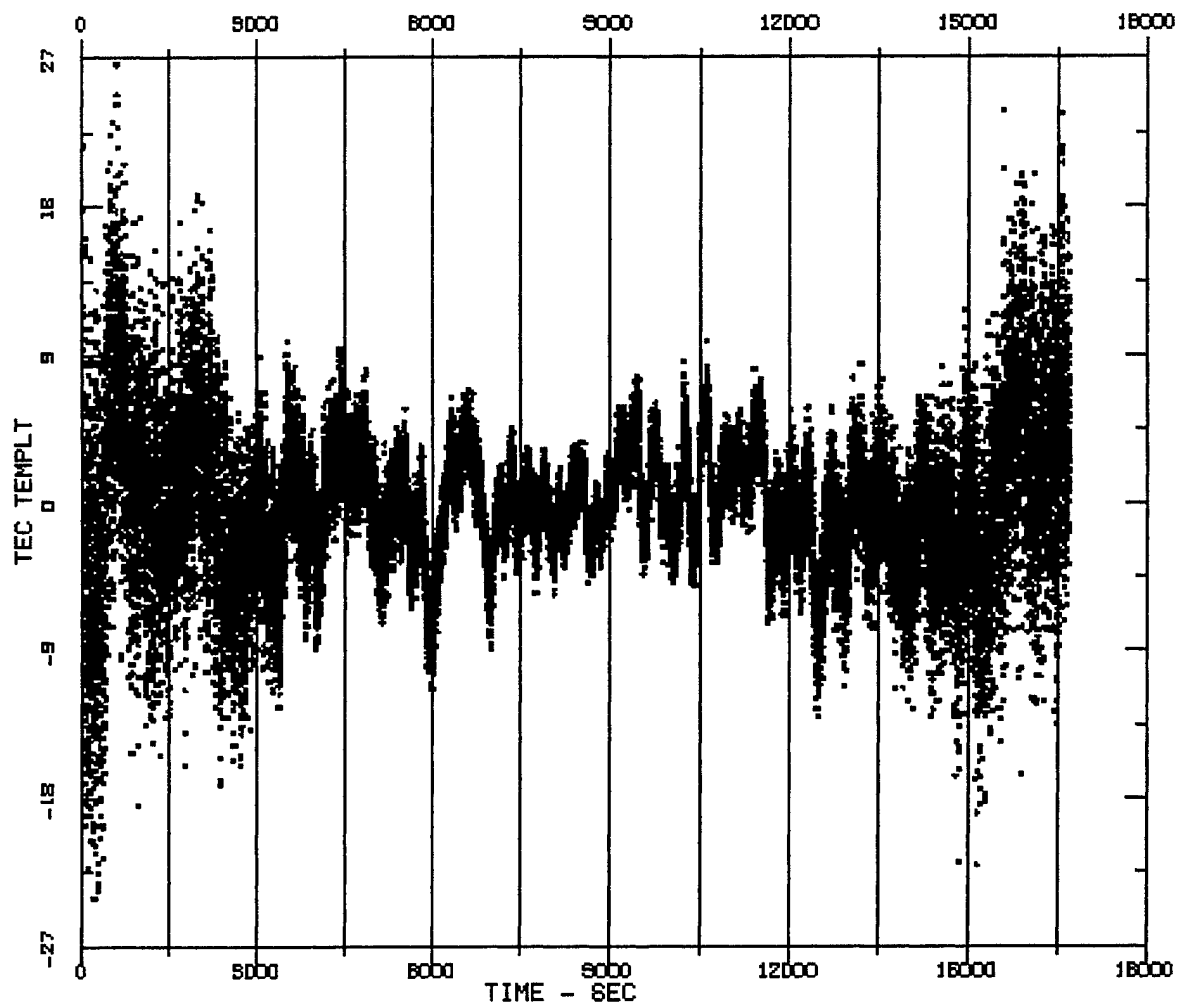


Figure 10. Multipath template from Nashua IMS, Day 002, 2004, PRN 1.

NASHUA  
20040061100-01.ABC



**Figure 11.** Multipath template from Nashua IMS, Day 005, 2004, PRN 1.

The ultimate goal would be to automate the template creation and application processes. Development and implementation of automated methods to establish criteria for selection of a quiet day for template creation, to determine sufficient data continuity, to evaluate stability of the multipath environment, to determine the period of effectiveness for a given template, and to provide for data indicators in the event that no usable template is available, will require a significant amount of additional time and effort. Additionally, a study of the impact in high-scintillation environments, like Thule, Greenland, and of the creation and use of multipath templates needs to be conducted.

#### 2.1.2 IMS Documentation

A set of documents was generated to provide formal documentation of the upgraded IMS, covering both hardware and software. The scope, contents, and format of this documentation were coordinated with both the AFRL program manager (Mr. Greg Bishop) and, through him, with personnel at AFWA. The following documents are provided:

1. Overview: a general description of the IMS system.
2. Pictorial diagram of rack components: annotated pictures showing a front and back view of the upgraded IMS rack with labels identifying the various components.
3. Rack parts list: a shipping list for each new rack.
4. Rack components/connection diagram, consisting consists of the following diagrams:
  - a. new rack assembly instructions;
  - b. rack power connections;
  - c. rack data connections;
  - d. UHF component (the Scion receiver subsystem).
5. Software documentation: An update to the Draper Software Requirements Specification (SRS) and Software Design Document (SDD). This is a single document that provides (1) a description of what the modification process was designed to do in terms of changes from the SRS; (2) a description of what functionality described in the SDD remains on the HP system; (3) a description of what functionality described in the SDD has been migrated to the PC; (4) a description of functionality in the SDD that has been dropped; and (5) a description of new functionality not in the SDD. This document will define the software modules as used in other documentation. It includes a software description that provides a short description of the IMS software modules.
6. Maintenance documentation:
  - a. Site installation procedures. This document contains a checklist of actions required to bring a new rack from in-crate to operational, and a list of things that might go wrong.
  - b. IMS routine maintenance procedures. A checklist of things to do/check during a site preventative-maintenance visit.
  - c. IMS routine monitoring procedures. Describes ways to check the data for system performance evaluation, and a checklist of routine monitoring accomplished from off-site (i.e., routine system performance checks done from Nashua).
7. System Configuration Document. This will be a spreadsheet-format document which will provide the following:
  - a. A mapping of individual equipment items (by S/N when possible) that make up each IMS rack to an IMS system number (1-5). Does not include which GPS receiver or UHF receiver (tracked separately). [Note: This is likely to be the same document as described above as the IMS Rack parts list.]
  - b. A hardware configuration matrix that provides a listing of the following information for each site:
    - i) What IMS system is at the site;
    - ii) What GPS receiver(s) is at the site (include firmware info);
    - iii) What SCION UHF receivers are at the site (include software info);
    - iv) The date of the last physical maintenance visit.
  - c. A software configuration matrix that provides the software rev, rev date, and upload/install date for each IMS site by software module.

8. Operator interface document. A description of how a person standing in front of the rack is to work directly with it via the system console. A three- or four-page description of menu selections accessible on and off site, how to log in on/off site, and any Scion interface information. It will have three parts: GPS Processor (the HP UNIX system), UHF Processor (the Scion system), and Console Processor (the PC/Windows system). This will be a how-to document and not an exhaustive listing of everything that every software module can do.

These documents will be provided as a formal deliverable on a CD-ROM disk.

## **2.2 Measurements of Polar Patches**

Two separate campaigns for polar-patch measurements were conducted in the vicinity of Qaanaaq, Greenland, using GPS receivers. The first campaign occurred during autumn 2000 and winter 2001, using a set of three GPS receivers with a small (approximately 170 meters) triangular baseline configuration, augmented by a fourth GPS receiver approximately 1200 meters away, at the Danish Meteorological Institute (DMI). The second campaign occurred during winter 2002, using three GPS receivers and a considerably larger baseline (approximately 1700 meters, maximum), but with a configuration somewhat restricted by the adjacent coastal and highland regions. (See Figure 12.)

The 2001 small-array configuration used correlations among 20-Hz signal intensity measurements to attempt to determine patch drift velocities, with comparisons against a co-located digisonde. Initial assessments of the GPS measurements were in general agreement with the digisonde, but the accumulated GPS results were seemingly dependent on the apparent direction to the GPS satellite, even accounting for possible differences associated with the regions of sky coverage for each satellite. The intensity measurements also were influenced by multipath, from the use of GPS antennas with different rejection characteristics and variations in the local environment, with especially difficult conditions at the DMI site.

The 2002 large-array configuration used correlations among TEC measurements, which had not been possible during the 2001 campaign because of granularity problems with the 20-Hz dispersive phase measurements. Unfortunately, the correlations for TEC tended to have a rather broad maximum, so these results also lacked significant consistency. The analysis and display techniques were developed further for this campaign, with applicability to the intensity data as well as to the TEC data, but a comparative study of the intensity analysis against the TEC analysis remains a future endeavor.

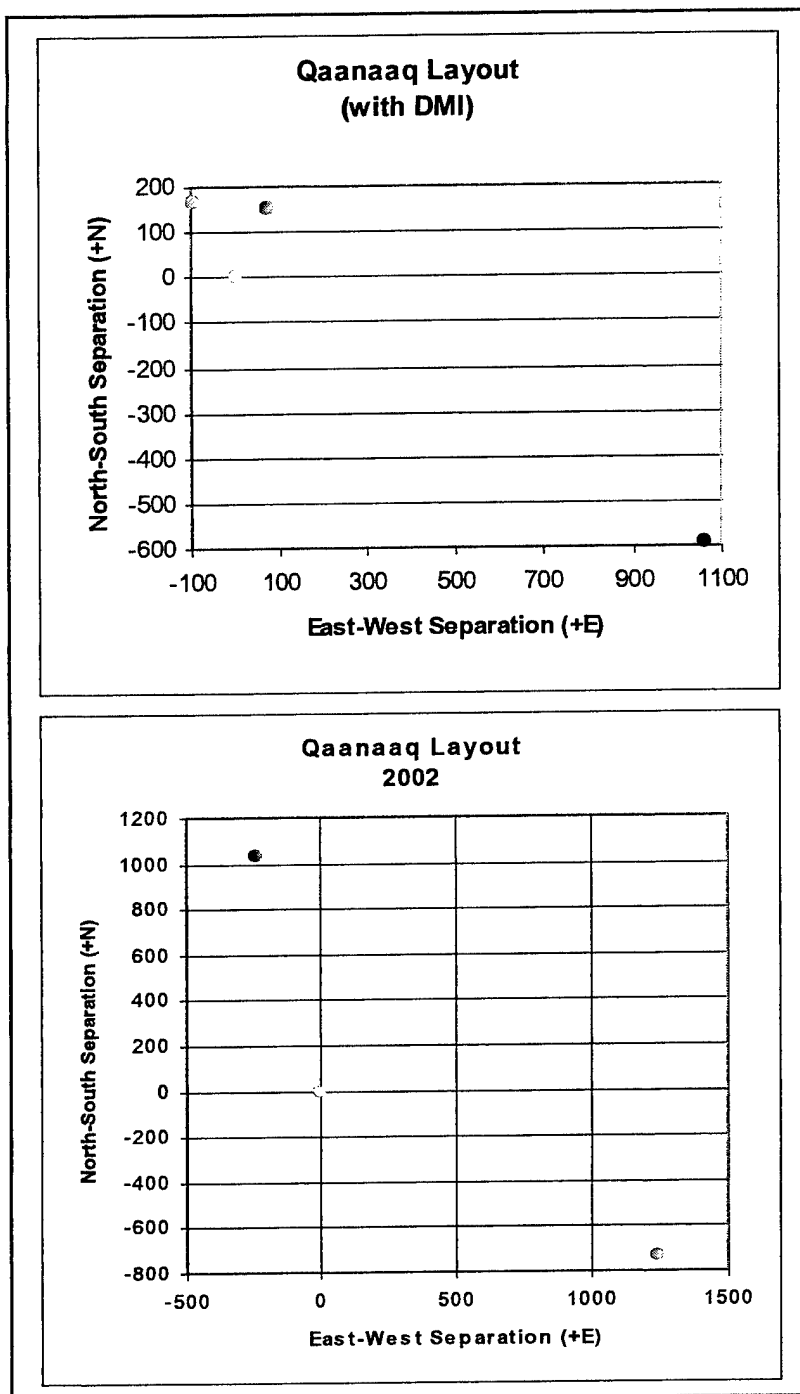


**Figure 12.** Configurations of receiver arrays for the two polar-patch drift campaigns at Qaanaaq, Greenland, with the DMI site at the southeast location for both.

### 3. DATA COLLECTION TO SUPPORT POLAR-CAP MODELING

Several sets of data were collected or retrieved from various archives in support of an effort to improve climatological models of ionospheric scintillation in the northern polar-cap region. Two instruments were deployed to northern Greenland for this purpose: an Ashtech Z-12 GPS receiver (the same model used by the IMS), and an NWRA ITS10S Transit receiver (similar to receivers used in the NWRA part of the Alaskan tomography chain). In addition, data were provided from an existing IMS system running at Thule, Greenland, and from an archive of data collected at Thule with an old STEL receiver during the solar-maximum year of 1989.

#### 3.1 Thule/GPS STEL Data Set

This data set was collected during the period 1988 through 1991 (with some time gaps) on paths from a receiver located at Thule, Greenland, to GPS satellites. We provided data from five months: October and November 1989, October and December 1990, and October 1991. Figure 13 is an example of the data from this set. The top panel shows the variation of relative slant-range TEC for an entire GPS satellite pass and the lower two panels show the S4 scintillation index derived from the L1 and L2 channels for the entire pass.

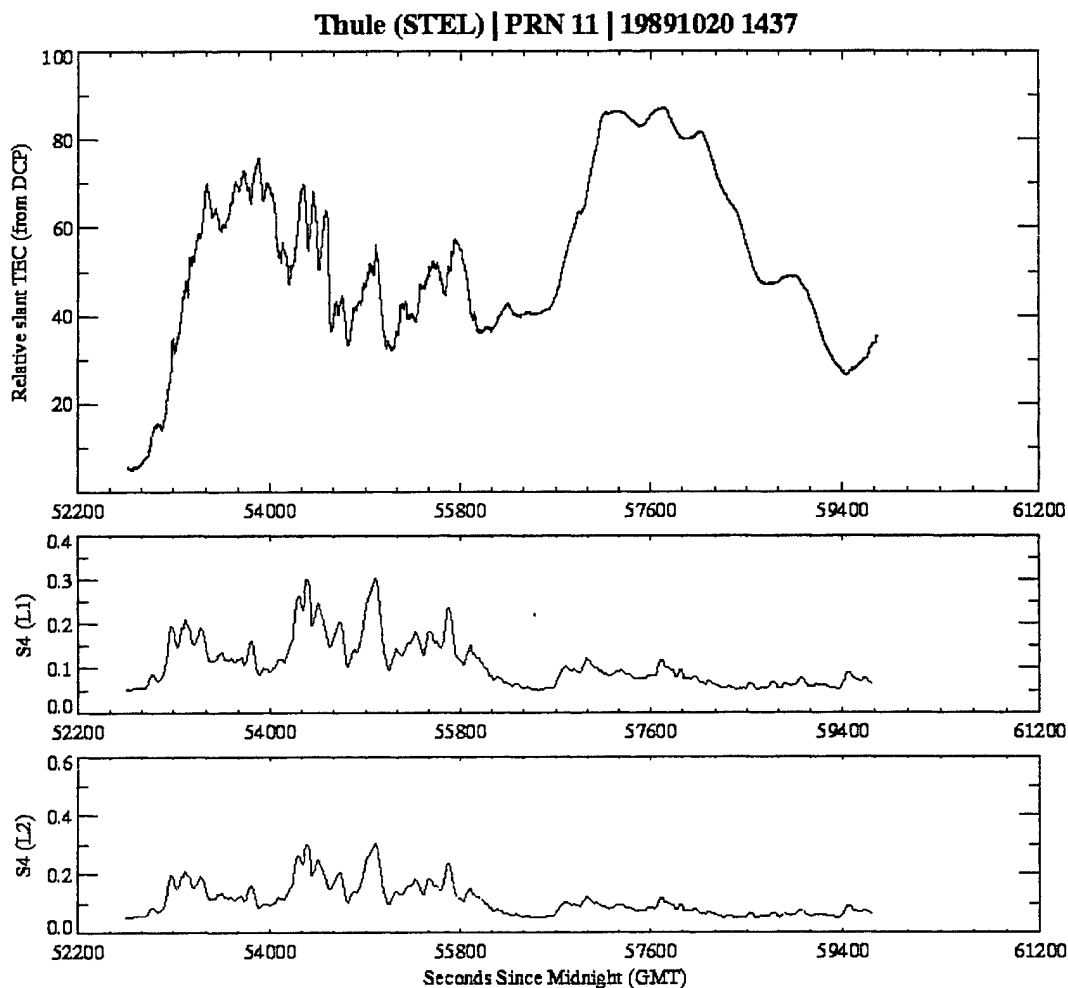


**Figure 13.** Sample data set from AFRL's STEL GPS receiver at Thule.

### 3.2 Thule/GPS IMS Data Set

This data set was collected from the USAF Ionospheric Measuring System (IMS) GPS receiver located at Thule, Greenland, in support of the NMD data collection campaigns during Winter 2000/2001 and Winter 2001/2002. Only data from the Winter 2000/2001 campaign had been provided by the time the model upgrade project was suspended. Data were provided for a total of seven days: 14 October 2000, 10 November 2000, 3 December 2000, 3 January 2001, 24 January 2001, 6 February 2001, and 31 March 2001. Figure 14 shows an example of an entire day of relative slant-TEC from the IMS for the 24 January 2001 period.

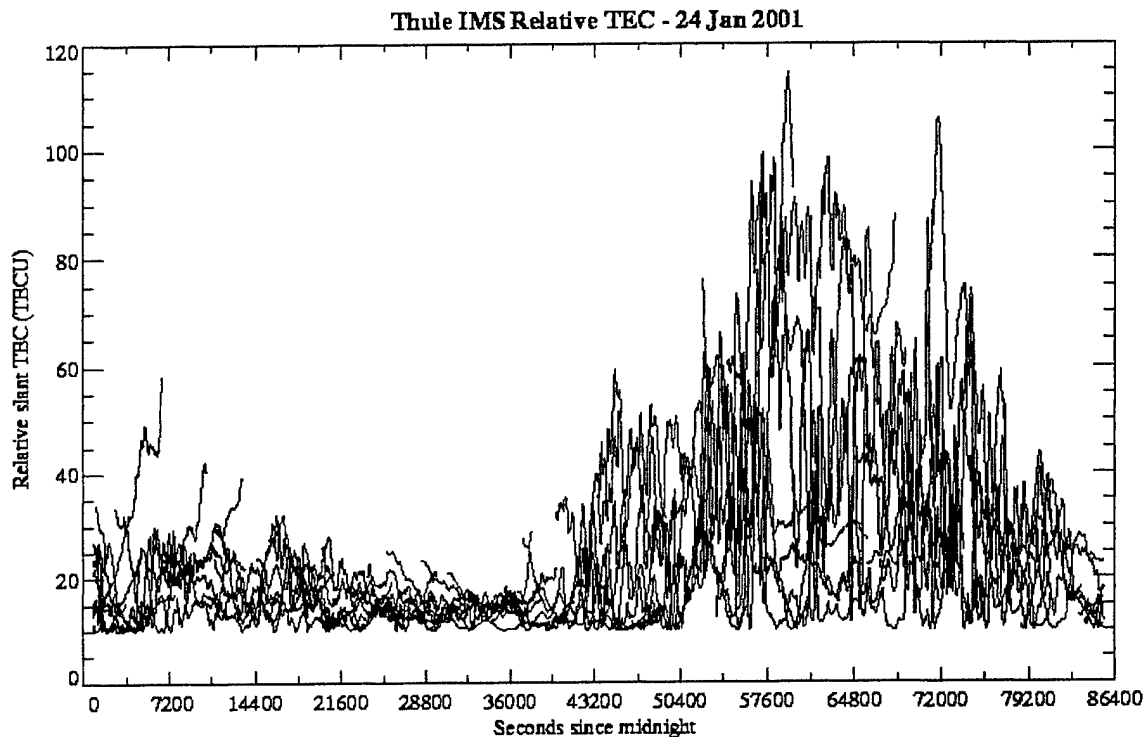


**Figure 14.** Relative slant-TEC from the Thule IMS for all GPS passes received on 24 January 2001.

### 3.3 Qaanaaq/GPS RTM Data Set

This data set was collected from a GPS receiver located at Qaanaaq, Greenland, and operated by NWRA. Data were collected during the Winter 2000/2001 campaign as part of a larger AFRL research campaign, and data from 14 October 2000, 10 November 2000, 3 December 2000, 24 January 2001, 6 February 2001, and 31 March 2001 were provided for use in the model upgrade project. Figure 15 provides an example of these data. The top two panels show the two components of the detrended intensity data (created using a low-pass filter with a 3-dB cutoff at 60 sec) and the lower two panels show the two components of the phase data taken from a GPS PRN02 pass on 10 November 2000. An Ashtech Z-12 system was purchased to support this project and was deployed to Qaanaaq in October 2001 for the 2001/2002 winter season. Data collected from this system was neither analyzed nor delivered due to termination of the scintillation model upgrade project.



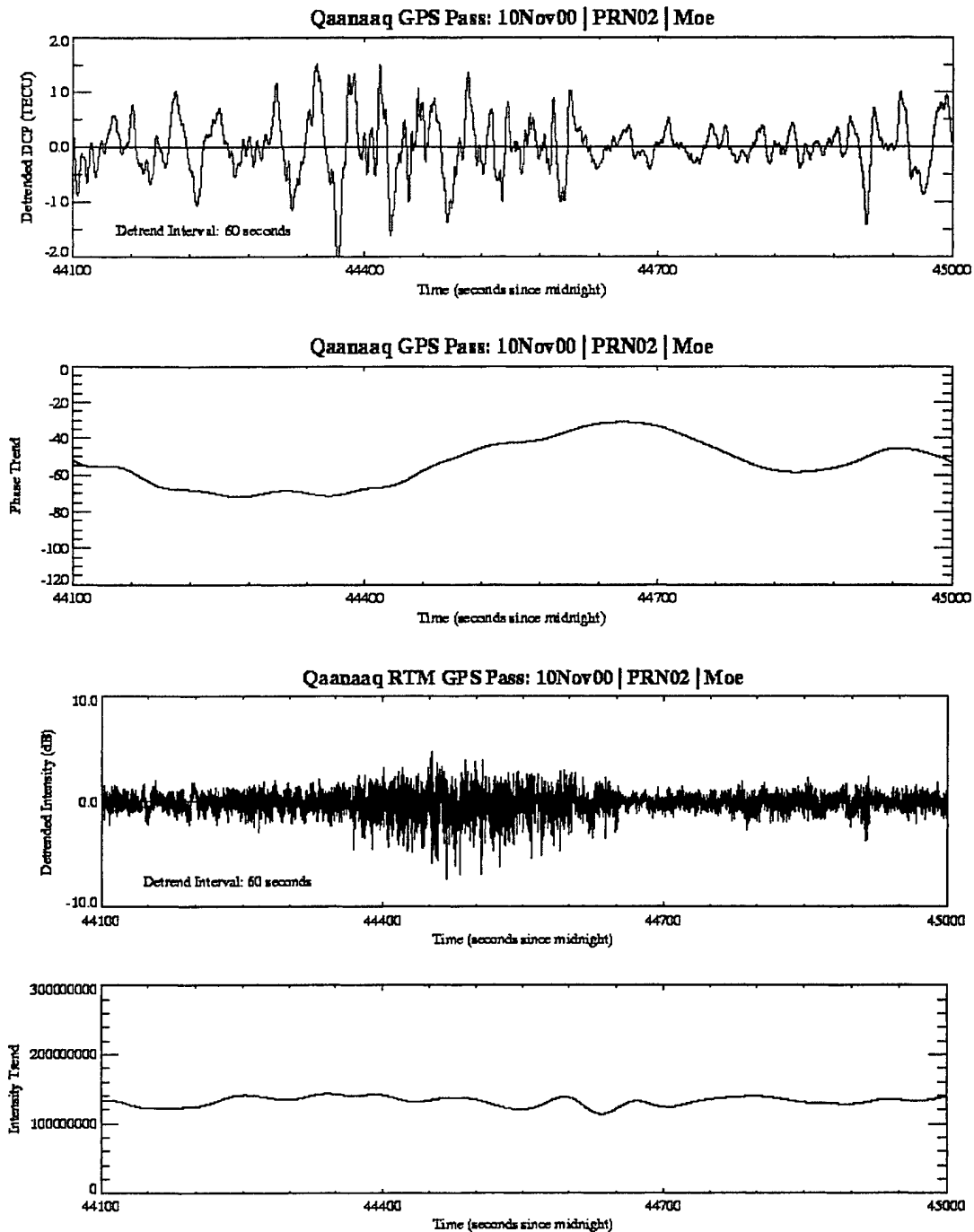


**Figure 15.** Data from the Qaanaaq GPS receiver from GPS PRN 02 taken on 10 November 2000. The top two panels are the detrended intensity and the intensity trend, and the lower two panels are the detrended phase and phase trend. In both intensity and phase, the trend and detrend components were separated using a low-pass filter with a 60-second cutoff.

### 3.4 Qaanaaq/LEO ITS10S Data Set

This data set was collected from an NWRA ITS10S receiver located at Qaanaaq, Greenland, which collects data from low-orbiting Transit and Transit-like satellites, operated by NWRA for AFRL. Data were collected during the Winter 2001/2002 campaign specifically in support of the NMD data collection campaign. These data included the dispersive phase between UHF and VHF as well as intensity at both frequencies (nominally 150 and 400 MHz). The data were processed to provide relative slant-TEC, S4 indices for VHF and UHF, and the  $\sigma_\phi$  phase scintillation index.

Figure 16 provides an example of these data. The top panel shows the relative slant-TEC for an entire Transit pass (satellite Oscar 32), the second panel shows the detrended dispersive phase, and the lower two panels show the detrended intensity on VHF and UHF. The pass geometry is illustrated beneath the data.

Data for the entire Winter 2001/2002 campaign were delivered to the model upgrade project. This instrument was left in operation at Qaanaaq after the campaign period, and continues to collect data, providing a near-continuous data set from late September 2001 through the present.

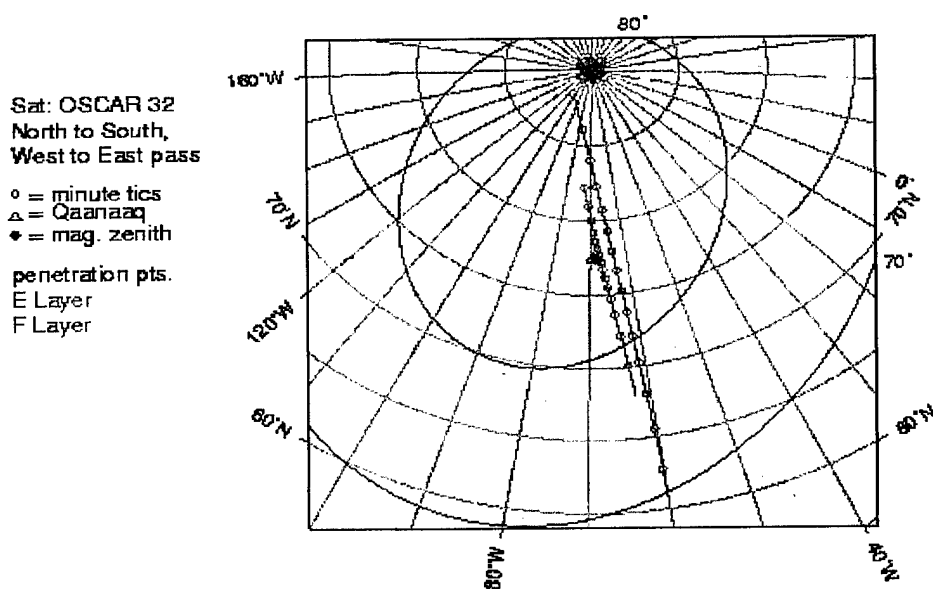
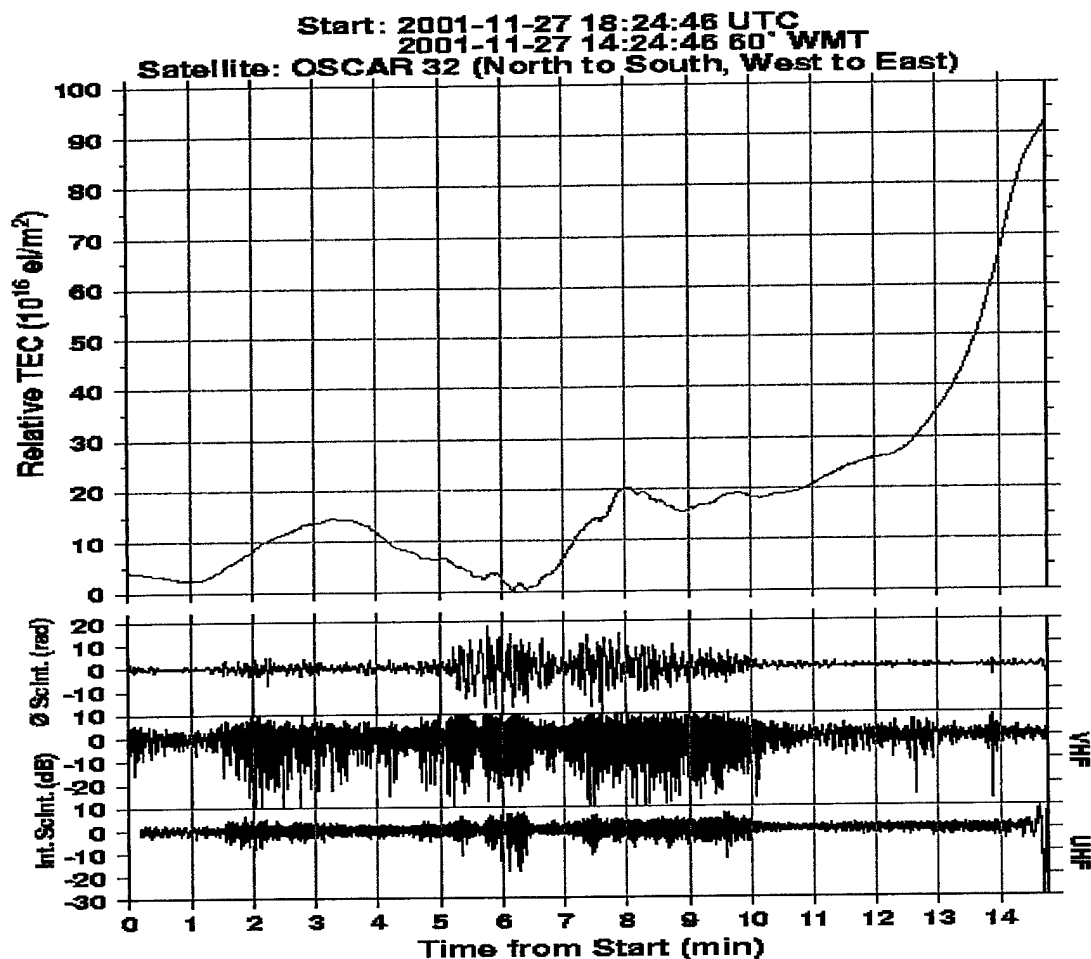


**Figure 16.** Sample data from a satellite pass over Qaanaaq, Greenland, obtained by means of the NWRA ITS10S receiver deployed there.

## **4. HAARP TOPICS**

While continuing to be improved, the HAARP facility near Gakona, AK, now is a functioning observatory at which research is conducted in upper-atmospheric and ionospheric physics and radio propagation. Under this contract, NWRA coordinated installation of enhanced diagnostic instrumentation and participated in research employing some of them. Our activities aimed at enhancing HAARP diagnostics were carried out primarily by NWRA Consultants John Rasmussen, A. Lee Snyder, and Jens Ostergaard. Their efforts are detailed in Appendices E, F, and G, respectively.

### **4.1 The Natural Ionosphere**

NWRA's research activities as part of HAARP centered on collection and analysis of transionospheric radiowave data. Transmission of two or more phase-coherent radio signals from satellites above the ionosphere to receivers on the ground permits measurement of the path integral of plasma density (so-called total electron content, or TEC) through the ionosphere. TEC is proportional to the dispersive (differential) phase between the two signals (and, with less precision but greater certainty, to differential group delay). Recording of rapid fluctuations in dispersive phase and in received signal strength yields measurement of trans-ionosphere radiowave scintillation.

Under this contract, NWRA measured TEC on slowly moving paths penetrating the entire ionosphere by recording dispersive phase and differential group delay registered on signals transmitted from satellites of the Global Positioning System (GPS) to Gakona, AK. We also measured both TEC and scintillation on paths between satellites moving rapidly over Alaska in high-inclination, low-earth orbits (LEO) just above the main ionospheric (F) layer and several ground stations. We report our GPS activities in Subsection 4.1.1 and those employing LEO satellites in Subsection 4.1.2.

#### **4.1.2 Ionospheric Research Employing GPS**

An Ashtech Z-FX Continuously Operating Reference Station (CORS), consisting of a 12-channel GPS receiver and an antenna, operated at Gakona, with data collection initially being performed by means of the RTM program, supplemented by a real-time process to convert one-minute reports from the RTM program into a database that becomes the source of calibrated measurements of absolute TEC displayed on the HAARP Web site.

Based on declining performance of the initial computer installed for GPS data collection, efforts were initiated in early 2001 to acquire and configure a replacement computer. Unfortunately, the Gakona computer experienced a disk-drive failure in late March 2001, shortly before preparation of the replacement computer was completed, so data collection was interrupted until the replacement computer was installed during a site visit in early April 2001. An updated heartbeat monitor also was installed with the new computer.

In addition to GPS data collection and preliminary display processing, this computer also supported automated calibrations of the ITS10S TEC measurements, using an extension of the Leitinger method (Leitinger et al., 1975), as implemented in the Self Calibration of Range Errors (SCORE) algorithm (Bishop et al., 1994), with calibrated GPS TEC measurements serving as supplementary references to the coordinated measurements among the NWRA ITS10S receivers (Mazzella et al., 2001). The GPS TEC calibrations were conducted by an operator-initiated and monitored process, in contrast to the automated ITS10S calibrations.

A summary of calibration techniques and observations was presented at the 2001 International Beacon Satellite Symposium, held at Boston College in June 2001 (Mazzella et al., 2001). Auroral and trough features in the vicinity of Gakona are evident in the observations presented.

Construction activities at the instrument site interrupted operations during the summer of 2001, with declining performance by the GPS antenna/receiver system during the following months, until the GPS antenna was replaced in late November 2001, after which the sky coverage improved significantly. The original GPS antenna was utilized at the NWRA Nashua facility for evaluation of its performance, and it failed completely during the first significant snowfall in late 2002. Some data artifacts resulted from sharing of the GPS antenna with a single-frequency Trimble Pathfinder receiver (for a separate effort supporting position determinations), and this shared configuration was discontinued in April 2002.

Normal operations prevailed until January 2003, when most GPS signals were lost for several days because of a significant covering of snow on the conical antenna cover, and then more persistent and progressive deterioration commenced in early February 2003, with persistent noise in the GPS dispersive-phase signals and declining sky coverage. A diagnostic site visit in March 2003 could not solve the problem, and a further significant deterioration in performance occurred in June 2003, with operations ceasing in July 2003. The receiver did not appear functional during subsequent examinations at the NWRA Nashua facilities, using other antennas, and it was sent to Thales (which had acquired Ashtech) for repairs.

#### 4.1.3 Ionospheric Research Employing LEO Satellites

##### 4.1.3.1 *Data Recorded*

Under this contract, we operated three NWRA ITS10S coherent receiving systems as elements of HAARP's diagnostic suite of instruments. Located approximately along the 145<sup>th</sup>-deg West meridian, they continue to operate at Cordova on the Gulf coast, at Gakona, and near Delta Junction, AK. Their purpose is to record latitudinal scans of VHF-UHF scintillation and slant-path relative TEC. An example of the recordings, taken from the HAARP Web site, appears in Figure 17, along with the observing geometry.

The upper panel shows slant-path TEC between an Oscar-class Transit satellite of the Navy Ionospheric Monitoring System (NIMS) and the receiver at the ITS10S station just south of Delta Junction. Immediately below the TEC are time series of detrended dispersive phase between the VHF and UHF signals transmitted from Oscar 32 as it traversed from over the Arctic Ocean to over the Gulf of Alaska at an altitude of approximately 1000 km. The fluctuations constitute dispersive-phase scintillation, which leads to diffraction patterns moving across the ground that were recorded as VHF and UHF intensity scintillation, also displayed.

Scintillation indices, S4 for intensity and rms values for phase, are computed over ten-sec intervals and posted on the HAARP Web site in both ASCII and netCDF files, along with numerical TEC values and data-quality codes. The ITS10S stations also record TEC and scintillation during passes of several other US and Russian satellites that have transmission characteristics similar to those of NIMS.

Start: 2002-06-02 12:40:48 UTC  
 2002-06-02 03:40:48 AST  
 Satellite: OSCAR 32 (North to South)

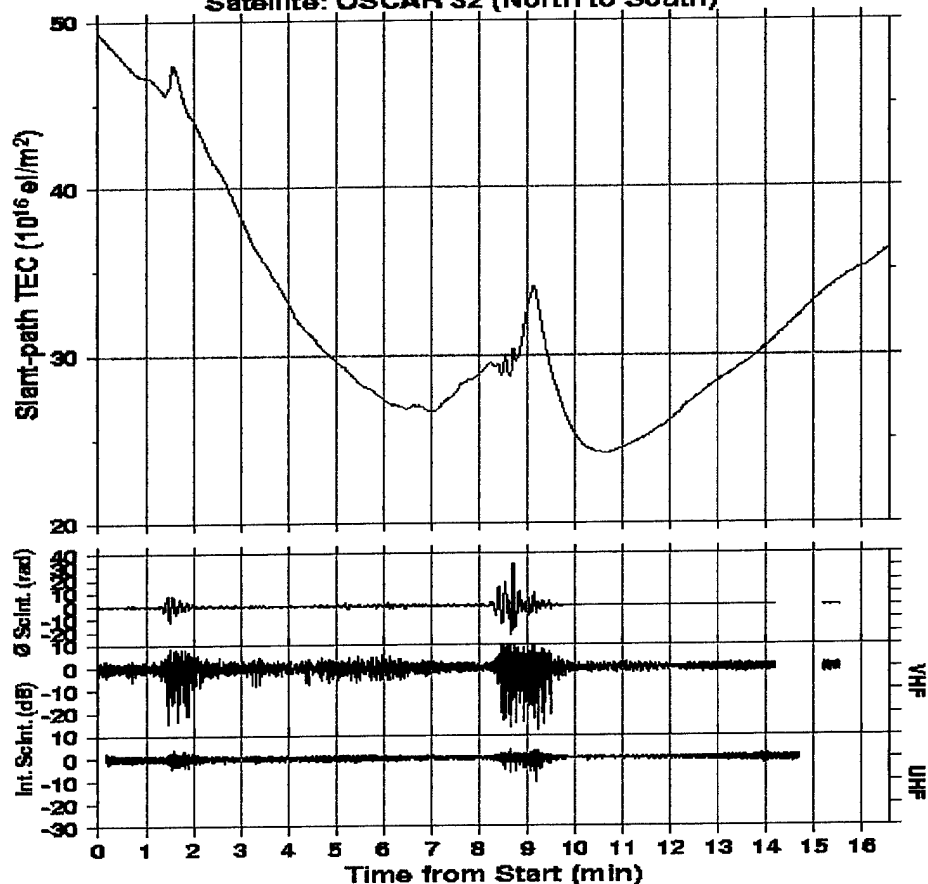
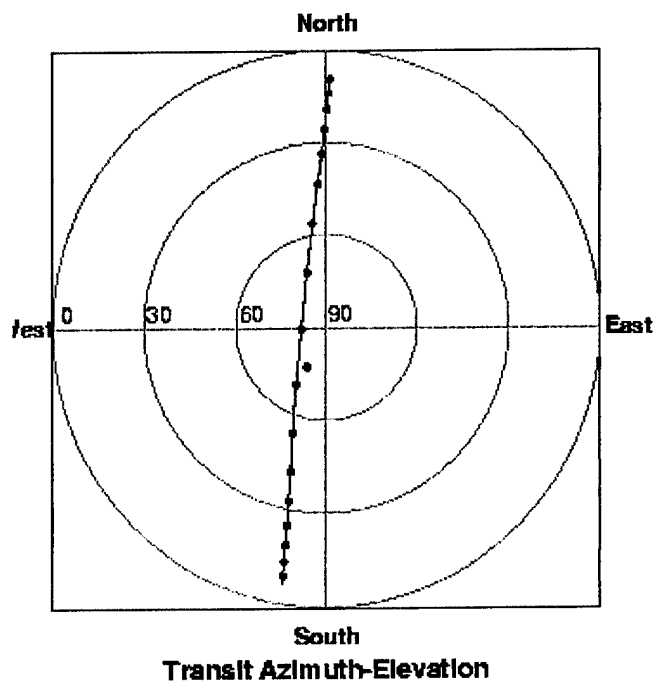


**Figure 17.** Slant-path TEC and scintillation observed at the Delta ITS10S station (geometry below).



Sat: OSCAR 32

North to South pass

o = minute tics

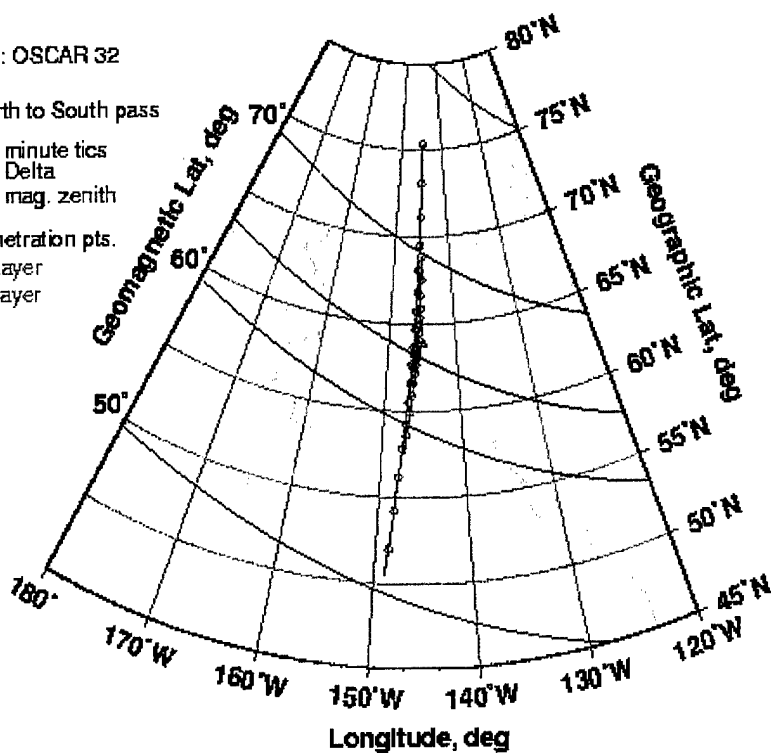
Δ = Delta

• = mag. zenith

penetration pts.

E Layer

F Layer



#### 4.1.3.2 Tomographic Imaging

##### 4.1.2.2.1 Procedures

A major reason for recording slant-path TEC between LEO satellites and multiple stations is that the records constitute measurements of the line-integral of plasma density on many rays through the ionosphere, a single satellite pass providing one look angle per station through each plasma-density "pixel." Mathematical inversion then yields a tomographic image of the ionosphere. Under this contract, NWRA entered into collaboration with the Geophysical Institute at the University of Alaska Fairbanks (UAF) to operate the five-station chain illustrated in Figure 18.

The three triangles show locations of the three NWRA ITS10S stations, and the squares show the locations of two stations operated by UAF and equipped with CIDR receivers developed by the Applied Research Laboratory (ARL) of the University of Texas Austin. Originally, UAF operated a surplus Navy navigation receiver to record TEC at Poker Flat, between Delta and Ft. Yukon, and planned to install a CIDR at Arctic Village, between Ft. Yukon and Kaktovik. A seven-station chain would have provided seven look angles through ionospheric pixels, but the receiver at Poker Flat soon failed, and a CIDR never was deployed to Arctic Village.

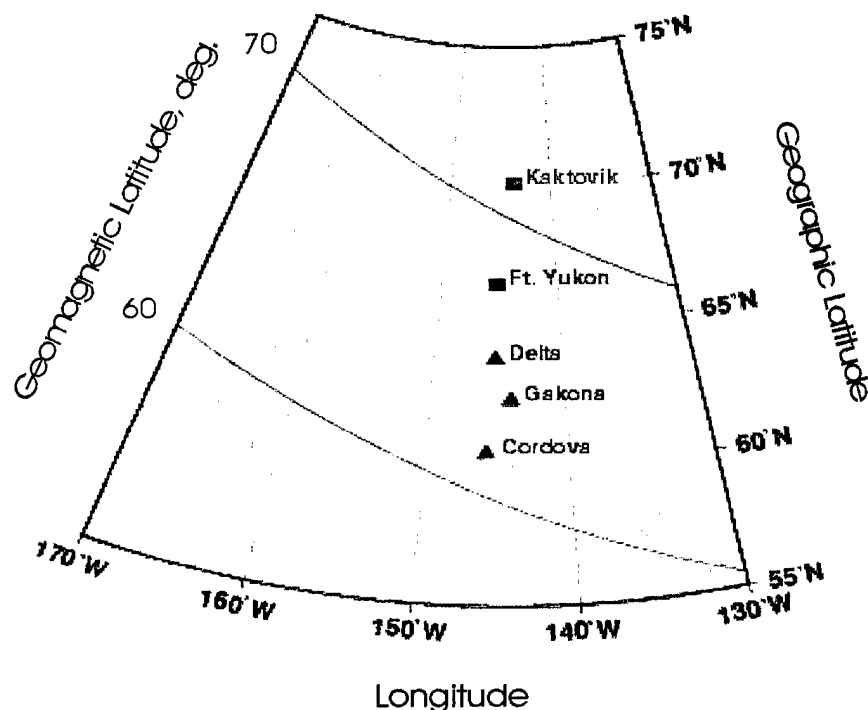


**Figure 18.** Five-station chain of TEC receivers deployed to image the ionosphere over Alaska tomographically.

Even five stations, if spanning sufficient latitude to provide low-angle rays as well as high-angle ones, can yield rather comprehensive images of the ionosphere. An example, for the pass depicted in Figure 17, appears in Figure 19. It shows substantial structure in the F layer following a period of moderate geomagnetic disturbance. The image in Figure 20, produced from an Oscar pass a little over two hours later, reveals how the features imaged have moved equatorward and changed in shape.

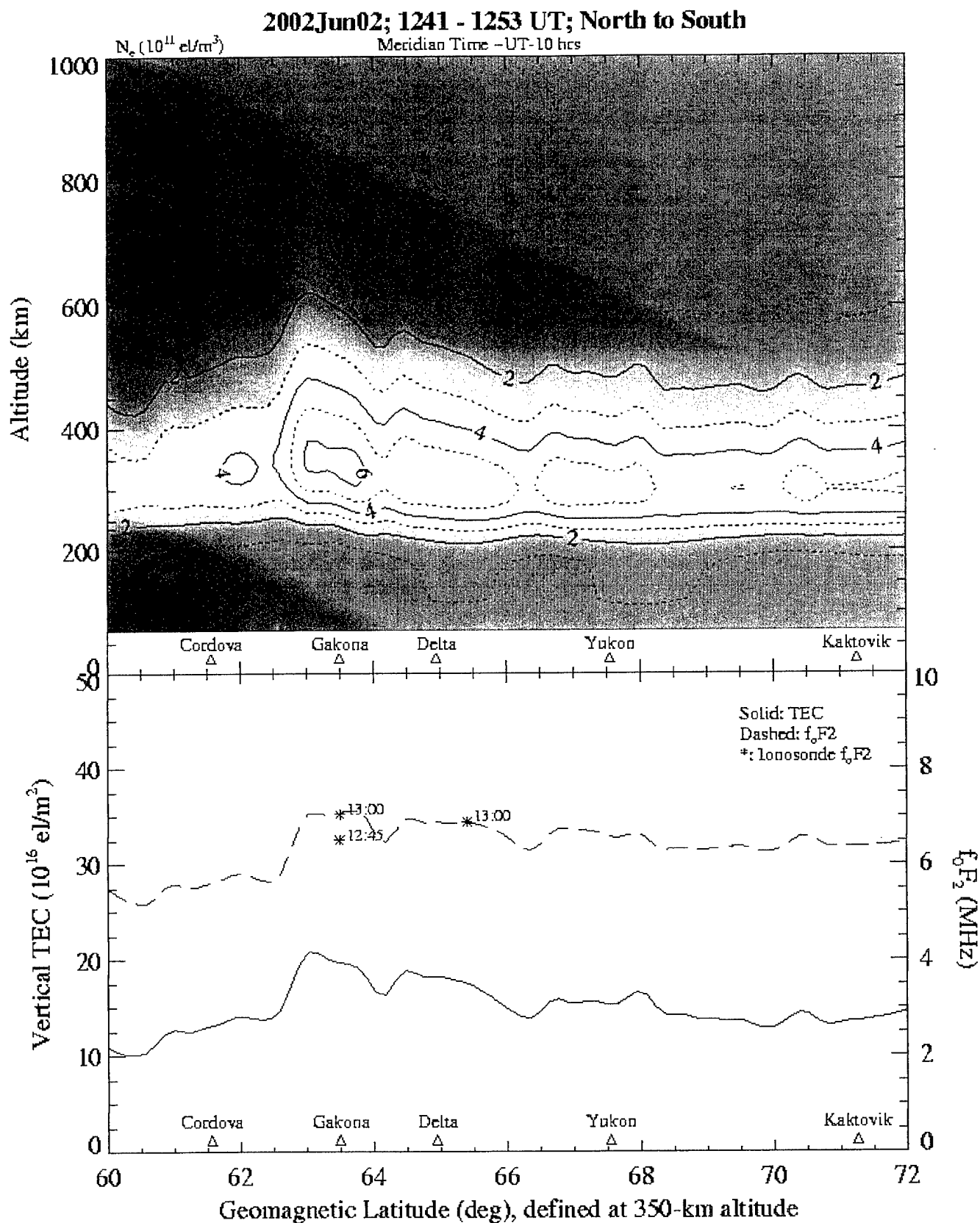


**Figure 19.** Tomographic image and parameters scaled there from (lower panel) obtained from TEC data shown in Figure17 and similar data obtained at the other four receiving stations indicated by triangles above the abscissa. Asterisks show comparative ionosonde measurements.



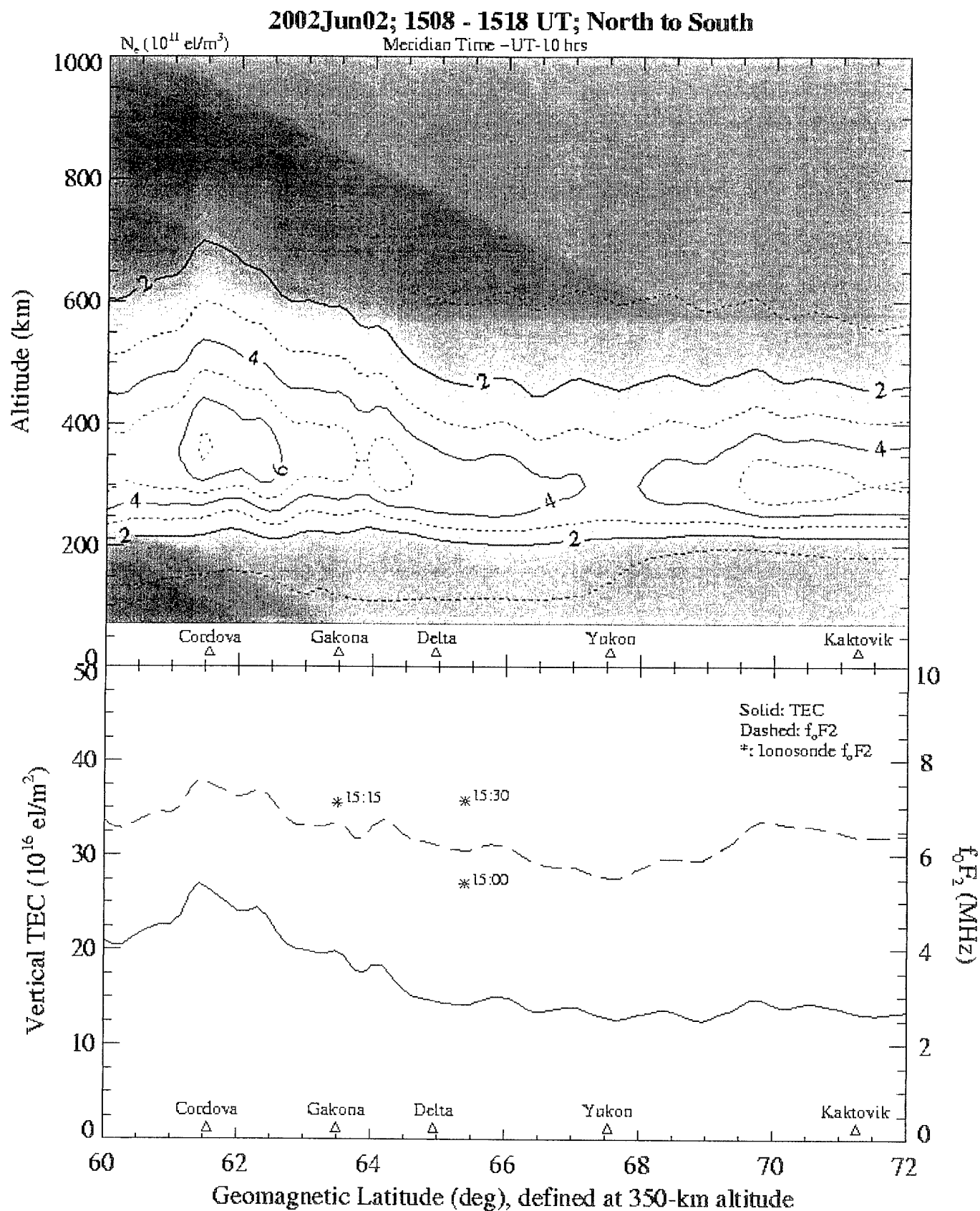


Figure 20. State of the ionosphere over Alaska some two hours after that depicted in Figure 19.

The panels beneath the images in Figures 19 and 20 display two parameters derived from them. The solid curve shows the latitudinal profile of vertical TEC, obtained by integrating vertically through the image. The broken one shows the latitudinal profile of the F-layer critical frequency ( $f_oF_2$ ) computed from the peak density in the image. For comparison, the  $f_oF_2$  values obtained from the ionosondes at Gakona and Sheep Creek (near Fairbanks), AK, at the times indicated are shown by asterisks.

The tomographic images posted on the HAARP Web site are generated using an updated version of the NWRA Ionospheric Tomography System (ITS) inversion processor described by Fremouw and Bussey, 1994. It employs weighted, damped, least-squares (WDLS) matrix inversion (Menke, 1989), as described by Fremouw et al. (1992, 1994). The images are developed from relative slant-path TEC records, with the unknown constant corresponding to a many-cycle ambiguity in dispersive phase being determined as part of the least-squares solution. The data flow and related archiving are detailed in Appendix H.

As detailed in Appendix H, we apply several editing criteria in selecting TEC data for tomographic inversion. These criteria include: (a) passage of an Oscar satellite (since the ARL instruments cannot receive signals from the Russian satellites, and non-Oscar U.S. satellites are less useful than the Oscars for a variety of reasons) that reaches at least  $60^\circ$  elevation at one or more stations and (b) receipt of data from at least three stations appropriately spaced.

A final criterion used in deciding whether to post an image is to compare the data employed with a replica thereof computed from the image. To do so, we integrate the electron density in the image along each raypath that was employed in the inversion. This results in a replica of the TEC record from each of the stations from which data were used. After subtracting the first value of the first point in each replica from all points therein (since the direct measurements are of relative TEC), we compute the differences between the replicas and the corresponding original records.

An example of the comparison between relative TEC records and their image-borne replicas appears in Figure 21, for the pass whose image appears in Figure 19. If the rms residual for all paths (differences for all records) exceeds one TEC unit ( $1 \text{ TECu} = 10^{16} \text{ electrons/m}^2$ ), the image is kept in NWRA's local archive but not posted on the HAARP Web site. A histogram of rms residuals for all images stored in the local archive as of this writing is shown in Figure 22.

Under this contract, we produced 11,990 images that met our criteria for posting on the HAARP Web site, covering the interval from January 2001 through March 2004. Tables 4 through 7 provide a summary of images generated from the Alaskan tomography network during the years 2001, 2002, 2003, and the first quarter of 2004, respectively, as a function of month. The upper panel separates the images by the set of stations used to generate each image. The entries in the columns under "Stations" indicate which stations contributed to the image; for example, the top row lists images generated from the station-set Kaktovik, Fort Yukon, and Delta Junction. The bottom panel shows the percentage of images in each month that included data from the station listed in the left-most column. (Note that the Copper Center station was deployed for only a limited time in support of the HAARP Irregularities Campaign.)

Unfortunately, the two northern stations (equipped with ARL CIDR receivers operated by UAF) have operated only intermittently (half to two-thirds of the time in 2001 and 2002, less in 2003, and none in the first quarter of 2004). Consequently many of our images employ data from three stations (equipped with NWRA ITS10S receivers operated by NWRA) spanning only about  $3.4^\circ$  of latitude.

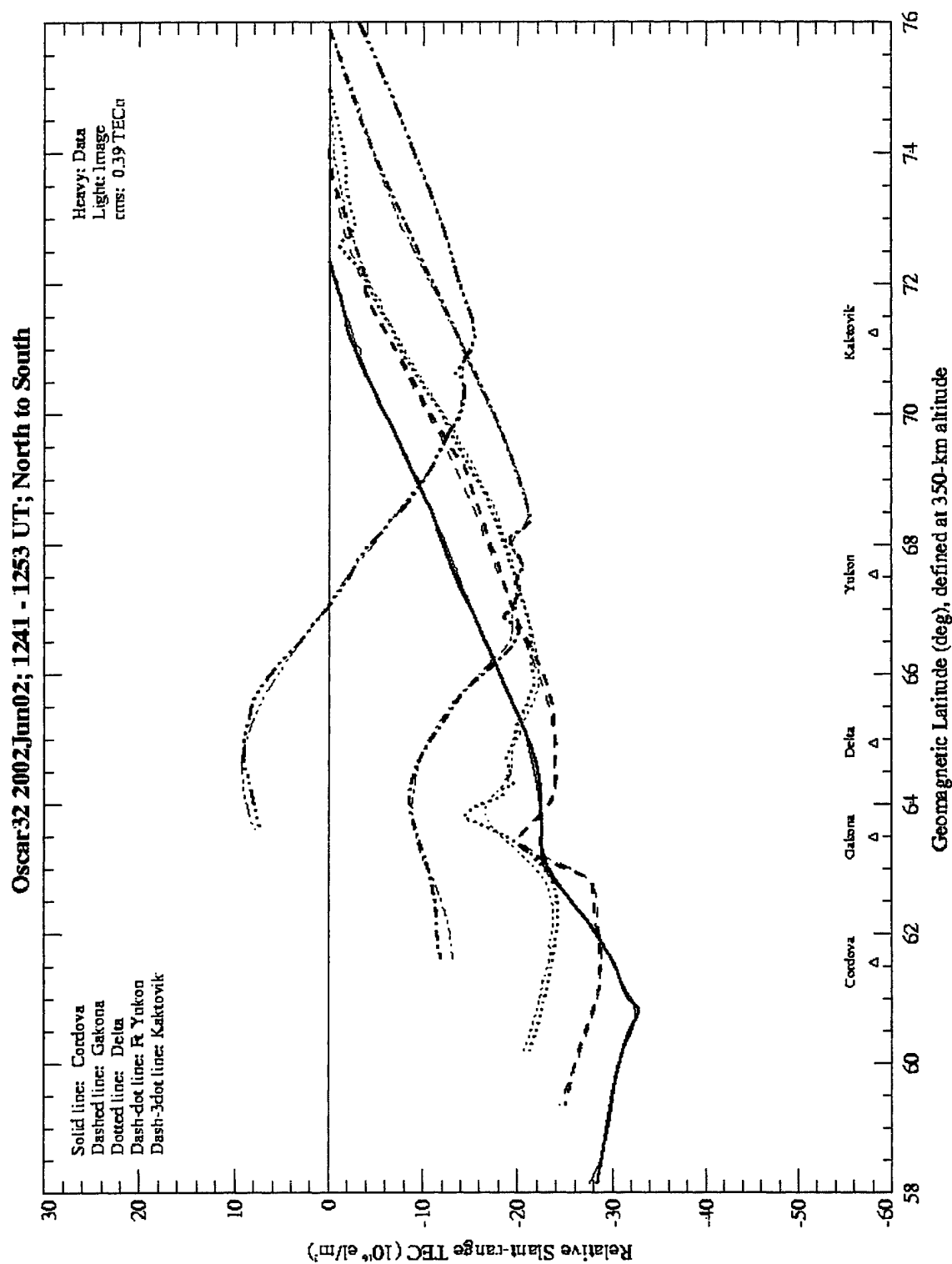


**Figure 21.** Comparison of measured relative TEC (heavy lines) and relative TEC on same raypaths to the receiving stations computed (light lines) by integrating through the tomographic image in Figure 19.

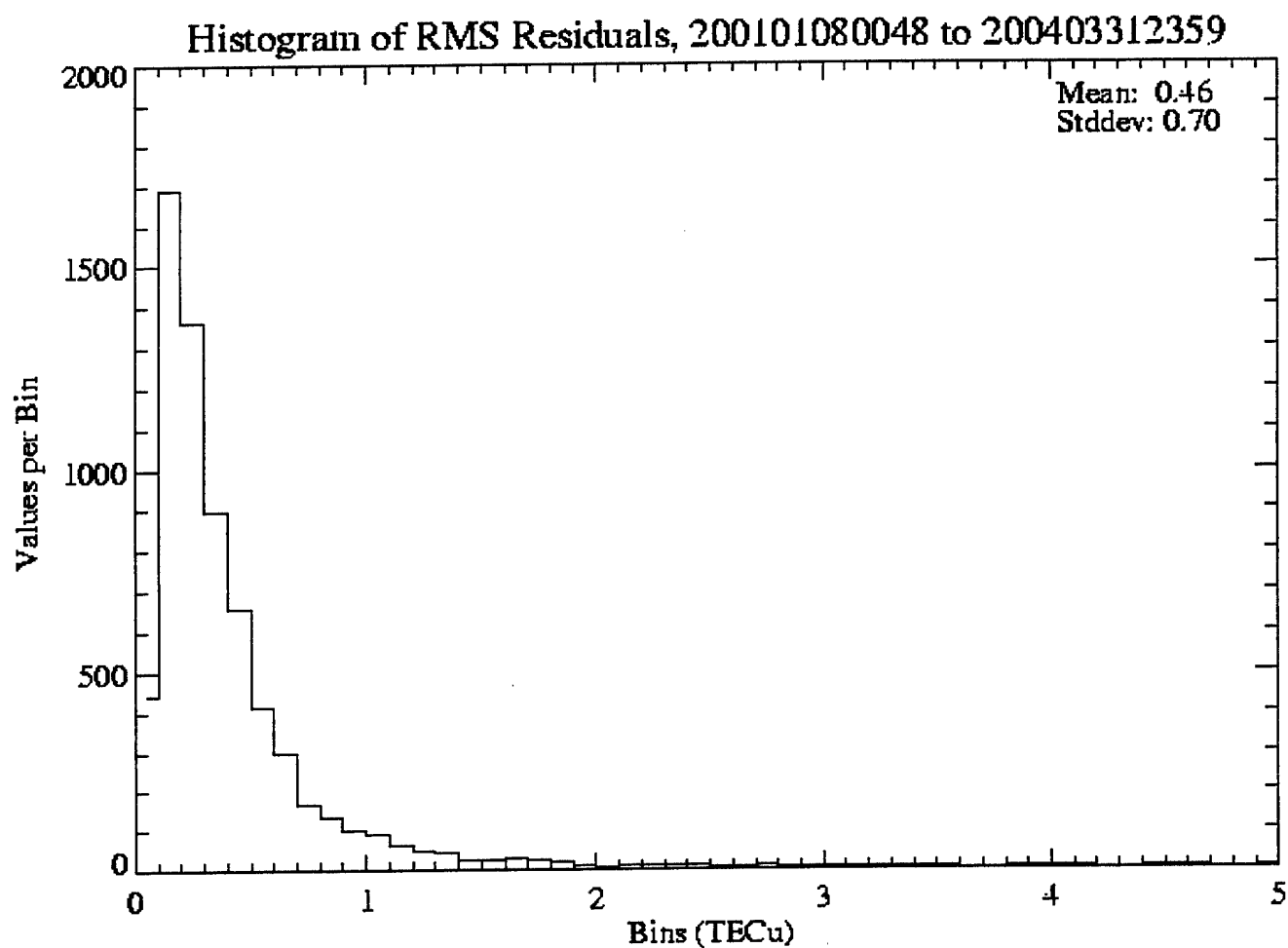


**Figure 22.** Histogram of rms residuals computed for all images produced to date. Images whose rms residuals reside in the tail of the histogram beyond 1.0 TEC unit are not posted on the HAARP Web site.

**Table 4.** Station-availability summary for tomographic images in 2001.

					Number of images												
Stations					Jan	Feb	Mar	Apr	May	Jun	Jul	Aug	Sep	Oct	Nov	Dec	All
Kak	For		Gak		0	3	0	4	0	0	0	0	0	0	0	2	9
Kak			Del	Gak	0	0	0	0	0	0	2	0	0	0	0	0	2
	For		Del	Gak	11	0	0	0	0	0	0	0	0	0	0	0	11
Kak	For			Cor	0	1	0	0	0	0	0	0	0	0	1	0	2
Kak			Del		Cor	0	0	0	0	0	26	0	44	0	0	0	70
	For		Del		Cor	4	0	0	0	0	0	10	0	0	0	0	14
Kak			Gak	Cor	0	0	0	0	0	0	1	0	0	0	1	0	2
	For		Gak	Cor	1	0	0	4	0	0	0	0	0	0	1	0	6
			Del	Gak	Cor	4	24	70	10	22	77	117	151	16	3	1	503
Kak	For		Del	Gak	1	11	1	0	0	2	0	0	0	5	5	0	25
Kak	For		Del		Cor	0	0	0	0	1	0	0	7	0	0	3	11
Kak	For			Gak	Cor	0	7	0	2	0	2	0	0	1	22	6	40
Kak			Del	Gak	Cor	1	4	34	2	0	44	0	21	18	25	3	152
	For		Del	Gak	Cor	129	39	42	93	93	1	0	16	72	1	5	491
Kak	For		Del	Gak	Cor	25	40	36	45	48	117	0	101	119	131	103	765
Summary					176	129	183	160	163	200	190	161	205	218	188	130	2103

Percent of images including specific stations

Station	Jan	Feb	Mar	Apr	May	Jun	Jul	Aug	Sep	Oct	Nov	Dec	All
Kaktovik	15	51	38	32	30	60	38	0	84	66	98	90	51
Fort Yukon	97	78	43	92	85	61	0	6	61	90	86	92	65
Delta	99	91	100	93	100	99	99	100	100	99	86	93	97
Gakona	97	99	100	100	100	99	85	93	75	100	99	98	95
Copper Center	0	0	0	0	0	0	0	0	0	0	0	0	0
Cordova	93	89	99	97	100	99	98	100	100	97	97	98	97

**Table 5.** Station-availability summary for tomographic images in 2002.

					Number of images												
Stations					Jan	Feb	Mar	Apr	May	Jun	Jul	Aug	Sep	Oct	Nov	Dec	All
Kak				Cor	0	0	0	0	3	0	0	0	0	0	0	0	3
	For			Cor	0	0	0	0	4	0	0	0	0	0	0	0	4
Kak	For		Gak		1	2	3	0	0	1	0	0	0	0	0	0	7
Kak			Del	Gak	3	0	0	1	0	5	0	0	0	0	0	0	9
Kak	For			Cor	0	0	1	1	11	0	0	0	0	0	0	0	13
Kak			Del		Cor	0	0	0	4	0	0	0	2	0	0	0	6
	For		Del		Cor	0	0	0	1	0	0	0	0	0	0	0	1
Kak			Gak	Cor	0	28	7	0	1	2	0	0	0	0	0	0	38
	For		Gak	Cor	1	0	1	0	0	0	0	0	0	0	0	0	2
			Del	Gak	Cor	4	0	0	10	10	48	45	170	153	122	30	602
Kak	For		Del	Gak	6	0	0	11	0	0	1	0	0	0	0	0	18
Kak	For		Del		Cor	1	1	0	20	1	0	0	0	0	1	0	24
Kak	For			Gak	Cor	9	30	153	3	0	0	0	0	0	0	0	195
Kak			Del	Gak	Cor	23	7	0	45	21	98	50	14	23	13	16	329
	For		Del	Gak	Cor	4	8	0	5	38	9	25	0	4	4	2	104
Kak	For		Del	Gak	Cor	91	99	16	108	126	44	78	0	8	29	96	782
Summary					143	175	181	184	239	208	199	184	190	168	145	121	2137

Percent of images including specific stations

Station	Jan	Feb	Mar	Apr	May	Jun	Jul	Aug	Sep	Oct	Nov	Dec	All
Kaktovik	93	95	99	92	78	72	64	7	16	23	77	88	66
Fort Yukon	79	80	96	69	84	26	51	0	6	19	67	76	53
Delta	91	66	9	97	91	98	100	100	100	100	100	100	87
Gakona	99	99	99	99	80	99	100	100	98	100	98	100	97
Copper Center	0	0	0	0	0	0	0	0	0	0	0	0	0
Cordova	93	98	98	93	100	97	99	100	100	100	100	100	98

**Table 6.** Station-availability summary for tomographic images in 2003.

						Number of images													
Stations						Jan	Feb	Mar	Apr	May	Jun	Jul	Aug	Sep	Oct	Nov	Dec	All	
Kak	For		Del			0	0	0	0	1	0	0	0	0	0	0	0	1	
Kak	For			Gak		0	0	0	0	0	1	0	0	0	0	0	0	1	
	For		Del	Gak		0	0	0	0	0	0	10	1	0	0	0	0	11	
Kak	For				Cor	0	0	0	0	0	1	0	0	0	0	0	0	1	
Kak			Del		Cor	1	0	0	1	0	0	0	0	0	0	0	0	2	
	For		Del		Cor	5	0	0	0	0	0	0	0	0	0	1	0	6	
Kak				Gak	Cor	0	0	0	1	0	0	0	0	0	0	0	0	1	
	For			Gak	Cor	0	0	0	1	0	0	9	0	0	1	25	0	36	
			Del	Gak	Cor	16	9	66	13	0	52	59	124	122	109	103	200	873	
			Del		Cop	0	1	2	0	0	0	0	0	0	0	0	0	3	
				Gak	Cop	0	3	0	0	0	0	0	0	0	0	0	0	3	
Kak	For		Del	Gak		0	0	0	0	7	8	0	0	0	0	0	0	15	
Kak	For		Del		Cor	0	0	0	5	0	0	0	0	0	0	0	0	5	
Kak	For			Gak	Cor	0	0	0	0	7	0	0	0	0	0	0	0	7	
Kak			Del	Gak	Cor	37	0	0	10	43	38	0	0	0	0	0	0	128	
	For		Del	Gak	Cor	52	24	54	78	0	1	112	38	29	76	31	0	495	
	For			Gak	Cop	0	1	0	0	0	0	0	0	0	0	0	0	1	
			Del	Gak	Cop	0	50	55	0	0	0	0	0	0	0	0	0	105	
Kak	For		Del	Gak	Cor	20	0	0	60	135	91	0	0	0	0	0	0	306	
	For		Del	Gak	Cop	0	64	0	0	0	0	0	0	0	0	0	0	64	
Kak	For		Del	Gak	Cop	0	1	0	0	0	0	0	0	0	0	0	0	1	
Summary						131	153	177	169	193	192	190	163	151	186	160	200	2065	

Percent of images including specific stations

Station	Jan	Feb	Mar	Apr	May	Jun	Jul	Aug	Sep	Oct	Nov	Dec	All
Kaktovik	44	0	0	45	100	72	0	0	0	0	0	0	23
Fort Yukon	59	58	30	85	77	53	67	23	18	40	35	0	45
Delta	100	97	100	98	96	98	95	100	100	99	84	100	97
Gakona	95	99	98	96	99	99	100	100	100	100	99	100	99
Copper Center	0	79	32	0	0	0	0	0	0	0	0	0	9
Cordova	100	100	100	100	96	95	94	99	100	100	100	100	99

**Table 7.** Station availability summary for tomographic images in 2004 (first quarter only).

Number of images																		
Stations						Jan	Feb	Mar	Apr	May	Jun	Jul	Aug	Sep	Oct	Nov	Dec	All
			Del	Gak	Cor	191	132	148	0	0	0	0	0	0	0	0	0	471
Summary						191	132	148	0	0	0	0	0	0	0	0	0	471

Percent of images including specific stations

Station	Jan	Feb	Mar	Apr	May	Jun	Jul	Aug	Sep	Oct	Nov	Dec	All
Kaktovik	0	0	0	0	0	0	0	0	0	0	0	0	0
Fort Yukon	0	0	0	0	0	0	0	0	0	0	0	0	0
Delta	100	100	100	0	0	0	0	0	0	0	0	0	100
Gakona	100	100	100	0	0	0	0	0	0	0	0	0	100
Copper Center	0	0	0	0	0	0	0	0	0	0	0	0	0
Cordova	100	100	100	0	0	0	0	0	0	0	0	0	100

#### 4.1.2.2.2 Application to Trough Characterization

A major image analysis undertaken under this contract was aimed at quantitatively characterizing plasma-density troughs in the sub-auroral and auroral F layer, in collaboration with researchers at the University of Wales at Aberystwyth (UWales), working under a subcontract. As agreed with our UWales colleagues, our primary criterion for identifying a trough was that vertical TEC (VTEC) in the trough must drop to a value at least as low as 80 percent of the average VTEC in the image. Using this criterion, we pre-selected 271 candidates for analysis. Adapting

search algorithms developed by UWales personnel, we then processed the candidates to eliminate those that did not qualify according to this and other agreed criteria and to evaluate trough parameters defined in collaboration with AFRL's Technical Monitor, Gregory Bishop. Of the 271 candidates pre-selected, 260 passed the selection criteria. An example appears in Figure 23.

The resulting analysis is illustrated in Table 8 and Figure 24. For more complete definitions of the trough parameters, see Appendix B of Andreasen et al. (2003), which contains the interim subcontract report from UWales. Of the 260 candidates from Alaska that survived the selection criteria, 212 provided full analyses, with the remaining 48 missing one or more characterization parameters. The complete analysis, including statistical characterization, for all 260 Alaska cases and 618 satellite cases from the larger UWales database of tomographic images from the western European sector is being provided in a separate scientific report under this contract.

#### *4.1.3.3 Enhancements to the NWRA Tomographic Inversion Processor*

##### *4.1.2.3.1 Imposing Positivity*

As related in Section 3.1.2.2, the central algorithm in the NWRA ITS processor employs WDLs matrix inversion. As implemented in the processor, the WDLs algorithm operates in a transform space consisting of empirical orthogonal functions (EOFs) vertically and Fourier terms horizontally. As reported by Pryse (2003), the technique is particularly adept at rendering latitudinal changes in F-layer height. We have found it capable, also, of resolving E-layer plasma. Operating in the transform space, however, makes it difficult to impose constraints, such as positivity, in configuration space. Pryse et al. (1998) combined the WDLs algorithm with a modified version (Mitchell et al., 1997) of the algebraic reconstruction technique (ART), described by Austen et al. (1988), which operates in configuration space.

Previously, we averaged the plasma density in any negative-density pixels (typically located at the very bottom or top of the WDLs image) with that in adjacent pixels, thus giving up some resolution for the sake of establishing positivity. Under this contract, we investigated adding the modified ART algorithm as a post-processor to our WDLs-based processor. This approach iteratively imposes positivity by (very modestly) redistributing plasma to deficient pixels from elsewhere on rays passing through them, doing so in a manner that is consistent with the input TEC data.

Implementation of the modified ART algorithm required a slight modification of an existing program (*ion\_image*) and development of two additional programs (*pixelsegs* and *postproc\_tomo*). The *ion\_image* program converts the images produced by the tomographic processor from our transform space into a pixilated image in configuration space (altitude and latitude). The modification to *ion\_image* generates an additional output file containing information about the paths along which TEC observations were available, the TEC offsets generated by the tomographic processor, and the relative-TEC observations. This information is used in the *pixelsegs* program to generate a file defining the segmentation of the paths into smaller segments within image pixels. An initial version of this program operated in a single two-dimension space (latitude and height along a constant longitude), but we discovered that as the maximum elevation of the pass moved away from vertical, artifacts were introduced in the final image by miscalculation of the length of pixel subsegments. The final implementation of *pixelsegs* uses a full spherical three-dimensional image space for its calculations.

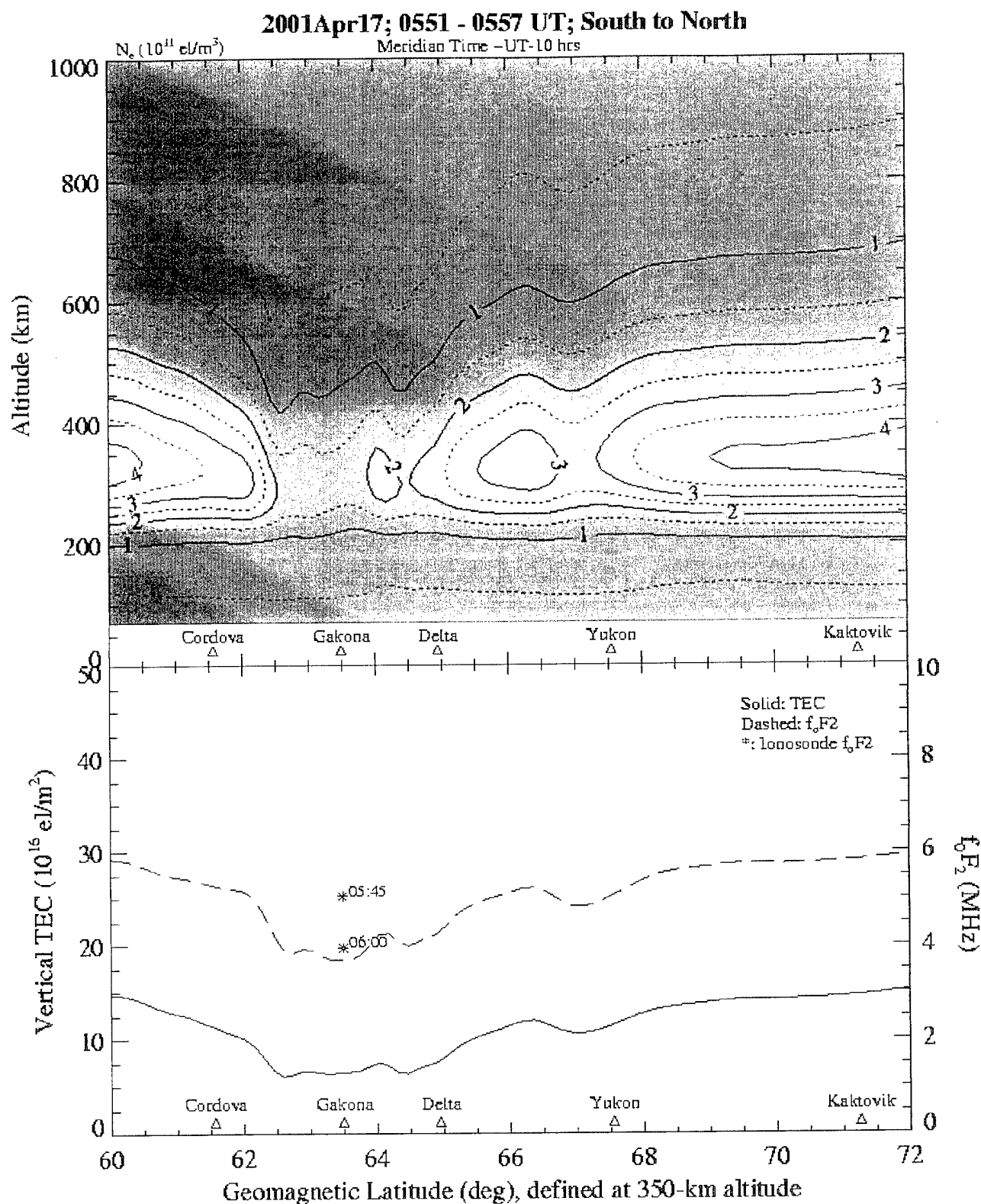


**Figure 23.** Example of a plasma-density trough imaged tomographically and selected for quantitative characterization.



**Table 8.** Analysis parameters for trough shown is Illustrated in Figure 23.

```
PlotInfo: 15.17 25.00 5
Pass ID: 200104170548o29
Built by: trough_parms | version 1.03 | 10 June 2003
Built on: 20030613 112033
GMLat range searched: 61.30 70.69
```

GMLat	TEC	Comments
60.00	11.40	Average TEC
72.00	11.40	
60.00	14.80	Equatorward Pass Gradient (GE)
63.00	6.66	Gradient (TECU/deg): -2.71
61.44	11.66	Equatorward Trough Gradient (GTE)
62.60	6.03	Gradient (TECU/deg): -4.85
62.60	6.03	Poleward Trough Gradient (GTP)
66.07	11.60	Gradient (TECU/deg): 1.61
60.00	14.80	Equatorward Peak (LE)
61.44	11.66	Equatorward Edge (BE)
62.02	10.05	Equatorward Midpoint (HE)
62.60	6.03	Trough Minimum (LM)
64.33	6.44	Poleward Midpoint (HP)
66.07	11.60	Poleward Edge (BP)
66.36	11.95	Poleward Peak (LP)

The *postproc\_tom* program implements the modified ART algorithm. It reads in the image generated by the *ion\_image* program, the pixel segments calculated by *pixelsegs*, and the absolute TEC estimates (observed relative TEC plus the TEC offsets evaluated in the WDLS process). It then modifies the image in an iterative process controlled by inputs of a maximum number of iterations and a relaxation parameter, which is a coefficient dictating the degree of plasma redistribution afforded by each iteration.

Our investigation involved trials of the number of iterations to employ and choice of the relaxation parameter. We settled on a single iteration and a modest relaxation parameter. The result produces little change in the WDLS image, while imposing positivity without the need for arbitrarily averaging through errant pixels. While somewhat improving resolution, the ART procedure also slightly overrides the matrix regularization inherent in the WDLS technique. This fact results in apparently sharp “corners” on some localized ionospheric features where the second spatial derivative of plasma density approaches being discontinuous. We have overcome this behavior by “over-sampling” the computed plasma-density field when preparing to plot our image and then smoothing the over-sampled plot in the displayed result, using three-point triangular weighting. An example is presented in Figure 25, which displays the WDLS and WDLS/ART versions of the same image in, respectively, the top and bottom panels. The image is little changed, but plasma density has been redistributed to fill pixels reporting slightly negative plasma density rather than their being averaged with neighboring pixels.

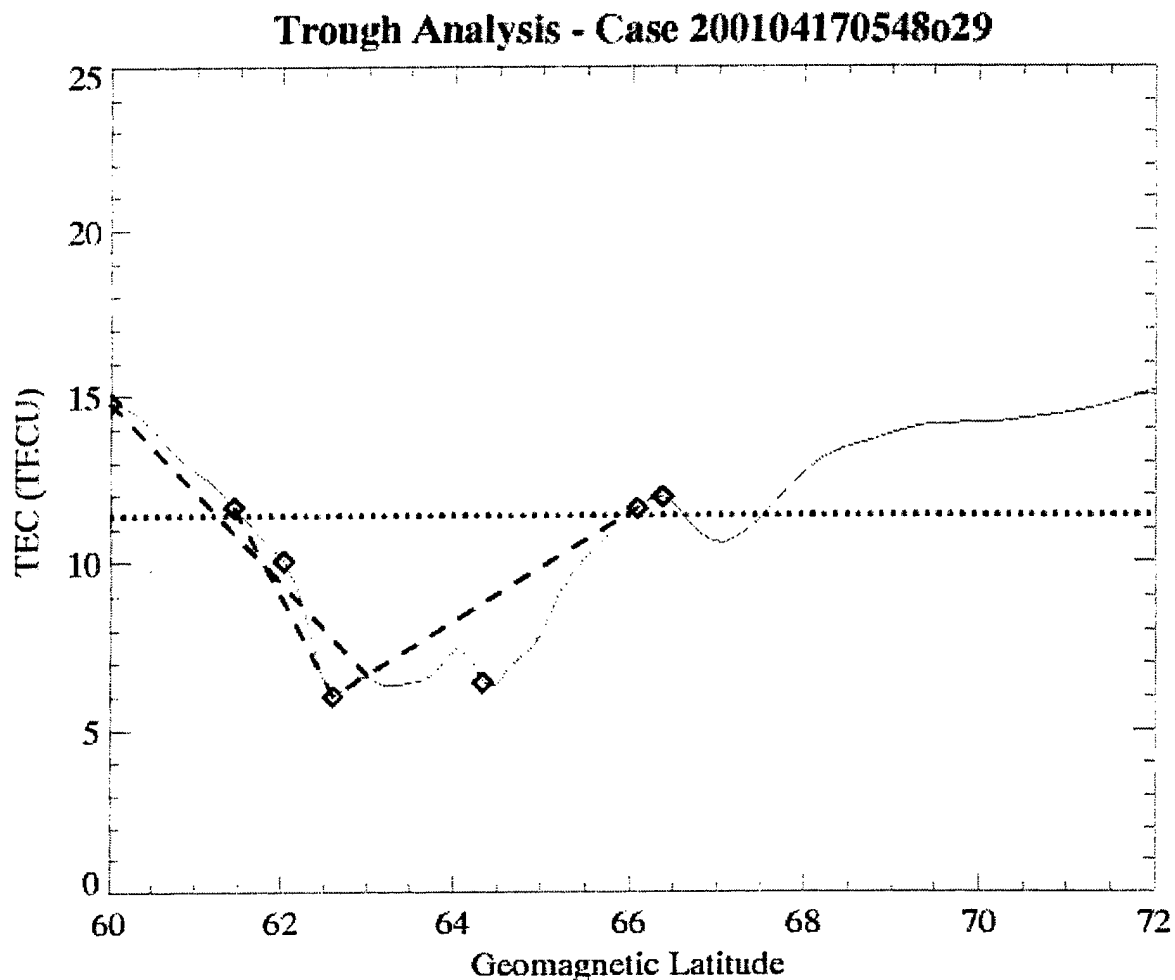


**Figure 24.** VTEC (solid line), gradients (dashed lines) and other parameters (diamonds), as enumerated in Table 4, for trough illustrated in Figure 23.

#### 4.1.2.3.2 Assimilating Complimentary Data

There is no inherent limitation in the mathematical framework underlying the tomographic processor that precludes incorporation of other types of ionospheric electron-density measurements. Other types of data available at or near HAARP are vertical-incidence electron-density profiles or profile parameters (such as  $f_oF_2$ ) from digisondes at Gakona and Sheep Creek, absolute TEC from GPS receivers, and *in situ* electron-density measurements from nearby DMSP passes. In the future, there may also be electron-density profiles from an Incoherent Scatter Radar (ISR). Under this contract, we developed a general method for incorporating local measurements of electron density that is directly applicable to all of the aforementioned data types except the GPS TEC, which we plan to address at a later time.

2002Feb05; 0508 - 0522 UT; South to North

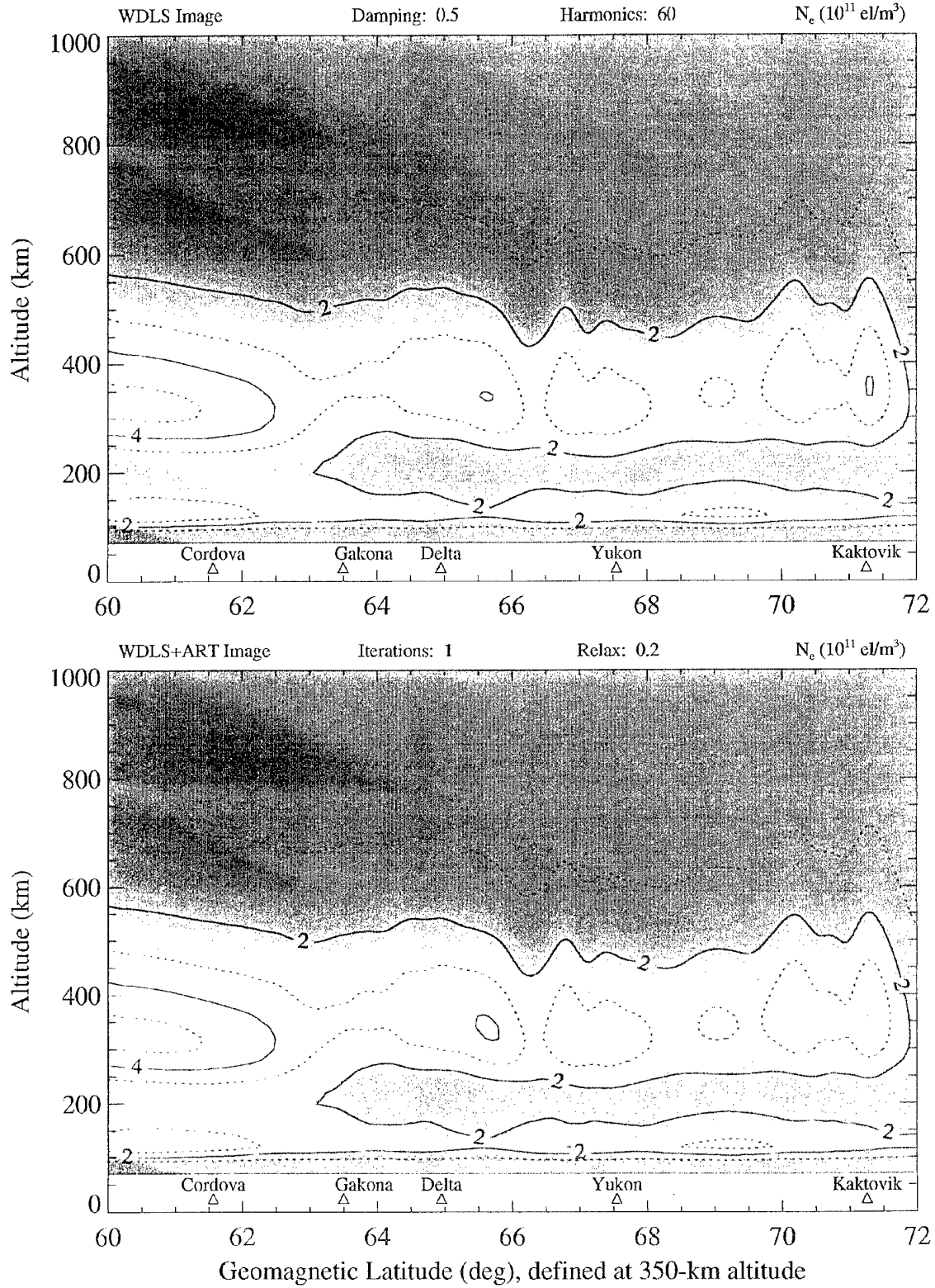


**Figure 25.** Image produced by standard WDLS inversion (top) and by combined WDLS/ART inversion (bottom).

The simplest way to incorporate such data is to make them as similar as possible to the data already used by the processor: electron density integrated along a specified path within the region to be imaged. A zeroth-order approach is to convert all the observations that provide electron density as a function of some distance along a path (vertical and off-vertical profiles from digisondes and ISRs; electron density along a satellite track for DMSP) to the integrated electron content along that path. The integrated density would then be input as an absolute "TEC" along the specified path (contrasted with relative TEC from the LEO beacon satellite measurements). This approach, however, loses much information regarding the variation of electron density along the path, and it also does not lend itself to input of information such as  $f_oF_2$  and  $h_mF_2$ .

We expanded the foregoing simple approach by dividing each along-path measurement into a series of segments, each segment centered on a measurement of electron density. These are converted to TEC "observations" along small segments (either vertical or horizontal) by assuming constant density along the segment and calculating TEC from the product of the observed density and the length of the segment. Each segment is provided to the tomographic processor as a path and the integrated density (TEC) along that path, which is handled internally in much the same manner as the beacon-derived relative TEC.

The only modifications required to the tomographic processor were to account for the fact that these measurements are of absolute rather than relative TEC, so separate model parameters are not required for the unknown offsets in the measurements, as is done with the relative-TEC data. This was not a major modification; most of the work to incorporate these data was to convert the observations to segments and the bookkeeping required to handle additional TEC paths.

One additional piece of information required for these measurements is an estimate of the uncertainties in the observations. In the present study, we have applied this new technique using data from digisondes (both full profiles and only the  $f_oF_2$  and  $h_mF_2$  profile parameters). Estimates of the uncertainty in these measurements were made based on discussions with Dr. Terry Bullett of AFRL (private communication). At his suggestion, we specify the uncertainty in the densities in the true-height profiles in terms of an rms uncertainty in the true height. For purposes of this application, we have settled on rms uncertainty measures of 7 km in height for the digisonde data. It should be noted that these estimates are somewhat crude, although not unreasonable, and should be studied in a bit more detail before using them in further work.

At the time of this study, we had data from only the three NWRA receivers located near the HAARP facility (Cordova, Gakona, and Delta). Figure 26 shows the image generated from a Transit pass on 19 March 2001 (top panel) and the TEC and  $f_oF_2$  derived from the image (bottom panel), using the tomographic processor and only the relative TEC from the three stations. Included on the TEC and  $f_oF_2$  plot are the  $f_oF_2$  observations from the Gakona digisonde at 0415 UT and 0430 UT. Note that the  $f_oF_2$  derived from the image is about 1.5 MHz low, and note the rather broad nature of the height profile of electron density in the image.

We repeated the analysis using the Gakona digisonde measurement of  $f_oF_2$  and  $h_mF_2$ , using a segment length of 20 km oriented horizontally. The result is shown in Figure 27, which is identical in form to Figure 26. Note now how the  $f_oF_2$  from the image is very close to the observed  $f_oF_2$  (which was input to the processor) and how incorporation of this single absolute observation of density at a given position within the image has changed the character of the profile shape across the image. The  $f_oF_2$  has increased across the image, and the topside section of the image has reduced in density and scale height.

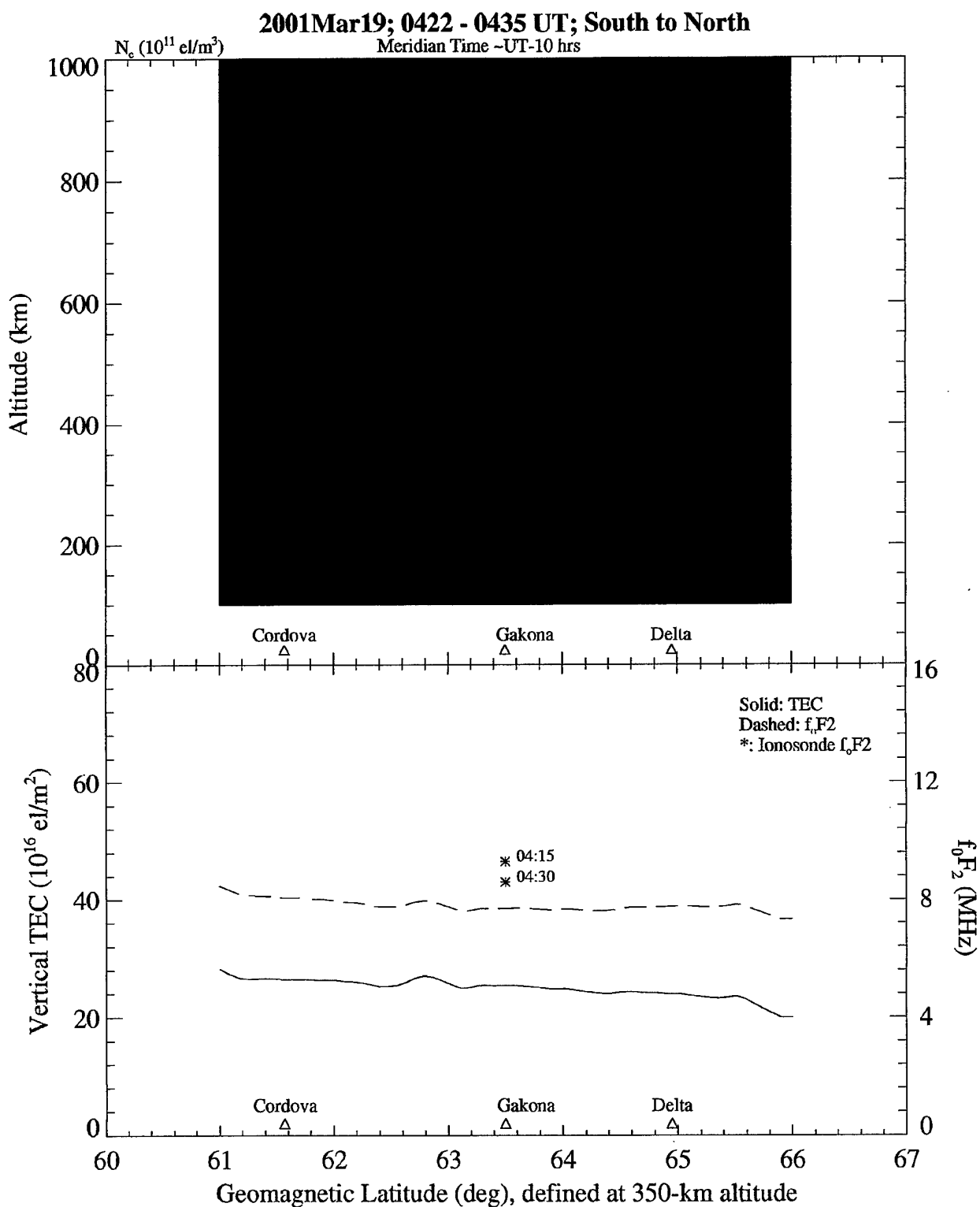


**Figure 26.** Electron-density image (upper panel) and latitude variation of TEC and  $f_oF_2$  (lower panel) generated using only TEC data. The two time-tagged asterisks indicate  $f_oF_2$  as measured by the Gakona digisonde at the indicated times (UT).

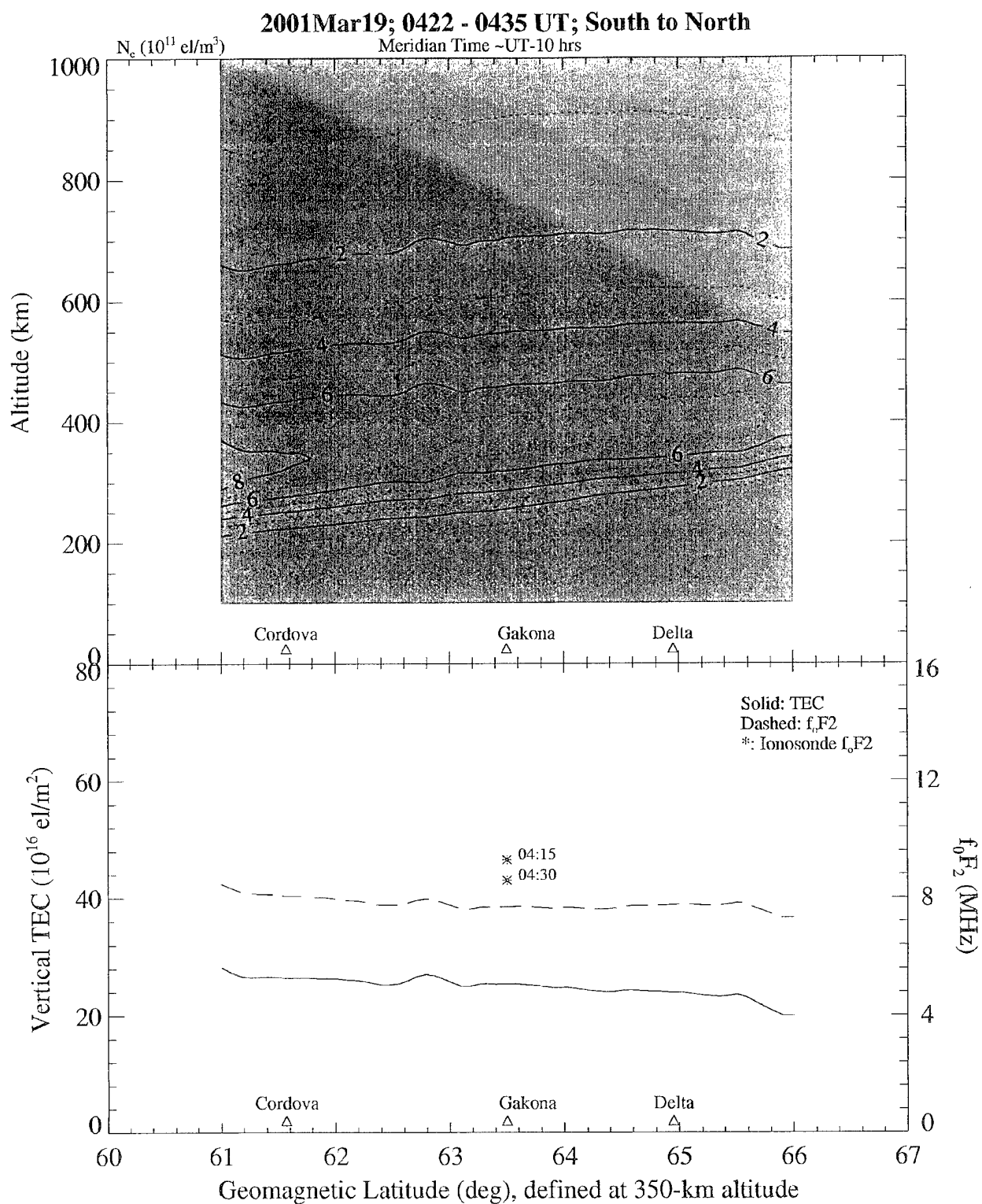


**Figure 26.** Electron-density image (upper panel) and latitude variation of TEC and  $f_0F_2$  (lower panel) generated using only TEC data. The two time-tagged asterisks indicate  $f_0F_2$  as measured by the Gakona digisonde at the indicated times (UT).

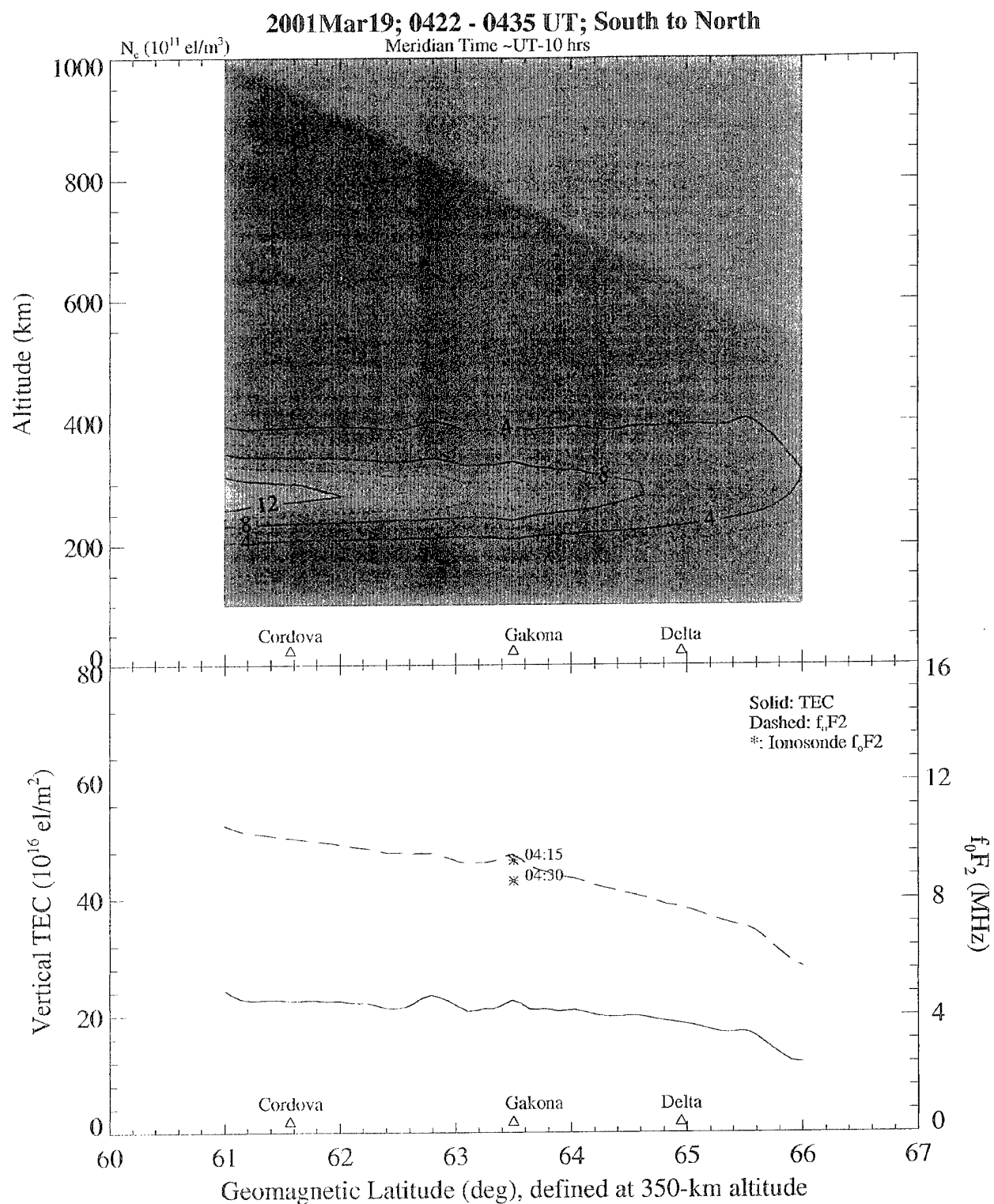


**Figure 27.** Image and plots of TEC and  $f_oF_2$ , as in Figure 24, generated using both TEC and digisonde data.

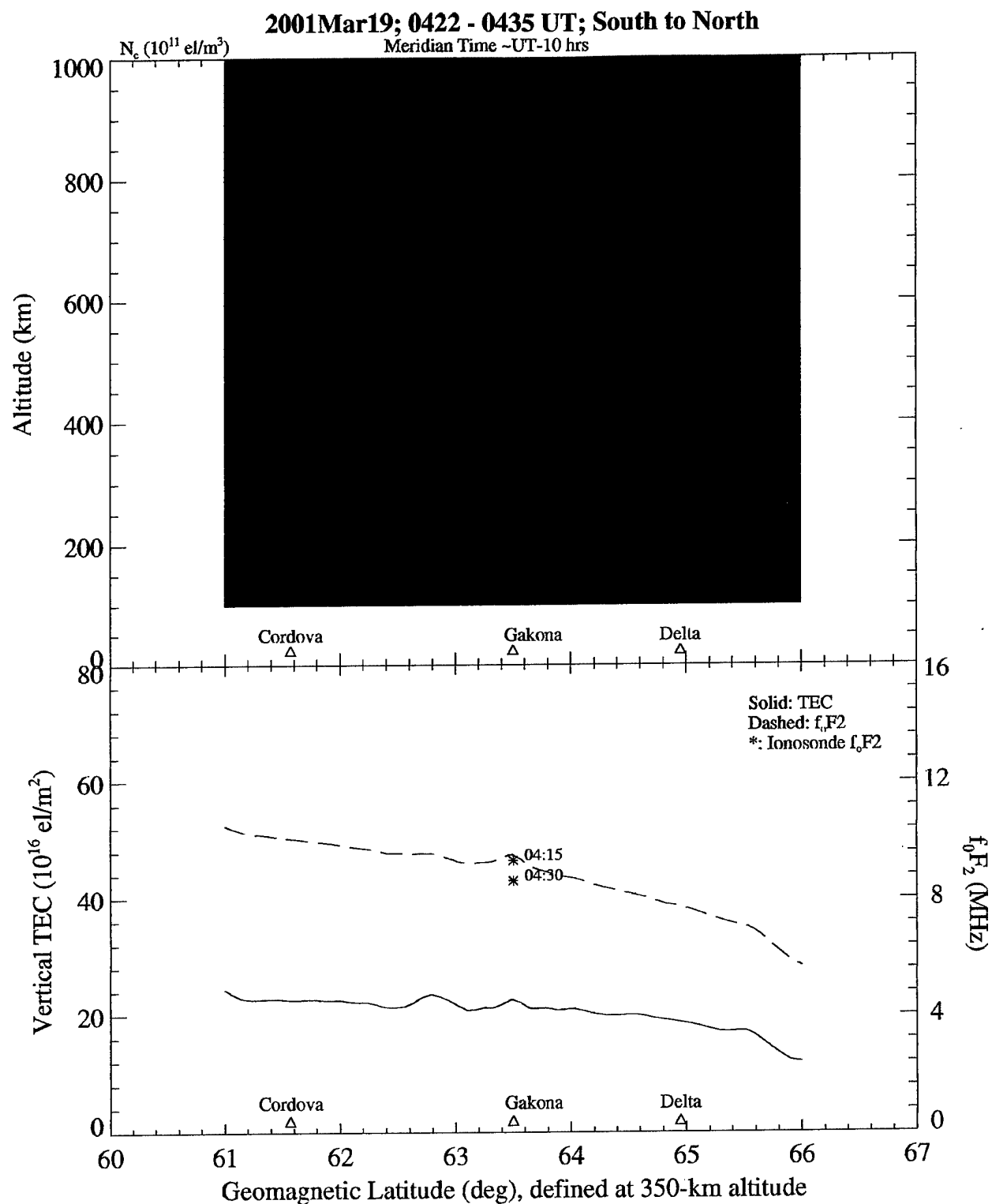


**Figure 27.** Image and plots of TEC and  $f_0F_2$ , as in Figure 24, generated using both TEC and digisonde data.



In an independent check of this result, we were able to obtain observations of the *in situ* plasma density from the DMSP SSIES instrument for several passes in the approximate vicinity of HAARP near the time of the image. These data were provided by Dr. Fred Rich of AFRL (private communication). Figure 28 compares electron density at the nominal DMSP altitude of 840km derived from the original image (top panel) and that incorporating the digisonde data (bottom panel) with observations from two such DMSP passes. As could be surmised from Figures 26 and 27, the 840-km density derived from the images is lower when the digisonde data were incorporated. What is noteworthy is that the densities derived from the digisonde-aided image match the DMSP observations better than those from the TEC-only image.

While this is a positive gain, there are two unresolved issues. First, the F-layer tilt appearing in Figure 26 is substantially shallower in Figure 27. We do not understand why an essentially point measurement should have such an effect. Second, close inspection of the image (and, particularly, the  $f_oF_2$  and vertical TEC plots) in Figure 28 shows a plasma-density enhancement located at the latitude of the Gakona digisonde. We worked on some simple approaches to mitigating this artifact, which can be altered by changing the size and orientation of the segment used in the incorporation process (orientation to a lesser extent than size), but we were unable to determine the optimum solution for a given situation.

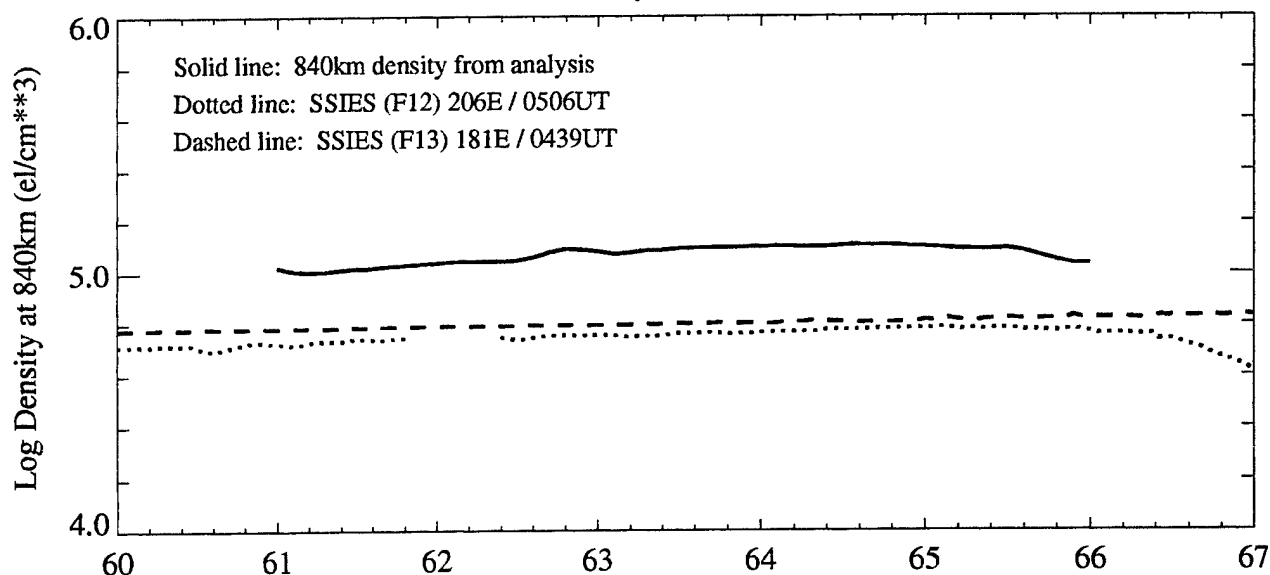
Assimilation of complementary data will have to await further study and development, and we have chosen not to incorporate the Gakona digisonde data in our automated images. Rather, we plot the digisonde observations on the  $f_oF_2$  plots made from the images to provide viewers with an independent estimate of accuracy in the TEC-only images. We note also that individual measurements of  $f_oF_2$  from the Digisonde can be in error due to frequency gaps in the sounder's authorized transmission band and to interfering signals.

#### **4.2 The Ionosphere Perturbed by HF Heating**

Ionospheric heating due to high-power HF transmissions has been observed to produce hectometer-to-kilometer-scale irregularities detected as weak intensity scintillation at UHF and VHF (Basu et al, 1983, 1987; Livingston, 1983). No such scintillations have been detected during HAARP operations with transmission power available to date. During a HAARP field campaign in March 2001, however, we observed fluctuations in VHF-UHF dispersive phase (Fremouw et al, 2001) that we believe were heater-induced. Figure 29 compares the relative TEC and detrended

# 2001Mar19; 0422-0435 UT; South to North

Only TEC Data



TEC and Digisonde Data

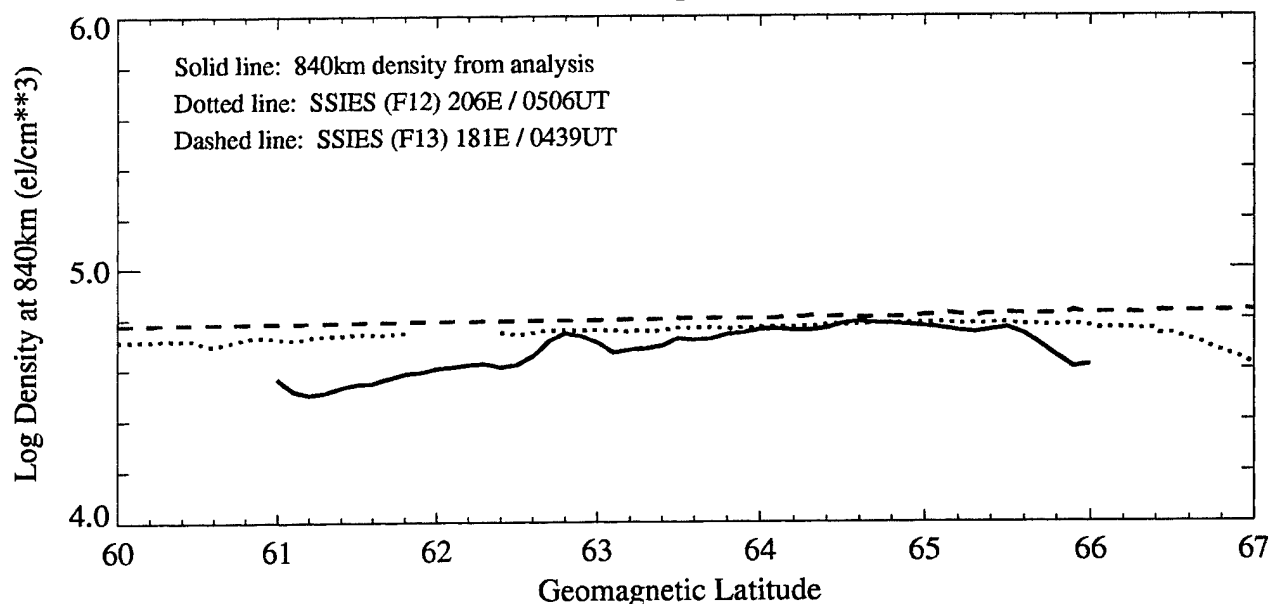


**Figure 28.** Comparison of electron density at an altitude of 840 km extracted from the TEC-only image (solid line, upper panel) and from the TEC+digisonde image (solid line, lower panel) with observations of density measured by DMSP during nearby (in time) passes.

dispersive phase recorded by the ITS10S receivers at Gakona (left) and Cordova (right). The upper panels show that the natural ionosphere was very smooth and essentially identical as viewed from the two locations, as also was recorded by the ITS10S at Delta. The tomographic image developed from inversion of these three relative TEC records is displayed in Figure 30. Although this image failed to pass our criterion that only images producing an rms residual of less than one TECu will be posted on the HAARP Web site, it shows a smooth and dense mid-latitude ionosphere developing to the south. The fact that the southward gradient is not evident in the two digisonde values of  $f_oF_2$

displayed beneath the image is surprising since the two TEC records in the upper panels of Figure 29 (and that from Delta, as well) clearly show a much denser and/or thicker ionosphere to the south.

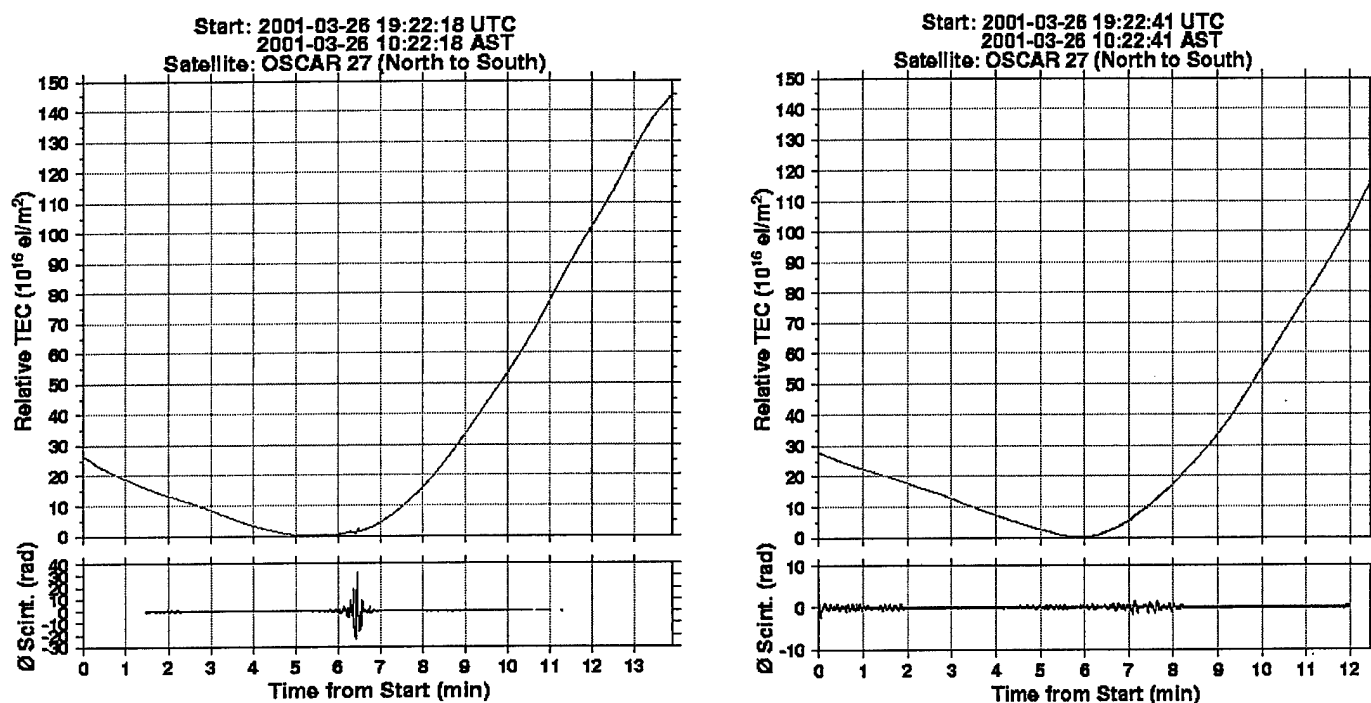


**Figure 29.** Slant-path TEC and phase scintillation observed Gakona (left) and Cordova (right) during operation of HAARP's HF transmitter on 25 March 2001. Note different scales in the lower panels (displaying phase scintillation).

The lower strips in Figure 29 display 50-sps phase residuals obtained after detrending by subtraction of the output from a low-pass filter having a sharp cutoff at 0.1 Hz (i.e., after removal of trends with periods greater than ten sec). Nearly all passes that scan near the magnetic zenith show some scintillation close to the field point, a geometrical enhancement due to a high degree of field alignment by natural irregularities (Singleton, 1970; Fremouw and Lansinger, 1981). Both the Cordova and Delta records contained this effect (very weakly, due to the unusually smooth conditions), shown between seven and eight minutes in the Cordova record in Figure 29 (right).

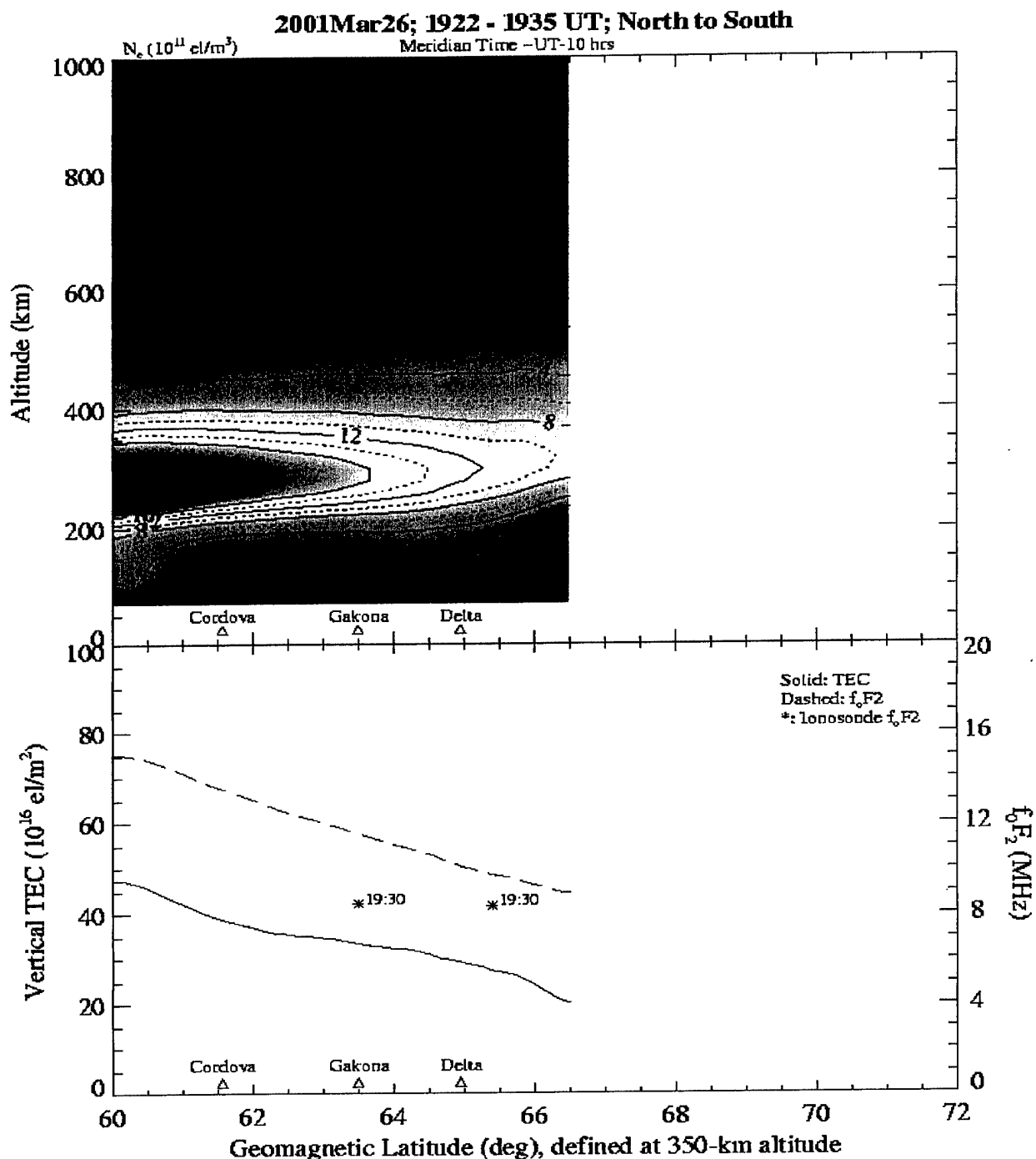


**Figure 30.** State of the ionosphere during the heating experiment in which the dispersive-phase fluctuations displayed in the left panel of Figure 26 and the corresponding TEC perturbations quantified in the upper panel of Figure 29 were observed.

In contrast to the unusually weak field-point phase scintillation in the Cordova record, the Gakona receiver recorded strong and very isolated phase fluctuations between six and seven minutes into the pass there. [Note that the phase-scintillation scales differ by a factor of 3.5 ( $-30$  to  $+40$  rad for Gakona vs.  $\pm 20$  rad for Cordova).] This pass occurred during the HAARP Spring 2001 field campaign, in a time window allotted to search for TEC/scintillation effects produced by the

HF transmitter. The transmitter had been directed at azimuth  $93.2^\circ$ , elevation  $86.1^\circ$  for one hour and 13 minutes prior to passage of the line of sight to the satellite through this point of closest approach to Gakona's geometric zenith. The isolated perturbation contained in the phase-scintillation chart was recorded from seven sec before to 53 sec after this time of closest approach. This time span corresponds to an F-layer patch some 200 km in latitudinal extent and centered about 70 km south of the point of closest approach.

This patch clearly contained plasma structures, quite likely field-aligned and located on a geomagnetic flux tube passing through the F layer close to the heater beam. The line of sight from Cordova through this patch would have cut obliquely across such structures, with the net TEC (and, therefore, phase) effect being close to zero. The weaker phase perturbations noticeable in the Cordova record most likely were produced by very weak natural irregularities aligned along the flux tube passing through the F layer just south of that site. What we believe to be a heater effect was some 13 to 40 times as strong as the natural ones observed at Delta and Cordova, respectively.

Irregularities smaller than the radio Fresnel zone in the F layer (several hundred meters at UHF and about a km at VHF) produce diffractive effects that obviate a direct correspondence between measured phase perturbation and TEC variation. Larger ones, however, can be interpreted as a measure of TEC fluctuation, as illustrated in Figure 31. The upper panel contains an expansion of the isolated dispersive-phase perturbation recorded at Gakona, displayed in TEC units (using a somewhat longer detrend interval to capture all relevant perturbations). The lower panel shows the angle between the line of sight to the satellite and the geomagnetic field at several ionospheric heights.

The observed perturbation coincided exactly with the minimum off-field angle, namely five deg. It comprised TEC depletions with a maximum value of 0.9 TECu and enhancements with the same maximum value. The maximum value of depletion and that of excess was about 2.5 percent of the ambient TEC over Gakona, as determined by integrating vertically through the tomographic image. The north-south extent of the main depletion in the F layer (assuming 350 km altitude) was about 20 km; that of the main enhancement was less, approximating 10 km. From the measurements at Delta and Cordova, we infer that the TEC measure of naturally occurring irregularities when viewed at similar angles to the field were substantially less than 0.1 TECu (of order 0.1 percent).

Gurevich et al. (2002) have interpreted the Gakona measurement in terms of theoretical considerations that predict a large-scale plasma depletion on the order of 10 percent, due to pump-wave self-focusing, being aligned along field lines and located away from the reflection region of the pump wave. They also pointed out that excess plasma is to be expected around the depletion but that "the theory so far developed does not provide a fully self-consistent description of the observed phenomena."

To our knowledge, other attempts by any means to record heater-produced scintillations at HAARP have been unsuccessful, including our own. In the Irregularities Campaign of March 2003, we fielded an ITS10S near Copper Center, AK, to record dispersive phase and intensity scintillation on nearly vertical paths through HAARP's geomagnetic field point in the F layer while doing so nearly simultaneously from Gakona on paths nearly aligned with the flux tube through the transmitter. Figure 32 displays the relevant geometry.

# HAARP Transit Pass 26 Mar 2001 | Gakona | Oscar 27

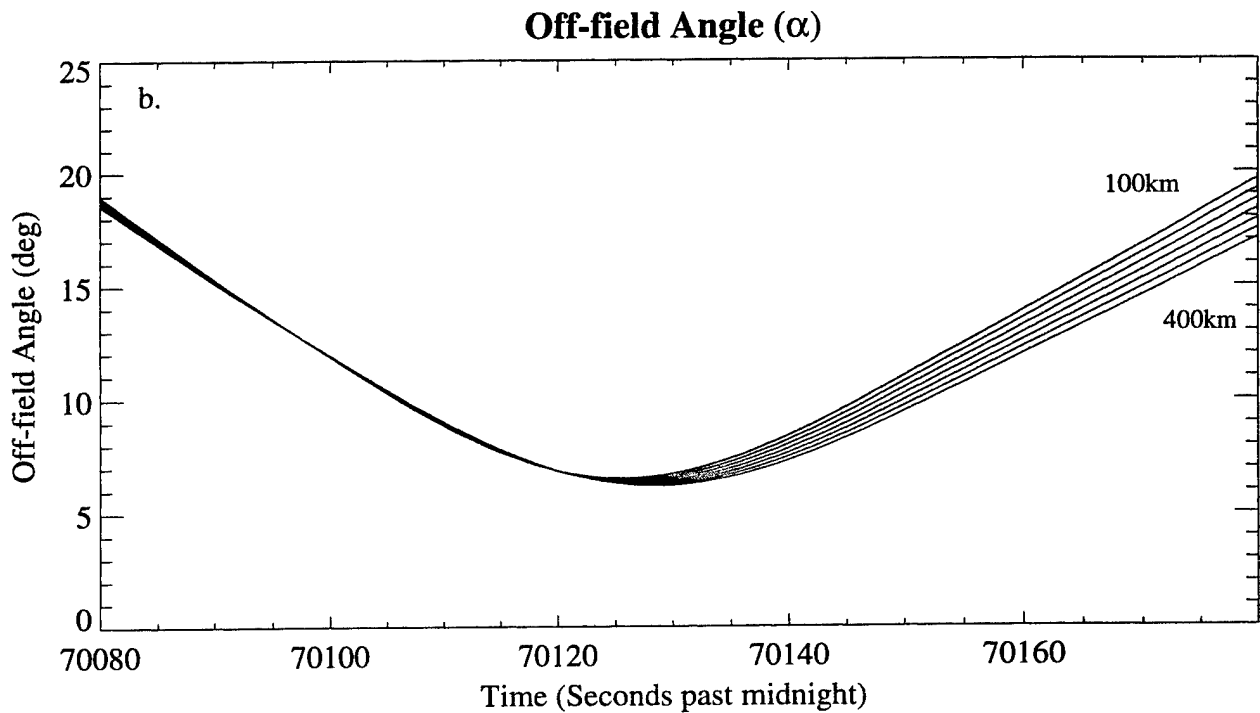
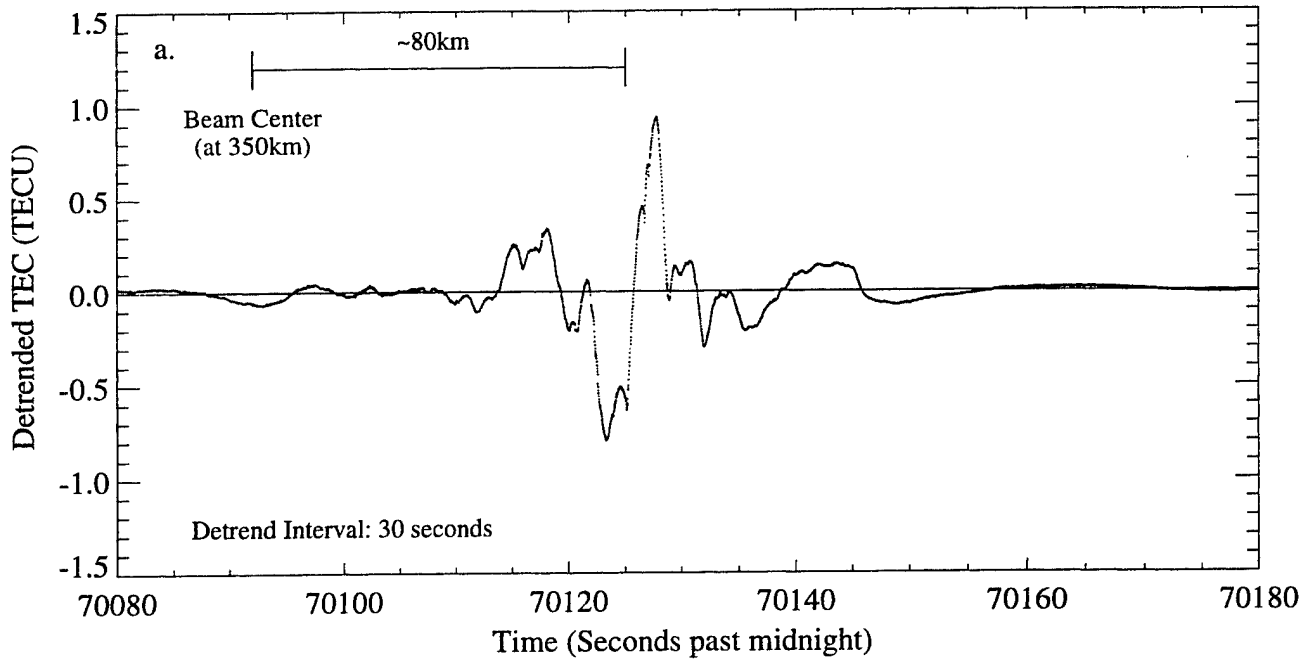


**Figure 31.** Detrended dispersive phase (top) and angle (bottom) between magnetic field and ray-path from satellite to Gakona.

The only difference between the left and right panels in Figure 32 resides in the cross-hatched lines, which demark the loci of ray-path ionospheric penetration points (IPPs) at 350 km altitude during the pass as seen from each station, with the tic marks indicating ten-sec intervals. The

numbers at the top and bottom of these lines indicate time in seconds since UT midnight. The plan positions of Gakona and Copper Center are shown as diamonds, and the points in the sky where a line of sight from each station is parallel to the local geomagnetic field at an altitude of 350km (i.e., the IPP of the local field for each station) are shown by asterisks. The dotted lines through the asterisks show the intersection of the L-shell passing through the magnetic-field IPP and a constant altitude shell at 350 km. The heavy dotted and solid ellipses indicate the estimated boundaries of the heater beam at 350 km altitude with half-widths of  $30^\circ$  and  $8^\circ$ , respectively. The former represents the approximate half-power beam width, while the latter is based on the size of artificial airglow emissions typically observed in optics campaigns (Pedersen, private communication).

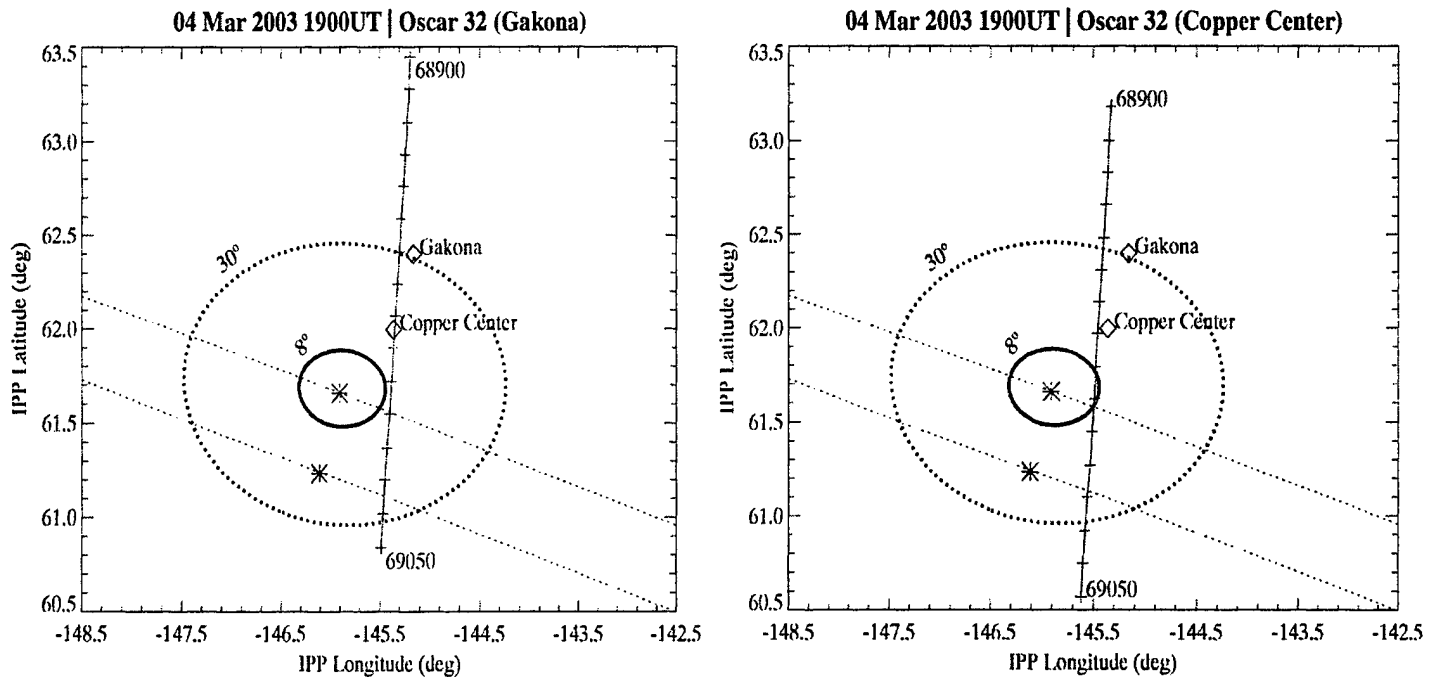


**Figure 32.** Geometry of Oscar 32 satellite pass near 1900 UT on 04 March 2003 corresponding to the Gakona (left) and Copper Center (right) data plots displayed in Figure 33. See text for details.

Detrended phase records similar to that depicted in the upper panel of Figure 31 are displayed for this March 2003 pass in the upper panels of Figure 33 (without conversion to TEC units), along with the corresponding off-field angles (lower panels). Although superficially similar to the heater-produced phase fluctuations observed in the earlier (March 2001) pass, these are about an order of magnitude weaker and are comparable to phase scintillations observed well away from the heated region, at Delta and Cordova, in both these events. Moreover, the perturbations displayed in Figure 31 both occurred at the point of closest approach to the local magnetic zenith. Nothing special was observed from Copper Center at the point closest to the flux tube passing through the heater at Gakona (skimming the 8-deg ellipse, as demarked in the upper right panel of Figure 33).

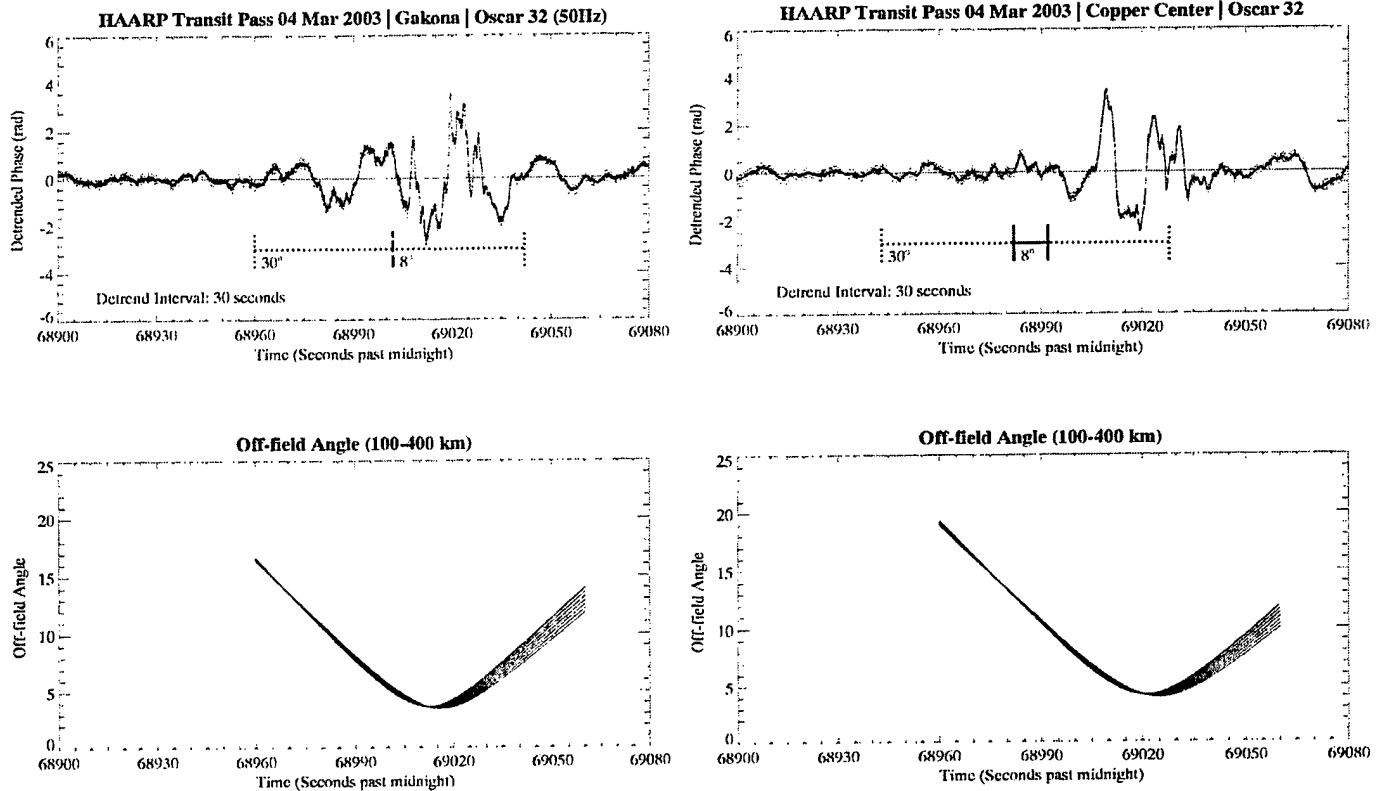


**Figure 33.** Detrended phase (upper panels) observed at Gakona (left) and Copper Center (right) during pass whose geometry is shown in Figure 32, together with the angle (bottom panels) between the Oscar-satellite ray paths and the local geomagnetic field in the ionosphere.

Figure 34 sheds some light on the null result expressed in Figure 33. It shows backscatter as a function of range recorded at the azimuth of HAARP by the SuperDARN radar on Kodiak Island, AK, for two hours around the time of the subject Oscar-32 pass. The extreme blue lines demark turn-on and turn-off of the HAARP heater, while the middle blue line indicates the time of Oscar's closest approach. The record shows strong fine-scale irregularities developing in the HAARP range bin (between 800 and 900 km) promptly at turn-on, but decaying over the few minutes preceding closest approach. We conclude that neither strong meter-scale nor km-scale irregularities produced by the heater were present in the ionosphere at the time of closest approach. Thus, we are left to ponder why the heater produced km-scale TEC structures on 26 March 2001 and not on 4 March 2003 at about the same time of day.



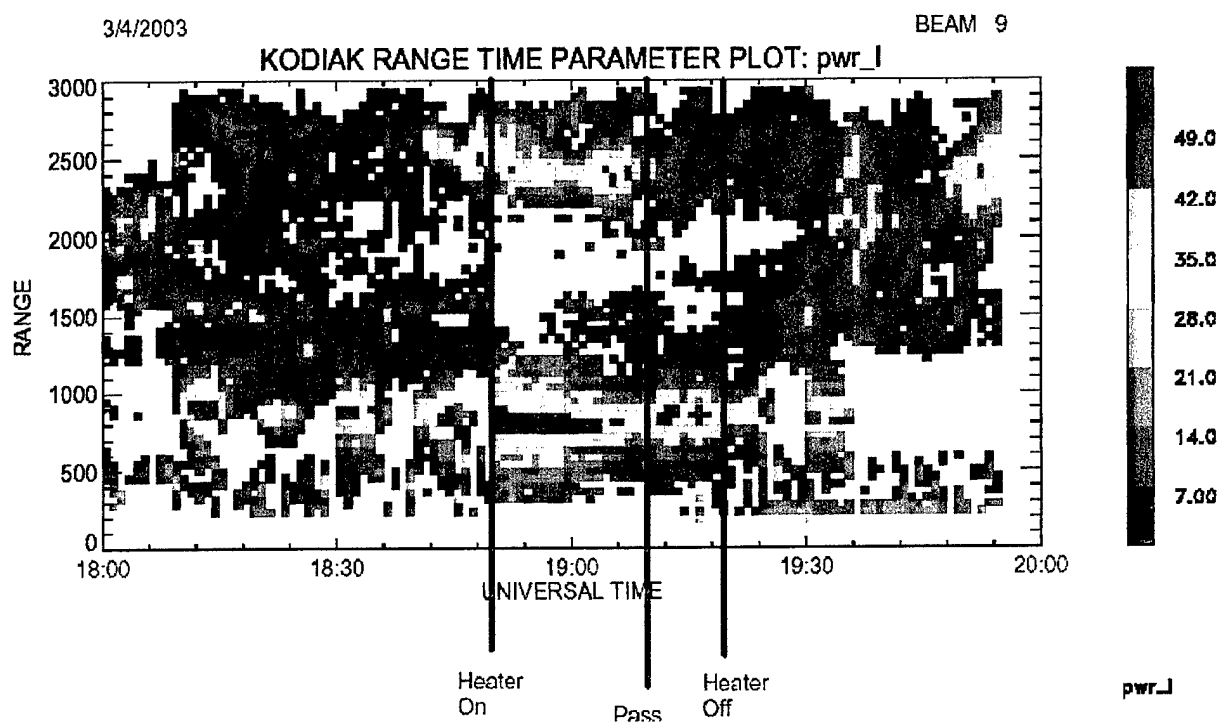


**Figure 34.** Range-vs-time plot of the echo strength from the Kodiak SuperDARN during 1800-2000 UT on 4 March 2003. Blue lines indicate times that the HAARP heater turned on and off and the time of closest approach of the Oscar-32 pass. Red color indicates strong meter-scale structures in the ionosphere for that range/time bin.

## 5. PUBLICATIONS AND PRESENTATIONS

The following publications and presentations resulted, in part, from research carried out under this contract.

Fremouw, E.J., "Ionospheric Tomography Studies at Trough and Higher Latitudes," Session 3B chaired at *International Beacon Satellite Symposium*, Boston College, June 2001.

Fremouw, E.J., "Ionospheric Tomography," lecture presented at *RF Ionospheric Interactions Workshop*, Santa Fe, NM, April 2002

Fremouw, E.J. and J.A. Secan, "Early Images from the Alaska Tomography Array," poster paper presented at *International Beacon Satellite Symposium*, Boston College, June 2001.

Fremouw, E.J. and J.A. Secan, "Preliminary Transit TEC/Scintillation Results from the 2003 HAARP Irregularities Campaign, poster paper presented at *RF Ionospheric Interactions Workshop*, Santa Fe, NM, April 2003.

Fremouw, E.J., J.A. Secan, M. Conde, and G. Bust, "First Multi-station Images from the Alaskan Tomography Chain," poster paper presented at *RF Ionospheric Interactions Workshop*, Santa Fe, NM, April 2001.

Gurevich, A, E. Fremouw, J. Secan, and K. Zybin, "Large-scale Structuring of Plasma-density Perturbations in Ionospheric Modifications," *Phys. Lttrs. A***301**, 307-314, 2002.

Kersley, L., S.E. Pryse, M.H. Denton, G. Bust, E. Fremouw, J. Secan, and N. Jakowski, "Radio Tomographic Imaging of the Northern High-latitude Ionosphere on a Wide Geographic Scale," *Rad. Sci.*, to be submitted, 2004.

Kuo, S.P., "Cascade of Parametric Instabilities in Ionospheric Heating Experiments," poster paper presented at *RF Ionospheric Interactions Workshop*, Santa Fe, NM, April 2001.

Kuo, S.P., "Generation of Extra and Very Low-frequency (ELF/VLF) Radiation by Ionospheric Electrojet Modulation using High-frequency (HF) Waves," *J. Plasma Phys.*, **68** (4), 267-284, 2002.

Kuo, S.P., "On Parametric Instabilities in HF Heating of the Ionosphere," *J. Plasma Phys.*, **69**, 2003.

Kuo, S.P. "On the Cascade Spectrum of Langmuir Waves Observed in Arecibo Heating Experiments," *Physica Scripta*, 2003.

Kuo, S.P., "Parametric Excitation of Lower Hybrid Waves by Langmuir Waves," poster paper presented at *RF Ionospheric Interactions Workshop*, Santa Fe, NM, April 2003.

Kuo, S.P. "On the Cascade Spectrum of Langmuir Waves Observed in Arecibo Heating Experiments," *Physica Scripta*, **69**, 115-119, 2004

Kuo, S.P., S.H. Lee, D. Bivolaru, P. Kossey, M.C. Lee, R.J. Riddolls, P. Jastrzebski, and D. Sentman, "Experimental and Numerical Studies on ELF/VLF Wave Generation by Amplitude-modulated HF Heating Waves," *Physica Scripta*, 2003.

Kuo, S.P., Paul Kossey, James T. Huynh, and Steven S. Kuo, "Amplification of Whistler Waves for the Precipitation of Trapped Relativistic Electrons in the Magnetosphere," *IEEE Trans. Plasma Sci.*, **32** (21), 2004.

Mazzella, A.J., J. Begenisich, E.A. Holland, E.J. Fremouw, and J.A. Secan, "Coordinated TEC Measurements for HAARP Using TRANSIT and GPS", poster paper presented at *International Beacon Satellite Symposium*, Boston College, June 2001.

Ostergaard, J.C., "A New Riometer for HAARP with Direct Computation of Quiet-day Curves," poster paper presented at *RF Ionospheric Interactions Workshop*, Santa Fe, NM, April 2003.



## REFERENCES

- Andreasen, A.M., C.C. Andreasen, E.J. Fremouw, E.A. Holland, A.J. Mazzella, G.S. Rao, and J.A. Secan, "Measurements in the Ionosphere and Protonosphere in the Wake of Solar Maximum," *R&D Status Report 10 on Contract F19628-01-C-0005*, 10 July 2003.
- Austen, J.R., S. J. Franke, and C. H. Liu, "Ionospheric Imaging using Computerized Tomography," *Radio Sci.*, **23**, 299-307, 1988.
- Basu, Sa., Su. Basu, S. Ganguly, and W.E. Gordon, "Coordination Study of Subkilometer and 3-m Irregularities in the F Region Generated by High-power HF Heating at Arecibo," *J. Geophys. Res.*, **88** (A11), 9217-9225, 1983.
- Basu, Sa., Su. Basu, P. Stubbe, H. Kopka, and J. Waaramaa, "Daytime Scintillations Induced by High-power HF Waves at Tromso, Norway," *J. Geophys. Res.*, **92** (A10), 11,149-11,157, 1987.
- Bishop, G.J., D. Walsh, P. Daly, A.J. Mazzella, and E.A. Holland, "Analysis of Temporal Stability of GPS and GLONASS Group Delay Correction Terms Seen in Various Sets of Ionospheric Delay Data," *Proceedings of ION GPS-94*, The Institute of Navigation, Washington, D.C., 1994.
- Caton, R., SCINDA Message Files for upgrade to opSEND, 29 August 2001
- Draper Laboratory, Mathematical Specification for the Trans-Ionospheric Sensing System (TISS) Application Software, Document 305838, Rev 3, Contract No. F04606-89-D-0035-0013, Cambridge, MA, 29 Oct 1993.
- Fremouw, E. J., The Polar BEAR ionospheric experiments: a pre-launch overview, DNA-TR-86-156, Defense Nuclear Agency, Washington, DC, 1986.
- Fremouw, E.J. and R.M. Bussey, "Central-processor Computer Programs in the NWRA Prototype Ionospheric Tomography System (ITS), *NWRA-CR-94-R119*, Software Documentation Report prepared under Contract F19628-90-C-0116, June 1994.
- Fremouw, E.J. and J.M. Lansinger, "Dominant Configurations of Scintillation-producing Irregularities in the Auroral Zone," *J. Geophys. Res.*, **86** (A11), 10,087-10,093, 1981.
- Fremouw, E. J., and L. A. Wittwer, The HiLat satellite program: introduction and objectives, Johns Hopkins APL Tech. Dig., 5, 98, 1984.
- Fremouw, E.J., James A. Secan, R.M. Bussey, and B. M.. Howe, "A Status Report on Applying Discrete Inverse Theory to Ionospheric Tomography," *Int. J. Imaging Syst. & Tech.* **5** (2), 97-105, Sept.-Summer 1994.
- Fremouw, E.J., J.A. Secan, M. Conde, and G. Bust, "First Multi-station Images from the Alaskan Tomography Chain," poster paper presented at RF Ionospheric Interactions Workshop, Santa Fe, NM, April 2001.
- Fremouw, E.J., James A. Secan, and Bruce M.. Howe, "Application of Stochastic Inverse Theory to Ionospheric Tomography," *Rad. Sci.* **27** (5), 721-732, Sept.-Oct. 1992.
- Fremouw, E. J., R. L. Leadabrand, R. C. Livingston, M. D. Cousins, C. L. Rino, B. C. Fair, and R. A. Long, Early results from the DNA Wideband experiment – Complex-signal scintillation, *Radio Sci.*, **13**, 167-187, 1978.

- Gurevich, A, E. Fremouw, J. Secan, and K. Zybin, "Large-scale Structuring of Plasma-density Perturbations in Ionospheric Modifications," *Phys. Lttrs.* **A301**, 307-314, 2002.
- Leitinger, R., G. Schmidt, and A. Tauriainen, "An Evaluation Method Combining the Differential Doppler Measurements from Two Stations that Enables the Calculation of the Electron Content of the Ionosphere," *J. Geophys.*, **41**, 201-213, 1975.
- Livingston, R.C., "Heater-generated Intermediate-scale Irregularities: Spatial Distribution and Spectral Characteristics," *Rad. Sci.* **18**, 253-262, 1983.
- Mazzella, A.J., Jr., J. Begenisich, E.A. Holland, E.J. Fremouw, J.A. Secan, "Coordinated TEC Measurements for HAARP Using Transit and GPS," *Proceedings of the International Beacon Satellite Symposium*, 2001.
- Menke, William, *Geophysical Data Analysis: Discrete Inverse Theory*, Academic Press, San Diego, 1989.
- Mitchell, C. N., L. Kersley, J. A. T. Heaton, S. E. Pryse, Determination of the vertical electron-density profile in ionospheric tomography: experimental results, *Ann. Geophysicae*, **15**, 747-752, 1997.
- Nickisch, L. J., A power-law PSD model of TEC structure in the polar region, in Proceedings of the IES2002 Ionospheric Effects Symposium, 7-9 May 2002, in press, 2002.
- Pryse, S. E., Radio tomography: A new experimental technique, *Surveys in Geophys.*, **24**, 1-38, 2003.
- Pryse, S. E., L. Kersley, C. N. Mitchell, P. S. J. Spencer, and M. J. Williams, A comparison of reconstruction techniques used in ionospheric tomography, *Radio Sci.*, **33**, 1767-1779, 1988.
- Secan, J. A., An assessment of the application of in situ ion-density data from DMSP to modeling of transionospheric scintillation, Scientific Report #1, AFGL-TR-87-0269, Air Force Geophysics Laboratory, Hanscom AFB, MA, September 1987.
- Secan, J. A., and R. M. Bussey, DMSP SSIES Flight Data Processing System Documentation, Volumes I-V, NWRA-CR-87-R011, Northwest Research Associates, Inc., Bellevue, WA, 1987.
- Secan, J. A., and R. M. Bussey, An assessment of the application of in situ ion-density data from DMSP to modeling of transionospheric scintillation, Scientific Report #2, AFGL-TR-87-0269, Air Force Geophysics Laboratory, Hanscom AFB, MA, September 1988.
- Secan, J. A., C. C. Andreasen, E. J. Fremouw, E. Holland, A. Mazzella, Analysis of Ionospheric Monitoring System (IMS) Total Electron Content (TEC) data and equatorial phase-scintillation data, *PL-TR-95-2116*, Phillips Laboratory, Hanscom AFB, MA, 1 Jul 1995.
- Singleton, D.G., "Dependence of Satellite Scintillations on Zenith Angle and Azimuth," *J. Atmos. Terr. Phys.*, **32**, 789-803, 1970.

## Appendix A

### Revised IMS Archive Data File

#### === 2-Hz Data ===

Item	Source	Data Type	Length (Bytes)
Ada Overhead	Ada	Character	16
Record Header	Ada	Character	8
Milliseconds of GPS Week	Ada	Integer	4
Satellite PRN#	MBEN	Integer	1
L1 Good/Bad Flag	MBEN	Integer	1
Satellite Elevation (degrees)	MBEN	Integer	1
Satellite Azimuth ("bi-degrees")	MBEN	Integer	1
Receiver Channel	MBEN	Integer	1
L1 Warnings Status Word (P1)	MBEN	Integer	1
L1 Phase Quality Indicator (P1)	MBEN	Integer	1
L1 Carrier to Noise Ratio (P1)	MBEN	Integer	1
L2 Warnings Status Word (P2)	MBEN	Integer	1
L2 Phase Quality Indicator (P2)	MBEN	Integer	1
L2 Carrier to Noise Ratio (P2)	MBEN	Integer	1
L2 Good/Bad Flag	MBEN	Integer	1
Code-Based TEC (TEC units)	MBEN/Ada	Real	8
Phase-Based Relative TEC (TEC units)	MBEN/Ada	Real	8
Sequence ID	MBEN	Integer	2
(Not Used)	---	Character	2
C/A Warnings Status Word	MBEN	Integer	1
C/A Phase Quality Indicator	MBEN	Integer	1
C/A Carrier to Noise Ratio	MBEN	Integer	1
C/A Good/Bad Flag	MBEN	Integer	1
Footer ('END_TEC')	Ada	Character	8

#### === Position Data ===

Item	Source	Data Type	Length (Bytes)
Ada Overhead	Ada	Character	16
Header	Ada	Character	8
ECEF X-coordinate (m)	PBEN	Real	8
ECEF Y-coordinate (m)	PBEN	Real	8
ECEF Z-coordinate (m)	PBEN	Real	8

Quality Metric	PBEN	Integer	2
GPS Week Number	PBEN	Integer	2
Milliseconds of GPS Week	PBEN	Integer	4
Footer ('END_PBEN')	Ada	Character	8

=== Ephemeris ===

Item	Source	Data Type	Length (Bytes)
Ada Overhead	Ada	Character	16
Header	Ada	Character	8
Fit Interval Code	SNAV	Integer	2
GPS Week Number	SNAV	Integer	2
Time of GPS Week (msec)	SNAV	Integer	4
Group Delay (sec)	SNAV	Real	4
Clock Data Issue	SNAV	Integer	4
Clock Time (sec)	SNAV	Integer	4
Time Adjustment (sec/sec <sup>2</sup> )	SNAV	Real	4
Time Adjustment (sec/sec)	SNAV	Real	4
Time Adjustment (sec)	SNAV	Real	4
Orbit Data Issue	SNAV	Integer	4
Correction to Avg. motion (semicircles/sec)	SNAV	Real	4
Mean Anomaly (semicircles)	SNAV	Real	8
Eccentricity	SNAV	Real	8
Sq. Root of SemiMajor Axis (m <sup>1/2</sup> )	SNAV	Real	8
Epoch Time (sec)	SNAV	Integer	4
Harmonic Correction CIC (radians)	SNAV	Real	4
Harmonic Correction CRC (radians)	SNAV	Real	4
Harmonic Correction CIS (radians)	SNAV	Real	4
Harmonic Correction CRS (radians)	SNAV	Real	4
Harmonic Correction CUC (radians)	SNAV	Real	4
Harmonic Correction CUS (radians)	SNAV	Real	4
(Not Used)	---	Character	4
Longitude of Asc Node (semicircles)	SNAV	Real	8
Argument of Perigee (semicircles)	SNAV	Real	8
Inclination (semicircles)	SNAV	Real	8
Ascending Node Rate (semicircles/sec)	SNAV	Real	4
Inclination Rate (semicircles/sec)	SNAV	Real	4
Accuracy Code	SNAV	Integer	2



Health Code	SNAV	Integer	2
Satellite PRN#	SNAV	Integer	1
(Not Used)	---	Character	3
Footer ('END_SNAV')	Ada	Character	8



## Appendix B

### File Formats for Processed IMS TEC and Scintillation Data

2-Hz Pass File: Direct Access, binary, 43 bytes per record

Header Item	Type	Length (Bytes)
GPS satellite identifier	Integer	4
Day of year	Integer	4
Year	Integer	4
Last record number	Integer	4
Time of first sample (GPS week and fraction)	Real	8
Time of last sample (GPS week and fraction)	Real	8

Data Item	Type	Length (Bytes)
Time of Current sample (seconds of day)	Real	8
Elevation (degrees)	Integer	1
Azimuth (degrees)	Integer	2
Dispersive Group Delay (DGD) (TEC units)	Real	8
Dispersive Carrier Phase (DCP) (TEC units)	Real	8
L1 Warnings Status Word	Integer	2
L1 Phase Quality Indicator	Integer	2
L1 Carrier to Noise Ratio	Integer	2
L2 Warnings Status Word	Integer	2
L2 Phase Quality Indicator	Integer	2
L2 Carrier to Noise Ratio	Integer	2
Receiver Channel (1 - 12)	Integer	2
Sequence ID	Integer	2

1-Minute average data (samples reported every 30 seconds)

Header Item	Format	Field Width
GPS satellite identifier	I2	2
Day of year	I3	4
Year	I4	5
Initial Dispersive Carrier Phase (DCP) value (TEC units)	F17.3	18

Data Item	Format	Field Width
GPS Time of day (sec, with rollover extension)	F8.1	8
Dispersive Group Delay (DGD) (TEC units)	F13.3	13
Offset from initial DCP value in header (TEC units)	F16.3	16
Azimuth (degrees)	F9.2	9
Elevation (degrees)	F9.2	9
Ionospheric Penetration Point (IPP) latitude (degrees)	F8.3	8
IPP longitude (degrees, positive East)	F9.3	9
L1 Carrier to Noise ratio (IREG units) (see note 1)	F9.2	9
L2 Carrier to Noise ratio (IREG units) (see note 1)	F9.2	9
L1 Phase Quality (averaged)	I4	4
L2 Phase Quality (averaged)	I4	4
Number of 2-Hz samples in first 30-second average	I4	4
Number of 2-Hz samples in second 30-second average	I4	4
Phase averaging adjustment, for current lock (TEC units)	F16.3	16
Cumulative number of 1-Min samples for phase averaging	I5	5
Loss of lock occurrences in time interval	I4	4
L1 Warning Flag (see note 2)	I4	4
L2 Warning Flag (see note 2)	I4	4
Equivalent vertical TEC, calibrated (TEC units)	F13.3	13
Combined satellite and receiver bias (TEC units)	F10.4	10

Notes:

- 1) With wrapping elimination at 255/0 transition
- 2) Composed as bitwise OR for Z mode check (bit 6)

### 15-Minute summary data (reported every 15 minutes)

Description	Format	Field Width
GPS satellite identifier	I3	4
GPS week number	I4	5
GPS time of week at midpoint of interval (sec)	F11.3	11
GPS time of week at maximum VTEC in interval (sec)	F11.3	11
IPP latitude at midpoint of interval (degrees)	F6.1	6
IPP longitude at midpoint of interval (-180:180) (degrees, positive West)	F6.1	6
IPP latitude at maximum VTEC in interval (degrees)	F6.1	6
IPP longitude at maximum VTEC in interval (-180:180) (degrees, positive West)	F6.1	6
Maximum VTEC in interval (TEC units)	F10.2	10
Minimum VTEC in interval (TEC units)	F10.2	10
Average VTEC in interval (TEC units)	F10.2	10
Standard deviation of VTEC in interval (TEC units)	F10.2	10
General quality indicator (see note 1)	I4	4
Percentage of possible (2-Hz) samples acquired	I4	4
Average L2 signal-to-noise ratio (IREG units)	I4	4
Average L2 phase quality indicator	I4	4
Number of minutes with phase lock	I5	5
Health code	I4	4
Loss of lock count for interval	I4	5
WGS-84 X-coordinate for site (m) (from receiver) (see note 2)	F14.3	14
WGS-84 Y-coordinate for site (m) (from receiver) (see note 2)	F14.3	14
WGS-84 Z-coordinate for site (m) (from receiver) (see note 2)	F14.3	14

#### Notes:

1) General data quality indicator is accurate only for last satellite in interval

2) Site coordinates are listed only with first satellite in interval

# 15-Minute scintillation statistics table (from 2-Hz data)

Data Item	Format	Field Width
Satellite PRN number	I2	2
Year of data	I4	5
Day-of-year of data	I3	4
Starting time of data interval (Universal Time seconds)	I5	6
Azimuth for first valid data sample (degrees) (positive clockwise from North, to East; 0:360)	F5.1	6
Elevation for first valid data sample (degrees)	F4.1	5
Ionospheric penetration point (IPP) latitude, for first valid data sample (degrees) (positive North)	F5.1	6
IPP longitude, for first valid data sample (degrees) (positive West)	F6.1	7
Maximum $S_4$ from L1 in 15-minute interval	F6.2	7
Maximum $S_4$ from L2 in 15-minute interval	F6.2	7
Average $\sigma_\phi$ , in radians, over 15-minute interval	F6.3	7
30 One-minute $S_4$ values for L1 (every 30 seconds)	F5.2	6
30 One-minute $S_4$ values for L2 (every 30 seconds)	F5.2	6
30 One-minute $\sigma_\phi$ values, in radians (every 30 seconds)	F6.3	7

## Appendix C

### Description of Software for IMS 20-Hz Scintillation Analysis

This appendix describes the developmental testing conducted on the algorithms and software to be used as part of the upgraded Ionospheric Measuring System (IMS) and provides formal documentation of the results of that testing. The goal of this testing was to demonstrate that the software to be incorporated within the IMS processing system performs its functions correctly when compared with a set of algorithms and programs developed over a 20-plus year period for analysis of data from a series of scientific experiments. Note that the intent of this testing was not to assess the performance of the IMS as a tool for measuring ionospheric scintillation, but to make note of performance issues that should be investigated further.

The software being tested is designed to generate estimates of the  $S_4$  intensity-scintillation and  $\sigma_\phi$  phase-scintillation indices and of the T (strength) and p (slope) parameters which are used to characterize the phase-scintillation power-density spectrum. The input data are 20Hz data-rate samples of intensity from the L1 signal and differential carrier phase (DCP) between L1 and L2, and 2Hz data-rate samples of intensity from the L2 signal. The output estimates are to be  $S_4$  (for both L1 and L2),  $\sigma_\phi$ , T, and p for 60-second data segments at 30-second intervals (i.e., with 50 percent overlap between the data segments from adjacent analyses); the average of each of these parameters over 15-minute intervals (the standard IMS analysis record length); and the maximum value for each parameter over the same 15-minute interval. These estimates will be inserted into standard-format TELSI messages by other software in the IMS processing system, a functionality not included in this testing.

#### C.1 IMS Software

The basis for the algorithms and software developed for the IMS to perform these functions are a set of analysis codes developed over the past three decades by NorthWest Research Associates, Inc., (NWRA) in support of a series of satellite experiments designed to study ionospheric scintillation including the Defense Nuclear Agency (DNA) Wideband (Fremouw et al., 1978), HiLat (Fremouw and Wittwer, 1984), and Polar BEAR (Fremouw, 1986) satellites. These algorithms have also been used in analysis of scintillation data collected from the Navy Transit satellites using the NWRA ITS-10S receivers. Some of these algorithms have also been used in analysis of *in situ* observations of ionospheric plasma-density irregularities from the Defense Meteorological Satellite Program (DMSP) SSIES scintillation-meter data (Secan, 1987; Secan and Bussey, 1988) and were included in the software developed by NWRA for USAF use in operational analysis of these data (Secan and Bussey, 1987). The most recent version of these research codes, developed for analysis of scintillation data as part of an upgrade of the WBMOD ionospheric scintillation model, serves as the benchmark against which the new software is compared.

The processing algorithms to be employed for the 20Hz data (DCP and L1 intensity) are as follows:

1. The data are prepared for analysis by replacing all "bad" data (missing-data values only at present). At the start and end of the 15-minute period, this is done by simply filling back to the start from the first good data value or from the last good value to the end with the good value. For interior bad points, linear interpolation from the good values on either end of the gap is used to fill in. The number of data points "fixed" in this manner is counted for each 60-second analysis block. Present limitation: (1) no attempt is made to look for data which is non-missing but still invalid in some manner (such as outliers); (2) the data used to fill the missing-data gaps is not checked to make sure it is not invalid in some manner prior to use.

2. The phase data are processed as follows:

a. The DCP time-series is detrended by using a Butterworth time-domain low-pass filter to generate a trend which is then subtracted from the input data to produce a detrended DCP time series. At present, a 6-pole, two-directional (to avoid time-offsets) filter with a 1/60 Hz cutoff frequency (the 3dB point in the PDS) is used. Prior to detrending, a simple linear trend is created by a line between the first and last data points and is removed from the entire series. The series is then extended on both ends by adding zero-filled blocks of length LPAD (see the section on array size parameters). These are both done to mitigate first-order start-up effects from the filter. The detrended data is stored into 60-sec records (1200 samples) with center-times 30 seconds apart. (There is an option to use a polynomial to generate the detrended records in the first and last few 60-sec records in order to mitigate "start-up" problems with the Butterworth filter.)

b. The RMS phase ( $\sigma_\phi$ ) is calculated in the time domain for each 60-second record. In order to minimize the impact of second-order start-up problems with the filter used to detrend the data, a specified number of data points are excluded from this calculation in the first and last 60-second record of the 15 minute set (at present, 200 data points are excluded). (This is not necessary if the polynomial option described in the previous paragraph was used.)

c. A power-density spectrum is constructed from each 60-second record by (1) selecting the center 1024 data points from the set (for FFT efficiency), (2) windowing the data using a full cosine-taper window, (3) using an FFT to generate the spectrum, and (4) smoothing the resulting PDS using a 5-point centered binomial smoothing function.

d. The T and p parameters are calculated by fitting a straight line to the (log) PDS. At present, this fit is over the frequency range 0.5 to 7.0 Hz. (Note: As a study topic for enhanced performance, we should investigate using the HiLat noise-floor locator algorithm to adjust the high-frequency end of the fit range.)

3. The 20-Hz L1 intensity data are processed as follows:

a. The intensity time-series is detrended by using the process described for the DCP processing to generate a trend which is then divided into the input data to produce a detrended intensity time series (this detrending acts as an after-the-fact automatic gain control (AGC)). The same filter described in the phase section is used here. The detrended data is stored into 60-sec records (1200 samples) with center-times 30 seconds apart. (An alternative is to detrend  $\log(\text{intensity})$ .)

b. The  $S_4$  index is calculated in the time domain for each 60-second record. In order to minimize the impact of start-up problems with the filter used to detrend the data, a specified number of data points are excluded from this calculation in the first and last 60-second record of the 15 minute set (at present, 200 data points are excluded).

4. The  $\sigma_\phi$ ,  $S_4$ , T, and p time series are then further processed to calculate the average and maximum values and time of maximum for each parameter for the entire 15 minute period. Values which were calculated from 60-sec records containing more than a certain number of "bad" data points are excluded from this process (at present, if more than 120 (10 percent) of the record was bad the corresponding analysis values are excluded).

The processing of the 2Hz L2 intensity data is identical to the processing described above for the 20Hz L1 data. This is done in a separate code which is tailored to the different data rate.



## C.2 Test Results

The testing was accomplished by processing a set of GPS data with both the standard research code and the new IMS codes (both the 20Hz and 2Hz versions), all using the same configuration parameter (sample size, detrender parameters, window type, etc.), and comparing the resulting scintillation estimates.

The plots in Figure C-1 show the data set used in testing. These data were collected on 23 October 2001 using a 20Hz-capable Ashtech GPS receiver located at Qaanaaq, Greenland. The four plots in Figure C.1 from top to bottom show the detrended L1 intensity, the L1 intensity trend, the detrended DCP, and the DCP trend. These trend and detrend records were generated using the standard codes with a detrend cutoff frequency of 60Hz. Note that there are several clear cases of enhanced scintillation in this record, and there is also evidence of what appears to be multipath at the low-elevation ends of the intensity record. (Also note that the "raw" non-detrended data were processed by the prototype IMS codes, not the detrended data shown in these plots.)

Data from this pass were processed by both the research codes and a test-bed version of the IMS codes which allowed us to process data not in the format to be used in the IMS during operations. Figures C-2 and C-3 show the results from the IMS codes for the entire pass, with the full set of estimates (one every 30 seconds) in Figure C-2 and the 15-minute average and maximum values in Figure C-4. From top to bottom, both figures show  $S_4$  from L1,  $\sigma_\phi$  from DCP, and  $p$  and  $T$  from the DCP power-density spectrum. The two horizontal lines on the two plots of  $p$  will be discussed in the later section describing issues which should be investigated further.

The four plots in Figure C-4 show the results of the comparison of the L1  $S_4$ ,  $\sigma_\phi$ ,  $p$ , and  $T$  from the prototype IMS codes (along the Y axis) to the results generated by the standard processing codes (along the X axis). As can be seen, the results generated from the prototype code are nearly identical with those obtained by the standard processing codes. There are a few departures from equality in the  $S_4$  and  $\sigma_\phi$  plots which are due to detrender effects.

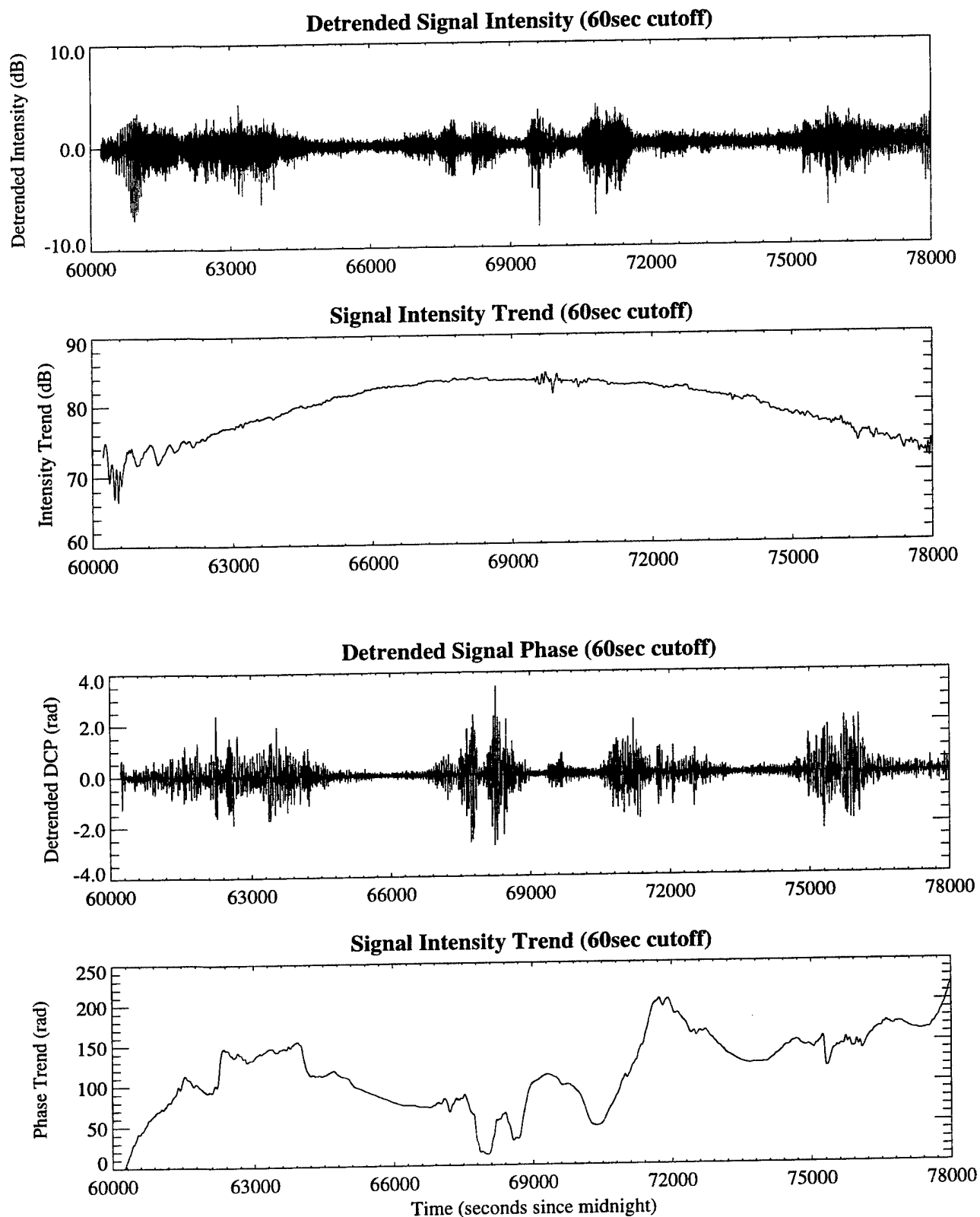


**Figure C-1.** Data from PRN01 pass on 23 October 2001 at Qaanaaq, Greenland, used in this analysis. From top to bottom, the plots are the intensity detrended, intensity trend, phase detrended, and phase trend time-series for this pass.

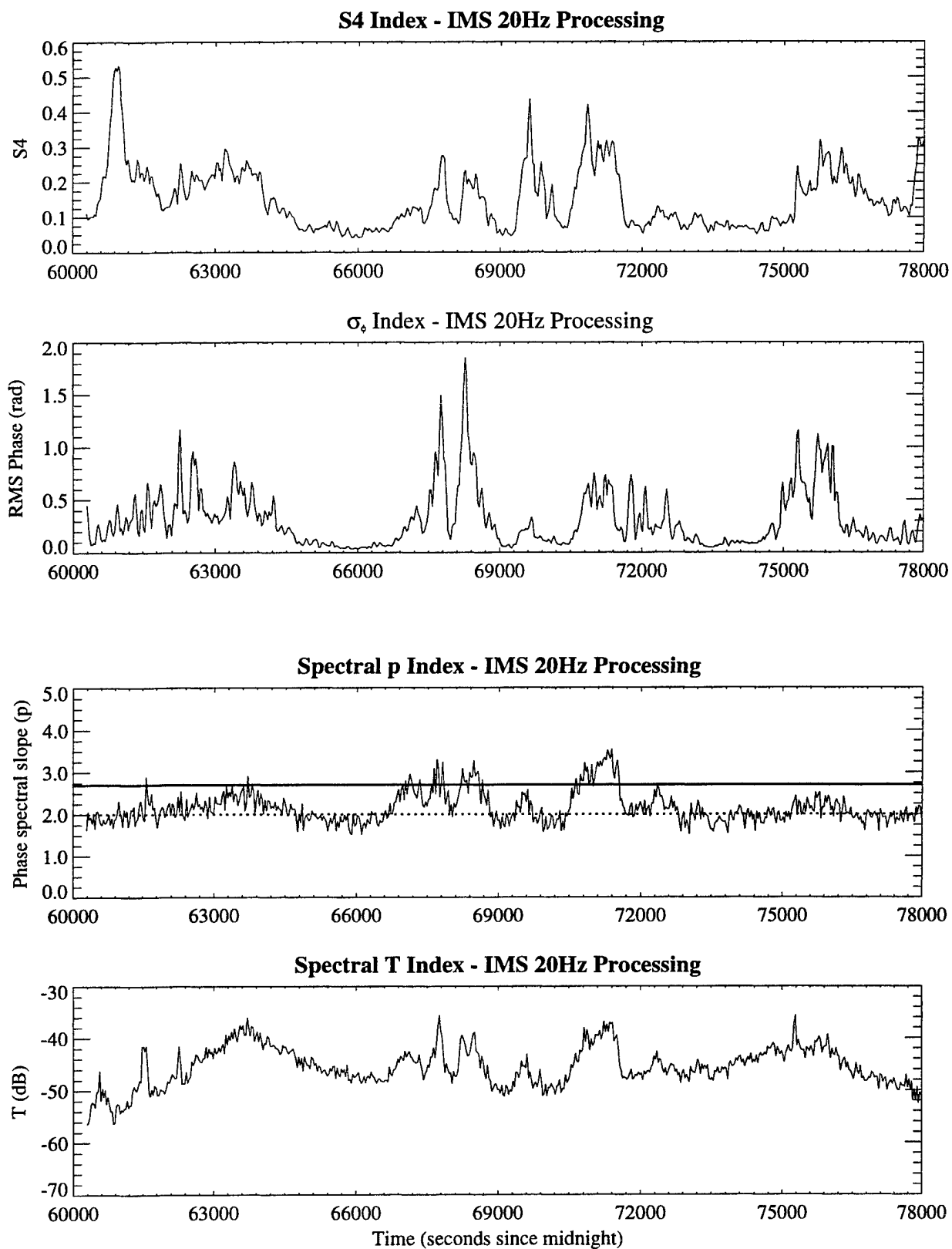


**Figure C-2.** Analysis results from the IMS 20-Hz processing. The plots are, from top to bottom,  $S_4$ ,  $\sigma_\phi$ ,  $p$  (phase spectral slope), and  $T$  (phase spectral strength).

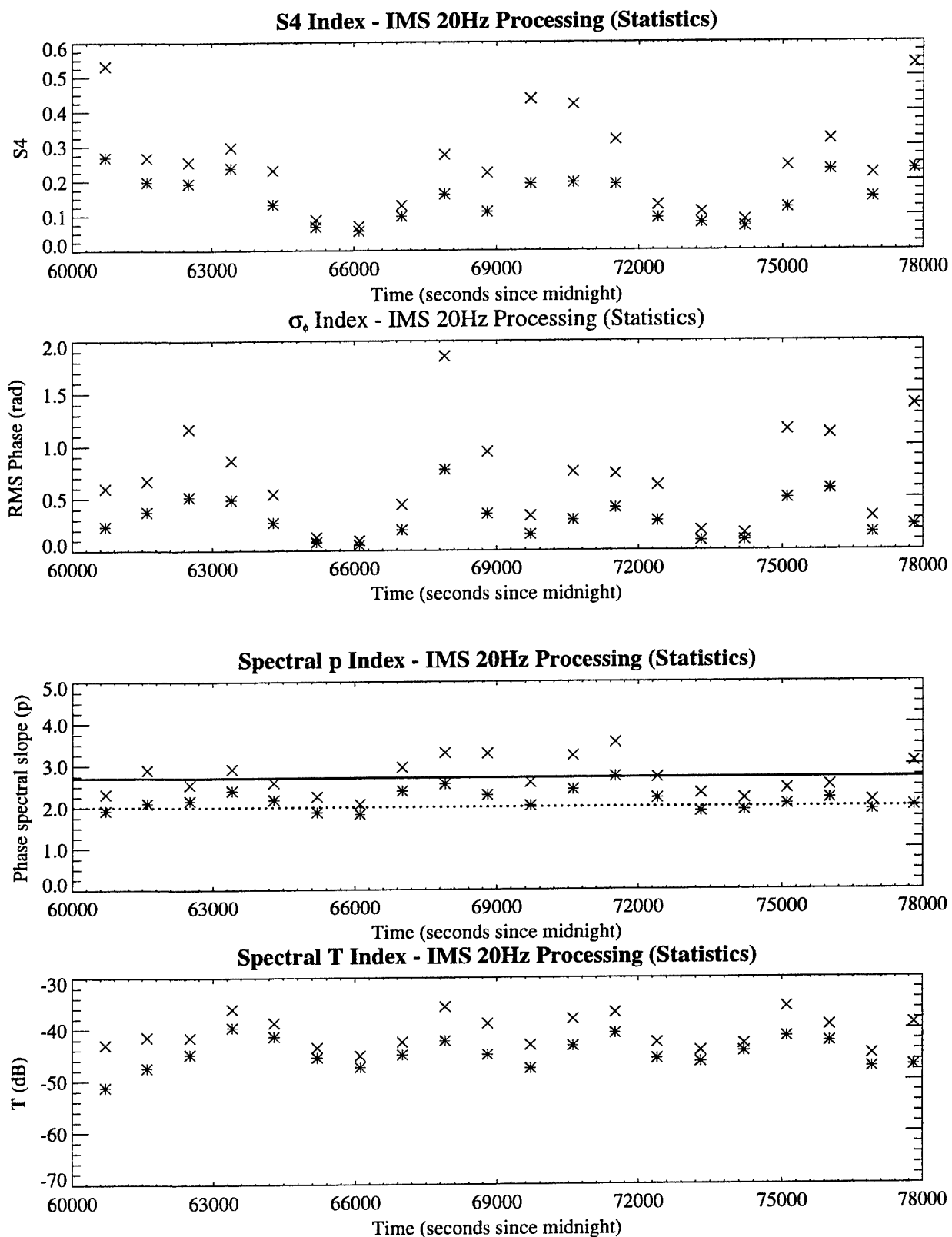


**Figure C-3.** Analysis results from the IMS 20Hz processing. The plots are, from top to bottom, average (asterisk) and maximum (cross)  $S_4$ ,  $\sigma_\phi$ , p (phase spectral slope), and T (phase spectral strength).

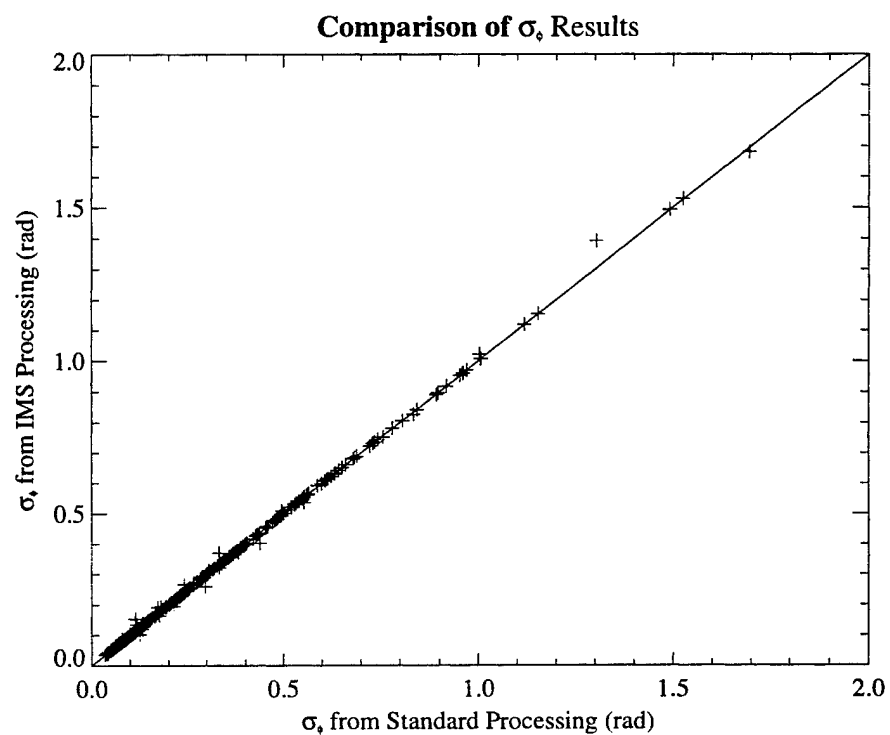
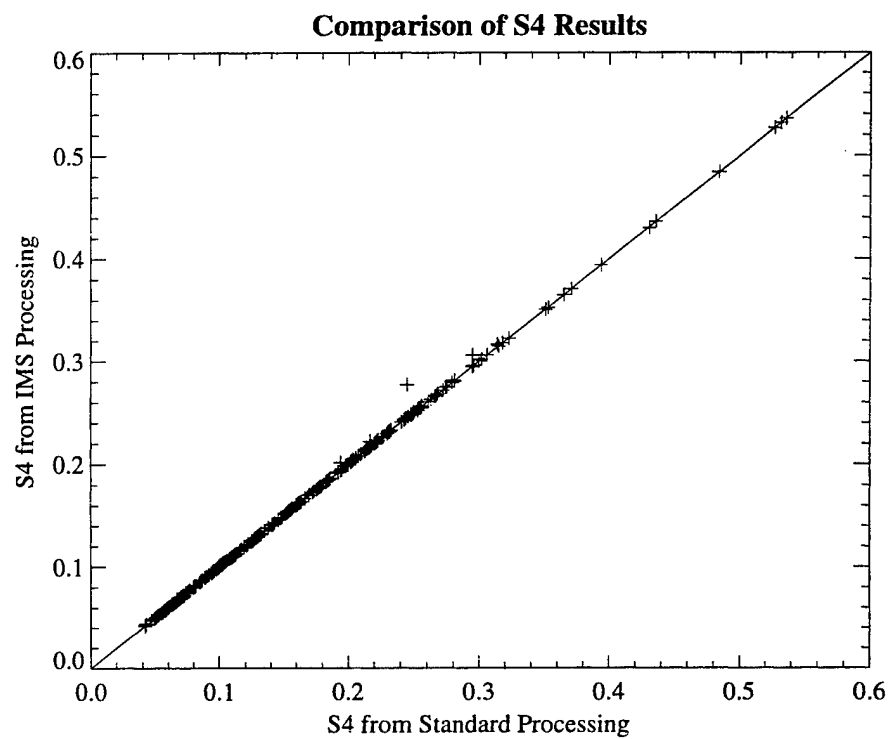


**Figure C-4.** Comparison of the S<sub>4</sub> (top plot) and  $\sigma_\phi$  (bottom plot) indices from the standard processing software (along the X axis) and IMS processing software (along the Y axis).

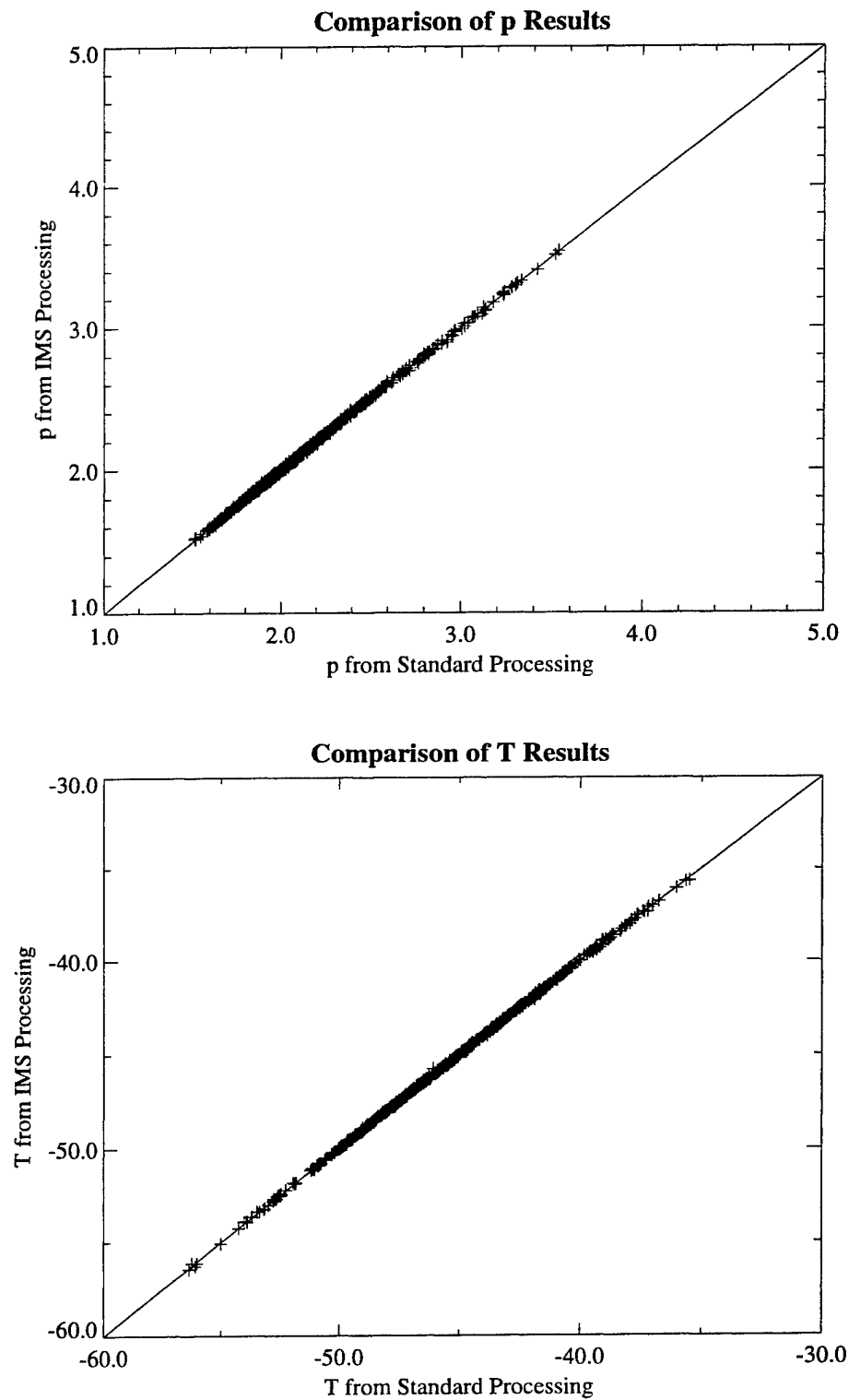


**Figure C-4 (cont).** Comparison of the p (top plot) and T (bottom plot) parameters from the standard processing software (along the X axis) and IMS processing software (along the Y axis).

This is most clearly seen in Figure C-5, which shows the detrended DCP for a single 60-second sample which corresponds to the point on the  $\sigma_\phi$  plot in Figure C-4 which departs the most from the equality line. The solid line in this figure is from the standard code and the dotted line is from the IMS prototype code. It is evident that there is a slight difference in these two curves, which result in different estimates of  $\sigma_\phi$ . This difference is due to the start-up issue mentioned earlier. This particular data sample is the last sample from a 15-minute data block in the IMS processing. Since the IMS processing detrends each 15-minute sample independently (which must be done in operational use in order to provide analysis in a timely fashion) and the standard processing code detrends the entire pass as a unit, there will be small differences in the trends generated by the filter due mostly to start-up effects of the filter at either end of the time-series record. This is not a major problem: the largest difference in this test sample was 7 percent and the RMS error for the entire test set (600 data points) was under 3 percent. This could be improved by delaying the scintillation analyses provided by the IMS to permit collection of additional data, thus avoiding start-up problems, but this would require major changes to the way in which the IMS processing system works, something that we feel is not warranted by this level of potential inaccuracy.

Another consideration here is the excellent reproduction of T and p by the prototype code. We have for years preferred using T and p in our research and modeling efforts because these parameters are not affected by detrender effects (if the appropriate care is taken). Given that the IMS prototype code works well on these parameters, we feel comfortable accepting the level of inaccuracy in the  $\sigma_\phi$  parameter described above.

We did not have the corresponding 2-Hz L2 intensity data for this pass, so testing of the 2Hz IMS prototype code was done using the L1 data set decimated down to 2Hz by selecting every 10<sup>th</sup> data point. Figure C-6 shows the comparison of the 2Hz L1  $S_4$  values (Y axis) to the 2Hz L1  $S_4$  values from the standard code (X axis). The results shown here are similar to that shown in Figure 4 for the 20Hz analyses. This figure also shows a plot of the 2Hz L1  $S_4$  values (Y axis) to the 20Hz L1  $S_4$  values from the standard code (X axis). This is shown to provide a look at the degradation in the  $S_4$  estimates due to the lower sampling rate for one pass. While this is not a definitive measure of the level of degradation, it at least indicates that for low-to-moderate levels of  $S_4$  we may obtain useful estimates from the 2Hz L2 data.

### C.3 Issues for Further Study

The algorithms implemented in the software described in this report were largely developed and employed in studying data collected from satellites in low-earth orbit (LEO, typically around 1,000 km altitude) and at VHF and UHF frequencies. They are now to be applied to data from satellites in high-earth orbit (HEO, around 20,000 km altitude), which results in a slower scan rate through the ionosphere than the LEO systems, and at L-band. While these differences will have possible impact on the interpretation of the  $S_4$  and  $\sigma_\phi$  measurements and their conversion into environmental parameters such as RMS  $\Delta N_e$  or  $C_k L$ , it is not expected that they have any impact on the calculation of these parameters using the LEO-derived algorithms. This may not, however, be the case for the phase spectrum parameters T and p.

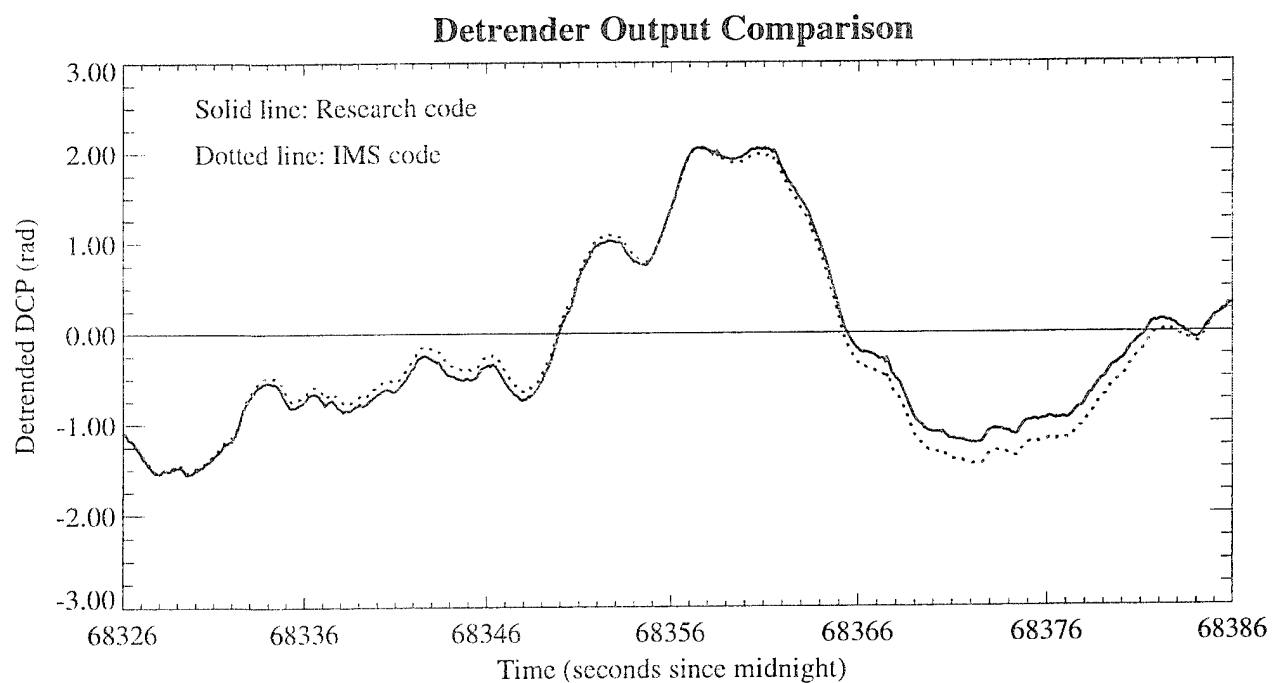


**Figure C-5.** Comparison of the detrended phase records from the standard processing ("Research code" shown as a solid line) and the IMS processing (dotted line) for a single 60-second record.



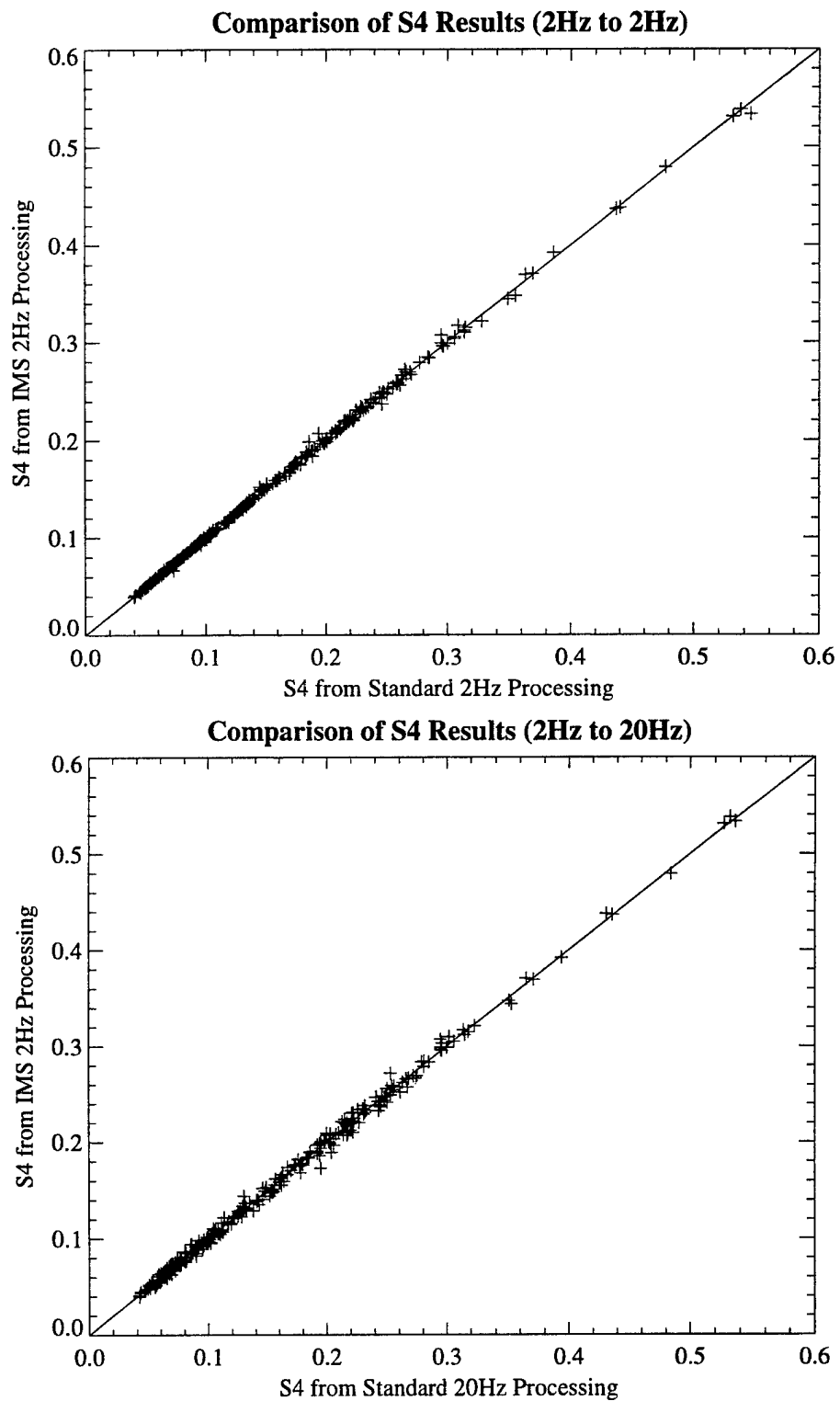


**Figure C-6.** Comparison of the 2Hz  $S_4$  results with (1) 2Hz  $S_4$  generated using the standard processing code (top plot), and (2) 20Hz  $S_4$  generated using the IMS processing code (bottom plot).

The "red flag" which led us to investigate this issue is illustrated in the plot of the phase spectral slope,  $p$ , in Figure C-2. The two horizontal lines on this plot show the nominal value for  $p$  from the WBMOD ionospheric scintillation model (the solid line at 2.7) and a line at  $p=2.0$ . The fact that most of the values were well below the nominal model value (which was recently verified in work done by Mission Research Corporation looking at GPS data from the polar region [Nickish, 2002]) and tend to cluster around a value of 2.0, which we have in the past found is an indicator of possible analysis or processing problems, led us to take a close look at the spectral processing. Given the limited resources (both funding and time) for studies, our goal was to see if we can identify whether there is indeed a problem with the processing and either develop a corrected processing algorithm or develop a mitigative solution to be replaced at a later time with an improved algorithm.

Figure C-7 illustrates what we were able to determine in this limited study. This plot shows two phase spectra taken from 60-second data samples with the lowest and highest  $\sigma_\phi$  values in the pass we have been using in our testing. The straight lines plotted over the spectra are the least-squares fits from which  $T$  and  $p$  were derived. The important things to note here are (1) that the two spectra merge into one another at around 1.0 to 2.0 Hz, and (2) that this region above the "merge point" doesn't look like a "normal" noise-floor. In looking at many spectra from this pass, we found that what is shown in Figure C-7 is very typical: all of the spectra tend to be very similar above a spectral frequency of about 2.0 Hz.

To assess the impact of this, we redid the spectral analysis (this was done using the standard processing software which has the flexibility to allow this sort of analysis) and produced fits over two frequency regimes: 0.1 to 2.0 Hz and 2.0 to 10.0 Hz. The plots in Figure C.8 show  $p$  and  $T$  from both the lower-range fit (the top two plots) and the upper-range fit (bottom two plots). The spectral slopes produced from the fit over the low-frequency range are now varying in the range expected from previous studies (in fact, the average value from this analysis is 2.73). The slopes from the high-frequency range are almost non-varying across the entire pass and are very nearly 2.0 throughout the pass. The  $T$  value derived from the high-frequency fit is also devoid of significant variations across the pass despite large variations in both  $S_4$  and  $\sigma_\phi$ . The  $T$  value from the low-frequency fit is nearly identical to that derived from the fit across the entire spectrum, as illustrated in Figure C-9 which is a plot of the  $T$  value from the low-frequency fit range plotted against the value derived from a fit to the entire spectrum. So this as-yet unexplained behavior at the high-frequency end of the phase spectrum has more impact on the estimate of the slope of the spectrum than on the  $T$  value.

There are two approaches to dealing with this issue: (1) limit the frequency range over which the least-squares fits are calculated to 0.1 to 2.0 Hz, or (2) develop and test an algorithm to automatically locate and exclude the unwanted part of the spectrum. Given the limited resources at this time, we have taken the simpler approach of simply setting the frequency range to a fixed interval. We did investigate the use of a "noise-floor locator" algorithm that was developed for use with the HiLat and Polar BEAR data sets, and modified in a later study, to find "breaks" in a phase spectrum (Secan et al., 1995). Although the approach has merit, producing a robust algorithm and testing it was not possible within the given time constraints. The results of our analysis using the fixed range, as shown in Figure C-8, however, show that this is a viable alternative for the initial capability.

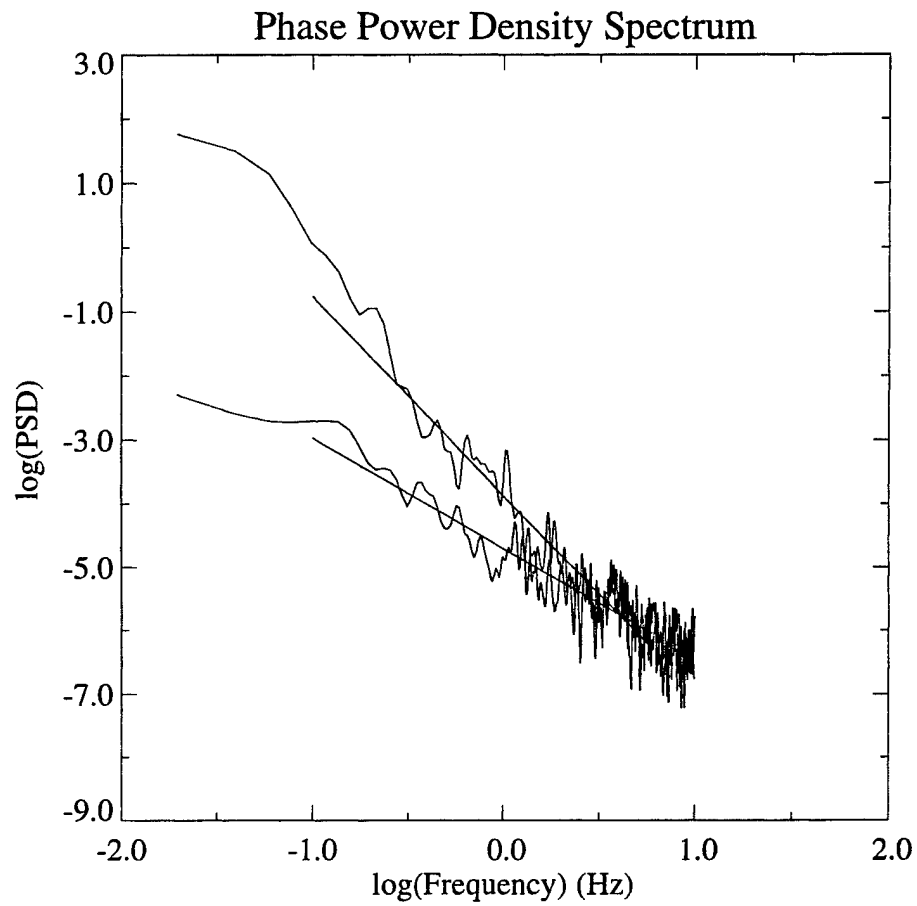


**Figure C-7.** Sample phase power-density spectra from the 60-second data samples with the highest and lowest  $\sigma_\phi$  values in the pass. The spectrum for the highest  $\sigma_\phi$  is at the top and the spectrum for the lowest is at the bottom. The straight lines shown overplotted are least-squares fits to the spectra.

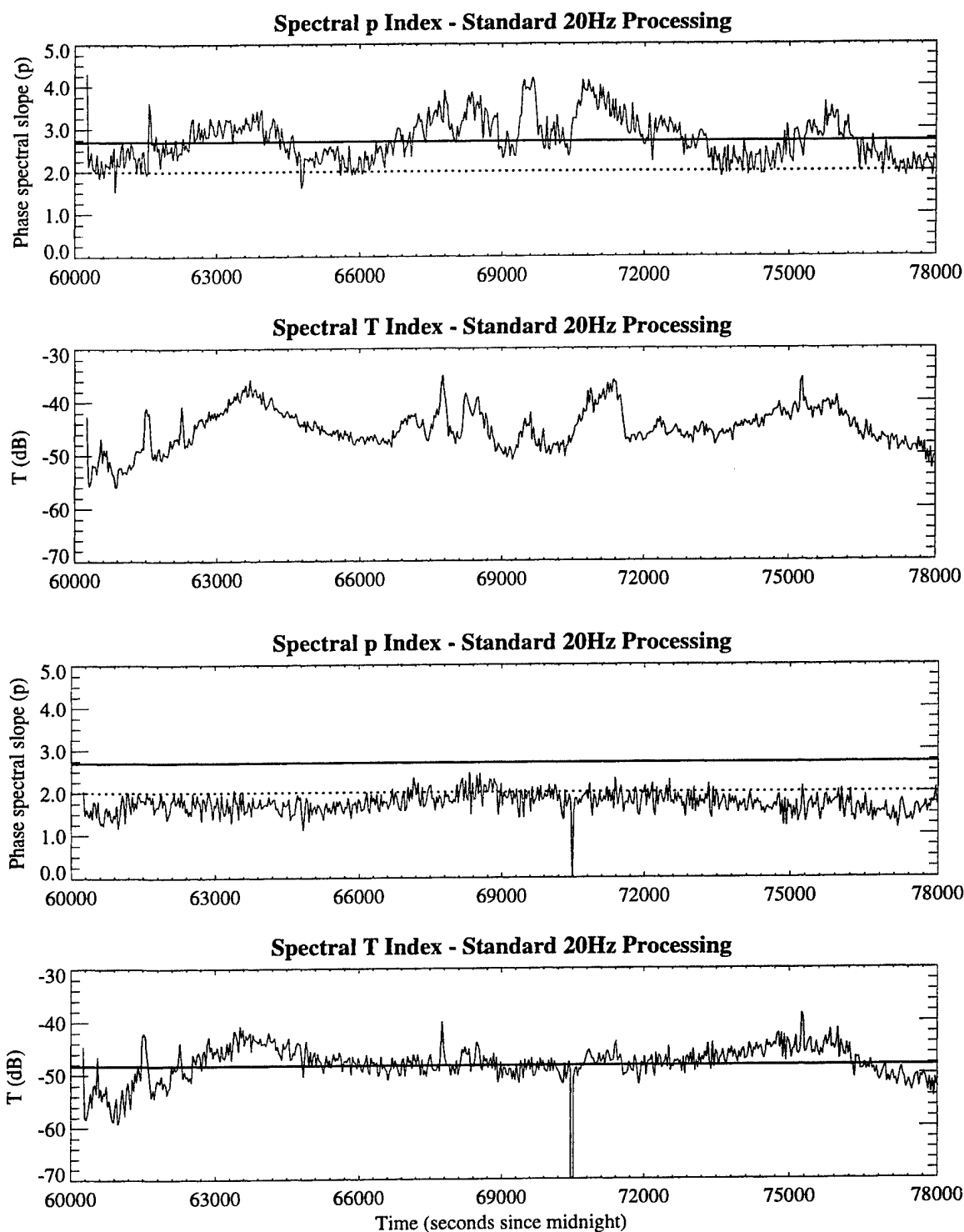


**Figure C-8.** The p and T values calculated using fits over the spectral frequency range of 0.1 to 2.0 Hz (top two plots) and using fits over the range 2.0 to 10.0 Hz (bottom two plots). The solid lines on the p plots are the WBMOD model value and the dotted lines are  $p=2$ . The solid line on the lower T plot is the average T for the pass.

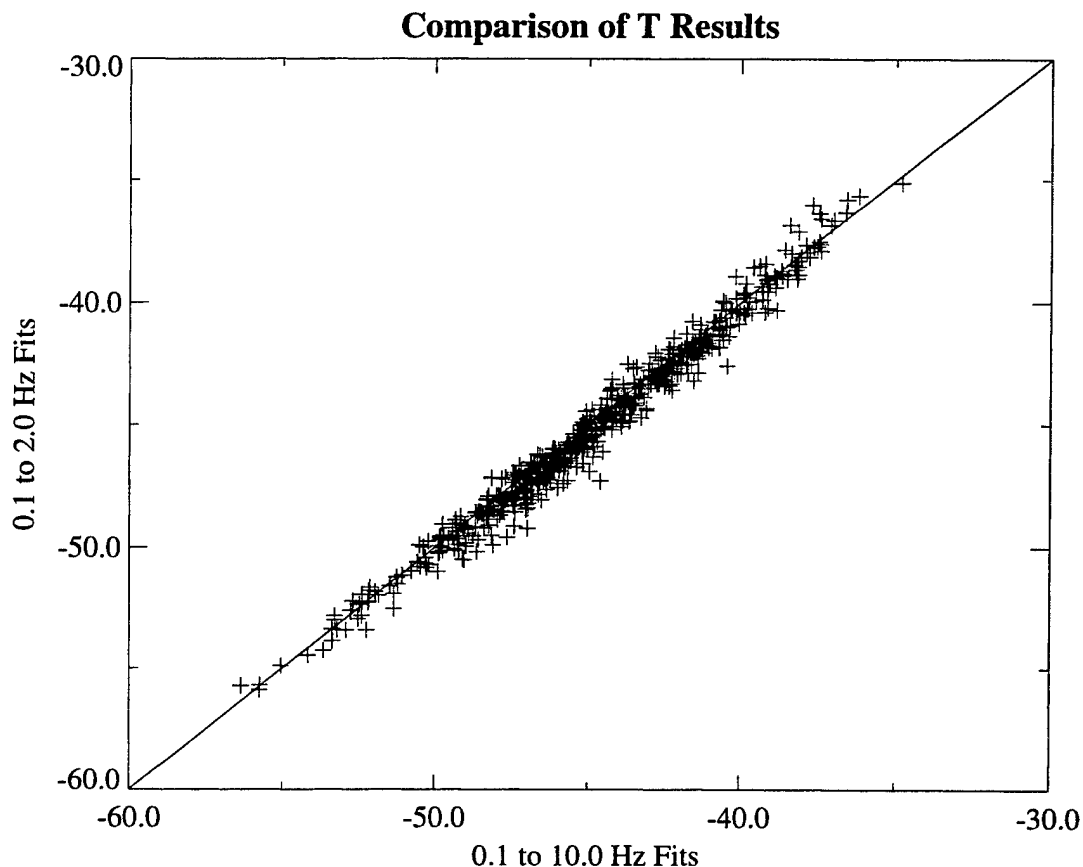


**Figure C-9.** Comparison of T calculated from the 0.1 to 2.0 Hz range (Y axis) to that calculated from the 0.1 to 10.0 Hz range (X axis).

We recommend that this issue be pursued further as more data become available. Two potential tests would be to use the GPS testbed at Wright-Patterson AFB (if the phase-noise problem identified in the last testing period can be corrected) or to collect data at mid-latitudes during the day when scintillation will be very low. This will allow more detailed study into this phenomenon in the absence of ionospheric effects. Once the non-ionospheric spectrum is better understood, a better algorithm for dealing with it can be developed and implemented in the operational IMS processing. [NOTE: See addendum to follow.]

Note that this analysis has not included discussion of the effects of multipath on the scintillation parameters, although there is evidence of these effects in the plots shown in Figure C-1. This issue is to be addressed in another task of this project, along with development of methods for mitigating these effects where possible or, at minimum, identifying when the results are contaminated by multipath.

Finally, as more data are collected from these systems there needs to be an ongoing study of how well the entire system is performing in its role as a scintillation monitor. It is impossible to assess this based on a single pass with no other data against which to corroborate the results.

#### **Addendum**

As will be described in Appendix D to this report, we were given the opportunity to investigate the issue of the odd behavior seen in the phase spectrum described in this appendix with data generated using the WPAFB hardware simulator. We now speculate that when the Ashtech Z-12

receiver is operating in Z-mode, internal processing of the phase data acts as a smoother which results in the loss of power at the smallest spectral scales. This leads to the effect noted in this appendix, wherein the spectral slope steepens as the strength of the scintillation increases and the power in high-frequency end of the spectrum remains nearly constant regardless of the scintillation level.

## **Appendix D**

### **GPS Scintillation Studies**

Three sets of data were analyzed during the course of this project looking at various issues relating to the performance of the IMS Ashtech Z-12 GPS receivers in the role of observing ionospheric scintillation. The first of these was a set of data collected at a testbed facility located at Wright-Patterson AFB in which a series of known scintillation signatures, both amplitude and phase, were applied to GPS signals generated by a GPS constellation simulator and passed to a Z-12 receiver. The goal was to assess the performance of the receiver in replicating known scintillation signals and severity levels. The second set of data was collected using the IMS located at Nashua, NH, which was used to investigate the noise levels in the receiver by observing the ionosphere during quiet (non-scintillation) conditions. The third set was collected by a pair of receivers located at Ascension Island, which was used to look at scintillation observations made during severe scintillation conditions and at the receiver behavior when it was operating in encrypted (Y) P-mode.

#### **D.1 Benchtop Testing at WPAFB**

The AFRL Sensors Directorate hardware-in-the-loop GPS Test Bed, located at Wright-Patterson AFB (WPAFB), was used for a series of tests with a spare IMS Ashtech Z-12 receiver during the period 3-5 September 2002. The tests were run by personnel at the WPAFB facility, primarily Mr. Dana Howell, and Dr. Ted Beach of AFRL Hanscom. The purpose of these tests was to determine whether this test system could be used to measure the performance of the Z-12 receivers in the role of scintillation measuring systems. Towards this end, NWRA provided two sets of simulated L-band scintillation records (L1 and L2 amplitude, L2 phase relative to L1): one set derived from a Wideband pass observed at Ancon, Peru, and a second set consisting of mono-frequency sine-wave "tones" with varying amplitudes and periods. Each of these two cases was run through the testbed twice: once with the receiver operating in Ashtech's proprietary Z-mode (Lorenz and Gourevitch, 1995), and once with the test-bed configured to force the receiver to operate in P-mode. The simulation was also run without any scintillation signal being imposed on the GPS signal being fed to the receiver, providing a total of six different cases: three scintillation types (none, Wideband simulation, tones) for each of two modes (Z-mode and P-mode). Note that while we would have liked to run the simulator in Y-mode on a keyed receiver, which is the most likely field scenario, this was not possible because the WPAFB simulator cannot operate in Y-mode.

This concept of forcing the receiver to operate in P-mode was the idea of Mr. Howell, and his serendipity paid off by answering questions we had previously about apparent phase-smoothing, as will be described later. This was accomplished by setting the anti-spoofing (AS) bit in the GPS NAV message generated by the simulator either ON (which induces the Z-12 to operate in Z-mode) or OFF (P-mode). The Z-mode operation is Ashtech's implementation of an algorithm to allow higher-precision navigation solutions when the GPS constellation is operating in encrypted (anti-spoofing) mode (Y-mode) without the use of a de-encrypting chipset. As will be shown, this algorithm has an effect on the signals made available by the Z-12 receiver for scintillation calculations. Note that while altering the mode in which the Z-12 operates can be accomplished in the lab, doing so works only because the signal generated by the WPAFB simulator is not encrypted, regardless of the setting of the AS bit. In the field, if the GPS constellation is operating in AS mode (which it is at present), the only choices are to operate the Z-12 in Z-mode or to upgrade them so that they can be keyed to operate in Y-mode.

All data shown in this report were derived from the 20-Hz data output by the Z-12 in FST and DEL data records. The data are the DCP between L1 and L2 and the intensity at L1.

### D.1.1 No Scintillation

The purpose of this part of the testing was to establish, if possible, the characteristics of noise in the Z-12 receiver in the absence of scintillation. The phase and intensity data from one PRN (PRN 08) for both Z- and P-mode data sets were processed using the standard scintillation processing software to obtain detrended time-series and spectra of both phase and intensity.

Figure D-1 shows representative samples of data from both modes. In this figure, the top plot in each of the four panels is a 51.2-second data sample (1024 data points) of detrended phase and the bottom plot is the power-density spectrum generated from that data sample. The straight line plotted over the spectra is the result of a least-squares fit to the spectrum in  $\log(\text{frequency})$  and  $\log(\text{density})$  over the frequency range 0.01 to 10.0 Hz. The T (spectral strength at 1 Hz) and p (slope) parameters from this fit are shown in the lower-left corner of the spectrum plot. The top two panels show data from P-mode operation, and the lower two from Z-mode. It is apparent from both the time-series plots and the spectrum plots that the Z-mode algorithms are modifying the DCP in some sort of smoothing or filtering fashion. The RMS phase values (shown in the lower-left corner of the time-series plots), which are  $\sigma_\phi$ , reflect the noisier nature of the P-mode data, and the values for these four samples (0.04 rad for P-mode; 0.02 rad for Z-mode) are fairly representative of the data sets processed. The spectral slopes shown (near zero for P-mode; between 1.7 and 1.9 for Z-mode) were also representative of the data processed.

The situation is different for the intensity data, shown in Figure D-2. The layout for this figure is the same as for Figure D-1. The two modes give very similar results for intensity, with a bit more irregular structure in the Z-mode time-series records. This does not markedly affect the  $S_4$  values, shown as the RMS value in the lower-left corner of the time-series plots. For both modes, the mean  $S_4$  for the data set was around 0.03. This extra high-frequency structure in the Z-mode data is interesting, and it shows up also in the spectra as a small upward tic in the last bin of the spectrum in both of the plots shown in Figure D-2 (and in all spectra inspected from this data sample). Figure D-3 is an expanded view of 10 seconds of data from the central portion of the records shown in panels (b) and (d) of Figure D-2. This extra structure is evident in a high-frequency, nearly point-to-point (at 20 Hz), fluctuation in the Z-mode data which is absent from the P-mode data. It is not clear what the source of this might be.

### D.1.2 Wideband Simulation

One set of scintillation modulation provided to WPAFB for this testing was based on data from a Wideband pass collected at Ancon, Peru, on 11 February 1977 (pass identifier AN-0424). The WPAFB simulator has a limitation that the phase signal imposed on the GPS signals cannot exceed the range  $\pm\pi$  radians. This particular data set exceeded that range, so the phase and intensity data were normalized so that the phase was constrained to this range (using a simple scaling) and the intensity was reduced to be not-inconsistent with the phase. Figure D-4 shows the intensity at L1 (top panel) and phase (bottom panel) provided to WPAFB. We also provided L2 intensity, which was just a simple downward scaling in frequency from the L1 time-series shown in Figure D-4. As in the no-scintillation case described above, we processed data from this simulation collected in both Z-mode and P-mode.



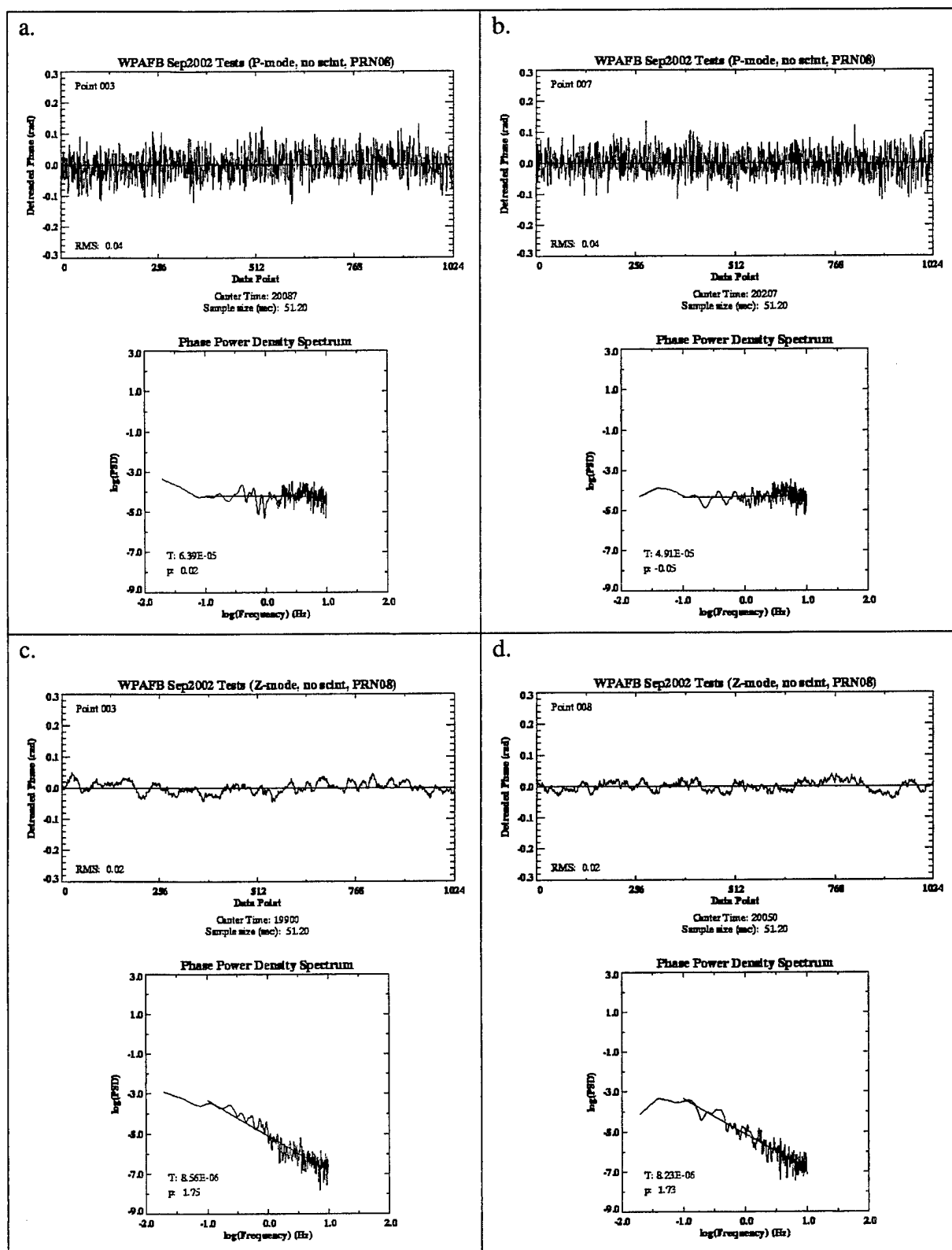
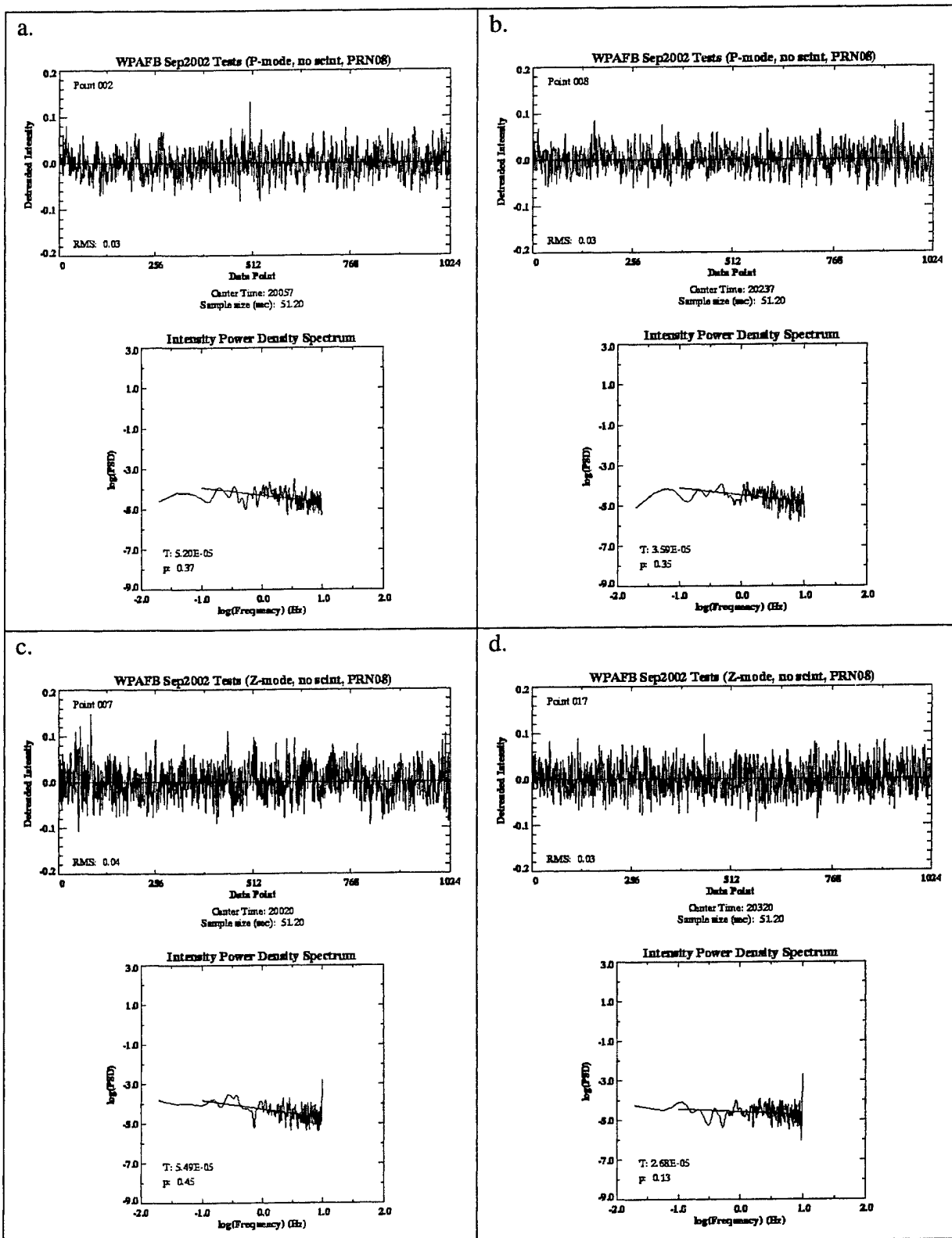
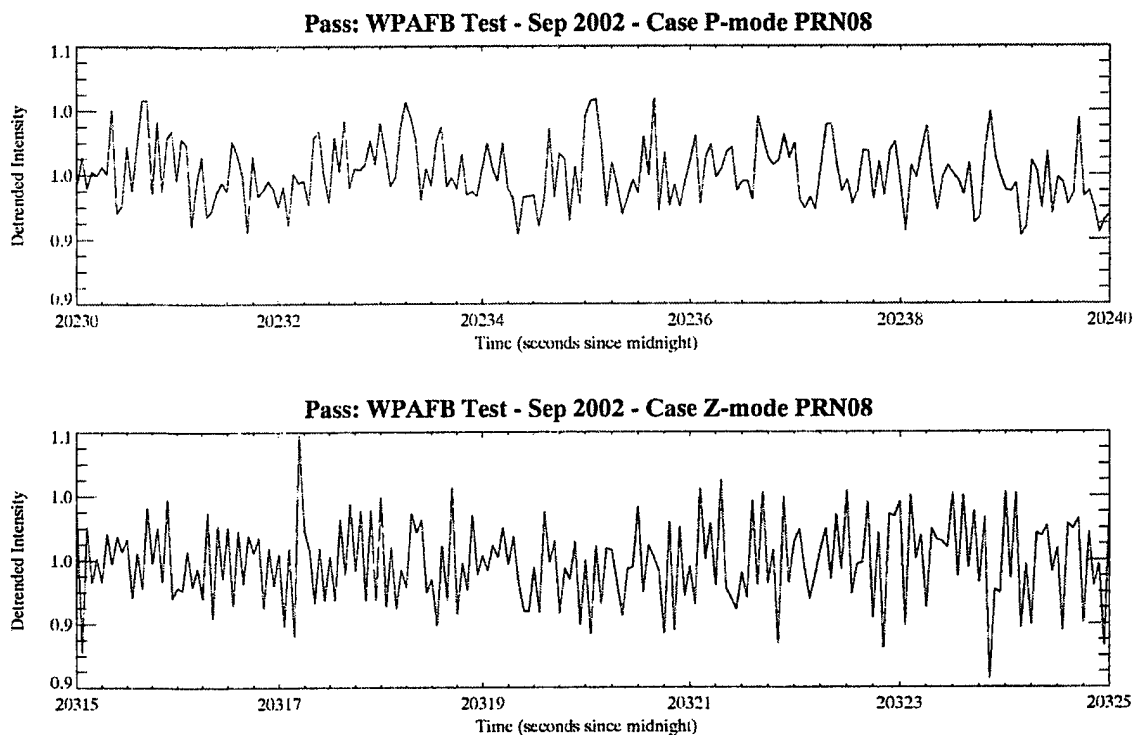


Figure D-1. Examples of phase time-series and spectrum from no-scintillation cases. Plots (a) and (b) are data collected in P-mode, and plots (c) and (d) are Z-mode.



**Figure D-2.** Examples of intensity time-series and spectrum from no-scintillation cases. Plots (a) and (b) are data collected in P-mode, and plots (c) and (d) are Z-mode.



**Figure D-3.** Time-series plots of 10 seconds of detrended intensity data from the center of the time-series records shown in Figure D.2 (plots (b) and (d)).

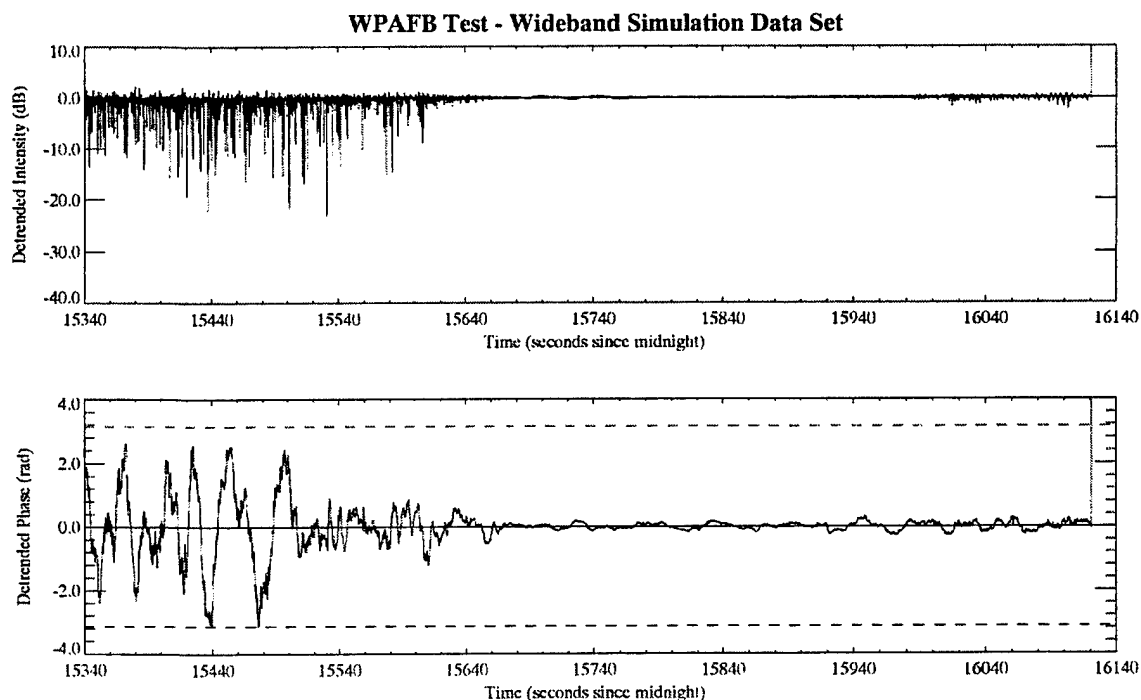


**Figure D-4.** The L1 intensity (top plot) and DCP (bottom plot) generated from a Wideband Ancon pass for use in the WPAFB GPS testing. The dashed lines in the DCP plot indicate the  $\pm\pi$  radian limit on phase fluctuations imposed by the WPAFB simulator.

### D.1.2.1 Phase Results

Figure D-5 shows the detrended phase (DCP) results. The top plot is the input signal derived from the Wideband data set, the middle plot is the DCP calculated from the 20-Hz P-mode data, and the bottom plot is the DCP calculated from the 20-Hz Z-mode data. While both of the receiver-output results show a good replication of the input signal, the P-mode noise and Z-mode smoothing are evident as well. Both of these phenomena can be clearly seen in Figure D-6, which is a 100-second sub-sample of the data in Figure D-5.

These data are to be used to calculate estimates of the  $\sigma_\phi$  phase-scintillation index and the T and p phase spectrum parameters (the phase spectral strength at 1Hz and the phase spectral slope, respectively). These parameters were calculated from 1024-sample (51.2 second) data samples with the results shown in Figure D-7. The T and p parameters were derived from fits to the phase spectrum over the frequency range 0.01 to 2.0 Hz. In all three figures, the results from the input simulation are shown as a heavy solid curve, P-mode a dashed curve, and Z-mode a dotted curve. A more detailed look at these results is provided in Figures D-8 and D-9, which show the phase spectra from all three sets generated from a segment during high (Figure D-8) and low (Figure D-9) scintillation levels.

Starting with the  $\sigma_\phi$  results, both P-mode and Z-mode track the values calculated from the input simulation quite well. The largest differences, located near the peak values, are due to slight differences in the detrending process that results in differences in the effect of the detrender on the low-frequency part of the spectrum in one time-series and not in another. Since there is more power at the lower frequency section of the spectrum, this results in larger (or smaller)  $\sigma_\phi$  values for fairly small differences in the appearance of the spectrum. This high sensitivity to how the low-frequency part of the phase spectrum is handled is a well-known problem with the  $\sigma_\phi$  parameter. It adds a certain amount of uncertainty to any  $\sigma_\phi$  estimate, and we believe the results shown in Figure D-7 are within the expected uncertainty.

The T and p results are quite different from the  $\sigma_\phi$  results, but both are consistent with the qualitative picture of the differences in the Z-mode and P-mode phase data we have constructed up to this point. Roughly speaking, the P-mode results are better in the section where scintillation levels are high, and the Z-mode results are better in the section where the levels are low. The two sets of spectrum plots in Figures D-8 and D-9 provide representative examples of these two regimes.

Looking first at Figure D-8, the spectrum generated from the P-mode data can be seen to be very similar to that derived from the simulation data directly. There is a bit of extra noise at the higher frequencies (as can also be just-barely seen in the time-series plot), but it is not significant. The Z-mode spectrum and the corresponding time-series record tell a different story. Here there is obviously some process going on within the receiver (most likely) in Z-mode that acts as a smoother with a response that is a function of the (fluctuation) frequency with the most severe impact seen in loss of power at the highest frequencies by several tens of dB. This results in a much steeper spectrum (higher p) and lower power-levels at 1Hz (T) as is seen in the results plotted in Figure D-7.

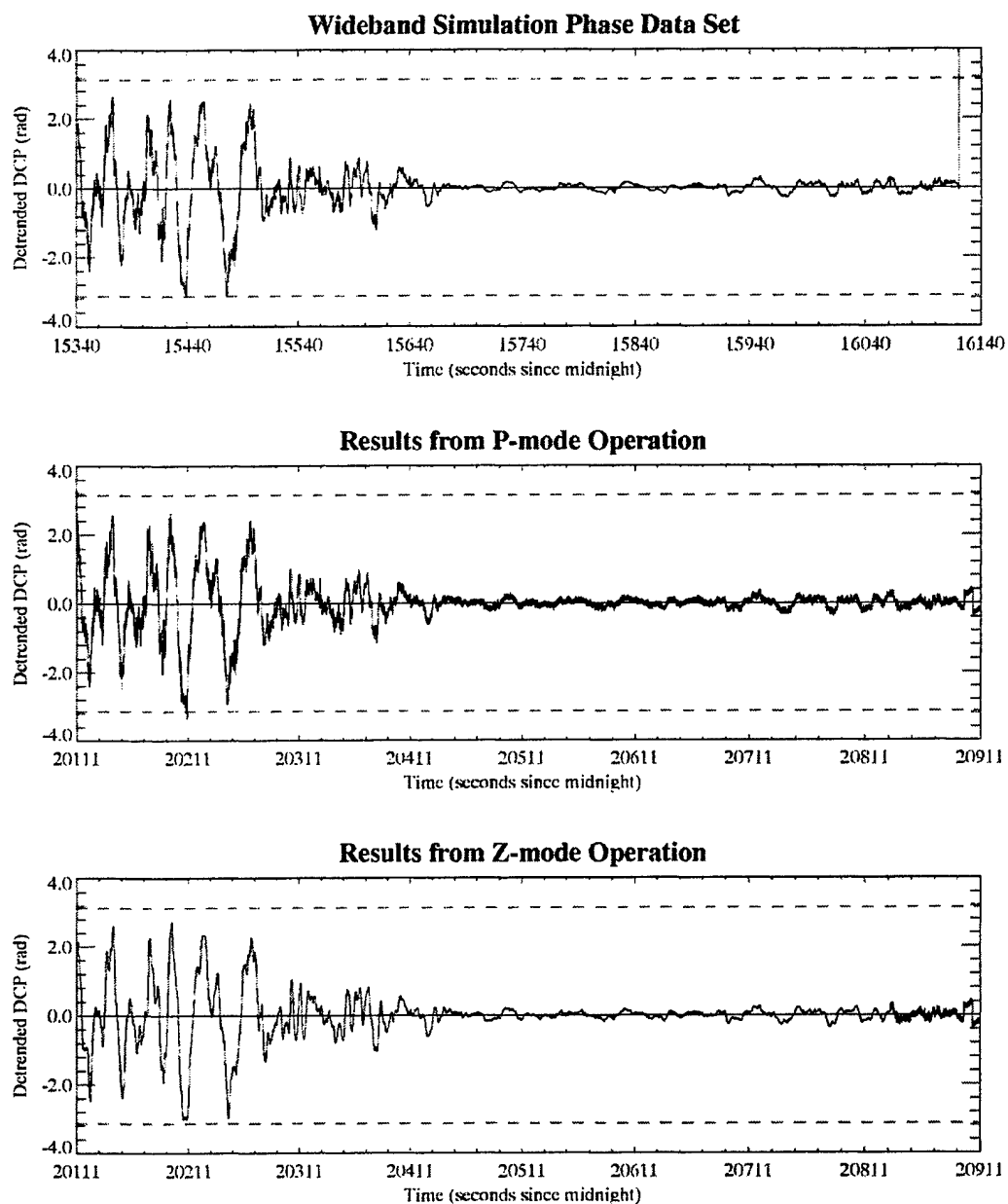


**Figure D-5.** Phase (DCP) results from the Wideband simulation data set. The top panel is the DCP signal provided to the WPAFB simulator, the middle panel is the DCP derived from the P-mode data, and the bottom panel is the DCP derived from the Z-mode data.

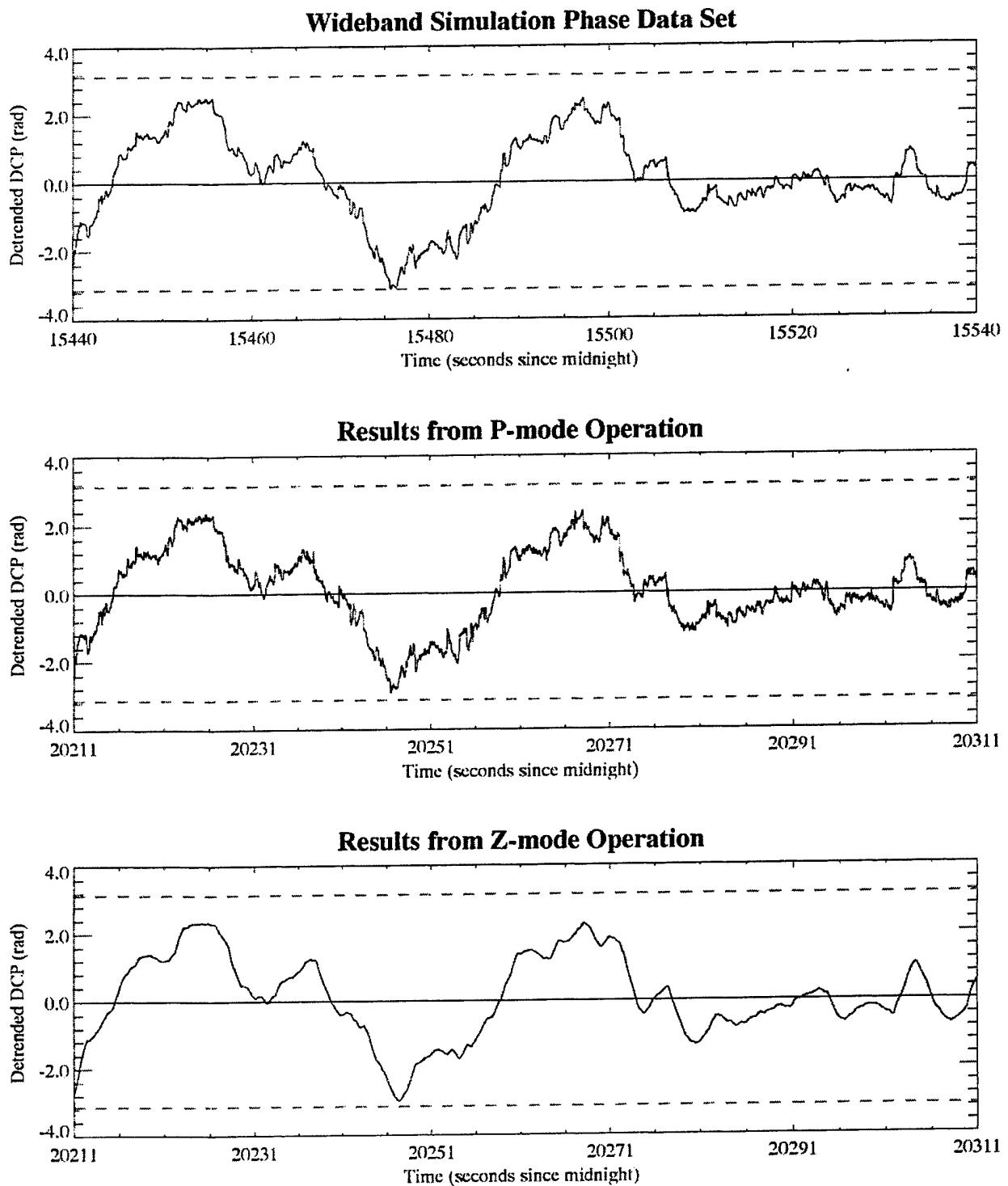


**Figure D-6.** Reduced time-span plot of phase (DCP) data plotted in Figure D-5.

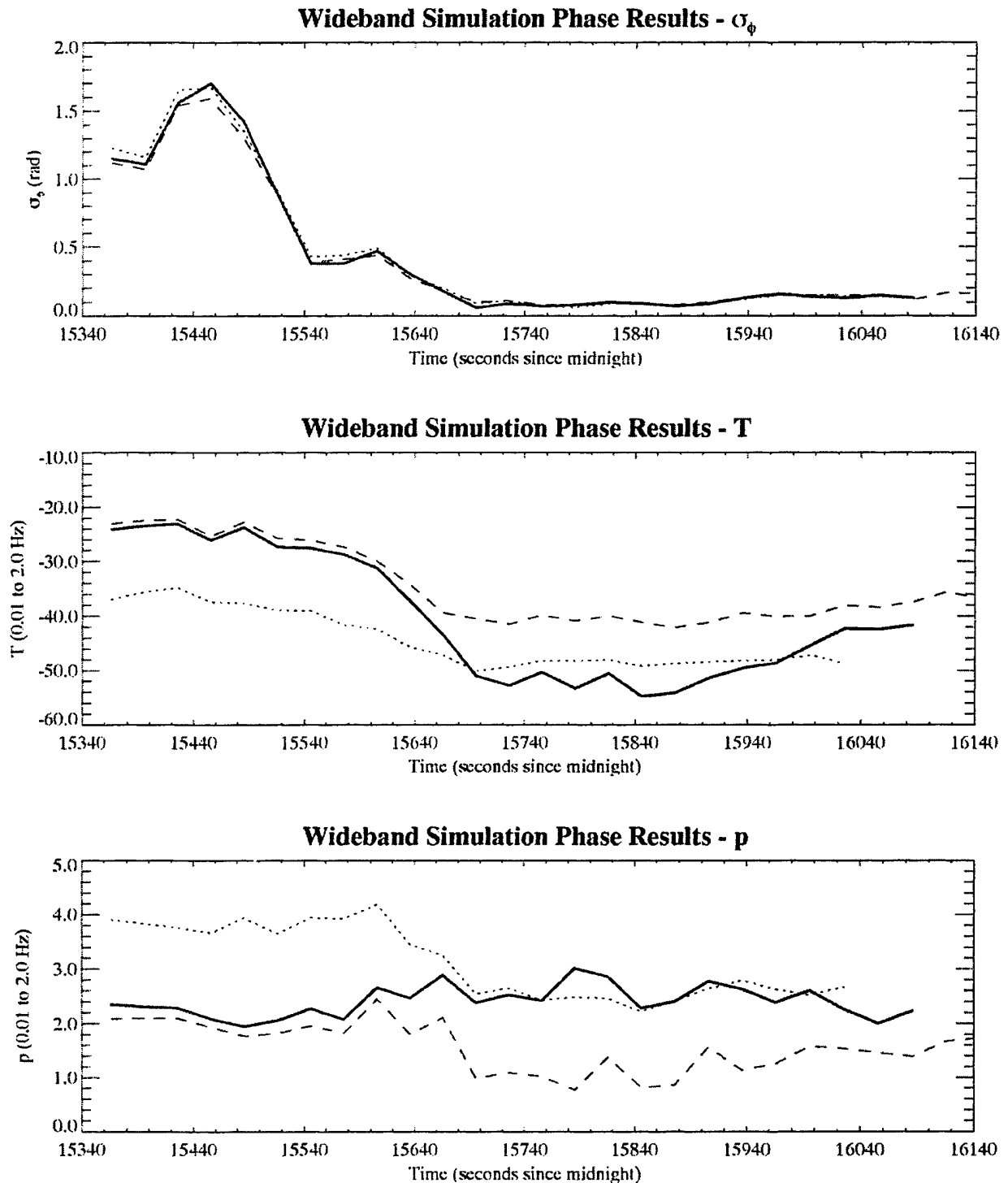


**Figure D-7.** Phase scintillation parameters calculated from the phase (DCP) time-series records shown in Figure D-5. Top plot is  $\sigma_\phi$ , middle plot is the phase spectrum parameter T (the spectral density at 1Hz), and the lower plot is the phase spectrum slope, p. In all three plots, the heavy solid line is from the simulation data, the dashed line is P-mode, and the dotted line is Z-mode.

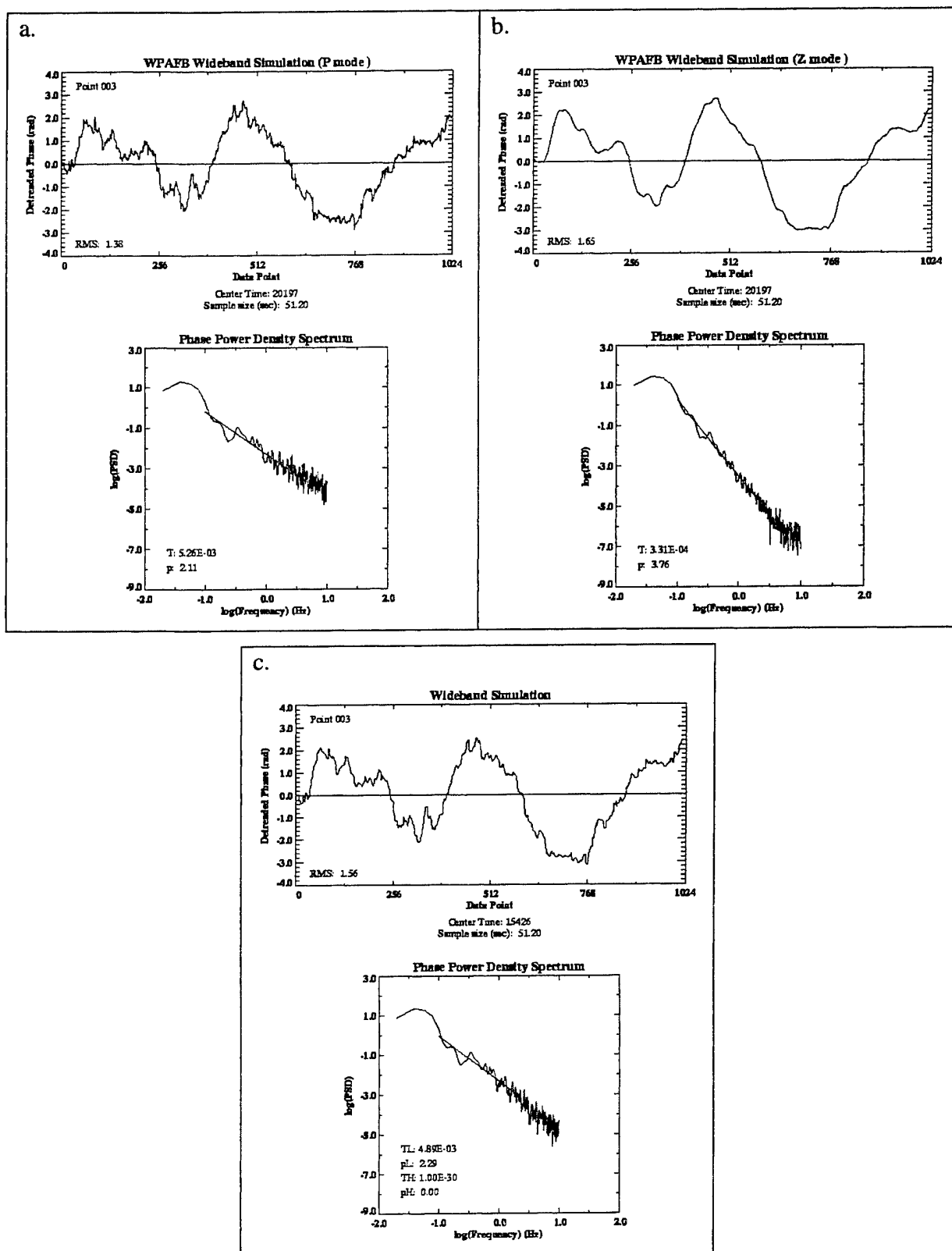


**Figure D-8.** Phase (DCP) spectra from a 51.2-second data sample centered at time 15426 (simulation-record time) from the time-series records shown in Figure D-5. The plot in panel (a) is from the P-mode set, (b) is from the Z-mode set, and (c) is from the simulation input.



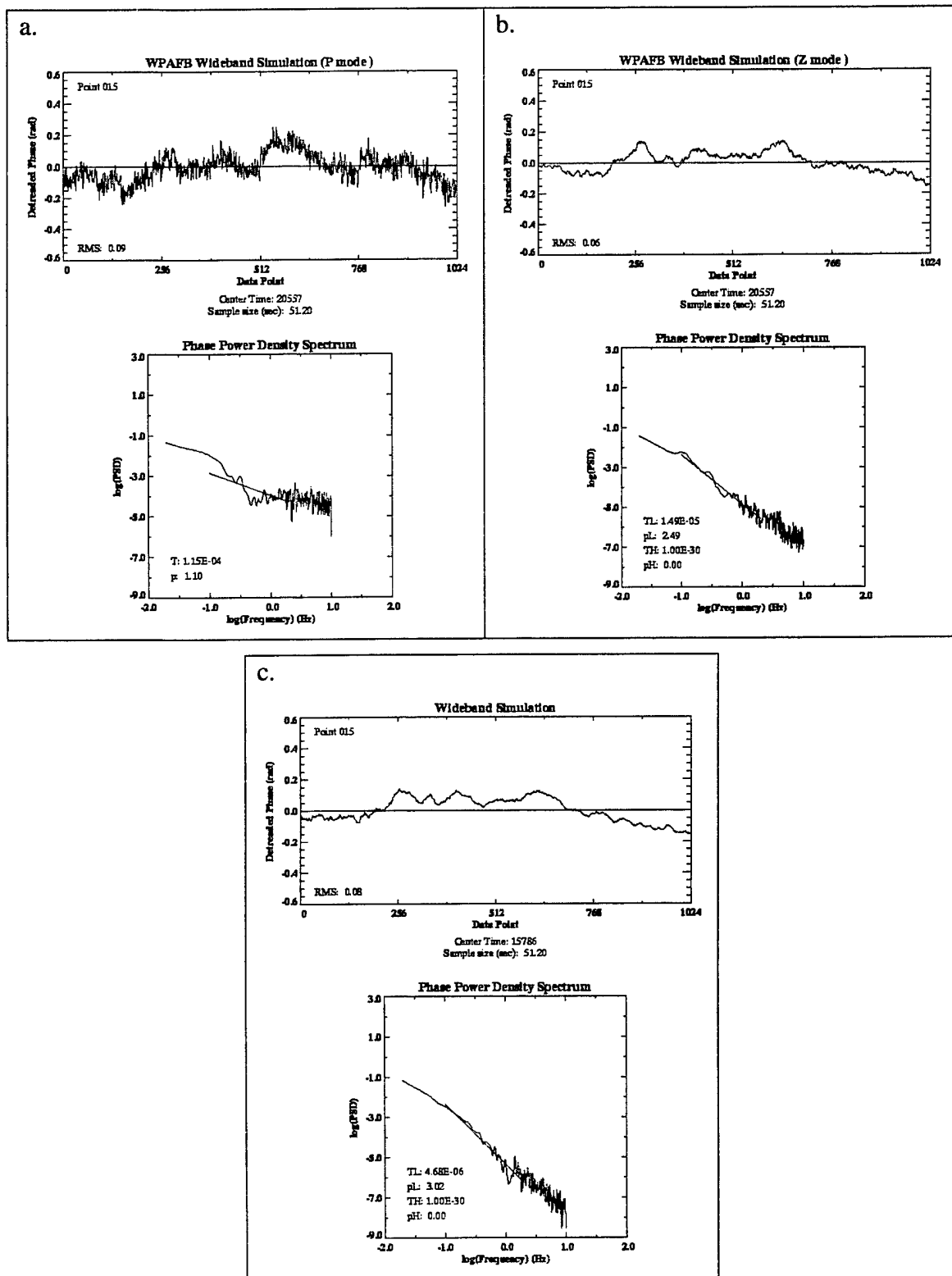


**Figure D-9.** Phase (DCP) spectra from a 51.2-second data sample centered at time 15786 (simulation-record time) from the time-series records shown in Figure D-5. The plot in panel (a) is from the P-mode set, (b) is from the Z-mode set, and (c) is from the simulation input.

Moving on to the low-scintillation case shown in Figure D-9, the source of loss of accuracy in the P-mode data can be clearly seen to be the loss of usable spectrum as it drops below the high (relative to Z-mode) noise floor as observed in the no-scintillation data described earlier. The Z-mode spectrum, on the other hand, seems to have fallen below some threshold below which whatever process is affecting the DCP data in Figure D-8 acts. The high-frequency end of the spectrum is nearly identical with that in Figure D-8, and in fact it hardly varies throughout this entire sample (a similar effect was seen in a pass collected at Qaanaaq, Greenland, which was in Z-mode). This behavior may then result in the good agreement between the Z-mode T and p values when the scintillation levels were low strictly by coincidence for this particular case. This may not be the case, however, because the agreement between low-frequency portions of the simulation and the Z-mode spectra is quite good.

In summary, we see phase results that are consistent with what we found in the no-scintillation data sets, that there is increased high-frequency noise in the P-mode data and some type of smoothing being applied to the Z-mode data by (we assume) processing inside the Z-12 receiver. This results in the P-mode data yielding the best spectral results when scintillation levels are high and Z-mode doing better when they are low. Whether or not we can apply the P-mode results to the field situation where we will be dealing with either Z-mode or Y-mode (if the receivers are all keyed) is not clear. We will revisit this question in the later section describing analysis of Y-mode data collected recently at Ascension Island.

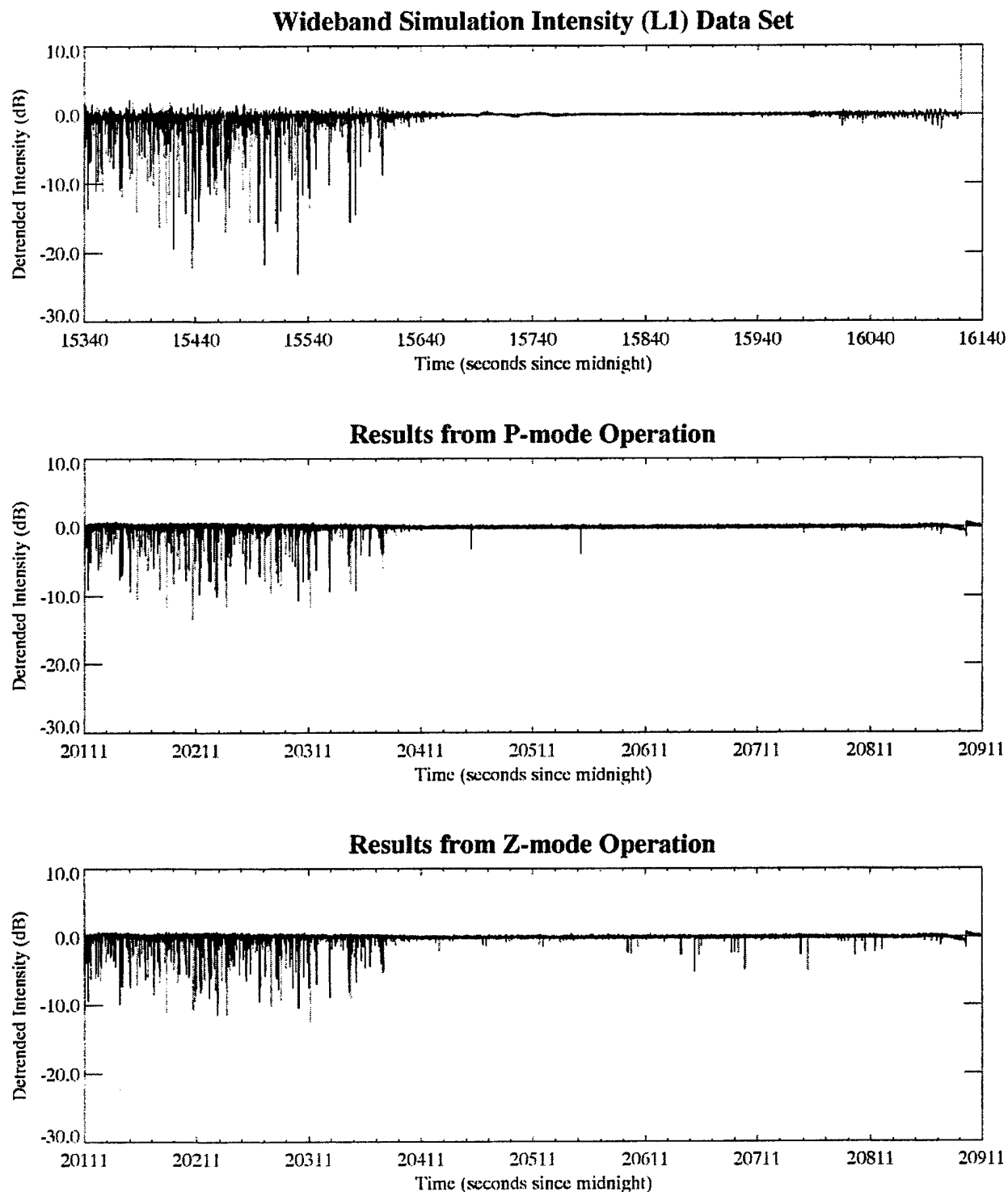
#### *D.1.2.2 Intensity Results*

Figure D-10 shows the detrended L1 intensity data from this test. The top plot is the input signal derived from the Wideband data set, the middle plot is the L1 signal calculated from the 20-Hz P-mode data, and the bottom plot is the L1 signal calculated from the 20-Hz Z-mode data. While it appears that there was little, if any, identifiable contamination of the phase data from the WPAFB GPS simulator system, it seems clear that something happened to the intensity data. This can be seen in Figure D-10 in the lower fade levels in the P-mode and Z-mode outputs than in the original record, a point that is even clearer in Figure D-11 which shows the same 100 sec of data shown in Figure D-6. While the pattern of fades is similar, the fade depths are much less. Another issue can be seen more clearly in Figure D-12, which shows the intensity data from Figure D-13 plotted as intensity rather than in dB. There are clear enhancements of the signal seen in the simulation data at the top of this figure, which all but disappear in the two receiver output plots.

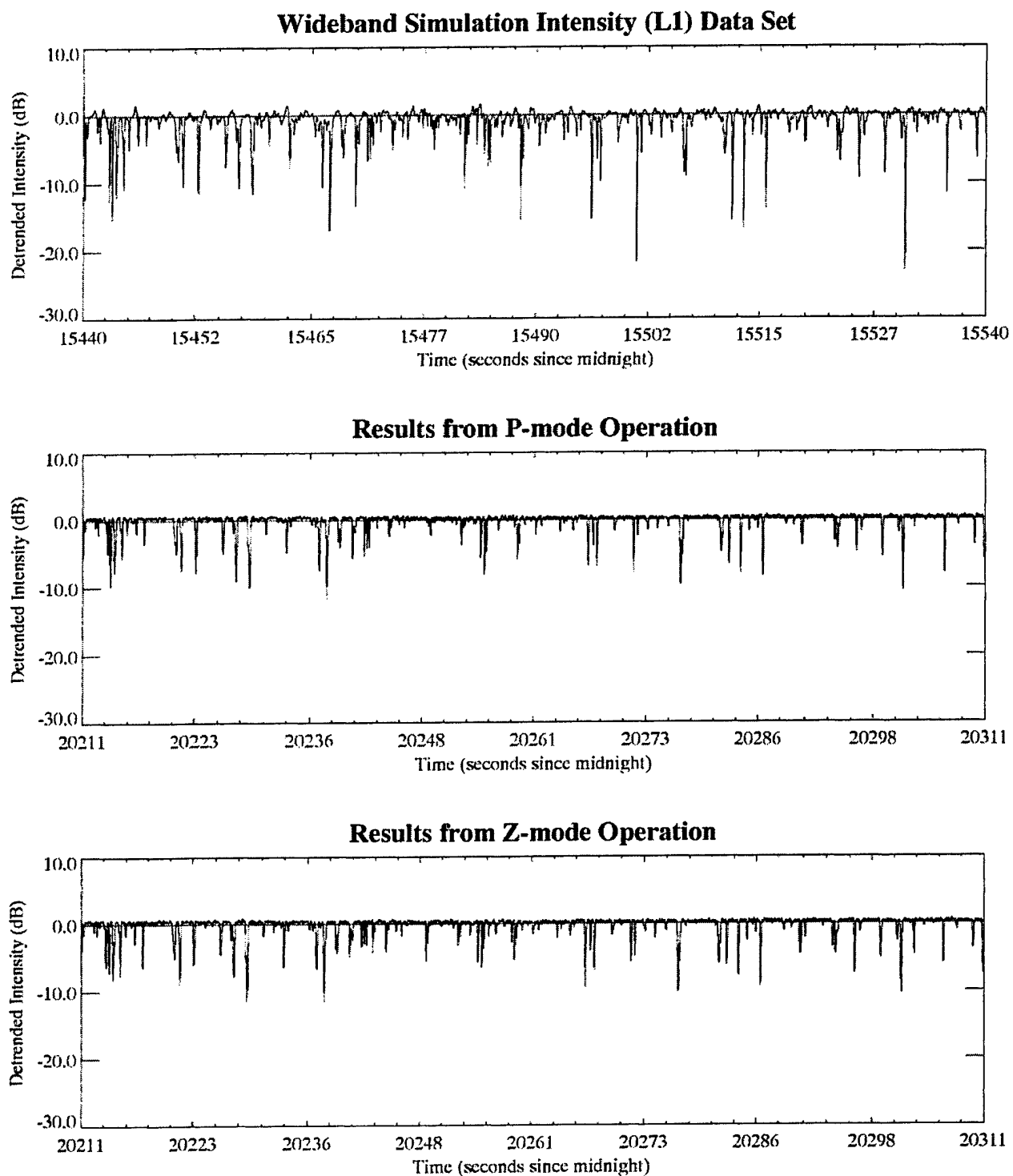
The situation is actually a bit more complex, as can be seen in Figure D-13, which shows a 10-sec sample from all three sets. Note that not only are the signal enhancements missing, but also the larger enhancements (near time 15380/20151 and 15383/20154) appear to be "folded over" into fades. The reduction in the fade levels is also evident, particularly in the deep fades just after 15380/20151 and just prior to 15383/20154. As we will show later, this effect was also seen in the "tones" data set. We are not certain as to the source of this effect. The data were processed by two independent codes to ensure that there was not a problem in the processing code, and we believe we have ruled out that possibility.

Figure D-14 shows the  $S_4$  values calculated from the data records shown in Figure D-10. As should be expected given the reduction in both fades and enhancements seen in previous plots, the  $S_4$  values from the receiver outputs is generally low by 10-15 percent during the early part of the data when scintillation levels were high. The agreement later in the set when levels are low may simply be due to similar statistics in the noise floor and the low-levels of scintillation imposed on the signals in that section. Until the source of these apparent artifacts is determined, it is difficult to

make any assessment of the performance of the intensity data in either Z- or P-mode from these tests.



**Figure D-10.** Intensity (L1) results from the Wideband simulation data set. The top panel is the L1 intensity signal provided to the WPAFB simulator, the middle panel is the L1 intensity derived from the P-mode data, and the bottom panel is the L1 intensity derived from the Z-mode data.



**Figure D-11.** Reduced time-span plot of L1 intensity data plotted in Figure D-10. This is the same time interval plotted in Figure D-6.

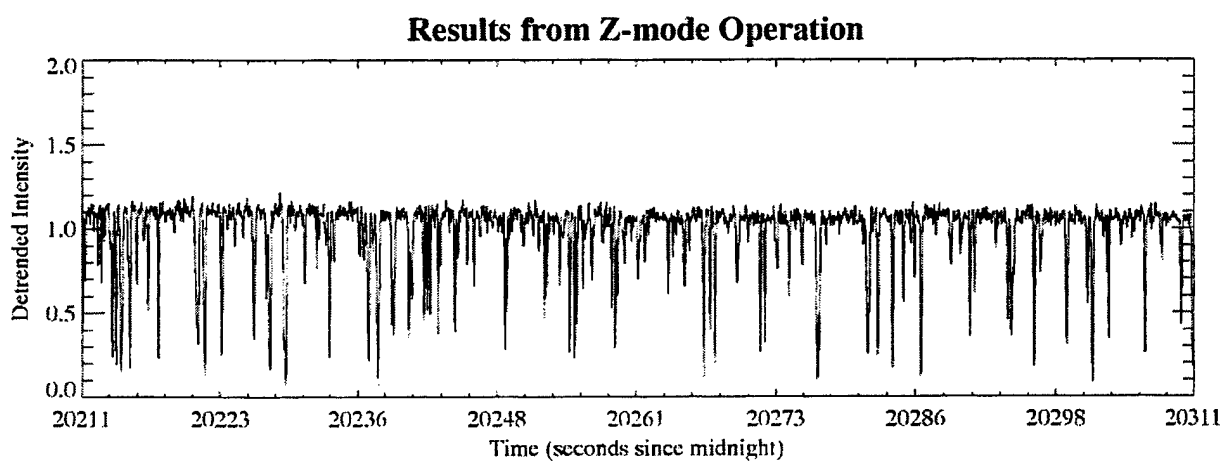
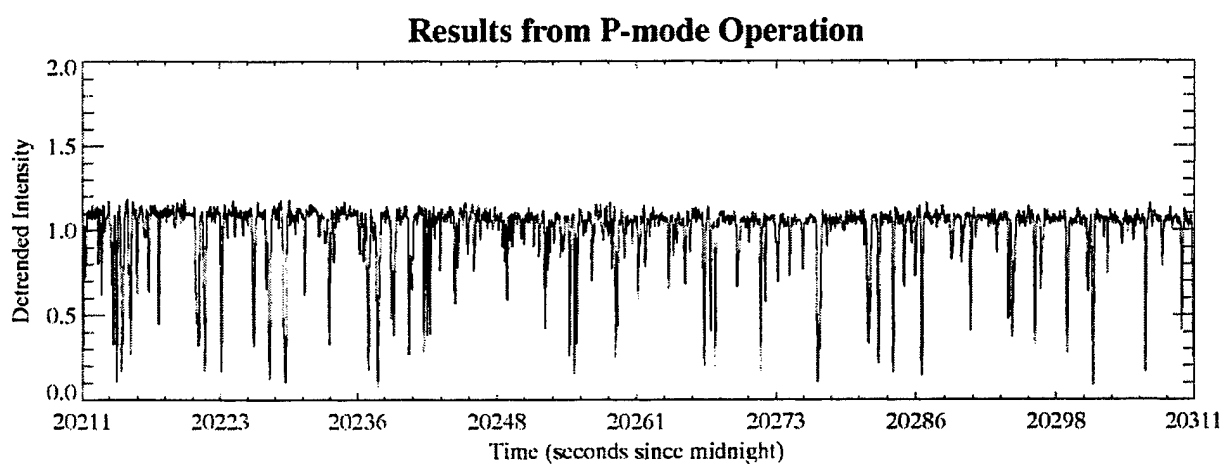
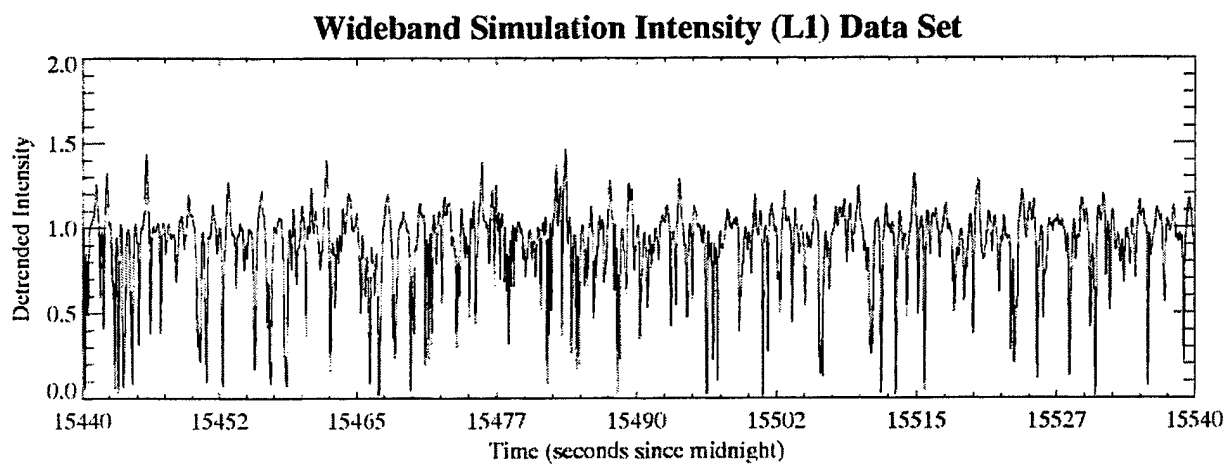


**Figure D-12.** Same data plotted in Figure D-11, but plotted as normalized intensity rather than in dB.

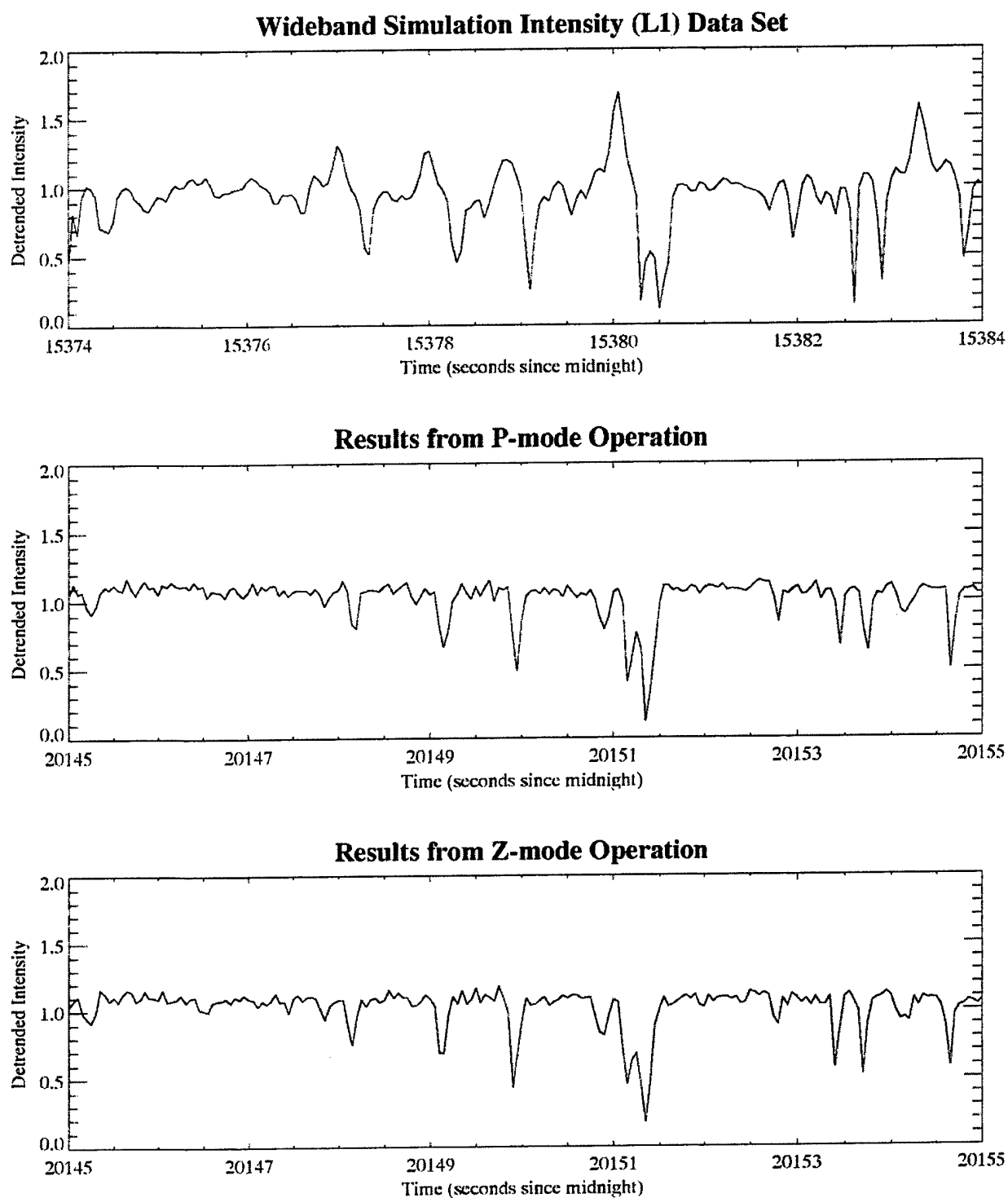


**Figure D-13.** A ten-second data sample extracted from the data shown in Figure D-10. Note that this is also plotted as normalized intensity rather than in dB.

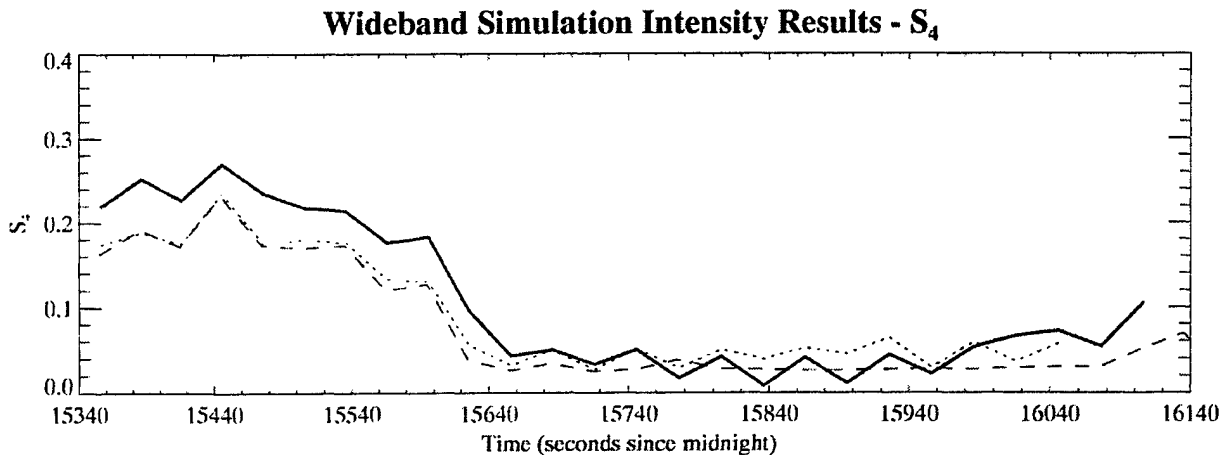


**Figure D-14.** The  $S_4$  intensity scintillation parameter calculated from the L1 intensity time-series records shown in Figure D-10. The heavy solid line is from the simulation data, the dashed line is P-mode, and the dotted line is Z-mode.

#### D.1.3 Tones Simulation

The tones simulation set was a set of DCP and L1 and L2 intensity values generated using simple sine-wave curves with various amplitudes and frequencies. The results from these add little to what has already been shown, and there were some serious problems with these data as will be described, but we will present a summary of the results and some suggestions for redoing this experiment if the WPAFB GPS test system be used again in the future for this sort of testing.

Figure D-15 shows a section of the phase records from the tones simulation testing. As will be discussed later, these plots actually start with the second set of sine functions in the full set. In both P- and Z-mode, the very deep and very long fades in the intensity oscillation (on the order of 30dB for many seconds) forced the receivers to lose lock on the signals. The results were either no signal or a very hard-to-interpret result. This can be seen in Figure D-16, which shows in the bottom two figures the phase trend that was removed from the receiver output DCP records to obtain the detrended records shown in Figure D-15. There is a small amount of phase oscillation in the P-mode data (an oscillation which was not part of the simulation record), but a very large oscillation at the start of the Z-mode record (note the change in scale along the Y-axis for this plot). We believe that this large phase trend at the start of the Z-mode record was due to problems the receiver was having with the large fades at the start of this simulation.

In looking at Figure D-15, one can see that the receiver outputs were, by and large, replicating the input simulation. However, the fidelity of the reproduction is not nearly as good as was seen with the Wideband simulation set in either P-mode or Z-mode, although the P-mode set is a better match up until the point where the noise inherent to the P-mode operation swamps the simulation signal. Another issue, and one that may have some bearing on the issues of phase smoothing evident in the analyses presented earlier, is illustrated in Figure D-17. This is an expanded plot of a transition from an oscillation with an amplitude of 0.5 radians to one of 0.2 radians. The P-mode observation retains this amplitude (imposed on a non-simulation low-frequency oscillation), but the amplitude of the Z-mode data is only about 0.1 radians. The source of this is unclear, but it might be a signature of what the Z-mode processing is doing to the phase data. Another possibility is that the simulation run inadvertently jumped ahead to the next section which does have an amplitude of 0.1 radians, but the frequency of the oscillation in that section also changes, so that scenario is unlikely.

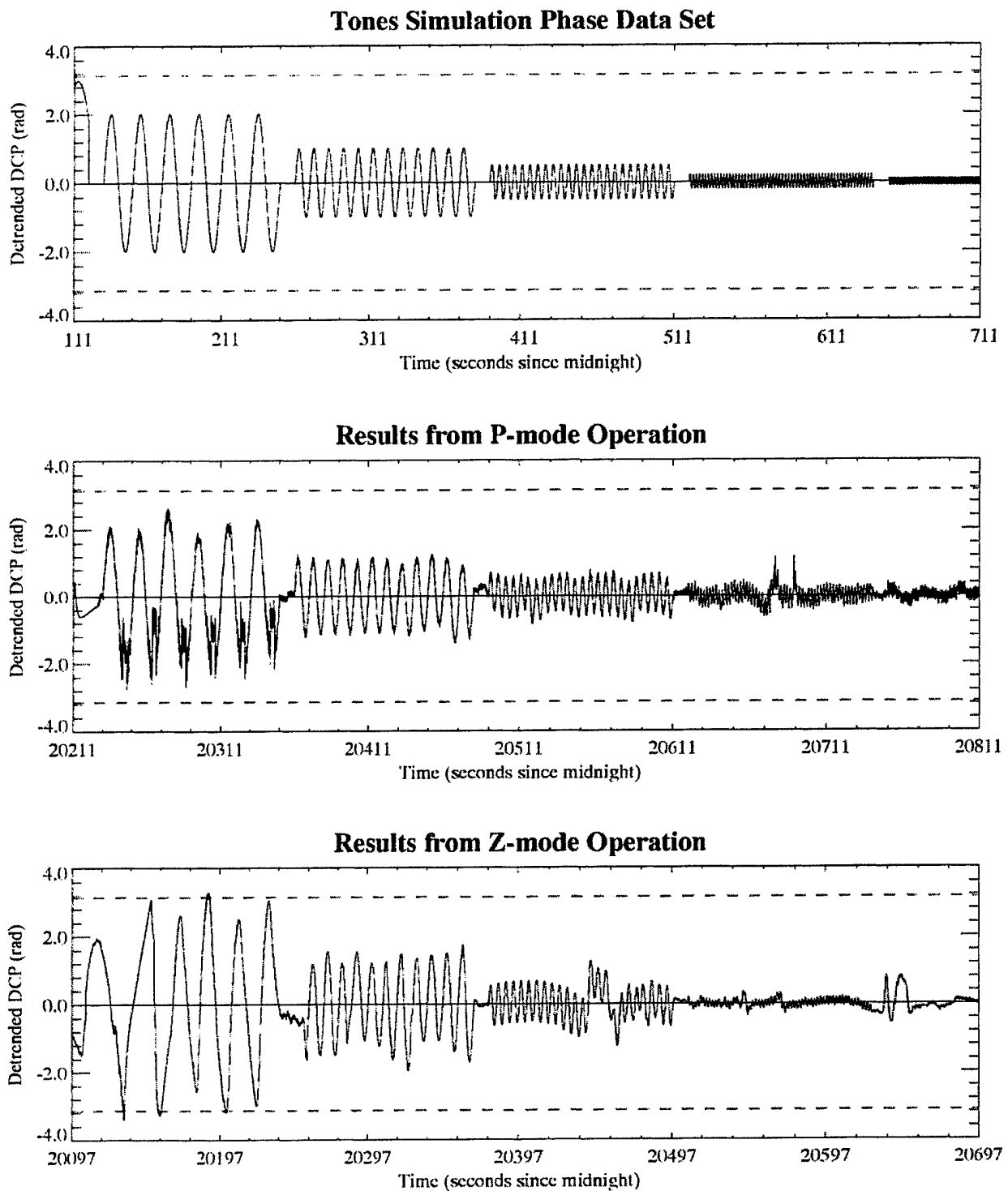


**Figure D-15.** Phase (DCP) results from the tones simulation data set. The top panel is the DCP signal provided to the WPAFB simulator, the middle panel is the DCP derived from the P-mode data, and the bottom panel is the DCP derived from the Z-mode data.



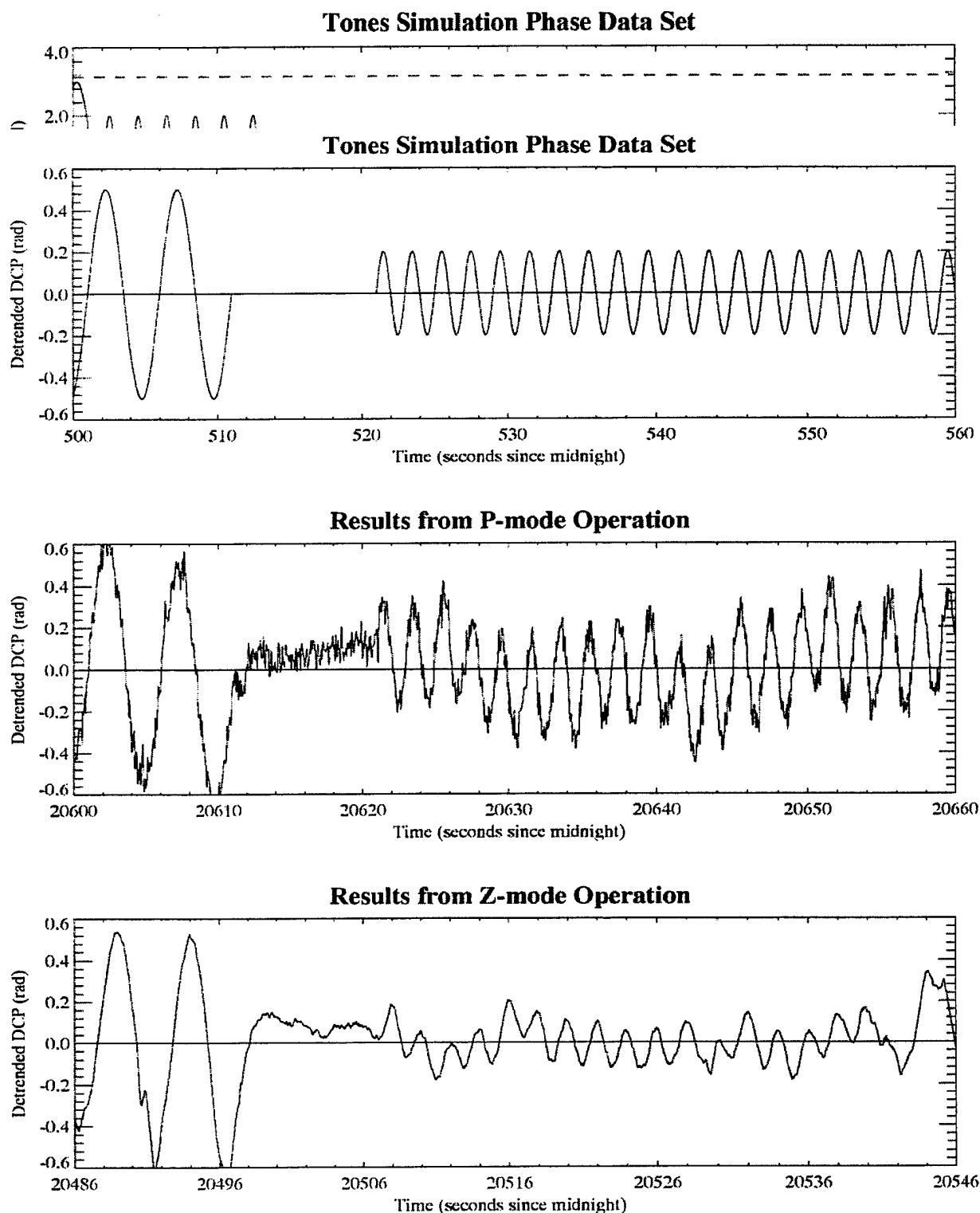


**Figure D-16.** Phase (DCP) trends removed from the P-mode (middle plot) and Z-mode (bottom plot) data to produce the detrended-phase records in Figure D-15.

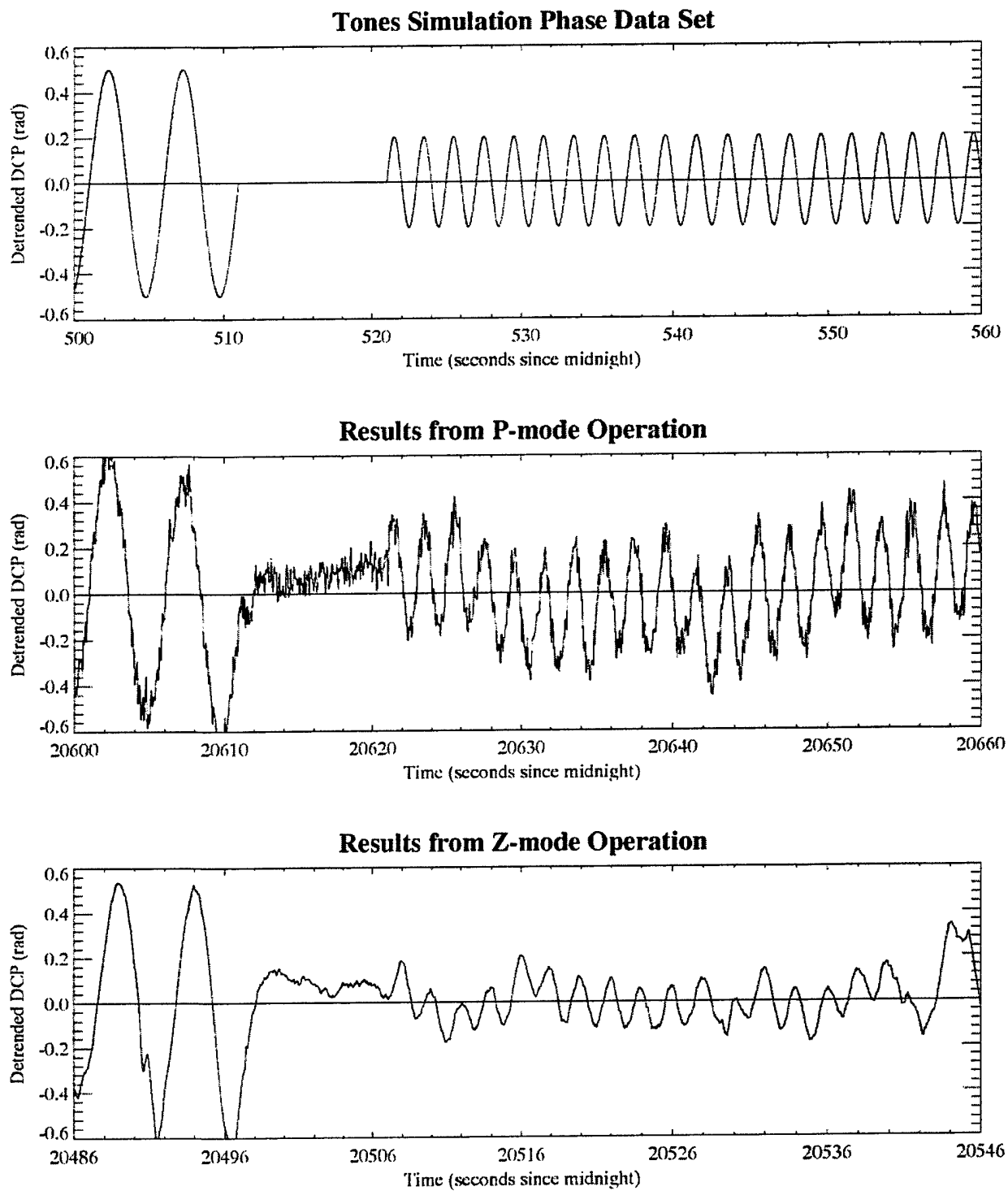


**Figure D-17.** A subset of the phase (DCP) data shown in Figure D-15.

The situation is even less clear with the intensity results, although again they are consistent with what was found in the analysis of the Wideband simulation. Figure D-18 shows the L1 intensity data for the same time span as Figure D-15. Again, this segment starts with the second case in the tones set. Two items of note are (1) again, there is serious clipping or folding-over for intensity enhancements, and (2) all evidence of the simulation oscillation disappears after the first set shown in Figure D-18. Both of these points are clearly shown in Figure D-19 which shows the full 120 sec of the second and third cases in the tones simulation with the input simulation shown as a light line and the P-mode results as a heavy line. The intensity appears to follow the fades fairly well in the upper plot, although the folding-over of the intensity enhancements is very evident. There is no evidence at all of any signal showing in the P-mode (or Z-mode) for the third case shown in the lower plot.

There was little clear value in this particular simulation test, although it did agree with findings from the Wideband simulation. It did confirm that there is some process, most likely within the WPAFB simulation but possibly in the receiver, that is clipping intensity enhancements or "folding" them over into intensity fades. We learned that care must be taken in how deep and how long a fade we construct in this sort of test, and we should probably (if this test is run again) modulate only phase or intensity in a given test.

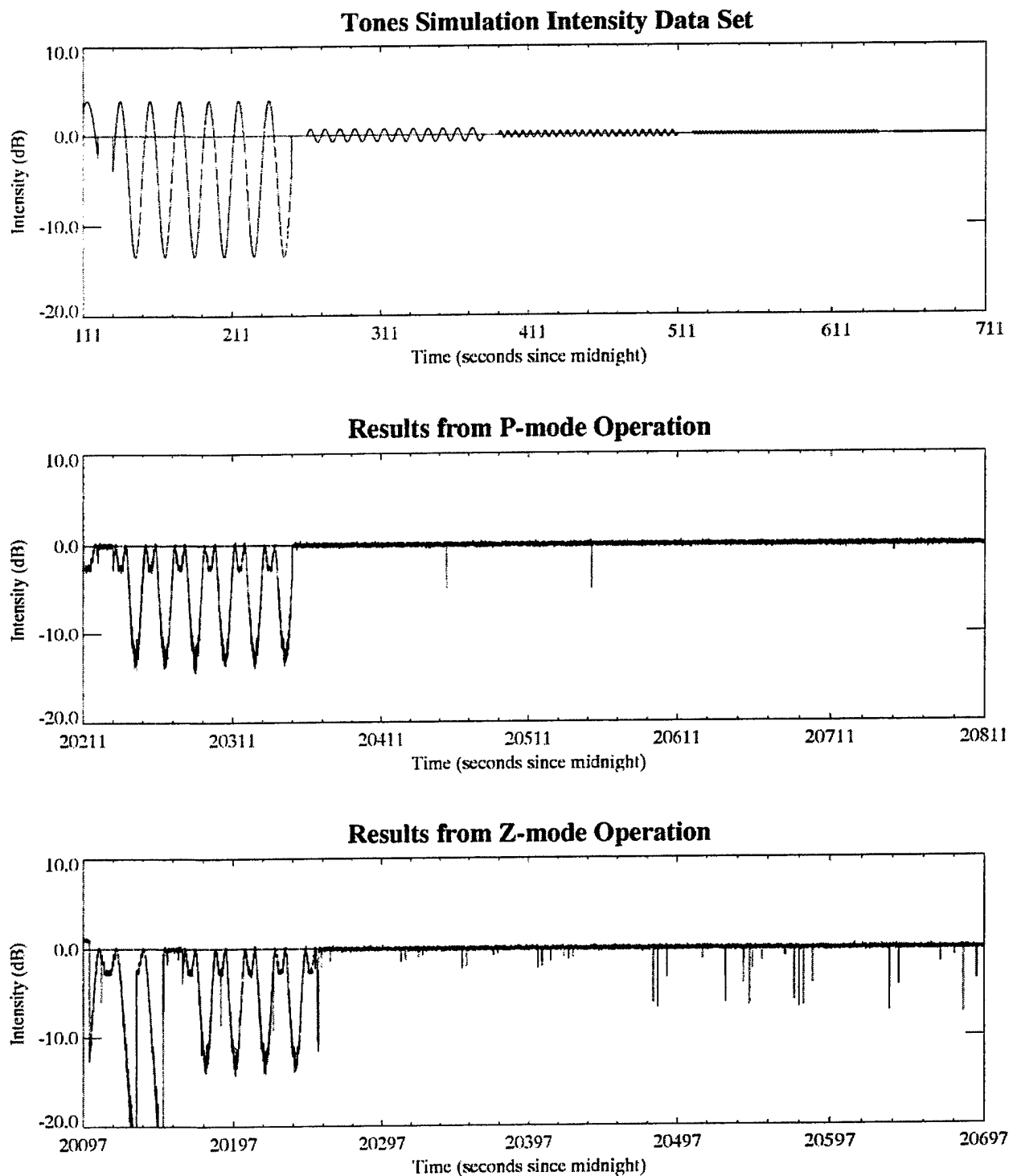


**Figure D-18.** L1 intensity results from the tones simulation data set. The top panel is the L1 intensity signal provided to the WPAFB simulator, the middle panel is the L1 intensity derived from the P-mode data, and the bottom panel is the L1 intensity derived from the Z-mode data.

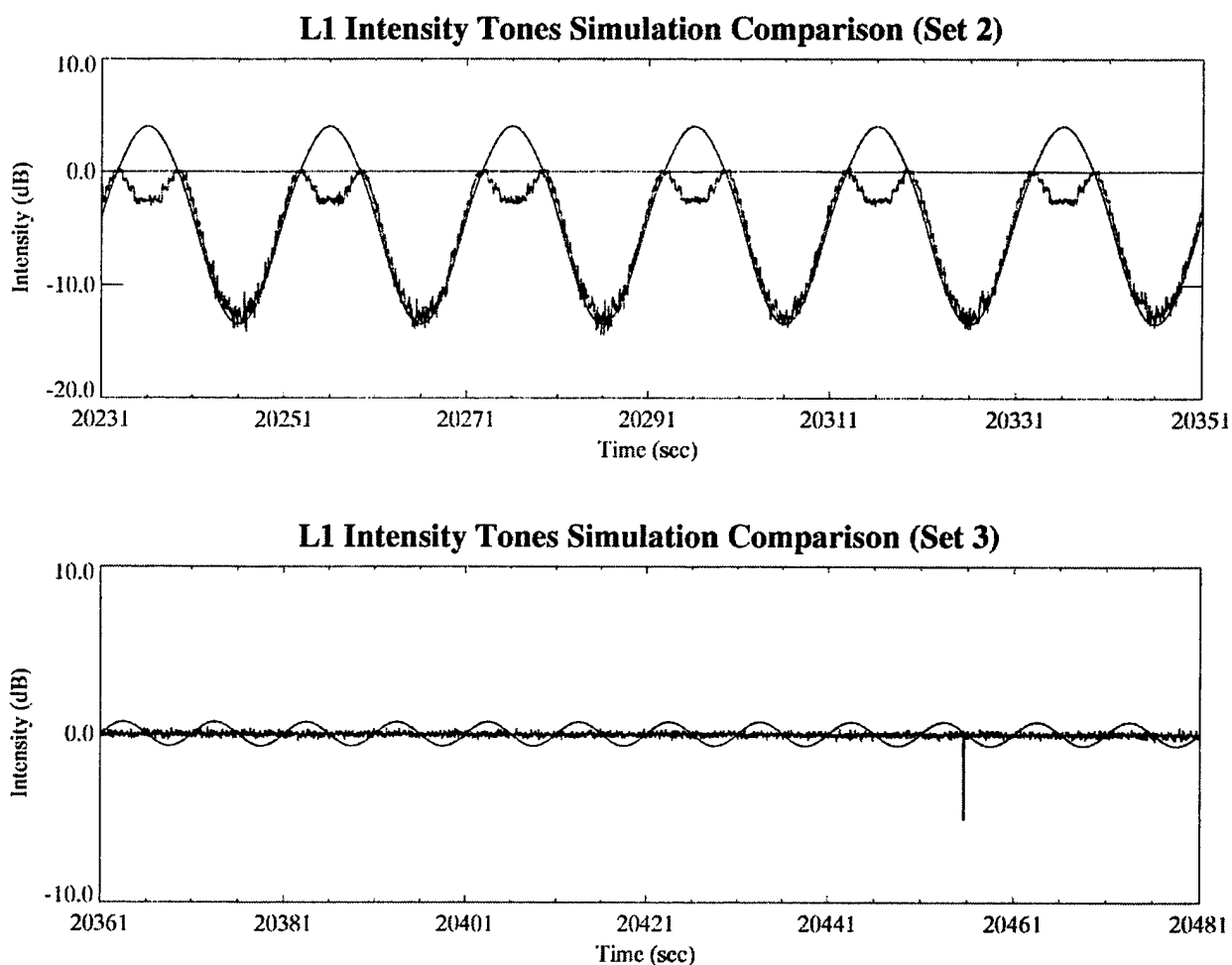


**Figure D-19.** Comparison of the L1 intensity for the second and third cases in the tones simulation set. The light curves are the input simulation values and the heavier curves are the P-mode output.

## D.2 Analysis of Nashua Z-12 Data

One complete pass of data collected using a Z-12 receiver from NWRA's Nashua, NH, facility was analyzed to address issues of observations of receiver noise characteristics as seen in the field. The pass selected, from PRN 11 at mid-day on 29 July 2002, was selected as a high-elevation pass collected during geomagnetically-quiet conditions. Figure D-20 shows (from top panel to bottom) the L1 intensity detrend and trend records, the satellite elevation and azimuth angles. The average  $S_4$  for this pass was about 0.03, consistent with what was observed in the WPAFB no-scintillation data set (see section 5). The  $S_4$  for the entire pass is shown in Figure D-21.

Given that we were looking at conditions in which it is highly unlikely for there to be any ionospheric scintillation, the  $S_4$  shown in Figure D-21 can be viewed as a combination of inherent system noise and multipath. The other two curves shown in this plot are estimates of a noise contribution to  $S_4$  from an algorithm developed by A. J. Van Dierendonck (Van Dierendonck, 1993; Equation 14 on page 1339) (dashed line, denoted the "AJ model") and one of uncertain origin from the original IMS system specification (Draper, 1993; Equation 18 on page 40) (dotted line, denoted the "Draper model"). Both of these model curves are functions of the mean signal level, and thus they reflect the variation in signal strength evident in the second panel down in Figure D-20. The

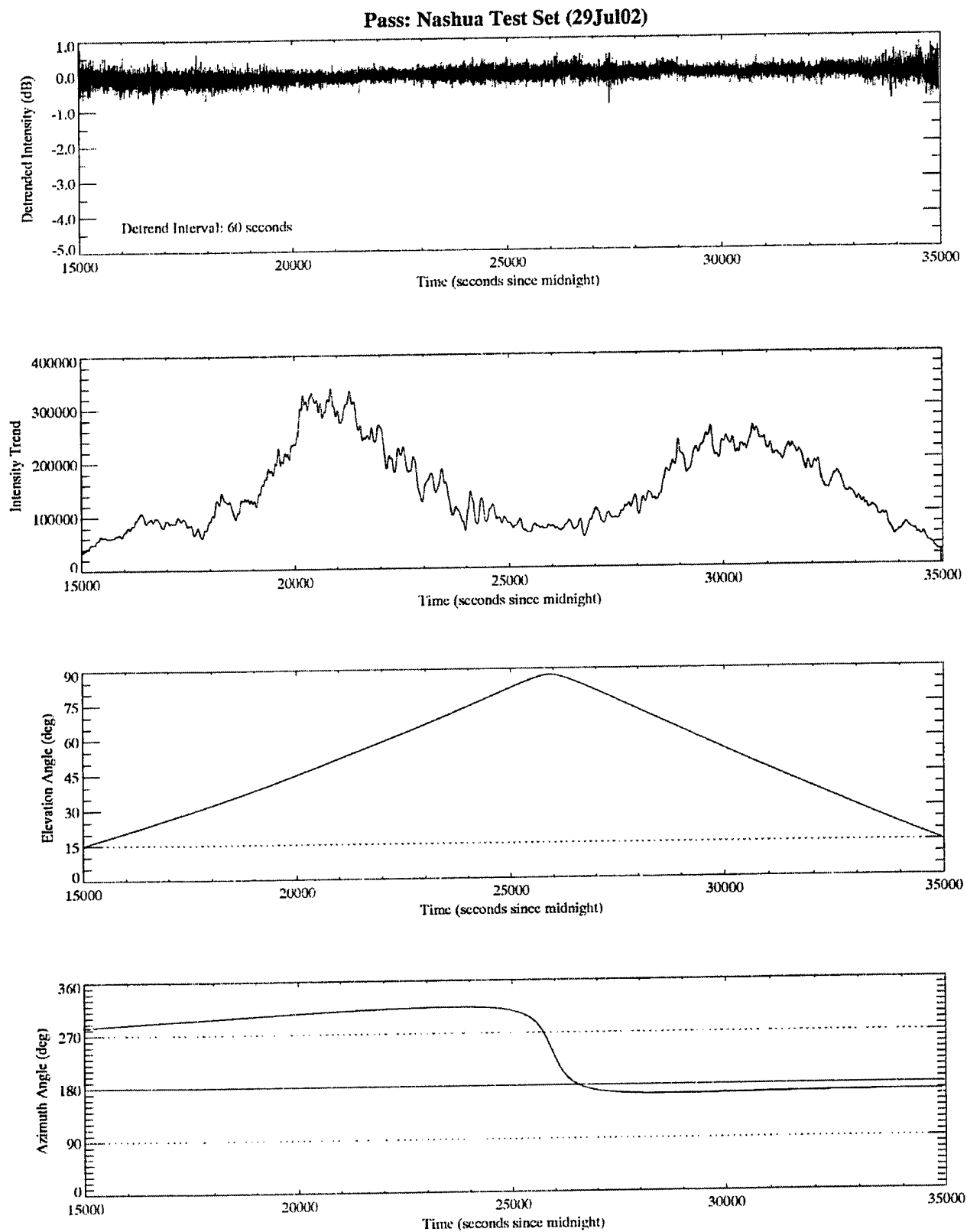


**Figure D-20.** The L1 intensity detrend and trend time-series records from the Nashua quiet-day data set with the satellite elevation and azimuth angles.

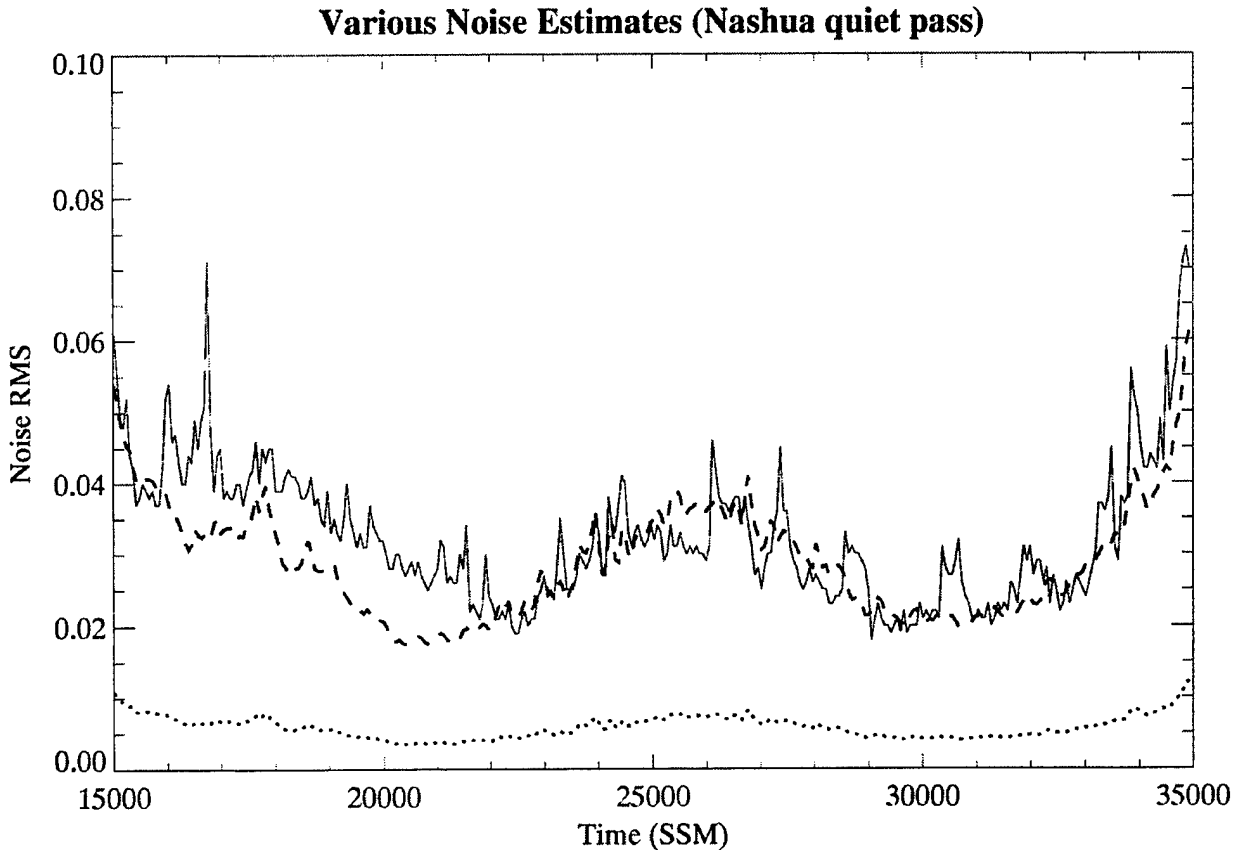


**Figure D-21.** The RMS detrended intensity ( $S_4$ ) calculated from the time-series in the top panel of Figure D-20 (solid curve). The other two curves are from the AJ model (dashed line) and the Draper model (dotted line).

results, however, are very different. The AJ model appears to do a much better job at characterizing the mean noise level across the path, while the Draper model does much less well. (A caveat here with regards to the use of the Draper model. This model includes a parameter,  $\gamma$ , identified only as "the average signal-to-noise ratio over the fading interval" which we have taken to be the SNR reported from the Z-12 receiver. This same value was used as input to the AJ model.)

At this time, we presume that the departures from the AJ model evident at the start of the pass and sporadically throughout the pass are mostly due to multipath effects. We hope to repeat this experiment at some later time to see if these structures repeat from day to day using the same PRN.

Returning to issues raised in the analysis of the no-scintillation cases collected during the WPAFB testing, Figure D-22 shows two randomly-selected samples of intensity (top two panels) and phase (bottom two panels) spectra from this data set. This shows similar characteristics to the spectra found in the WPAFB data (compare with Figures D-1 and D-2), including the smooth phase data with a slope of about 1.85 and a small uptick in the highest-frequency bin of the intensity spectrum in panel (a). This last feature is missing, however, in the spectrum shown in panel (b), and a qualitative study of the time-series records corresponding to the two spectra appears to support this presence of a bit more high-frequency noise in the sample in panel (a). Again, we have no suggestions as to the cause of this, and further investigation will be required to determine how often it is present.

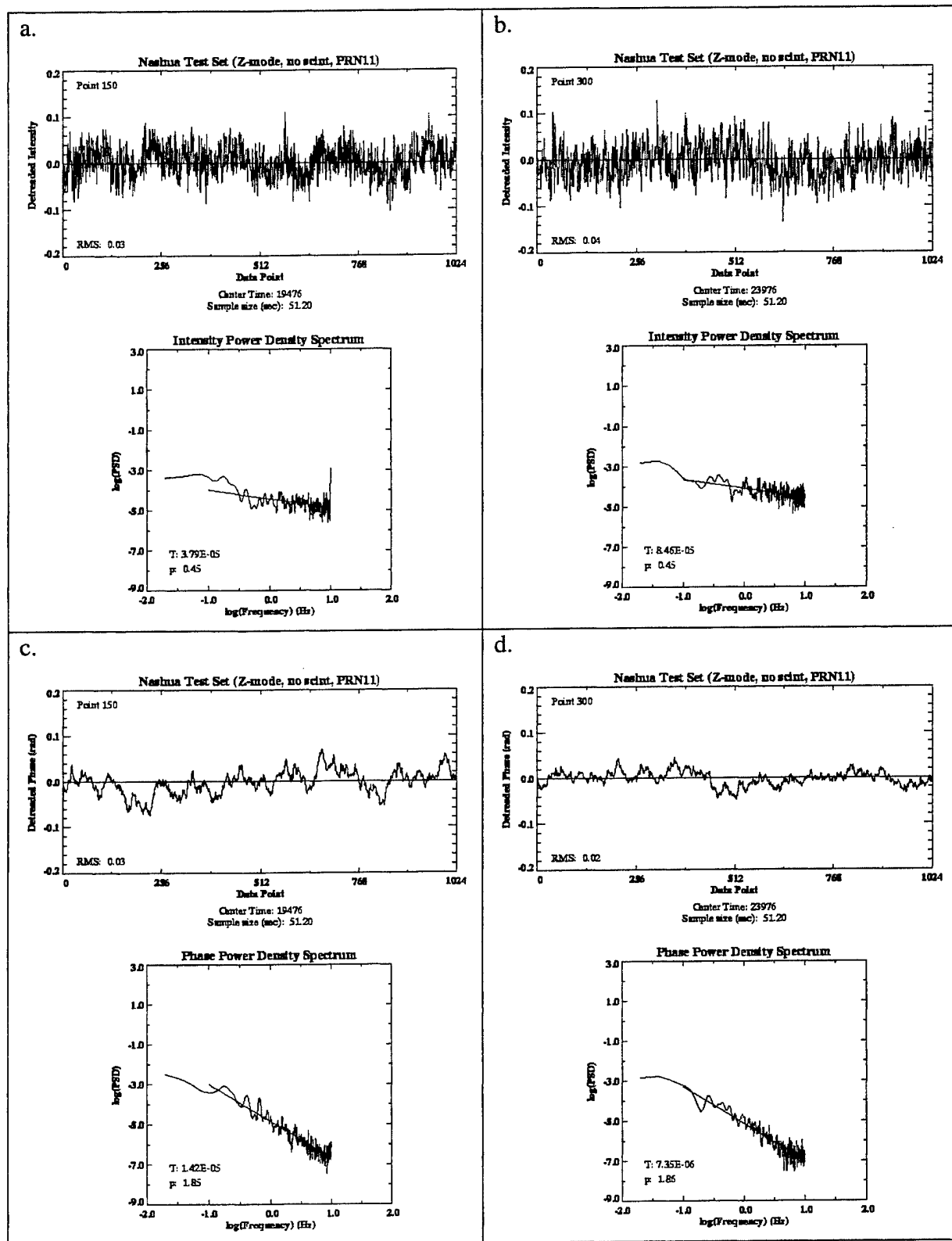


**Figure D-22.** Samples of intensity (panels (a) and (b)) and phase ((c) and (d)) time-series and power-density spectra from the Nashua quiet-day data set shown in Figure D-20.



### D.3 Analysis of Ascension Island Z-12 Data

Towards the end of the period we were provided eight one-hour data sets collected by two GPS receivers which were operated at Ascension Island during March 2002. The data were provided by Dr. Todd Pedersen of AFRL, and it included two hours taken during daylight hours (assumed to be non-scintillation cases, a very good assumption for equatorial latitudes) and two hours taken during local night hours just after sunset to provide scintillation cases. Of the two receivers, one was operating in standard Z-mode (named "localhost") and the other was periodically operating in Y-mode (named "scinda" – note that this is *not* a SCINDA receiver but a GPS receiver tagged with that name). Both receivers used output from the same antenna. The goal of this analysis is to determine the characteristics of both Z-mode and Y-mode data taken in the field and to compare the Y-mode results with the P-mode results from the WPAFB simulation tests. We will be presenting only two preliminary results in this report.

While we do not yet have logs, which identify times that the scinda GPS receiver was operating in Y-mode, we do believe that the data sample provided from the daytime of 19 March 2002 was from that mode. Figure D-23 shows two representative samples of phase (DCP) spectra taken from that hour of data. In both cases, the spectra are relatively flat similar to the P-mode "no scintillation" spectra collected in the WPAFB tests (see Figure D-1), but they are at a higher spectral level (by almost 10 dB) than the P-mode data and the spectra are more structured. At this time, it is impossible for us to even speculate on the source of either the structure or the higher noise level. At this time, we are simply reporting these as observations.

The second result we want to present is a possible case of contamination or interference in the GPS signal. Figure D-24 shows four spectra from a pass of satellite PRN08 on the evening of 8 March 2002. The two spectra on the left of this figure are from the localhost receiver and those on the right are from the scinda receiver. The two top panels are for the same time, and so are the bottom two panels. The feature of interest is the odd noise that is clearly present in both localhost samples, is completely absent in the first scinda sample, and starts part-way through the second scinda sample. This interference has a strong peak at about 4Hz, and is very periodic as can be seen in Figure D-25, which is an expanded plot of the data from localhost and scinda in the center of the data in the lower plots in Figure D-24. This signal is very regular, both in period and in amplitude. The source is a complete unknown, as is how this contaminant is present in data from one receiver but not the other when they share the same antenna.

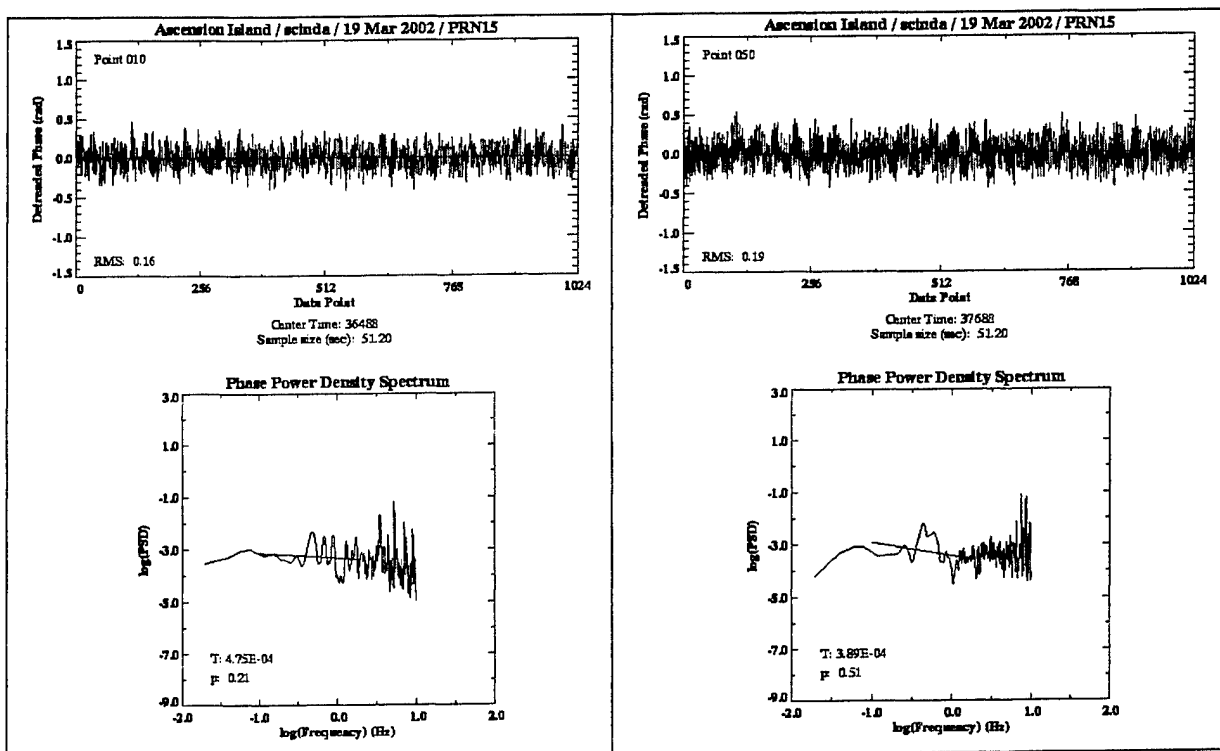


**Figure D-23.** Phase (DCP) spectra from the AFRL "scinda" GPS Ashtech Z-12 receiver located at Ascension Island. These data were taken when the receiver appears to have been operating in Y-mode (keyed) during a time when there was little if any ionospheric scintillation present.

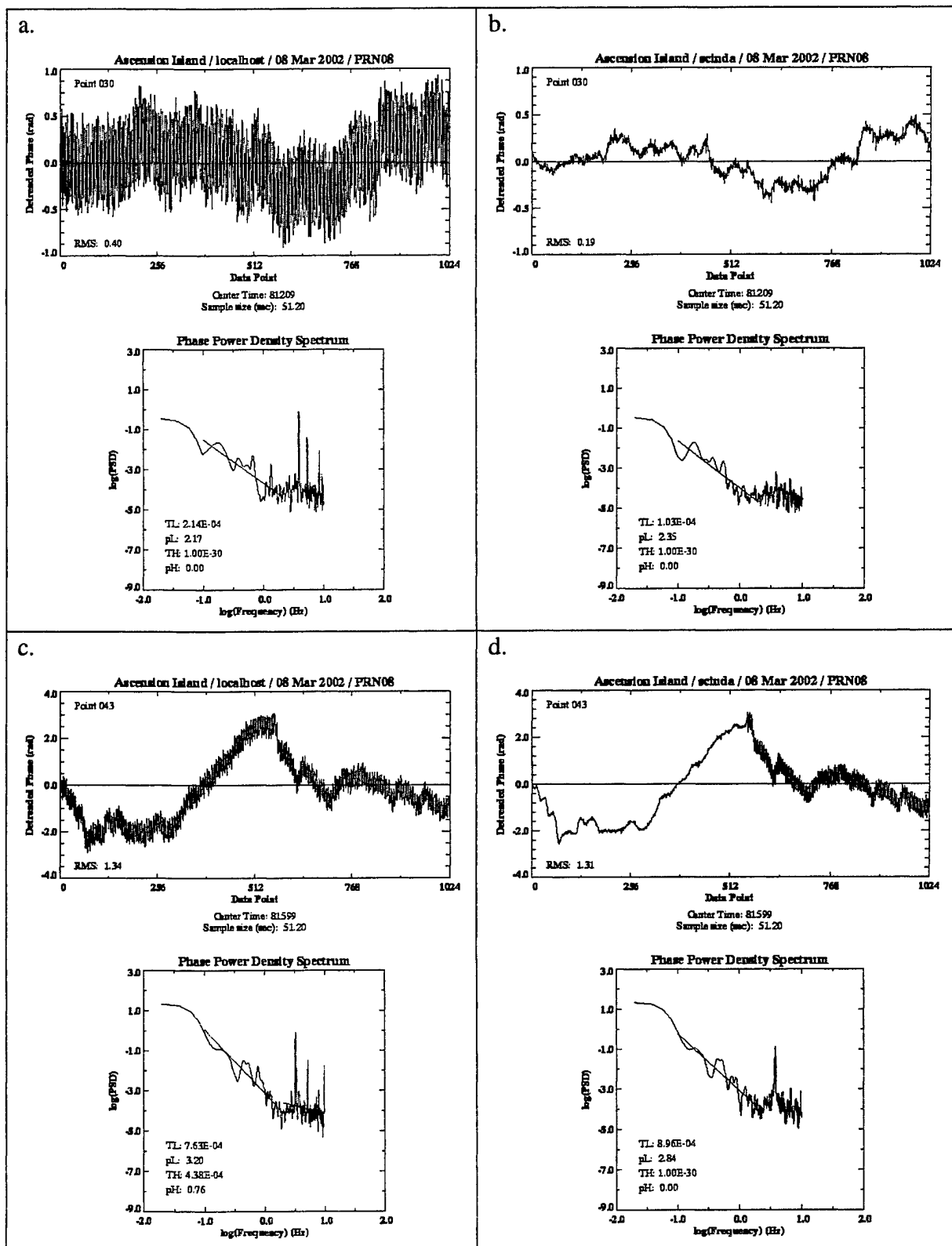


**Figure D-24.** Phase (DCP) time-series samples and spectra from data collected by the localhost (panels (a) and (c)) and scinda (panels (b) and (d)) GPS receivers at Ascension Island. These data are from the same GPS satellite and times.

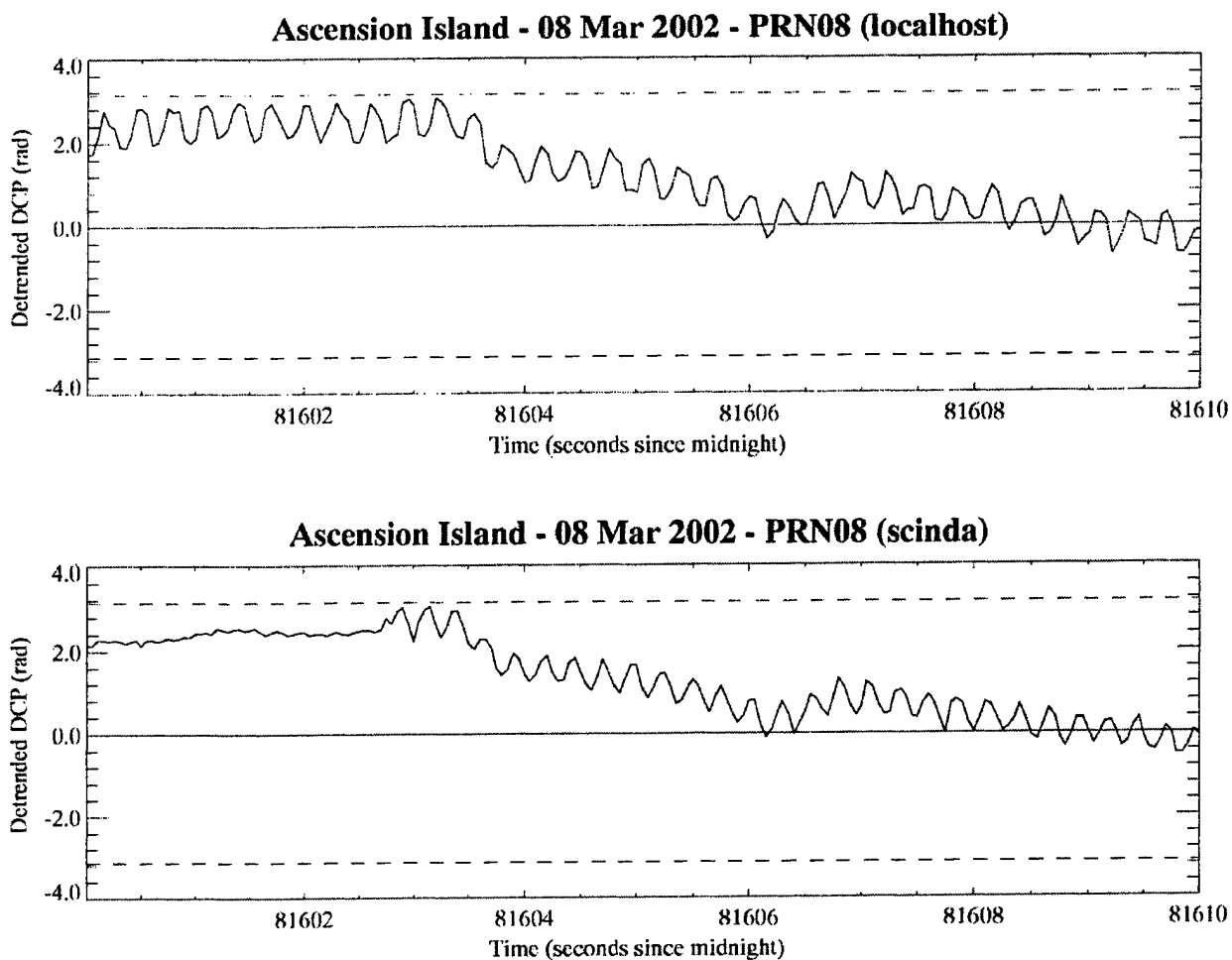


**Figure D-25.** Expanded plot of the phase (DCP) from the center of the time-series records in the two bottom panels of Figure D-24. Data from the localhost GPS receiver is in the top plot and data from the scinda GPS receiver is in the lower plot.

## Appendix E

### Consultant Support under NWRA Sub-project AFRL-0005.24

by

John E. Rasmussen

**Diagnostic Instrumentation Coordination:** During this contract period NWRA has coordinated significant additions and enhancements to the HAARP suite of diagnostic instruments and the supporting infrastructure.

**Instrumentation Coordination:** NWRA has been involved in coordinating the installation of essentially all of the diagnostic instruments located at the HAARP facility as well as remote sites and in providing the infrastructure required for their successful operation. Examples include:

**Imaging Riometer:** NWRA has provided support in installing instrumentation, repairing moose damage to the antenna array, replacing cables and coordinating the performance testing of the instrument.

**30 MHz Riometer:** In addition to the work of Jens Ostergaard, NWRA has provided additional support in installing foundations and guy anchor points for the antenna array and has assisted in the installation and testing of instrumentation.

**Magnetometer:** NWRA coordinated the location and installation of both the Fluxgate Magnetometer operated by the University of Alaska Fairbanks and the Induction Magnetometer operated by the University of Tokyo.

**139 MHz Coherent Backscatter Radar:** NWRA provided the infrastructure for the 139 radar in the form of a support structure for the antenna array, a moose fence, a small shelter for the preamps and a standard instrument shelter for the radar and processing equipment.

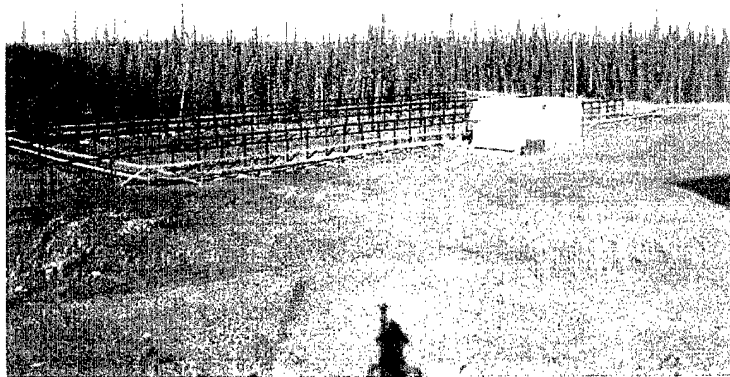


**Figure E-1.** Shelter and array support structure for 139 MHz Radar.

Incoherent Scatter Radar: In addition to the extensive work by Dr. Snyder to acquire an ISR for HAARP, NWRA provided the antenna support structure, fence and instrumentation shelter for the testing of the initial ISR panels.

Optical Imager: Coordinated the construction of a temporary shelter for Optical Campaigns. This shelter supported a five foot acrylic dome for the narrow field of view imager and its computer controlled AZ/EL mount.

Lidar: Although a lidar has not been installed at HAARP, several planning meetings were held to determine the long term requirements and resources required.

**Infrastructure Coordination:** NWRA has been instrumental in assuring that the HAARP diagnostic instruments and the associated research scientists have the facilities available to work efficiently. This support has ranged from major acquisitions such as instrumentation shelters to making sure that general purpose computer terminals are available in the shelters to provide network access without interrupting dedicated diagnostic computers.

The diagnostics access road was extended one half mile and two additional instrumentation pads built. The first additional pad, referred to as Science Pad 2, measures 100 ft square and is used as an HF receiving site. NWRA installed an instrumentation shelter with facilities and UPS power to support research operations. In addition NWRA provided the foundations on this pad for a NRL Spiracone HF antenna.

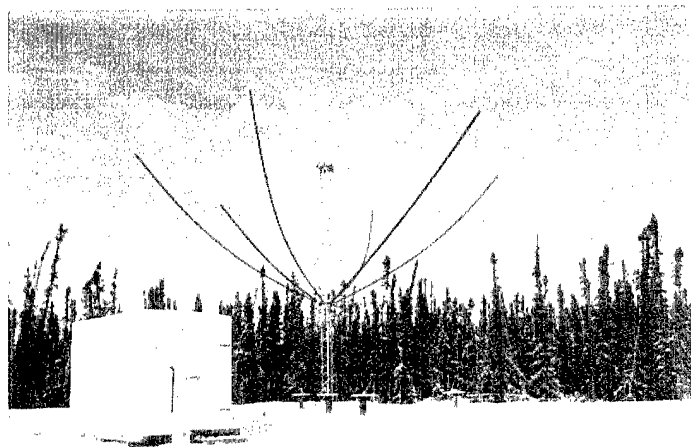


**Figure E-2.** Pad-2 Instrumentation Shelter and Spiracone Antenna

The second new pad, referred to as Science Pad 3 is located at the end of the diagnostics road, farthest from the HF heating transmitter. This site is designated for instruments requiring an RF quiet location, such as riometers, and optical instruments that need to be remote from light sources. The Optics Shelter, acquired by NWRA under an earlier contract was moved from Pad 1 to Pad 3. In addition, NWRA procured a second shelter for Pad 3, which supports a 30 MHz riometer, two magnetometers, an SEE receiver and two VLF receivers.

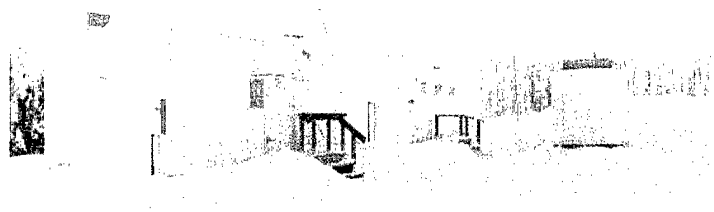


**Figure E-3.** Pad-3 Instrumentation Shelters

To replace the Optics Shelter that was moved from Pad 1, NWRA acquired and furnished a new instrumentation shelter. This shelter supports the HF Ionosonde, a seismic monitor, a GPS receiver for scintillation measurements and a Transit and GPS receiver used for TEC and tomography measurements.



**Figure E-4.** Pad-1 Instrumentation Shelter and Satellite Antennas

**Research Campaign Support:** NWRA has provided coordination as well as logistical and material support for general research campaigns along with ELF/VLF, optical and irregularity campaigns.

**HAARP Diagnostics Brochure:** NWRA developed and updated the brochure that included descriptions of over twenty HAARP diagnostics along with a general description of the HAARP facility and the diagnostic infrastructure.

**Special Activities:** NWRA has participated in many special HAARP activities including the RF Ionospheric Interactions Workshop, Summer School, Open House, Educational Outreach and Distinguished Visitor Tours.

NWRA has represented the HAARP diagnostics in program planning meetings, presenting the status of the instruments and advocating for the resources necessary to operate reliably and produce the best possible product.



## **Appendix F**

### **Consultant Support under NWRA Sub-projects AFRL-0005.24 & AFRL-0005.28**

by

Arnold L. Snyder, Jr.

1. **Future Directions for HAARP Panel:** The HAARP Program Directors at the Air Force Research Laboratory (AFRL) and the Naval Research Laboratory (NRL) chartered a Panel to consider what future directions HAARP might undertake. I served as the Panel Executive, with the sponsors prepared the Panel Charter, and with the Panel Chairman, Dr. Anthony J. Tether, organized three Panel meetings and coordinated the preparation of the final briefing. The final briefing was discussed with the sponsors on 19 June 2001 and presented to Dr. Timothy Coffey at NRL on 20 June 2001. On 27 September 2001, Dr. Tether, then DARPA Director, presented and discussed the briefing with the Office of Naval Research management. The Panel recommended the completion of HAARP to address five defense applications, including radiation belt remediation; the Panel also recommended the acquisition of an incoherent scatter radar to bring HAARP to a world class research facility. The Panel Chairman and Panel members Lewis M. Duncan and William E. Gordon were supported in their Panel work under consultant agreements with NorthWest Research Associates.
2. **Review Team for Assessment of Radiation Belt Remediation:** Following the Panel that considered future directions for HAARP, the HAARP Program Directors at AFRL and NRL chartered a Review Team to consider Panel methodology for radiation belt remediation. I served as the Team Executive and with the Team Ex Officio member Dr. Gregory P. Ginet (AFRL, Hanscom), organized two meetings, and coordinated the Team's report and executive summary. Team members included Drs. Harry E. Petschek and Michael Schulz, both supported as consultants by NorthWest Research Associates. The Review Team concluded that radiation belt remediation should be pursued and confirmed the methodology proposed by the Future Directions for HAARP Panel.
3. **USAF/USN/DARPA Memorandum of Agreement (MOA):** I, along with Paul Kossey (AFRL) and Edward Kennedy (NRL), drafted a memorandum of agreement to implement the recommendation of the Future Directions for HAARP Panel to cooperatively complete the HAARP HF transmitter and undertake a research and development program for radiation belt remediation through wave-particle interactions using the HAARP HF transmitter. The MOA was signed to share the construction costs to complete the 3600 kW HAARP transmitter. While the signed MOA does not include support for a research and development program, radiation belt remediation investigations are moving forward with USAF and DARPA support.
4. **Incoherent Scatter Radar:** At the 29 April – 2 May 2001 Santa Fe RF Ionospheric Interactions Workshop, Dr. John C. Kelly (SRI International) summarized the status of the ISR development being conducted for the National Science Foundation. In response to Dr. Kelly's summary, several scientists suggested that approximately eight panels of the SRI design would provide useful diagnostic measurements for HAARP and would be an affordable modular start for a HAARP ISR. I coordinated the development of an informal cost estimate for an eight-panel radar with SRI International. Drs. Lewis Duncan and William Gordon documented the measurements that could be made with the eight-panel radar.

I arranged for Dr. John Kelly (SRI International), Steve Hopkinson (VECO), Dr. Brenton J. Watkins (University of Alaska Fairbanks), and David K. Barton (Radar Consultant) to visit the HAARP site 18 October 2001 to discuss three ISR related topics: 1) interface and adaptation of the SRI design for employment at HAARP; 2) development progress and potential acquisition of an eight-panel radar as the first step in the modular development of a HAARP ISR capability; and 3) possibility of one or more SRI radar panels being made available for the Summer School 2002. On 19 October, Dr. Watkins, Mr. Barton, and I also visited Clear AFS to assess the condition of the AN/FPS-49/92 tracking radar dish and pedestal for potential use at HAARP. Based on the information gathered, a decision was taken not to pursue the AN/FPS-49/92 radar and/or pedestal.

I arranged for Dr. Paul Kossey, Edward J. Kennedy, and John E. Rasmussen to visit SRI International and the Stanford University Radio Science Field Site. The visit was held on 12 December 2001 and included an overview of the ISR development and then a visit to the Field Site to see the prototype subarrays undergoing test.

I arranged for Dr. Brenton J. Watkins (University of Alaska Fairbanks), David K. Barton (Radar Consultant) Dr. Lewis M. Duncan (Dartmouth College) and Dr. Allan C. Schell (Radar Consultant) to visit the Air Force Research Laboratory on February 7, 2002 to discuss three ISR related topics: 1) need for additional testing beyond what SRI International has accomplished; 2) development progress and potential acquisition of an eight-panel radar as the first step in the modular development of a HAARP ISR capability; and 3) specific diagnostic radar activities to be accomplished with FY02 radar designated funding. From the 7 February meeting came the recommendations for a NEC analysis to predict the performance of the full array and a radar range measurement program that could be accomplished with the radar panels operating in the receiver mode. Dr. Paul Kossey (AFRL/VSBXI) approached AFRL/SN and requested their support to conduct the NEC analyses and the radar measurement program.

AFRL/SN conducted the electromagnetic performance analyses and radar measurement program at their Ipswich, MA Test Facility and provided preliminary summary briefings of their work. I coordinated the analysis and measurement program with SRI International personnel, NSF, and HAARP radar advisors (David K. Barton, Lewis M. Duncan, William E. Gordon, Allan C. Schell, and Brenton J. Watkins). I arranged several meetings between the various participants. These included a planning meeting with AFRL/SN 23-24 April 2002, including HAARP advisors David Barton, Lewis Duncan, Allan Schell and Brenton Watkins and NSF representative Richard A. Behnke; 28 May 2002 to review Ipswich test progress with AFRL/SN and Allan Schell; and 13 June 2002 for an initial review of the Ipswich test results, including David Barton, Lewis Duncan, Allan Schell, Brenton Watkins and NSF representatives Richard A Behnke and Robert M. Robinson.

With AFRL/SN coordinated the planning for near-field calibration of the two SRI AMISR (Advanced Modular Incoherent Scatter Radar) panels when temporarily installed for demonstration at the HAARP field site, Gakona, AK.

With John Rasmussen's support, coordinated, acquired, and constructed the HAARP site's temporary radar infrastructure, including a 12' x 24' Alchem shelter for radar operation and 60 to 400 Hz electric power conversion, antenna support structure for two SRI radar panels, wooden safety and moose protection fence, and a 38' fiberglass pole on which the near-field

calibration transmitter and receiver were mounted. With John Rasmussen, coordinated the purchase of a Jetway PWM-120 PLUS 60-400 Hz electric power conversion unit.

With SRI and University of Alaska Fairbanks personnel, coordinated the planning for testing and demonstration of the radar during the 2002 HAARP / NSF sponsored Polar Aeronomy and Radio Science (PARS) Summer School.

With Gene Laycock (AFRL) and John Kelly (SRI International) coordinated the transportation and delivery of two engineering prototype Advanced Modular Incoherent Scatter Radar (AMISR) panels and a Jetway PWM-120 PLUS 60-400 Hz electric power conversion unit to the HAARP Gakona Research Station. With Michael Cousins and Todd Valentic (both from SRI International), installed the two radar panels on the support structure. I coordinated the installation of the Jetway unit in the shelter. This completed the temporary radar installation in preparation for demonstrations during the 2002 PARS Summer School.

In response to the decisions taken at the 7 February 2002 meeting at AFRL, Dr. Brenton Watkins (Geophysical Institute, University of Alaska Fairbanks) submitted to the Office of Naval Research a grant proposal for ISR related studies requiring the acquisition of eight AMISR panels. Additionally, NSF proposed to demonstrate eight AMISR panels at HAARP. This required infrastructure preparation including a support structure, movement of the shelter and Jetway unit from the initial HAARP site location, and the design and successful implementation of an access road, gravel pad, power, telephone and networking to a permanent ISR site; this work, with the exception of the radar support structure, has been completed. I coordinated the design of the radar foundation and proposed a team of HAARP's prime contractor (now British Aerospace Enterprises, [BAE]), their architectural engineering subcontractor USKH, and SRI's structural subcontractor VECO to design and develop a suitable foundation and scaffolding support structure to accept the HAARP radar panels.

A program review was arranged with SRI International and held on 11 December 2002, with NSF and HAARP representatives in attendance. The SRI International development schedule had slipped, with the first radar panels projected to be available for HAARP during fall 2003.

A meeting of government personnel and consultants was arranged and held at Hanscom AFB, MA on 15 January 2003. The purpose of this meeting was to review the findings of the 11 December 2002 meeting held with NSF and SRI International. A summary of the 15 January meeting was prepared and distributed to all attendees, Dr. Robert Robinson (NSF) and Dr. John Kelly (SRII). The conclusions reached at the meeting included: a) AFRL/SN will undertake a simulation of the antenna element unit and radar system performance using data provided by SRI; b) the University of Alaska Fairbanks (Dr. Brenton Watkins) under an Office of Naval Research grant should proceed with plans to acquire eight 32-element radar panels for deployment and test at HAARP; c) AFRL Ipswich facility personnel will determine the antenna aperture performance under various snow levels using antenna elements provided by SRI. The snow level radar performance data were acquired, analyzed, and provided to and discussed with SRI. A significant result is an increase in the return loss when the antenna elements are covered with snow; this result points to a requirement to either prevent the snow from building up or remove the snow to ensure adequate performance.

I coordinated the schedule and arrangements for the HAARP ISR Advisory Team to participate in the SRI International Design Review 9-11 July 2003. This Review was the final technical assessment prior to SRI International's subcontractor (Sanmina) manufacture of 40 antenna

element units (AEUs) for component and radar design verification testing. At this July 2002 Review, David K. Barton and Livio Poles were appointed and agreed to serve on a separate SRI International Radar Advisory Panel. Allan C. Schell serves as an ex-officio member of the Advisory Panel.

I coordinated the schedule and arrangements for the HAARP ISR Advisory Team to participate in the SRI International Design Review 9 January 2004. This review considered the Sanmina manufacture of 40 antenna element units and associated test results. The SRI Advisory Panel gave the go-ahead for the manufacture of 512 AEUs. The first radar panels available to HAARP were rescheduled for late spring or early summer 2004.

5. **Aircraft Alert Radar:** I served as an integrated product team (IPT) member in coordinating a joint HAARP site team to conduct an AN/TPS-63 electromagnetic compatibility and siting survey. Team members included representatives from HAARP, Office of the Secretary of Defense, Marine Corps, and Alaskan Air Force units from Eielson and Elmendorf AFBs. The IPT arranged for logistical support from the Elmendorf and Eielson units. During assembly of the transportable radar, damage was noted that was likely caused by fork lifting the unit from the wrong side. Attempts were made to operate the radar. Several damaged parts were replaced, but the radar still did not operate correctly. Following the January 2001 test period, the IPT arranged for the swap of the damaged radar with a USMC unit in Barstow, CA and a second test period was scheduled. I prepared and coordinated flight test plans with Harley McMahan, a Gakona, AK bush pilot to fly a Super Cub as a test target. The rescheduled tests were successful and interest was expressed to have the radar available at HAARP to support Alaskan Air Force exercises. The radar was then transported to Eielson AFB, AK for maintenance and installation of an identification friend or foe (IFF) unit. The radar was returned in July 2001 to the Gakona HAARP site following repair at Eielson AFB, AK. The radar was temporarily installed for approximately 10 months of operation anchored to the gravel pad. This older version of the AN/TPS-63 was deemed inappropriate (being an older radar, the configuration was not standard and logistically not supportable) for Alaskan Air Force exercises and was subsequently removed from the HAARP site.

ONR established a contract with a USN organization at Patuxent River Naval Air Station, MD to integrate a 60 kW Furuno S-band radar with a transponder-based traffic control and collision avoidance system (TCAS) and SureTrak aircraft tracking and data fusion software. In August 2003, this integrated system was installed at HAARP to replace the Pathfinder S-band radar and provide improved aircraft detection and tracking in the proximity of HAARP's FAA defined controlled firing area. With Edwin Lyon drafted and implemented a test plan for evaluating the radar/TCAS/SureTrak system against bush aircraft flown in the HAARP area. I arranged for Harley McMahan to fly a Super Cub as an aircraft test target. With Edwin Lyon evaluated the test results, which revealed ground clutter masking of radar returns from target aircraft flying in the southeast quadrant. The TCAS system and the SureTrak software perform well.

6. **Permafrost Observatory:** Recent analyses indicate a correlation between climate change and permafrost temperatures, especially in marginal permafrost areas such as those found at HAARP. Additionally, steps must be taken in facility design and construction at HAARP to ensure permafrost stability for the system design lifetime. I recommended to HAARP management that a permafrost observatory be established at HAARP to monitor permafrost conditions and to be used as an alerting system if Alaskan warming continues. I coordinated the

University of Alaska Fairbanks (Geophysical Institute and International Arctic Research Center [IARC]) submission of a proposal and establishment of an ONR grant for a HAARP permafrost observatory. Plans for the work associated with the Observatory were also coordinated with the prime contractor (BAE), USKH, and their permafrost consultants to ensure the proposed work compliments and does not duplicate prime-contract activities.

7. **PARS Summer School:** Following HAARP's Summer 2000 Student / Faculty Science Campaign initiative, the Geophysical Institute, University of Alaska Fairbanks, under the Polar Aeronomy and Radio Science (PARS) grant, organized and conducted the Summer Schools. Working with HAARP's management team, I secured the joint sponsorship of the Summer Schools by the National Science Foundation and the development of announcement flyers by the Geophysical Institute.

The student-faculty experiment reports from the 2000 Summer School were edited and provided as an informal report to the sponsors. The sponsor requested that the informal report be published as an Air Force Research Laboratory (AFRL) Technical Memo. The informal report was edited to a uniform format and published as AFRL-VS-TR-2001-1668: Scientific Report Summer 2002 Student/Faculty Science Campaign, July 31-August 8, 2000, Arnold L. Snyder, Jr., Editor.

I coordinated the participation of NWRA consultants William Gordon and David Barton in the 2002 Summer School. David Barton provided an introductory radar lecture and William Gordon discussed the development history of incoherent scatter radar.

7. **Clear AFS Surplus Equipment and Furniture:** I visited Clear AFS, AK on 13-14 February to survey surplus equipment and furniture that might be useful for the Gakona, AK HAARP site. I tagged and photographed equipment and furniture believed to be useful for HAARP. I then coordinated transportation support from Elmendorf AFB and personnel support from the prime contractor., AFRL (Gene Laycock), and NWRA (John E. Rasmussen) to move the items from Clear AFS to Gakona, AK. This work was accomplished 3-10 May 2002.
8. **Statement of Work for Operation and Maintenance (O&M) and Completion of 3600 kW HAARP:** Participated in discussions to define the nature of the O&M SOW that was the basis of a FY02 competitive source selection; drafted several sections for the O&M SOW and coordinated on several drafts. Participated in discussions to define the nature of the SOW to complete HAARP to the 3600 kW RF power level. These discussions resulted in a decision for a sole source contract to complete HAARP with Advanced Power Technologies, Inc. (subsequently acquired by British Aerospace Enterprises [BAE]). I drafted several sections of the sole source SOW and coordinated on several drafts.
9. **Memorandum of Agreement with the Intelligence Systems Support Organization (ISSO):** With James C. Battis (AFRL), I drafted a memorandum of agreement (MOA) that defines responsibilities of the host HAARP and the resident tenant ISSO. The draft MOA includes HAARP site security and safety briefings.
10. **Science Campaign Support:** With John Rasmussen, I assisted with preparations for the 21 January – 8 February 2003 HAARP Optical Campaign. I operated the Digisonde for the HAARP Optical Campaign coordinating the modes of operation and data acquisition with

Campaign experimenters. During the Campaign, prepared an abbreviated guide to the Digisonde explaining how to setup and control the Digisonde operating modes and data acquisition over the Internet.

With John Rasmussen, I assisted with preparations for the 1-4 March 2003 HAARP Irregularities Campaign. Two four-hour periods were devoted to airglow observations; during these periods, the Digisonde operating mode and data acquisition were tailored to the optical measurements being conducted. During the second four-hour period, the Digisonde was operated cooperatively with the Kodiak, AK SuperDARN facility from the Geophysical Institute, University of Alaska Fairbanks.

With Dr. Frank T. Djuth, I suggested synchronizing and driving HAARP's HF array with the Digisonde waveform to acquire Digisonde skymaps of HF induced irregularities. I coordinated and conducted such a Campaign, 27 August – 1 September 2003. Preparations included obtaining support from Digisonde experts Bodo Reinisch and David Kitrosser (University of Massachusetts at Lowell [UML]), BAE planning and implementation of the Digisonde and HF synchronization, optical imager installation, and initial RF system checkout against satellites and meteors. James Secan (NWRA) provided information for several satellite passes; the synchronized system was unable to detect the satellites (radar cross section too small at the approximate 8 MHz frequency employed), but was successful in detecting meteors. This qualified the synchronized system for the night operations of 30 August – 1 September. Data acquisition was successful on three nights. This RF diagnostic technique will be available for use during future science campaigns.

11. **HAARP Digisonde:** During the 2003 HAARP Optical Campaign, I uncovered an apparent discrepancy between Digisonde directional ionograms and skymaps. I arranged for the UML repair of and update for the Digisonde and participation in the 27 August – 1 September 2003 science campaign. This work was accomplished 25-30 August 2003 and included UML installation of an upgraded digital signal processor board; this resulted in spatially consistent Digisonde directional ionograms and skymaps.
12. **DD Form 1494 Preparation for 3600 kW HAARP:** With Mr. Edwin Lyon, III (Science Applications International Corporation) and Dr. Michael McCarrick (BAE Systems) prepared a draft Application for Equipment Frequency Allocation (DD Form 1494) for the completed 3600 kW HAARP transmitter. Submission of the DD Form 1494 was coordinated through Ms. Suzanne Banacos (AFRL) and Mr. Gary Weaver (Electronic Systems Center Frequency Management Office).
13. **DD Form 1494 Preparation for HAARP ISR:** With Dr. John C. Kelly (SRI International) and Suzanne Banacos (AFRL), I coordinated the preparation and submission of the request for frequency certification and the Air Force Request for Frequency Assignment. Authorization to radiate with eight 32-AEU radar panels was granted through 31 October 2006.
14. **Planning and Support for Distinguished Visitor HAARP Tours:** I assisted with preparations and participated in the 10-12 July 2002, 20-24 July 2003, and 12 November 2003 Distinguished Visitor HAARP tours.
15. **HAARP Open House Planning and Support:** I assisted with the planning and preparations for and supported the 25-26 August 2001 HAARP Open House

16. **Meeting and Workshop Participation:** I participated in HAARP Strategic Planning, prime-contractor review, various university reviews, NorthWest Research Associates, Inc. review, PARS review, and HAARP campaign planning meetings. I participated in the 2001, 2002, and the 2003 Santa Fe RF Ionospheric Interactions Workshops.





## **Appendix G**

### **Consultant Support of the HAARP Classic Riometer under NWRA Sub-project AFRL-0005.24**

by

Jens Ostergaard

The 30 MHz riometer is part of the HAARP diagnostic instrumentation suite. The consultant work performed under this contract, over the last three years, included three tasks: maintenance and data-quality assurance; development of a procedure and software for computation of quiet-day curves; and development of a new riometer with embedded control.

#### Maintenance and Data-quality Assurance

Operation of the riometer was monitored from Maine. Data were transferred from the site to Maine for analysis, and calibrations were performed when necessary. The consultant visited the HAARP site once per year for maintenance work on the antenna array, cables, and computer system.

The instrument operated quite reliably throughout the period. The software has been stable, but a few hardware problems occurred. These included a broken balun in the antenna system, shifting of guy wires in the antenna array, and failure of a power supply in the computer. All were repaired.

#### Computation of Quiet-day Curves

Traditionally, the quiet-day curve for a riometer is determined by averaging data from a number of ionospherically quiet days. This procedure works quite well in the polar cap, where quiet days are abundant. At a sub-auroral location such as HAARP, however, very few truly quiet days occur. Thus, using the averaging method will produce an inaccurate quiet-day curve, at best.

It is straight-forward to compute the antenna temperature for a riometer array if the radiation pattern and the sky-noise temperature over the antenna aperture are known. The radiation pattern can be computed accurately using the Numerical Electromagnetic Code (NEC), and a map of the sky-noise temperature at 137 MHz is available. The sky-noise temperatures can be scaled to lower frequencies (including 30 MHz) using an inverse power relation with an exponent of -2.3.

Software was designed to compute the antenna temperature for a riometer antenna array as a function of location and sidereal time. The computed quiet-day curve has been used at HAARP for two years and has been proven to be very accurate. The results of this work were presented at the April 2003 Ionospheric Modification Workshop in Santa Fe.

#### Design and Construction of a New Riometer

The current riometer dates from the 1970s. It has run without hardware failure for many years. It is known to be non-linear, however, and to have periodic instabilities that destroy the calibration.

A new, inherently linear riometer was developed under this contract. The noise-balancing radiometer principle, used in both riometers and microwave radiometers, is used. This principle compares the antenna noise temperature with the noise from a stable, adjustable noise source in the riometer.

A stable noise source, combined with digital injection, is used for the noise-balancing process in the new riometer. An embedded microprocessor is used to control the noise balancing and data transmission over a serial link to the HAARP diagnostics computer network. An offset noise source is injected into the antenna branch of the riometer when the antenna noise temperature is less than 2000 K. This way, very low antenna noise temperatures can be measured during large ionospheric events, in which traditional riometers reach their lower limit.

The new riometer has been tested at HAARP and is slated for final installation in the summer of 2004.

## Appendix H

### ITS10S/Tomography Data Flow and Archiving Procedures

by  
John Begenisich

#### Computers Used

**ITS10 PCs** – The PCs connected to the ITS10S receivers run Windows NT 4.0. With the exception of the PC at Gakona, which coordinates its clock via Maestro, a GPS receiver is used to maintain precise time on the computer. Each computers' disks contain an archive of all relative TEC data acquired at that station. Administration of the PCs is performed remotely using pcAnywhere.

**Poi** – Poi is a PC running Linux located at the NWRA offices in Bellevue, WA. Its primary computational task is to build tomography images. Its disks contain an archive of all TEC from all ITS10S and UAF receiver stations. In addition, archives of tomography images, NORAD elements, and ionosonde data also are maintained on Poi.

**Gedds** – Gedds is the UAF server that provides data from the UAF receiving stations.

**Maestro** – Maestro is the main HAARP server, located at the Gakona site. It is used for building the NetCDF files and plots that are displayed on the HAARP web site. (The notable exception is that, due in part to the significant amount of CPU power required to build tomography images, said images are generated on Poi instead of Maestro.)

**Ash** – Ash is the PC attached to the GPS receiver at the HAARP site. Its task in this context is to produce absolute TEC from relative TEC recorded at the ITS10S stations.

#### Acquiring Relative Slant-path TEC from the ITS10-S Receivers

Attached to each ITS10S receiver is a PC running Windows NT, which facilitates data capture and transfer. The data-acquisition software generates four ASCII data files associated with each Transit-like satellite pass. The filename format is the date and time of the pass, a single-character station identifier, and a three-character extension indicating what kind of data the file contains. For example, a pass at 2003-08-12 23:42 from the Gakona ITS10 station would generate the following files:

- 200308122342g.its – full 50-Hz quadrature-component data
- 200308122342g.pro – processed intensity and phase data
- 200308122342g.mag – receiver diagnostic information
- 200308122342g.snt – scintillation data

After these four files are generated, the .its file is compressed and archived on the PC. Then, a .zip archive containing all four data files is built, and, using the Windows Remote Access Services (RAS), the PC creates a modem connection to the Internet via a local Internet Service Provider (except for Gakona, which is on the HAARP LAN, and therefore is able to send data via Ethernet.) The .zip file is transmitted using FTP to Maestro, the main HAARP server (link "A" in Fig. H-1). In addition, some other information is sent to Maestro as well: the pass.pln and its.log files, which are used for the "upcoming-passes" and "pass-summary" Web pages (for an example, see: <http://maestro.haarp.alaska.edu/haarp/its10/gakona/passplan.html>) and for determining whether any data have not been transmitted successfully from the ITS10S stations.

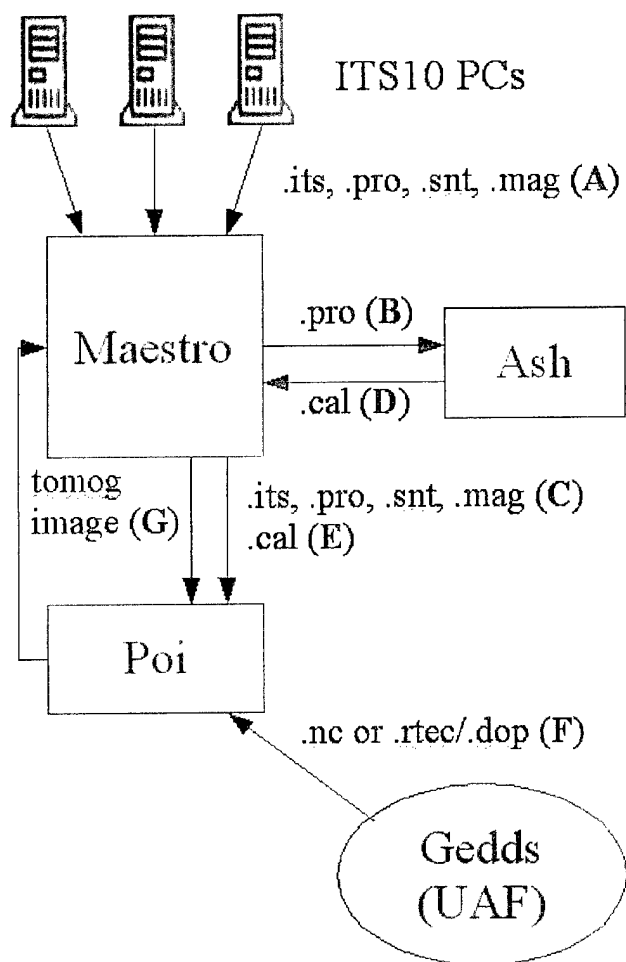


**Figure H-1.** Flow of data from ITS10S stations to HAARP's Maestro computer and of those data plus relative TEC records from the UAF stations via its Gedds computer to NWRA's Poi computer for development of tomographic images transmitted to Maestro for posting on the HAARP Web site.

#### Automatically Retrieving Missing Data from the Remote ITS10S Sites

Due to fluctuations in the quality of telephone connections at the remote ITS10 sites in Alaska, data occasionally are unable to be transmitted to the HAARP site. To compensate, a system is in place to retrieve this missing data from the ITS10S PCs.

On each ITS10S PC, an `its.log` file is maintained. It is essentially a list of satellite passes that the receiver has acquired or attempted to acquire. Software running on Maestro compares the `its.log`'s list of passes with data that have successfully made it to Maestro's stores. Any missing data are listed in a text file, which is retrieved by the ITS10S PC as part of the data-transfer sequence and sent to Maestro during the PC's next regular data transmission session.

#### Onto the World Wide Web

Once the ITS10S data arrive at Maestro, NetCDF files and plots are generated and made available on the HAARP Web site (example: <http://137.229.36.30/cgi-bin/its10/plot-tec.cgi>). At this time the data are sent via FTP to two places: to Ash, the PC attached to the GPS receiver (link "B" in Figure D-1), and to Poi (link "C" in Figure D-1), a computer located in NWRA's offices at Bellevue where it is archived and used for building tomography images.

## Absolute Slant-path TEC

Upon receiving relative TEC data from Maestro, the Ash PC sends those files back to Maestro, via FTP, along with the information required to "calibrate" these data (link "D" in Figure D- 1). Maestro then builds ASCII (".cal") and NetCDF (".cal.nc") files containing absolute slant-path TEC. The new absolute-TEC files and plot replace the old relative-TEC file and plot for that satellite pass. Maestro then FTPs the calibrated data to Poi for archiving (link "E" in Figure D-1).

## Building Tomography Images

Tomography images are built on Poi from ITS10S and UAF NetCDF files. Each ITS10S PC's its.log file is sent to Poi after each satellite pass. When a new its.log file arrives on Poi, software scans it to see if data were acquired from any OSCAR satellite that reached an elevation of at least 60° at at least one ITS10S station. If this condition is met, the code attempts to build a tomography image for that satellite pass.

The tomography image building process is as follows:

1. Retrieve NetCDF data for all ITS10 stations from local archive.
2. If present, get UAF data from local archive on Poi. If data are not available there (as is the case for all new tomography images), make an FTP connection (link "F" in Figure D-1) to Gedds (the UAF server). The code first looks for a NetCDF file and downloads it if it is available; otherwise it downloads .rtec and .dop files and generates a NetCDF file from them instead. UAF NetCDF files, whether downloaded or built locally, are placed in local archive, so that the tomography image is rebuilt (to incorporate tardy data, if necessary); an additional connection to Gedds is not required.
3. Check the lengths of satellite passes for each station. To build a proper tomography image, we require there be data from at least three stations, and the record from each station must be at least 600 sec in length. If these conditions are not met, the image-building process is aborted.
4. Employ the NWRA ITS inversion processor to build the tomography image.
5. FTP the tomography image to Maestro (link "G" in Figure D-1) for display on HAARP Web site (<http://137.229.36.30/cgi-bin/its10/plot-tom.cgi?archive>).

## Tardy Data

To account for data that arrive on Poi tardy due to occasional communication failures, tomography images are rebuilt 30 minutes, 3 hours, 1 day, and 4 days after their initial construction, as well as when an its.log file indicates previously absent ITS10S data now exists.